NASA Technical Paper 1803

Experimental and Analytical Study of the Longitudinal Aerodynamic Characteristics of Analytically and Empirically Designed Strake-Wing Configurations at Subcritical Speeds

John E. Lamar and Neal T. Frink

JUNE 1981

NASA

NASA Technical Paper 1803

Experimental and Analytical Study of the Longitudinal Aerodynamic Characteristics of Analytically and Empirically Designed Strake-Wing Configurations at Subcritical Speeds

John E. Lamar and Neal T. Frink
Langley Research Center
Hampton, Virginia

National Aeronautics
and Space Administration

**Scientific and Technical
Information Branch**

1981

SUMMARY

Sixteen analytically and empirically designed strakes have been tested experimentally on a wing-body at three subcritical speeds in such a way as to isolate the strake-forebody loads from the wing-afterbody loads. Analytical estimates for these longitudinal results have been made using the suction analogy and the augmented vortex lift concepts. The comparisons show that the pitch data, both total and components, are bracketed well by the high- and low-angle-of-attack modelings of the vortex lift theories. The lift data are generally better estimated by the high-angle-of-attack vortex lift theory and then only until maximum lift or strake-vortex breakdown occurs over the wing. The compressibility effects noted in the data for the strake-forebody lift are explained theoretically by a reduction in the wing upwash associated with increasing Mach number which leads to smaller potential and vortex lifts on the forward lifting surfaces.

Aerodynamic synergism was investigated experimentally; as expected, there was an additional lift benefit for all configurations as a result of the interaction. Furthermore, there was a delay in pitch-up associated with the synergism.

Mach number has a small effect on the "additional lifting surface efficiency factor" whereas changes in the strake geometry have larger effects. Geometry changes such as increasing area or slenderness ratio generally produce a more efficient strake. However, it is possible to obtain the larger values of this factor with approximately half the area of the original, also the largest, gothic strake by using a suitable analytical design for the gothic leading edge. These results correlate well with strake-vortex-breakdown observations in the water tunnel.

Strake geometry is also important in determining the maximum lift that a configuration will develop, with gothic leading-edge shaping being preferred for ratios of strake area to wing reference area of less than 0.25 based on the strakes considered herein.

INTRODUCTION

Strake-wing aerodynamics are becoming of increasing interest due to the mutual benefits derived from the combination. (See ref. 1.) For the wing, these benefits include: (1) minimal interference at or below the cruise[1] angle of attack, (2) upper-surface boundary-layer control at moderate to high angle

---

[1]In particular, at cruise it is possible that the small impact of the strake may only be attainable by the use of camber or dihedral so as to "unload" the strake under this condition. Neither one of these is addressed in this paper, as only planar strakes are considered.

of attack due to the strake vortex, (3) load redistribution due to effective use of the upper surface, and (4) reduced area required for maneuver loads. For the strake, these benefits are: (1) strake vortex strengthened by upwash from the main wing and (2) the need for only a small area - hence, wetted area and comparatively lightweight structure - to generate its significant contribution to the total lift because the strake provides large amounts of vortex lift.

In view of these strake benefits, it is appropriate to consider how best to maximize them by proper shaping of the strake. One way would be to use an empirical approach based on previous knowledge, a second would be cut-and-try, a third would be analytical, and a fourth would be a combination of the preceding three. At the time of development of the lightweight fighters F-16 and YF-17, only the first two procedures were available. After these airplanes were developed, reports were written, references 2 and 3, which summarized the wind-tunnel test results of about 100 different strakes for each airplane, along with an analysis to help guide future strake-wing integrations. However, these reports still do not give the aerodynamicist an analytical method for shaping the strake leading edge. One possible approach would be to isolate some critical parameter, such as leading-edge suction, and then design the strake in the presence of the wing while monitoring this parameter.

As a step in this direction, a simpler approach with the emphasis on delaying strake-vortex breakdown has been developed and reported in reference 4. There the shape of the isolated strake is determined uniquely in a flow which is simpler but related to the three-dimensional potential by specifying primarily the leading-edge suction distribution. Reference 4 reports the first design application of this method in which the resulting shape was area scaled until the three-dimensional suction distribution over both the strake and the wing was considered to be acceptable. The wind-tunnel test of the strake-wing combination showed it to perform well. However, to determine if this method could be used to develop better strakes, it was applied to the development of over 200 configurations. Only 24 were considered suitable, or interesting enough, for further evaluation. These, along with 19 empirically designed strakes mounted on the same wing-body, were tested, in a cooperative program with the authors, in the Northrop 16- by 24-Inch Diagnostic Water Tunnel. From the results reported in references 5 and 6, only 16 strake-wing configurations, 7 analytically designed and 9 empirically designed, were considered of sufficient interest to be tested on a similar wing-body in a wind tunnel. These tests, like those in water, were to be done at zero sideslip because of the large test matrix involved. It is recognized that the effects of sideslip and leading- and trailing-edge flaps are important with regard to vortex breakdown and the resulting amount of useful lift attainable; however, these effects are beyond the scope of the present study. This report documents the wind-tunnel results and presents the analytical estimates for both the complete configurations and the components using the method described in references 1, 4, and 7.

Use of trade names or names of manufacturers in this report does not constitute an official endorsement of such products or manufacturers, either expressed or implied, by the National Aeronautics and Space Administration.

SYMBOLS AND ABBREVIATIONS

Dimensional quantities are given in both SI Units and U.S. Customary Units. Measurements and calculations were made in U.S. Customary Units.

AD	analytically designed
b	span (b_w = 50.8 cm (20 in.))
C	constant pressure specification in strake design
C_D	drag coefficient, $\frac{\text{Drag}}{q_\infty S_{ref}}$
$C_{D,o}$	experimental value of drag coefficient at $C_L = 0$
C_L	lift coefficient, $\frac{\text{Lift}}{q_\infty S_{ref}}$
$C_{L,max}$	maximum value of $C_{L,tot}$
C_m	pitching-moment coefficient about 56.99 percent body length station, $\frac{\text{Pitching moment}}{q_\infty S_{ref} c_{ref}}$
ΔC_p	lifting pressure coefficient
C_S	leading-edge suction-force coefficient, $K_{v,le} \sin^2 \alpha$
C_T	leading-edge thrust-force coefficient, $\frac{\text{Leading-edge thrust}}{q_\infty S_{ref}}$
c	chord, cm (in.)
$\tilde{c}$	characteristic length used in determination of $K_{v,\overline{se}}$, cm (in.)
c_{ref}	reference chord, 23.33 cm (9.185 in.)
c_s	section suction-force coefficient, $\frac{\text{Section suction force}}{q_\infty c}$
dF_s	differential leading-edge suction force (see sketch D)
dl	differential leading-edge length
ED	empirically designed

f	additional lifting surface efficiency factor, $\dfrac{(C_{L,tot})_{swb}}{(C_{L,tot})_{wb}}\left(\dfrac{S_{ref}}{S_{ref}+S_s}\right)$
K_p	potential lift factor, $\dfrac{\partial(\text{Normal force}/q_\infty S_{ref})}{\partial(\sin\alpha\cos\alpha)}$ (KP in table IV)
K_v	vortex lift factor (KV in table IV)
$K_{v,le}$	leading-edge vortex lift factor, $\dfrac{1}{q_\infty S_{ref}}\dfrac{\partial\left(\lvert S.F.\rvert_{le,left}+\lvert S.F.\rvert_{le,right}\right)}{\partial\sin^2\alpha}$ (KV LE in table IV)
$K_{v,se}$	side-edge vortex lift factor, $\dfrac{1}{q_\infty S_{ref}}\dfrac{\partial\left(\lvert S.F.\rvert_{se,left}+\lvert S.F.\rvert_{se,right}\right)}{\partial\sin^2\alpha}$ (KV SE in table IV)
$K_{v,\overline{se}}$	augmented vortex lift factor, $(K_{v,le}/l)\tilde{c}$ (see appendix A)
l	distance along leading edge from apex, cm (in.)
M	free-stream Mach number
P	polynomial pressure specification in strake design
q_∞	free-stream dynamic pressure, N/m^2 (lb/ft^2)
R_a	ratio of exposed strake area to wing reference area, S_s/S_{ref}
R_b	exposed semispan ratio, $[(b/2)_s/(b/2)_w]_{exp}$
R_s	strake slenderness ratio, $(\text{Length/Semispan})_{exp}$
r	radius of curvature, cm (in.)
S	area
S_{ref}	reference wing area, 0.1032 m^2 (1.1109 ft^2)
S.F.	potential-flow suction force
s	$=\dfrac{c_s c}{\alpha^2(b/2)}$
U	free-stream velocity, m/sec (ft/sec)

w_{net} sum of induced downwash and $U\alpha$ at $\alpha = 1$ rad, m/sec (ft/sec)

$\bar{w}_{net}$ average value of w_{net}, m/sec (ft/sec)

x,y local coordinates defining strake planform, cm (in.) (see table III)

x_c location of centroid of particular loading, cm (in.)

x_{ref} location of reference point from nose of model, 54.832 cm (21.587 in.) (X SUB REF in table IV)

$\bar{x}$ $= x_{ref} - x_{c,i}$, cm (in.) (i stands for subscripts p, le, se, and $\overline{se}$)

α angle of attack, deg (ALPHA in table IV)

$\Gamma(l)$ equivalent circulation associated with leading-edge suction, m^2/sec (ft^2/sec)

$\bar{\Gamma}(l)$ average value of $\Gamma(l)$, m^2/sec (ft^2/sec)

η fraction of exposed strake semispan

Λ leading-edge sweep angle, deg

ρ density of fluid, kg/m^3 (slugs/ft^3)

3-D three-dimensional

Subscripts:

BD-TE strake vortex breakdown at wing trailing edge in water tunnel

exp exposed

inb'd inboard

le leading edge

max maximum

outb'd outboard

p potential

r root

s strake

se side edge

$\overline{se}$ augmented side edge

swb strake-wing-body configuration

tot total configuration

$v\ell e$ vortex effect due to leading edge

vse vortex effect due to side edge

$\overline{vse}$ vortex effect due to augmented term

w wing

wb wing body

MODEL DESCRIPTION AND TEST CONDITIONS

The model was composed of a basic wing-fuselage onto which were mounted any of 16 pairs of strakes; the resulting configuration was tested in the Langley High-Speed 7- by 10-Foot Tunnel. Individual descriptions of the various model components follow.

Basic Wing-Body

The basic wing-body used in this test is shown in figure 1. The model features forebody and afterbody components separated by a metric break for multiple component aerodynamic testing. Total loads were measured by the main balance located in the aft fuselage while strake-forebody loads were measured by the forebody balance attached to, but ahead of, the metric break. Because a few strakes were very long, wings had to be mounted on the aft fuselage in an aft position for those runs. (See tables I and II for appropriate wing position and parametric descriptions of the strakes.) The aft wing position was 4.39 cm (1.73 in.) rearward of the more commonly used forward wing position which is shown in figure 1.

The wing has an untwisted, 44° swept trapezoidal planform with reference aspect ratio, taper ratio, and area of 2.5, 0.2, and 0.1032 m^2 (1.1109 ft^2), respectively. Its airfoil sections are symmetrical, uncambered, and biconvex and vary linearly in maximum thickness from 6 percent of chord at the wing-fuselage juncture to 4 percent at the tip. The preceding features are based on the reference wing which includes area between the leading and trailing edges projected to the model center line. The moment reference point is defined as the longitudinal position of the quarter-chord point of the wing at the wing-fuselage juncture when the wing is mounted in the forward position and corresponds to 56.99 percent of the body length.

Body and strake wipers were installed to prevent flow through the metric break between the two parts of the fuselage and the strake and wing. These wipers consisted of thin-gage steel tack welded to the lower surface of the strake and Mylar[2] glued around the forebody so as to transmit essentially no load from one component to the other. (See ref. 7.) Figure 2 shows a photograph of a typical model with wipers on.

No. 120 carborundum grit was applied to the forebody in a ring 2.54 cm (1 in.) aft of the nose. This same size grit was also applied 2.54 cm (1 in.) aft of the leading edges of the strake and wing on both the top and bottom surfaces.

Strakes

Figure 3 shows the strake planforms initially tested in the water tunnel (ref. 5), along with the prescribed suction distributions used to generate their shapes and whether constant pressure specification C or polynomial pressure specification P was employed. The 16 strakes selected for the present wind-tunnel tests are delineated by shading in figure 3. In table III, the planform perimeters of the 16 strakes are defined. The groups identified refer to either the basic shapes that resulted from the analytical studies - reflexive and gothic - or those strakes which were variations of the AD 24 strake and were therefore designated "empirically designed."

All strakes were constructed of 0.318 cm (0.125 in.) flat plate steel with the edges nominally beveled to a sharp edge. The strakes were attached to the forebody ahead of the metric break through the use of small body slots and minimal external brackets. (It should be mentioned that the strake-body was tested alone with no wing to aid in the assessment of lift and pitching-moment synergistic effects.) Figure 4 shows a photograph of some of the strakes.

Analytically Designed Strakes

There are seven strakes in the analytically designed group, and they are designated by an AD prefix. One (AD 24) is the original strake, two others (AD 22 and AD 23) are different area scalings of the AD 24 strake, and the remainder are composed of three gothic strakes (AD 14, AD 17, and AD 19) and one reflexive strake (AD 9). Note that the reflexive stake AD 9 (fig. 3(a)) has the same prescribed $s-\eta$ distribution as does the gothic strake AD 19 (fig. 3(b)); the primary difference in their design is due to the differing pressure specification. For additional details of these analytically designed strakes, see table I and reference 5.

Empirically Designed Strakes

The nine strakes in the empically designed group are designated by an ED prefix and are categorized by either being scaled (ED 12 and ED 13) or cut (ED 2, ED 4, ED 5, ED 6, ED 9, ED 10, and ED 11). The scaled strakes have their chords scaled to either 70 or 30 percent of the AD 24 strake. The cut series

---

[2]Mylar: Registered trademark of E. I. duPont de Nemours & Co., Inc.

are trimmed versions of the AD 24 strake having area removed along the apex, trailing-edge, or inboard-edge regions. However the strake is altered, it always abuts the fuselage and wing simultaneously. See table II and reference 5 for additional details.

Test Conditions and Corrections

The tests were conducted in the Langley High-Speed 7- by 10-Foot Tunnel at Mach numbers of 0.2, 0.5, and 0.7 and atmospheric conditions. These Mach numbers correspond to Reynolds numbers, based on c_{ref}, of 1.08×10^6, 2.39×10^6, and 2.87×10^6, respectively. The model was mounted on the high-angle-of-attack sting support system shown in figure 5 and was tested only at zero sideslip. The angle of attack varied from approximately -2° to approximately 53°.

Blockage and jet-boundary corrections have been applied to the data, and the angle of attack used herein has been corrected for sting deflection. All drag measurements have been corrected to a condition of free-stream static pressure in the balance chambers and on the forebody base. For the main balance, this correction was applied to the chamber only since the model base was feathered.

RESULTS AND DISCUSSION

Results from the wind-tunnel tests at the three test Mach numbers are presented herein with an analysis of the various geometrical effects; the test results are compared with theoretical estimates, where appropriate. The theoretical method used is detailed to show how the different aerodynamic components are treated in each angle-of-attack range. Aerodynamic synergism is discussed for both lift and pitching moment, along with the effects of Mach number and strake geometry on the "additional lifting surface efficiency factor." The latter is a measure of how efficient the strake-wing-body synergism is in relation to simply increasing the wing area by an amount equal to that of the strake.

Basic Data Presentation

The basic longitudinal data are presented in figures 6 to 8. In these figures the effects of Mach number on the aerodynamic loads are given for the complete configuration (fig. 6) and for the wing-afterbody and strake-forebody components (figs. 7 and 8, respectively).

Effect of Mach Number on Total Longitudinal Characteristics

Figures 6(a) to 6(p) present the total-model longitudinal aerodynamic characteristics at Mach numbers of 0.2, 0.5, and 0.7. For each of these three Mach numbers, the difference in maximum angle of attack was due to the model reaching the support system or balance limits, or encountering severe buffeting at different values in the pitch run. Increasing Mach number has the expected effect of increasing $C_{L,tot}$, although by a small amount, at the lower values of α, as well as providing a slight increase in the longitudinal stability below $C_{L,max}$. For shorthand notation, all strake-wing configurations will henceforth be denoted by the strake designation. Some of the strake-wing configurations, AD 9, AD 14, AD 17, AD 22, AD 23, AD 24, ED 9, and ED 11, exhibit a slight increase in the value of $C_{L,max}$ with increasing Mach number. A discussion of $C_{L,max}$ is presented in more detail in the section "Synergistic Effects." All but the smallest configurations ($R_a \approx 0.1$), AD 22, ED 4, ED 6, and ED 13, develop pitch-up at the higher values of $C_{L,tot}$ and $M = 0.2$ because the strakes generate a significant portion of the total lift once the strake-vortex breakdown has progressed ahead of the wing-strake juncture. For the test Mach number range, the drag-coefficient results show no strong effect of compressibility on $C_{D,o}$; thus, there is little difference in C_D with changing Mach number up to near $C_{L,max}$. The data themselves vary as $C_{D,o} + C_L \tan \alpha$.

Effect of Mach Number on Component Longitudinal Characteristics

Figures 7(a) to 7(p) and 8(a) to 8(p) show the effects of Mach number on the wing-afterbody and the strake-forebody longitudinal aerodynamic characteristics, respectively. There, C_D and C_m are plotted against $C_{L,tot}$ so that the contributions to the total model, shown in figure 6, can be isolated and presented in a similar format. In the discussion of figure 6 it was noted that C_L for the total configuration increased with M at a fixed angle of attack. From figure 7 the wing-afterbody is seen to behave in the same manner as the total configuration; whereas, from figure 8 the strake-forebody shows a reduction in lift with increasing Mach number. It is somewhat surprising that the strake-forebody lift coefficient should fall off with increasing Mach number since these 16 strake components are low-aspect-ratio lifting surfaces and hence should exhibit very little sensitivity to changes in Mach number. Evidently the cause for the reduction in C_L is the decrease in wing upwash associated with the increasing subsonic Mach number, as reported in reference 1. This is discussed in more detail later. However, it is not surprising that the increase in $C_{L,max}$, which occurs for some strake-wing-body configurations at $M = 0.5$, shows up on the wing-afterbody graphs since the wing is a moderate-aspect-ratio lifting surface and therefore Mach number sensitive. Due to model and/or balance limitations, $C_{L,max}$ was not reached at $M = 0.7$. Lastly, the pitch-up reported previously for certain configurations results from the pitch-down tendency of the wing-afterbody at higher values of α or $C_{L,tot}$ being exceeded by the pitch-up tendency of the strake-forebody. This has been alluded to already. Configurations of this type with vortex breakdown on the lee side would need to employ a low tail for stability and control.

The analytical estimation of the Mach effect on the longitudinal aerodynamic characteristics is taken up later for both a complete configuration and its components.

Theoretical Results

This section contains a description of the manner in which the strake-forebody and the wing-afterbody were theoretically modeled using the suction analogy. Also, comparisons are made between analytical estimates and data results for both total and component aerodynamic loads.

Modeling Method

The suction analogy has been used successfully to estimate the vortex-flow contributions to lift, drag, and pitching moment associated with the potential-flow edge force (i.e., unaugmented terms) for delta and rectangular wings. However, for configurations in which forward-shed vorticity passes over the aft part of the configuration, another contribution to vortex lift can arise (ref. 8). It is designated "augmented vortex lift" in reference 9, and its basic derivation is repeated in appendix A of the present paper for completeness. These two separate types of vortex lift (ref. 7) are illustrated in sketch A for a strake-wing configuration.

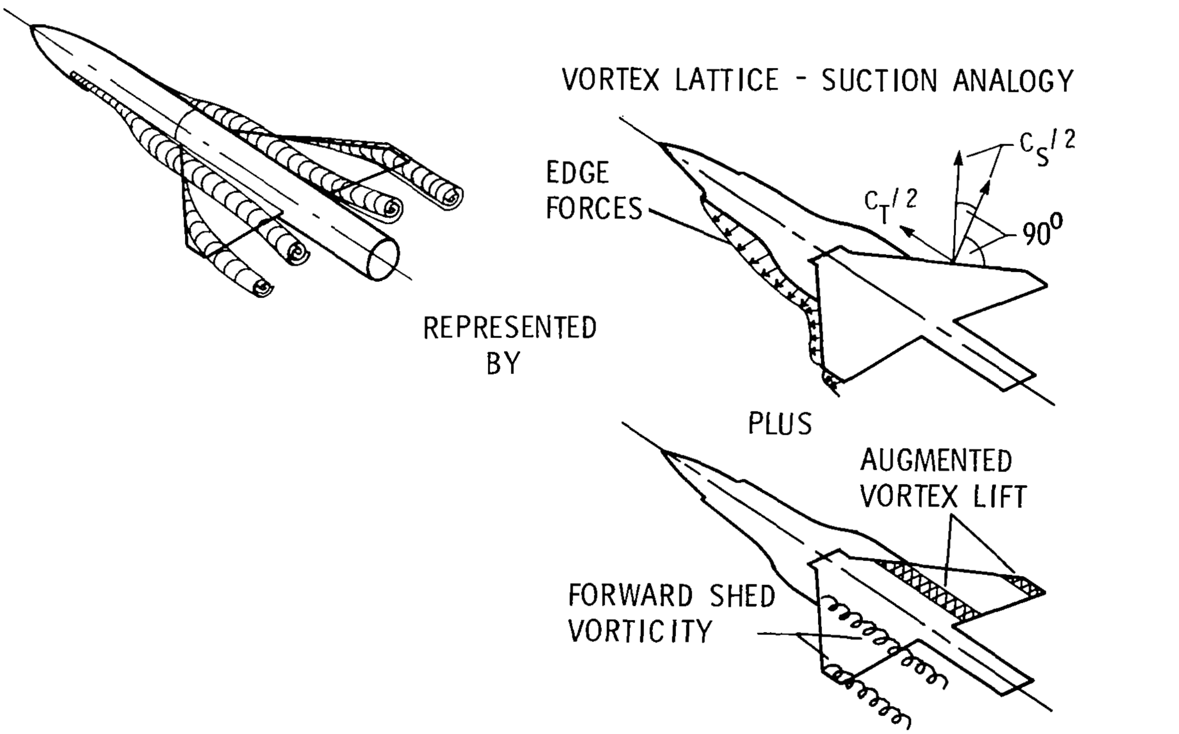

Sketch A.- Basic theoretical approach.

References 4 and 7 point out that, depending on the range of α, there are two different flow-field models which are appropriate for a strake-wing configuration. These two models (ref. 7), shown in sketch B, are determined from oil-flow and water-vapor photographs in the Langley wind tunnel and from dye studies in the Northrop water tunnel. Sketch B shows that at low angles

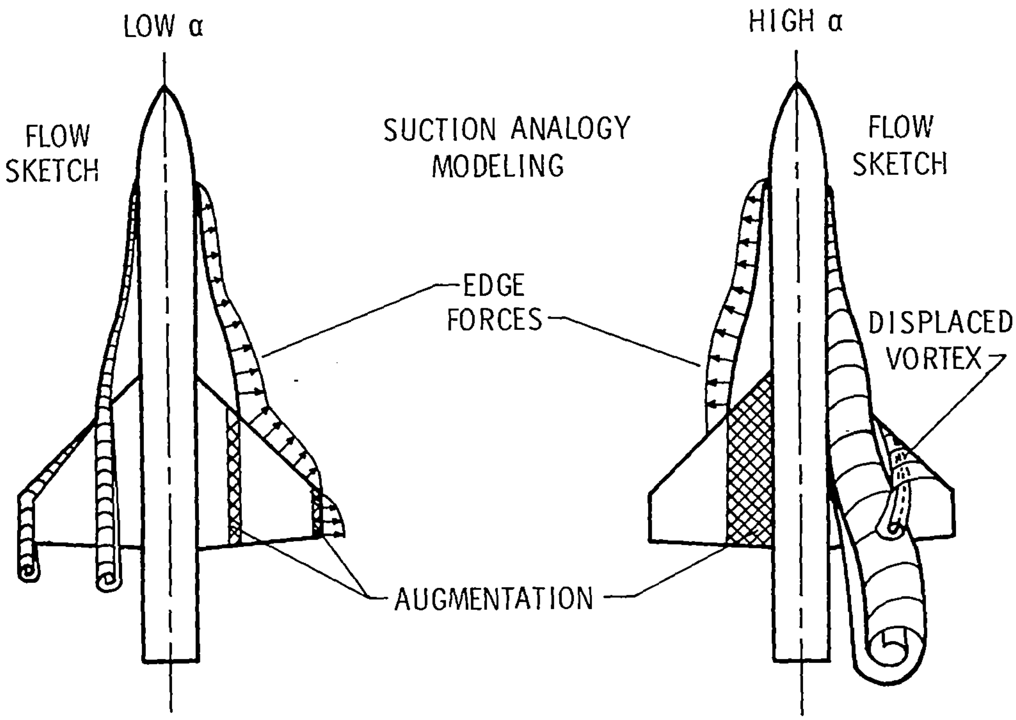

Sketch B.- Theoretical vortex lift model for strake wing.

of attack the strake and wing leading-edge vortices were individually distinguishable over the wing. However, at high angles of attack the wing surface flow pattern evidenced one region of spanwise vortex flow. Although the high-angle-of-attack flow patterns might be interpreted as strake- and wing-vortex coalescence, additional observations revealed the presence of the unburst wing leading-edge vortex core in addition to the strake core at the high values of α. These observations suggest that the wing vortex had not coalesced with the strake vortex but merely had been displaced away from the wing upper surface by the strake vortex, thus allowing the strake vortex to dominate the surface flow patterns. Accordingly, the vortex lift effects due to the wing leading-edge and side-edge vortices may be decreased at high angles of attack because of their vertical displacement.

Putting all the preceding concepts together leads to the generalized forms of the equations for C_L, C_D, and C_m associated with the following suction analogy. These equations contain the direct and augmented vortex lift terms and are explicitly

$$C_L = K_p \sin \alpha \cos^2 \alpha + (K_{v,le} + K_{v,se} + K_{v,\overline{se}})|\sin \alpha| \sin \alpha \cos \alpha \tag{1a}$$

$$C_D = C_{D,o} + C_L \tan\alpha = C_{D,o} + K_p \sin^2\alpha\cos\alpha + (K_{v,le} + K_{v,se} + K_{v,\overline{se}})\sin^3\alpha \tag{1b}$$

$$C_m = K_p \frac{\bar{x}_p}{c_{ref}} \sin\alpha\cos\alpha + \left(K_{v,le}\frac{\bar{x}_{le}}{c_{ref}} + K_{v,se}\frac{\bar{x}_{se}}{c_{ref}} + K_{v,\overline{se}}\frac{\bar{x}_{\overline{se}}}{c_{ref}}\right)|\sin\alpha|\sin\alpha \tag{1c}$$

where the particular $\bar{x}$-terms equal $x_{ref} - x_{c,i}$ with i standing for p, le, se, or $\overline{se}$. It is realized that each of the terms in equations (1) may be for a single planform or be representative of combinational terms of the same type for the strake-wing configuration. The values of $K_{v,le}$ and $K_{v,se}$ are easily obtainable for each planform by appropriate use of computer codes, such as the vortex-lattice method described in reference 10. However, the $K_{v,\overline{se}}$ terms require attention as to their computation (appendix A), origin, and angle-of-attack range of validity.

From sketch C it can be seen that at low angles of attack where the vortex is small, the negative augmentation factor associated with the swept-back

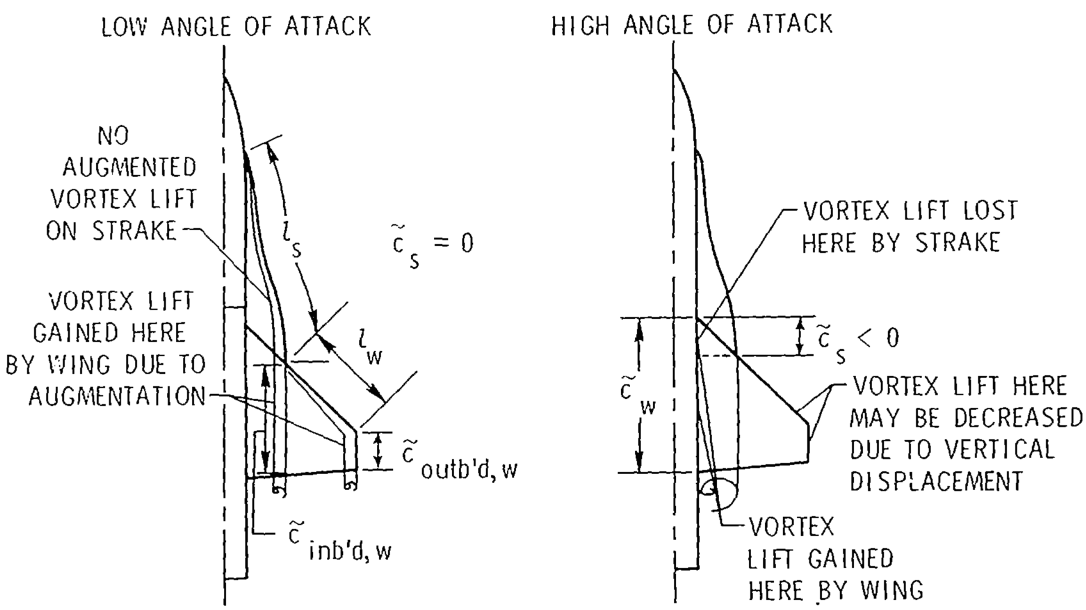

Sketch C.- Theoretical vortex lift parameters for strake wing.

trailing edge of the strake (ref. 9) will be negligible and is therefore taken to be zero in the computation. Augmented effects will occur on the wing due to both the wing and strake vortices and may be expressed as

$$\left(K_{v,\overline{se}}\right)_w = \frac{(K_{v,le})_w}{l_w}\tilde{c}_{outb'd,w} + \frac{(K_{v,le})_s + (K_{v,se})_s}{l_s}\tilde{c}_{inb'd,w} \tag{2}$$

where l_w is the length of the exposed wing leading edge, $\tilde{c}_{outb'd,w}$ is the tip chord, and $\tilde{c}_{inb'd,w}$ is the wing chord at the strake-wing juncture. (See sketch C.) At high angles of attack, vortex lift will be lost by the strake due to the trailing-edge notch as would occur for an isolated strake. However, this vortex lift will not be lost to the configuration; it will be recovered by the wing as part of the augmented-vortex-lift effect due to the strake vortex. To approximate the length which the strake vortex persists over the wing, the chord at the wing-fuselage juncture was chosen. The augmented effects at high angles of attack may be expressed as

$$(K_{v,\overline{se}})_s = \frac{(K_{v,le})_s + (K_{v,se})_s}{l_s}\tilde{c}_s \tag{3}$$

and

$$(K_{v,\overline{se}})_w = \frac{(K_{v,le})_s + (K_{v,se})_s}{l_s}\tilde{c}_w \tag{4}$$

Because vortex lift associated with the wing leading-edge and side-edge vortices may be decreased due to the aforementioned vertical displacement effects, it may be assumed that

$$(K_{v,le})_w = (K_{v,se})_w = 0 \tag{5}$$

as a limiting case for high angle of attack.

In the computation of C_m, the value of $x_{c,\overline{se}}$ associated with each individual piece of augmented vortex lift is taken to be coincident with the centroid of the affected geometrical area. For example, at low angles of attack along the wing tip, the term $\frac{(K_{v,le})_w}{l_w}\tilde{c}_{outb'd,w}$ acts at the center of the tip chord.

The preceding then is the method used to make the theoretical estimates of C_L, C_D, and C_m for the strake-forebody, the wing-afterbody, and the total configuration. For reference, the values of K_p, K_v, and $\bar{x}$ are summarized for both high-angle-of-attack and low-angle-of-attack solutions in table IV for all configurations at $M = 0.2$, in table V for the AD 19 configuration at $M = 0.2$, 0.5, and 0.7, and in table VI for the basic wing-body (both forward and aft wing positions) at $M = 0.2$, 0.5, and 0.7.

Comparison With Data at $M = 0.2$

Complete configuration.- Figures 9(a) to 9(p) present high-angle-of-attack and low-angle-of-attack vortex lift estimates, along with data for the longitudinal aerodynamic characteristics of complete configurations at $M = 0.2$. A comparison for C_D shows that up to $C_{L,max}$ or vortex breakdown, the high angle-of-attack vortex lift theory (including $C_{D,o}$) yields the better agreement with the C_L and C_D data. Within this range of α, the C_L data in some cases exceeds the high-angle-of-attack theory. This indicates that the wing may be contributing some vortex lift to the total, and, therefore, all of the assumptions for the high-angle-of-attack theory are not realized. Above this range of α neither theory appropriately models the flow. It is also seen that the two theories generally bracket the C_m data, again up to $C_{L,max}$ or vortex breakdown. The ability of the theories to do this is encouraging in that they are able to estimate collectively the general nonlinear C_m versus $C_{L,tot}$ characteristics for this class of configuration. It can be noted that the low-angle-of-attack vortex lift theory may, in general, estimate better the C_m results than those obtained with the high-angle-of-attack theory (fig. 9(m), for example). This occurs because the low-angle-of-attack theory produces a load center farther aft at a particular value of $C_{L,tot}$ even though this value is larger than the data at the same angle of attack.

The potential-flow curve is added to the $C_{L,tot}$ versus α plots for reference. It is interesting to note that for the configurations with the smaller values of R_a, in particular AD 22, ED 4, and ED 13, the $C_{L,tot}$ data at the higher angles of attack tend to follow the $C_{L,p}$ curve even though the flow there is nothing like potential.

Components.- The wing-afterbody and strake-forebody longitudinal aerodynamic data and the high-angle-of-attack and low-angle-of-attack estimates at $M = 0.2$ are given in figures 10(a) to 10(p). Just as for the complete configuration, the individual data components are generally well estimated by the high-angle-of-attack theory or a collective combination of theories up to $C_{L,max}$ or large-scale vortex breakdown. What is particularly useful is that the individual C_m components are tightly bracketed by the high-angle-of-attack and low-angle-of-attack vortex lift theories. The C_L data for the strake-forebody are, in general, reasonably well estimated by the two closely spaced theories until the strake vortex begins to break down on the strake at the higher values of α. The spacing between the two theories is larger for the wing-afterbody, with the data tending to be generally on or above the estimates from the high-angle-of-attack theory. This continues until the strake vortex begins to break down ahead of the wing trailing edge. From these figures it is seen that, in general, those configurations which have the higher values of R_b, i.e., AD 24, ED 4, ED 5, ED 6, ED 12, and ED 13, have their aerodynamic components better estimated by the high-angle-of-attack theory than do the others. A reason could be that the larger strake span is better modeled by this theory since it may provide proportionately more area for a given length, which in turn enables the strake vortex to act more completely on the strake and not on the fuselage. (See ref. 7.) Lastly, note that at the higher angles of attack the wing-afterbody lift variations follow the potential curves even though the flow is closer to a Helmhotz type.

Effect of Mach Number on the AD 19 Configuration

Figures 11(a) and 11(b) present for the AD 19 strake-wing-body a comparison of the effect of increasing Mach number on the total and component lift and pitching-moment characteristics for the high-angle-of-attack vortex lift theory and data as taken from figures 6(d), 7(d), and 8(d). Only one configuration was chosen with which to perform this study since, for the limited Mach range, no large differences in compressibility effects were expected to exist for these models. A comparison of the theory with data (fig. 11(a)) indicates at low angle of attack that both have the same trends for C_L and C_m, though a different magnitude of change with increasing Mach number. For $\alpha > 16^o$, the C_L estimates have an opposite trend with increasing Mach number than do data because the vortex lift contributions are decreasing faster than the potential lift terms increase. (See table V and the K_p and K_v usage in equation (1a).) These two trends are delineated in the component characteristics shown in figure 11(b). There the falloff in strake-forebody C_L is seen to be larger than the increase in wing-afterbody C_L with Mach number over the upper range of α. The comparison does confirm that the wing upwash is decreasing its effect on the strake as postulated previously because the changes that take place in the wing interference are automatically accounted for by the theory using the Prandtl-Glauert rule for compressibility, i.e., the equivalent wing in incompressible flow being stretched longitudinally.

Effect of Mach Number on Basic Wing-Body Configuration

Figures 12(a) and 12(b) show the effect of Mach number on the longitudinal data for the basic wing-body configuration with the wing in the fore and aft positions, respectively. Because of early vortex breakdown on the wing-body, the data will not likely demonstrate vortex lift and, therefore, may be approximated by potential theory though the flow is not potential. Even this approximation is seen not to be especially good for $\alpha > 17^o$. These data certainly point up the need for a flow control device, such as a strake, which is able to organize the wing flow field from $\alpha \approx 8^o$ up to $\alpha \approx 30^o$. Figure 12 also shows that the compressibility effects are of the same magnitude for the wing in either position, as would be expected. These wing-body data and theoretical estimates are used in the subsequent section "Strake Efficiency."

Synergistic Effects

The favorable interference often produced by placement of two (or more) lifting surfaces in close proximity so that the aerodynamic results measured exceed the sum of the individual components tested separately is oft-times referred to as a synergistic effect. Plots of lift synergism are often used (see, for example, ref. 1) since they provide a convenient way of displaying one of the principal benefits of strake-wing aerodynamics. Figures 13(a) to 13(p) present the lift synergism for the configurations reported herein. Lift synergism is determined using the lift-coefficient results obtained from three sources. (These three sources are indicated, for example, by the three curves of fig. 13(a).) The first is the total lift coefficient of the wing and body (short-dash curve). The second is the lift coefficient for the wing-afterbody obtained in the presence of the forebody and then added to the strake-forebody lift coefficient measured in the presence of the afterbody (long-dash curve). The third is the total lift coefficient for the strake-wing-body configuration (solid curve). A comparison of the first and second sources yields the direct area effect of adding the strake, while comparing the second and third sources provides the effect of aerodynamic synergism. (See fig. 13(a).)

Since lift-synergism plots have proven to be valuable, figures 14(a) to 14(p) have been prepared in order to determine the useful information that may be discerned from pitching-moment synergism. (Their construction is similar to the lift synergism.) Both kinds of synergism plots were generated by data interpolation, and they are discussed in this section.

Lift

From figures 13(a) to 13(p) it is clear for all the strakes tested in combination with a wing-body that favorable interference was experienced for $\alpha > 13^{\circ}$. The extent of the maximum synergistic effect, defined as the difference between the upper two curves divided by the middle curve times 100 percent, varied between configurations from a high of 53 percent for the ED 5 strake to a low of 21 percent for the AD 22 strake. The average value for these maximum effects is around 42 percent; and for a fixed strake shape, AD 22 through AD 24, the effect increases with increasing R_a. The maximum synergism effect generally occurs quite close to the value of α associated with $C_{L,max}$ for the complete configuration. This value of α is less than that for $C_{L,max}$ of the components added together and, hence, points up another useful feature of the aerodynamic synergism, i.e., a larger $C_{L,max}$ and that occurring at a lower α.

After $C_{L,max}$ has been reached for the upper and middle curves of figures 13(a) to 13(p), the lift coefficient C_L tends to fall off more rapidly for the synergistic combination (upper curve) than when the component lift coefficients are added together (middle curve). This falloff trend for the middle curve is most likely associated with its wing-afterbody component in that this component never has available to it the benefit of the strake forward-shed vorticity. Hence, when the strake-vortex effect is curtailed at the higher angles of attack on the synergistic combination, the reduction in wing-afterbody lift coefficient is much more severe.

Pitching Moment

By studying the pitching-moment synergistic plots, the data from figures 14(a) to 14(p) show that, apart from the expected lift-coefficient range extension, there are two general conclusions regarding longitudinal stability which result. They are discussed in order of their occurrence with increasing synergistic C_L. First, from low to moderate C_L, the stability is unchanged or slightly reduced by synergism; second, from moderate C_L to $C_{L,max}$, synergism causes a delay in pitch-up onset. The preceding conclusions are a result of the interference effects keeping the total load centroid in about the same location during most of the C_L range and then permitting the load center to move forward as $C_{L,max}$ is approached. This forward movement is associated with the wing upwash on the strake vortex causing the strake to generate a larger fraction of the total lift at the higher angles of attack as the synergistic sum decreases. (See figs. 10(a) and 13(a) as examples.) The $C_{L,max}$ occurs when the strake vortex breaks down in the vicinity of the strake-wing juncture (ref. 11). (See appendix B for additional discussion.) Thereafter, depending on the strake shape, the vortex breakdown point moves forward on the strake at a rate which may keep C_L near $C_{L,max}$ and thereby accentuate the positive moment generation tendency of the configuration.

Strake Efficiency

One way to assess strake efficiency with regard to maneuver capability is to compare the increase in lift obtained with the strake in place with what would have been expected by enlarging the wing area by an equal amount. In equation form, this can be quantified by the parameter f

$$f \equiv \frac{(C_{L,tot})_{swb}}{(C_{L,tot})_{wb}}\left(\frac{S_{ref}}{S_{ref} + S_s}\right) = \frac{(C_{L,tot})_{swb}}{(C_{L,tot})_{wb}(1 + R_a)}$$

$$\equiv \frac{\text{Total } C_L \text{ including aerodynamic synergism}}{\text{Scaled } C_L \text{ with increased area}} \tag{6}$$

which is given the name "additional lifting surface efficiency factor" in reference 7 where it was first presented. The condition of $f > 1$ will exist when the incremented increase in C_L associated with adding the area in the form of a strake exceeds the direct effect of that produced by increasing the basic wing area. The satisfaction of this condition means that, from a lift production standpoint, adding strake area is more efficient than just increasing wing area. Furthermore, with respect to weight, the low-aspect-ratio shape of the strake leads to a lighter weight structure (with lower gust response) than for the simply enlarged wing. Although this additional wing area would lead to an increase in span and therefore cruise lift-drag ratio, it cannot be done without an inherent weight penalty.

Figure 15 shows the manner in which f is presented and compares representative data (AD 19) with theory. The theory uses the high-angle-of-attack vortex lift theory for the strake-wing configuration (fig. 9(d)) and potential theory for the wing-body (fig. 12(a)) since each best approximates its respective data. Figure 15 shows that above $\alpha \approx 14^\circ$ the theoretical and experimental values of f exceed unity because of the synergistic vortex lift being generated on the configuration. This figure also shows that for $17^\circ \lessapprox \alpha < 40^\circ$ the experimental results produce values of f greater than predicted by the theory. This increase is due to the loss of lift effectiveness on the wing associated with its own leading-edge vortex breakdown and large-scale stall. If the usual leading-edge flow control devices were applied to the wing, the difference between the two f curves would be expected to diminish considerably. This experimental increase in f can be traced to figure 12(a) where, in particular for $M = 0.2$, $(C_{L,tot})_{wb}$ departs from the potential theory at $\alpha \approx 17^{\circ}$. As a further note, it can be seen by comparing figure 15 with figure 9(d) that the maximum or peak value of f occurs at the same angle of attack as the maximum $(C_{L,tot})_{swb}$, as would be anticipated. The second peak in f versus α, which occurs at $\alpha \approx 44^{\circ}$, results from the sudden post-stall loss of measurable lift on the wing-body, $(C_{L,tot})_{wb}$, at $M = 0.2$. (See figs. 12(a) and 12(b).)

Mach number effects on f for each strake-wing combination are discussed next, followed by a comparison of f for various combinations at $M = 0.2$ which highlight the various geometrical effects over the range of α tested. For the complete configuration, $C_{L,max}$ is discussed more fully at the end of this section.

Effect of Mach Number

Though the range of α is not as extensive for $M = 0.5$ and $M = 0.7$ as at $M = 0.2$ in figures 16(a) to 16(p), there is enough range to establish two general consequences of increasing Mach number on the plots of f versus α: (1) f increases near the largest test value of α and (2) f decreases near $\alpha = 6^{\circ}$. Thus, at the higher angles of attack, the effect of compressibility is to produce larger lifts on the strake-wing-body, and, conversely, at lower angles of attack the effect is larger on the wing-body.

An explanation may be that at lower angles of attack with the wing-body being more Mach number dependent than the more slender strake-wing-body, and with vortex flow not yet dominating the aerodynamic characteristics, the denominator of f, given in equation (6),

$$(C_{L,tot})_{wb}(1 + R_a)$$

increasingly exceeds its numerator

$$(C_{L,tot})_{swb}$$

thereby producing these smaller values with increasing Mach number. However, at the higher angles of attack the vortex flows dominate, with their effects being larger on the strake-wing-body (the more slender configuration) than on the wing-body. The $(C_{L,tot})_{swb}$ data indicate that near $\alpha \approx 16^{\circ}$ the effect of Mach number is small, due in part to the configuration slenderness but also due to the unchanging type of flow field since, for the latter, the vortex systems do not generally break down over the wing until a larger angle of attack is reached. Although true of the strake-wing-body, this is not true for the wing-body in that $(C_{L,tot})_{wb}$ falls off with increasing Mach number at $\alpha \approx 16^{\circ}$ because the leading-edge vortex has already undergone breakdown at a lower value of α. The post breakdown $(C_{L,tot})_{wb}$ characteristics indicate a reversing influence of increasing M and α to the extent that at $\alpha \approx 16^{\circ}$ an inverse Mach number effect is seen. (See figs. 12(a) and 12(b).)

Effect of Strake Geometry

This section examines the effect of strake geometry on f versus α by concentrating on the various geometrical features that can be totally or partially isolated. Among them are (1) area effect for a fixed leading-edge shape, (2) area and slenderness combination associated with simple chordwise scaling, (3) fixed area but with differing shapes, (4) shape effect for a fixed semispan, and (5) others which include the empirically designed series and the indirect effect of pressure specification, i.e., special strake shapes. For additional insight into these effects, corresponding strake-vortex breakdown angle data from the Northrop water tunnel is also discussed.

Area effect.- Figure 17 shows the effect of area scaling for a fixed strake shape, and therefore slenderness $R_s = 7.00$, by using the AD 22, AD 23, and AD 24 strake series. Three effects of increasing area are noted from this figure: (1) increasing f_{max} with R_a, (2) increasing α required to reach $f = 1$ with increasing R_a, and (3) the α at which the first f "hump" occurs increases with R_a. The first effect is simply associated with the larger strake developing the higher values of $(C_{L,tot})_{swb}$. The second effect is associated with the increasing downwash being imposed on the wing by the strakes of larger area, hence semispan, thereby requiring the configuration to reach a higher value of α before f becomes larger than unity. The third effect is due to the larger values of $(C_{L,tot})_{swb}$ occurring at larger values of α, with both being proportional to the R_a increase. Additional pertinent information has already been given in the section on lift synergism and the general discussion of strake efficiency. Both pertain to the third effect, hence it will not be discussed further for any of the other geometrical variations.

The α_{BD-TE} results from the water tunnel (ref. 6) follow the same trend with R_a as does f_{max}.

Chordwise scaling.- Figure 18 shows the AD 24, ED 12, and ED 13 configurations, all with the same value of $R_b = 0.297$ but each having a different fraction of the AD 24 chord variation. There are two major geometrical variations here: increasing area and slenderness ratio. Together they yield (1) increasing f_{max} and (2) increasing α required to reach $f = 1$. The impact of these geometrical features has been noted previously, particularly for the first item. The second item is caused by the larger area producing an additionally imposed downwash on the wing.

These α_{BD-TE} results also follow the same trend with R_a as does f_{max} (ref. 6).

Fixed area.- Figures 19(a) to 19(d) show the variation of f with α for a set of strakes having values of $R_a \approx 0.119$, $R_a \approx 0.169$, $R_a \approx 0.185$, and $R_a \approx 0.263$, respectively. For the empirically designed strakes, the effect of slenderness is slight on the first f "hump" at $R_a \approx 0.119$, but not so at

$R_a \approx 0.263$. The ED 9 strake (fig. 19(d)) is seen to have a larger value of f_{max}. This is apparently associated with the more stable vortex system arising from the more slender strake and its smoother leading-edge shape variation (ref. 5).

The analytically designed strakes in figure 19(b), $R_a \approx 0.169$, have the same value of R_s and R_b and differ only slightly in their shape. The one with a slightly higher value of R_a (less than 4 percent larger), lower initial sweep, and higher α_{BD-TE} (from ref. 6) has a higher value of f_{max}.

Figure 19(c) shows two analytically designed strakes and one empirically designed strake for $R_a \approx 0.185$. These results also show that, although there is less than 3 percent difference in R_a between the three strakes, the ED 5 (which has the larger value of R_a) has the largest value of f_{max}. The ED 5 has the largest value of R_b and produces $f = 1$ at the smallest value of α. This is different from what was noted for the area effect, which means that not only is area important but also its distribution - associated with the leading-edge shape - in producing relatively large values of $(C_{L,tot})_{swb}$ at lower angles of attack.

Fixed semispan.- Figure 20 shows results for four analytically designed strakes with R_b fixed at 0.212. The AD 14, AD 17, and AD 19 have values of f_{max} which, though approximately the same, vary in order of increasing R_a. (Note that these three strakes have more than 18 percent differences in R_a.) Reference 6 also shows the values of α_{BD-TE} to have that same order; and although all are of approximately the same value, there is a difference in maximum magnitude of about 2°. The AD 23 strake has a somewhat smaller value of f_{max} than do the other three, although its value of R_a is not that different from the value for the AD 14. They all have about the same value of α at which $f = 1$.

In figure 21 the AD 14, AD 17, and AD 19 configurations have curves of f versus α compared with those of the AD 24. The comparison shows f_{max} of all four to be similar, though the value of f_{max} for the AD 24 is slightly higher. What is particularly interesting is that the AD 14, AD 17, and AD 19 strakes have areas which range from 53 to 63 percent of the AD 24 strake and still produce these high values of f_{max}. This means that these smaller area strakes have efficiencies equivalent to the larger AD 24, up to f_{max} and may, therefore, be classified as "better" strakes. Two other features of figure 21, apart from the increased angle of attack required to reach $f = 1$ for the AD 24 (larger R_b), are that (1) f_{max} occurs at a slightly higher angle of attack for the AD 24 and that (2) the curve of f versus α beyond f_{max} is significantly higher for the AD 24 than for the other configurations. Both features are associated with the value of R_a for the AD 24 strake being larger; the first feature is attributed to the larger lift deficiency, in terms of f, which must be initially overcome, and the second feature results from the $(C_{L,tot})_{swb}$ retaining a higher value beyond f_{max}, which is associated with the larger area that the flow from the strake vortex can act upon.

Other parameters.- Figures 22(a) to 22(c) show the variations of f and α for the apex, trailing-edge, and inboard-edge cut series, respectively. Taking the cut series as a group, the ED 5 strake and ED 9 strake are as effective up to f_{max} as the AD 24 strake, while having areas of 58 percent and 80 percent less, respectively. Therefore, it can be seen that selected empirical alterations of an analytically designed strake are possible which have only a small impact on the value of f_{max}. The preferred methods of empirical-strake-shape altering appear to be those of removing small amounts of area along the inboard or trailing edges. Reference 5 also shows these methods leading to improvements in strake-vortex stability, i.e., larger values of α_{BD-TE}.

Figure 23 has been prepared to examine indirectly the effect of pressure specification on f versus α. The comparison is indirect because the different pressure specifications, constant and polynomial, taken in conjunction with the same suction prescription yield two different strake shapes. Figure 23 shows the value of f_{max} to be larger for the gothic strake (AD 19) - designed using the constant type - than for the reflexive strake (AD 9). The AD 19 strake does however have larger values of R_a and R_b than the AD 9, due in part to the AD 9 strake being very long (i.e., more slender) for the same value of R_b. Hence, on the surface one could conclude that the effect of R_a was the major cause for the difference. However, it can be seen from figure 21 that there are analytically designed strakes, of the same or smaller area and larger values of R_b than for the AD 9, which have values of f_{max} comparable to those of the AD 19. The strakes in figure 21 are all gothic and were generated with the constant pressure specification. Thus the area distribution/leading-edge shape are important. Also, since reference 5 determined that the polynomial pressure specification leads to strakes which tend to reflex toward the tip and have, as a group, lower values of α_{BD-TE}, it can be concluded that the constant pressure specification yields preferable strake shapes and characteristics of f versus α.

Generation of $C_{L,max}$

The maximum lift coefficients that the configurations generate are examined with the aid of figure 24. It is seen that for all analytically designed strakes using the constant pressure specification and for all those designed empirically and employed herein, the variations of $C_{L,max}$ with R_a follow the same curve. Though this curve has a markedly different gradient on either side of $R_a \approx 0.20$, the values of the curve are all well above those for the reference curve $(C_{L,max})_{wb}(1 + R_a)$. This is another way of seeing that addition of area in the form of a strake - some ranges of strake R_a are better than others - is a more efficient producer of $C_{L,max}$ than just enlarging the wing while keeping the reference area constant. The reason for the rapid reduction in $C_{L,max}$ with R_a for the gothic strakes having $R_a > 0.2$ is unclear. Further efforts in strake design may enable $C_{L,max}$ to be increased in such a way as to lie along the extrapolated curve.

Similar data for three empirically designed ogee (reflexive) strakes tested on the same wing-body were obtained from reference 12 and have been plotted in figure 24. A faired curve of these data passes very close to the data point for the analytically designed reflexive strake (AD 9) and has a different variation than the other data curve for R_a greater than approximately 0.20. In particular, for values of R_a below 0.25 the gothic or more gothic-like strakes generate a larger value of $C_{L,max}$ than do the empirically designed ogee strakes from reference 12 or the analytically designed reflexive strake reported herein.

Better Strakes

A criterion is sought by which the strakes may be more rigorously delineated into categories so that the "better" ones may be exposed. From the study of f versus α (figs. 17 to 23) and $C_{L,max}$ versus R_a (fig. 24) better performing strakes have been discussed; however, a concise statement as to what qualifies a strake to be a better one has not yet been established. This will now be attempted.

Since f is a function of R_a, $(C_{L,tot})_{swb}$, and $(C_{L,tot})_{wb}$ and since $(C_{L,tot})_{swb}$ is also a function of R_a, α, and M, it is clear that R_a is a prime variable. Therefore, one should seek, at an appropriate angle of attack, not only the maximum value of $(C_{L,tot})_{swb}$ and f but a way to maximize the variation of the aerodynamic synergistic effect with area change R_a, i.e., $(\partial f/\partial R_a)_{max}$. This can be formulated as

$$\frac{\partial f}{\partial R_a} = \frac{1}{1 + R_a}\left[\frac{1}{(C_{L,tot})_{wb}} \frac{\partial (C_{L,tot})_{swb}}{\partial R_a} - f\right] \tag{7}$$

where

$$f = \frac{(C_{L,tot})_{swb}}{(C_{L,tot})_{wb}(1 + R_a)}$$

One could solve directly for the value of R_a at which $\partial f/\partial R_a$ is maximized by examining $\partial^2 f/\partial R_a{}^2 = 0$. However, the determination of $\partial f/\partial R_a$ at a fixed α is difficult enough to accomplish from the data; hence the second partial derivative is even more subject to question. Thus, those strakes that maximize $\partial f/\partial R_a$ belong to a family which should produce better strakes; hence, this maximization may be used as one possible criterion.

Table VII presents the $\partial f/\partial R_a$ results for the gothic-like strakes at the value of α required for $(C_{L,max})_{swb}$. (Note that strakes having essentially the same value of α are used in the determination of $\partial (C_{L,tot})_{swb}/\partial R_a$ from figure 24 for use in eq. (7).) From the table it can be seen that those strakes which generally show up as the better ones all have values of $\partial f/\partial R_a > 3.0$, and furthermore these values are the largest obtained. By maximizing $\partial f/\partial R_a$ it is clear that the intention is to determine those strakes for which a given change in R_a produces the most benefit in f for a fixed value of α. This does not say whether $C_{L,max}$ or f_{max} is among the highest or not, only that for a value of α increasing R_a, for those strake shapes which have high values of $\partial f/\partial R_a$, should produce a rapid increase in f.

The preceding, therefore, provides another criterion for better strake shape determination, the criterion being that strakes from any source which have a value of $\partial f/\partial R_a > 3.0$ should be considered good shape candidates.

As a point of interest, if a strake could be designed so as to yield $(C_{L,max})_{swb} = 2.0$ at $R_a = 0.245$ (the end point of the extrapolated lower part of the curve as given by

$$\left.\frac{\partial (C_{L,tot})_{swb}}{\partial R_a}\right|_{\text{at } \alpha \text{ for } (C_{L,max})_{swb}} \approx 5.0$$

for gothic-like configurations in fig. 24), it would produce $f(\text{at } C_{L,max}) \approx 2.0$ with $\partial f/\partial R_a \approx 3.0$ at $\alpha \approx 28^{\circ}$. Hence, this configuration would have all the good features previously identified, i.e., large values of $C_{L,max}$, f_{max} (also, f at $C_{L,max}$), and $\partial f/\partial R_a$, and therefore be theoretically able to generate even larger values of f and $C_{L,max}$ if its shape were scaled up. (It should be noted that even without area scaling this value of f at $C_{L,max}$ is larger than any obtained to date.)

CONCLUSIONS

An experimental and analytical study has been presented for 16 analytically and empirically designed strake-wing-body configurations at Mach numbers of 0.2, 0.5, and 0.7. From the basic data, both total and component, synergism studies, comparisons with theoretical estimates, and the strake lift effectiveness study, the following conclusions have been made:

1. Pitch-up appears fundamental for many of the configurations and would therefore require a low tail for stability and control.

2. High-angle-of-attack vortex lift theory reasonably estimates the lift and the lift dependent drag up to strake-vortex breakdown.

3. High-angle-of-attack and low-angle-of-attack vortex lift theories bracket both the total and component pitching-moment data up to maximum lift or strake-vortex breakdown.

4. Overall compressibility effects are slight on the total components, due primarily to a falloff in lift and upwash on the strake-forebody compensated by an increase in lift on the wing-afterbody associated with the increasing subcritical Mach number.

5. Synergistic lift effect is usually accompanied by a delay in pitch-up.

6. It is possible to generate essentially the same level of f, the additional lifting surface efficiency factor, with gothic strakes having areas from about one-half to two-thirds the size of the original gothic analytically designed strake (AD 24).

7. Based on the strakes studied herein, those having $\partial f/\partial(\text{Strake area/Reference wing area}) > 3.0$ belong to a family of strakes that are better performers.

Langley Research Center
National Aeronautics and Space Administration
Hampton, VA 23665
February 24, 1981

APPENDIX A

AUGMENTED VORTEX LIFT

The concept of an augmented vortex lift term arises from the well-established fact that for many delta wings the leading-edge vortex generated on the wing persists for a considerable distance downstream and, therefore, can act on other surfaces such as the aft part of more generalized planforms or aircraft horizontal tails. Upon examining experimental results for the more generalized planforms, one concludes that the augmentation effect just introduced is not accounted for by the suction analogy although for simple deltas it is. The primary problem appears to be the interaction, or lack of it, when both leading-edge and side-edge vortex flows are involved. This situation as well as when the trailing edge of a simple delta is notched positively or negatively appear not to be modeled by the suction analogy. Sketch D shows examples of two systems employed that account for vortex lift

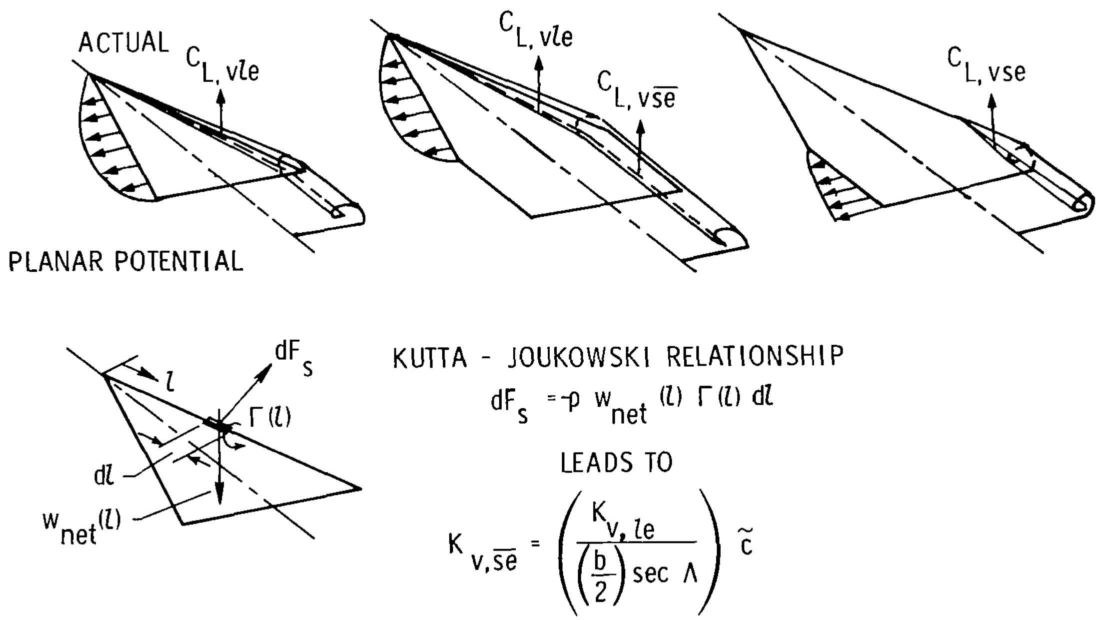

Sketch D.- Concept of augmented vortex lift.

on delta and cropped-delta wings; the first system is a theoretical one developed from a planar potential theory and utilizing the suction analogy along the leading edge and side edge, and the second system is an extension that accounts for the action of the leading-edge shed vortex in the vicinity of the side edge of cropped-delta wings. The following important points are made from sketch D: (1) The leading-edge suction distribution has a peak value somewhere along the leading edge away from the extremities and goes to zero at the tip because no-edge forces are present beyond the point of maximum span, and (2) for the cropped-delta wing, the aft part of the wing can generate additional (augmented) vortex lift (above that associated with the direct side-edge effect) because of the presence of the leading-edge vortex (as discussed in ref. 8).

In order to estimate the augmented vortex lift, it is first necessary to quantify the circulation of the shed vortex along the wing leading edge. This can be done as indicated by the lower sketch in sketch D. The Kutta-Joukowski law has been employed to relate the differential suction force along the leading edge to an unknown circulation $\Gamma(l)$ by $dF_s = -\rho w_{net}(l)\Gamma(l)\ dl$. Using a coordinate transformation, it can also be related to the leading-edge suction distribution along the span as

$$\frac{c_s c}{\alpha^2} = -2 \sec \Lambda \frac{\Gamma(l) w_{net,le}}{\alpha^2 U^2}$$

Sketch E shows an idealized distribution of the product $\dfrac{-\Gamma(l) w_{net,le}}{\alpha^2 U^2}$; note that it is basically linear, along with a fairly reasonable $\dfrac{-w_{net,le}}{U}$ (upwash)

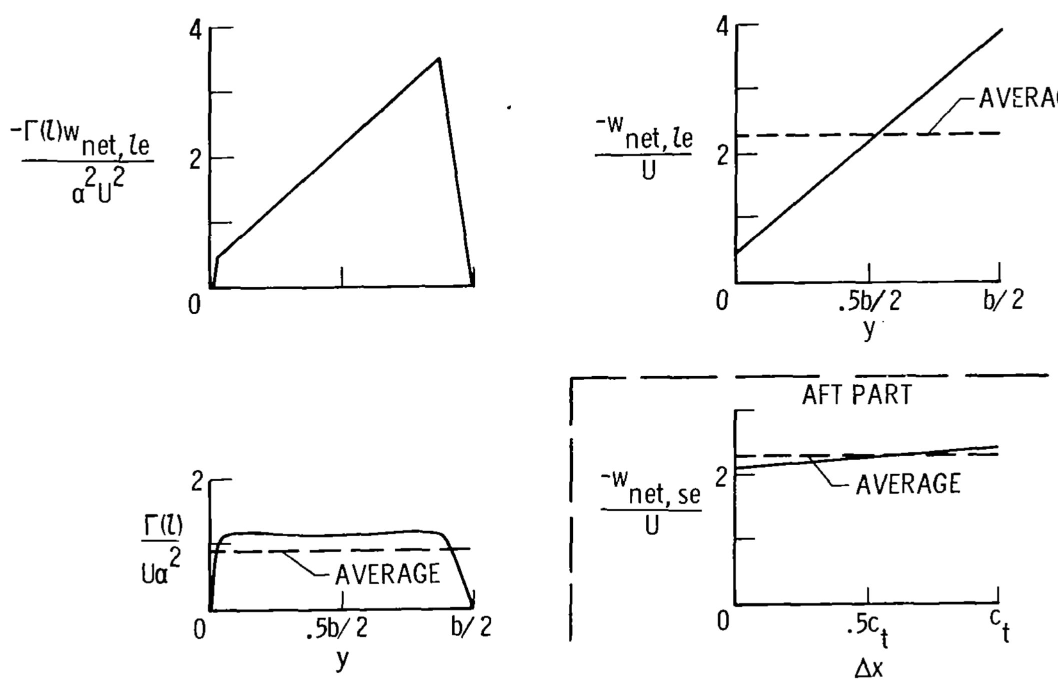

Sketch E.- Variables used in augmented-vortex-lift determination for cropped delta wings, delta part idealized. (Note: b = Wing span, c_t = Tip chord, Δx = Distance along side edge, and y = Distance along semispan.)

distribution for a cropped-delta wing, also basically linear. As a consequence, $\frac{\Gamma(l)}{\alpha^2 U}$ can be estimated as shown. Because the actual circulation does not go to zero (hence the vortex persists downstream), the distribution of circulation, essentially constant, cannot be used. Instead, an average value is employed. With an average value used for $\frac{\Gamma(l)}{\alpha^2 U}$, it is consistent to utilize an average value for $\frac{-w_{net,le}}{U}$ as well. This result can be expressed in terms of the leading-edge vortex lift factor by

$$\int_0^{b/2} \frac{c_s c\, dy}{\alpha^2} = \frac{K_{v,le}}{2} S_{ref} = -2 \sec \Lambda \frac{\bar{\Gamma}(l)\bar{w}_{net,le}}{\alpha^2 U^2} \frac{b}{2}$$

Hence,

$$\frac{\bar{\Gamma}(l)}{\alpha^2 U} = \frac{-K_{v,le} S_{ref}}{2b \sec \Lambda \dfrac{\bar{w}_{net,le}}{U}}$$

Employing this result in the Kutta-Joukowski law, this time along the side edge, permits the estimation of the augmented vortex lift. The details yield

$$\frac{\text{Augmented vortex lift along one edge}}{\alpha^2} = -\rho \bar{w}_{net,se} \frac{\bar{\Gamma}(l)}{\alpha^2} \tilde{c}$$

where the distribution $\frac{-w_{net,se}}{U}$ and its average are again reasonably depicted at the bottom right of sketch E, and $\tilde{c}$ is a characteristic streamwise length. By inspection of sketch E,

$$\frac{\bar{w}_{net,se}}{U} \approx \frac{\bar{w}_{net,le}}{U}$$

Then, defining the augmented vortex lift along one edge divided by α^2 as $\frac{K_{v,\overline{se}}}{2} q_\infty S_{ref}$ leads to

$$\frac{K_{v,\overline{se}}}{2} q_\infty S_{ref} = q_\infty \frac{K_{v,le}}{b \sec \Lambda} S_{ref}\tilde{c}$$

or

$$K_{v,\overline{se}} = \left[\frac{K_{v,le}}{(b/2) \sec \Lambda}\right] \tilde{c}$$

The term in brackets results from the use of average values and amounts to assuming that the leading-edge vortex lift factor is developed at a constant rate along the leading-edge length $(b/2) \sec \Lambda$. For cropped-delta wings the value of $\tilde{c}$ is taken to be the length of the tip chord.

From the preceding discussion, the contributions of the augmented term to vortex-flow aerodynamics are determined to be

$$C_{L,v\overline{se}} = K_{v,\overline{se}} |\sin \alpha| \sin \alpha \cos \alpha$$

$$C_{D,v\overline{se}} = K_{v,\overline{se}} \sin^3 \alpha$$

and

$$C_{m,v\overline{se}} = K_{v,\overline{se}} |\sin \alpha| \sin \alpha \frac{\bar{x}_{\overline{se}}}{c_{ref}}$$

where $\bar{x}_{\overline{se}}$ is taken from the reference point to the centroid of the augmented vortex lift. This location is generally taken to occur at the centroid of the affected area.

STRAKE-VORTEX BREAKDOWN IN AIR AND WATER

From previous sections in this paper, a qualitative correlation has been pointed out to exist between the f_{max} variation, determined from wind-tunnel data, and the angle for strake-vortex breakdown at the trailing edge, observed in the water tunnel (ref. 5). Based on that correlation, it is interesting to consider how well the quantitative values of α_{BD-TE} in air would agree with those observed in water. For delta wings the agreement was determined in reference 3 to be good; however, not as much is known about the agreement for configurations like that of the strake-wing-body. During the wind-tunnel test reported in this paper, the atmospheric water vapor and tunnel temperature were such as to cause the strake vortex, and sometimes the wing vortex, to be visible for the AD 24 configuration. Because of the vortex visibility a video tape was made for the range of α from 16° to >35° at $M = 0.3$. From the tape, still photographs have been prepared and are presented in figure 25. Since the AD 24 was also a configuration tested in the water tunnel, photographs from that test (ref. 5) are available over a similar range of α and are also presented in figure 25 for comparison. (The angles of attack for the water-tunnel data are corrected for wall effects using the wind-tunnel lift-coefficient data.)

From these two sets of flow-field data it can be seen that there are at least three items which deserve comment. The first is that the strake vortex is better able to persist in the wing pressure field while in air than in water. This is most likely associated with the Reynolds number (1.76×10^4 in water and 1.51×10^6 in air) and its effect on the upper-surface pressure field associated with the different characteristics of the boundary layers. The second item is the very rapid progression in air with small increase in α over the wing for the strake-vortex breakdown position once the trailing edge has been reached.

The different rates of vortex breakdown progression for configurations tested in the water and wind tunnel can also be seen for the delta wings of Wentz (ref. 13) tested in air and the water-tunnel results published by Headley (ref. 3). They are compared in figure 26 and even though the values of α_{BD-TE} agree, the higher swept deltas are seen to exhibit a much more rapid forward progression of vortex breakdown position in air than in water. The third item is that α for strake-vortex breakdown at the strake-wing junction is about 32° in both air and water. This signifies that once the wing pressure field is traversed, the strake-vortex breakdown progression commences from the same position at about the same α.

Based on the second item, one should expect some differences in the force data in the α range from approximately 22° to approximately 32°. Wind-tunnel data at the same Mach number (0.3) as that for the strake-vortex photographs are available and are presented in figure 27. Force data for the water-tunnel model is not available for comparison; however, it is interesting to examine the wind-tunnel data for C_L versus α in light of both sets of strake-vortex photographs. From these data it can be seen that $C_{L,max}$ occurs in the α range from 30° to 35°. It is in this range that the strake vortex begins to break down in air ahead of the wing trailing edge. This breakdown occurs at α values some 10° to 13° larger in air than in water, and so one might speculate that water-tunnel force tests would show $C_{L,max}$ occurring at a lower value of α.

Figure 9(g) presented the C_L versus α data for the AD 24 strake-wing-body configuration at $M = 0.2$ in comparison with theory and, thereby, demonstrates that the falloff in lift-curve slope is a part of an expected theoretical trend for $\alpha > 20^{\circ}$. This fact, coupled with the wind-tunnel strake-vortex-breakdown photographs for the model, should encourage the reader to employ caution in inferring from water-tunnel photographs quantitative information about the force data, as suggested in reference 11 for fighter-type configurations.

The use of water-tunnel photographs has been shown in reference 5 to be useful in sorting out the quantitative effects of different configurations. This appendix points out that further study is needed in order to more fully appreciate and account for the impact of Reynolds number on strake-vortex breakdown.

REFERENCES

1. Lamar, John E.; and Luckring, James M.: Recent Theoretical Developments and Experimental Studies Pertinent to Vortex Flow Aerodynamics - With a View Towards Design. High Angle of Attack Aerodynamics, AGARD-CP-247, Jan. 1979, pp. 24-1 - 24-31.

2. Smith, C. W.; Ralston, J. N.; and Mann, H. W.: Aerodynamics Characteristics of Forebody and Nose Strakes Based on F-16 Wind Tunnel Test Experience. Volume I: Summary and Analysis. NASA CR-3053, 1979.

3. Headley, Jack W.: Analysis of Wind Tunnel Data Pertaining to High Angle of Attack Aerodynamics. Volume I - Technical Discussion and Analysis of Results. AFFDL-TR-78-94, U.S. Air Force, July 1978. (Available from DTIC as AD A069 646.)

4. Lamar, John E.: Analysis and Design of Strake-Wing Configurations. J. Aircr., vol. 17, no. 1, Jan. 1980, pp. 20-27.

5. Frink, Neal T.; and Lamar, John E.: Water-Tunnel and Analytical Investigation of the Effect of Strake Design Variables on Strake Vortex Breakdown Characteristics. NASA TP-1676, 1980.

6. Frink, Neal T.; and Lamar, John E.: An Analysis of Strake Vortex Breakdown Characteristics in Relation to Design Features. J. Aircr., vol. 18, no. 4, Apr. 1981, pp. 253-258.

7. Luckring, James M.: Aerodynamics of Strake-Wing Interactions. J. Aircr., vol. 16, no. 11, Nov. 1979, pp. 756-762.

8. Lamar, John E.: Prediction of Vortex Flow Characteristics of Wings at Subsonic and Supersonic Speeds. J. Aircr., vol. 13, no. 7, July 1976, pp. 490-494.

9. Lamar, John E.: Some Recent Applications of the Suction Analogy to Vortex-Lift Estimates. Aerodynamic Analyses Requiring Advanced Computers, Part II, NASA SP-347, 1975, pp. 985-1011.

10. Lamar, John E.; and Gloss, Blair B.: Subsonic Aerodynamic Characteristics of Interacting Lifting Surfaces With Separated Flow Around Sharp Edges Predicted by a Vortex-Lattice Method. NASA TN D-7921, 1975.

11. Erickson, Gary E.: Water Tunnel Flow Visualization: Insight Into Complex Three-Dimensional Flowfields. J. Aircr., vol. 17, no. 9, Sept. 1980, pp. 656-662.

12. Luckring, James M.: Subsonic Longitudinal and Lateral Aerodynamic Characteristics for a Systematic Series of Strake-Wing Configurations. NASA TM-78642, 1979.

13. Wentz, William H., Jr.; and Kohlman, David L.: Wind Tunnel Investigations of Vortex Breakdown on Slender Sharp-Edged Wings. NASA CR-98737, 1968.

TABLE I.- PERTINENT GEOMETRIC PROPERTIES OF ANALYTICALLY DESIGNED STRAKES

[From ref. 5]

Strake designation	$\Lambda(\eta = 0)$, deg	R_s	R_b	R_a	Wing position
AD 1	76.76	4.92	0.212	0.100	Forward
AD 2	83.55	6.51	.212	.100	↓
AD 3	77.14	5.33	.212	.110	
AD 4	83.75	7.04	.212	.112	
AD 5	72.06	3.94	.212	.079	
AD 6	71.29	3.55	.212	.070	
AD 7	69.01	4.99	.212	.126	
AD 8	80.70	5.76	.212	.108	
AD 9[a]	75.10	10.65	.197	.183	Aft
AD 10	79.41	5.91	.212	.112	Forward
AD 11	73.29	3.56	.212	.066	↓
AD 12	73.43	3.01	.212	.038	
AD 13	77.19	8.69	.212	.199	
AD 14[a]	46.18	6.99	.212	.172	
AD 15	63.65	5.92	.212	.140	
AD 16	65.52	5.29	.212	.123	
AD 17[a]	70.78	7.77	.212	.185	
AD 18	74.54	4.98	.212	.103	
AD 19[a]	56.80	8.50	.212	.205	
AD 20	66.14	5.07	.212	.127	
AD 21	69.97	4.65	.212	.092	
AD 22[a]	60.65	7.00	.144	.077	
AD 23[a]	60.65	7.00	.212	.166	
AD 24[a]	60.65	7.00	.297	.325	Aft

[a]Strakes reported on in this paper.

TABLE II.- PERTINENT GEOMETRIC PROPERTIES OF EMPIRICALLY DESIGNED STRAKES

[From ref. 5]

Strake designation	$\Lambda(\eta = 0)$, deg	R_s	R_b	R_a	Chord modification	Wing position
AD 24[a]	60.65	7.00	0.297	0.325	(b)	Aft
ED 1 ED 2[a] ED 3 ED 4[a]	60.00 60.00 60.00 60.00	6.10 5.19 3.98 2.77	0.297 .297 .297 .297	0.305 .266 .195 .114	Removal of apex region	Forward ↓
ED 5[a] ED 6[a] ED 7 ED 8	60.65 60.65 60.65 60.65	5.83 5.22 4.53 3.65	0.262 .226 .181 .119	0.188 .124 .065 .021	Removal of trailing-edge region	
ED 9[a] ED 10[a] ED 11[a]	73.32 77.57 80.12	7.79 8.62 9.59	0.253 .208 .163	0.259 .192 .131	Removal of inboard-edge region	Aft Forward ↓
ED 12[a] ED 13[a]	56.89 50.42	5.18 2.78	0.297 .297	0.227 .098	Chordwise scaling	
ED 14 ED 15	50.42 50.42	2.78 2.78	0.297 .297	0.078 .076	Chordwise extension (snag) on ED 13 strake	
ED 16 ED 17 ED 18	50.42 50.42 50.42	5.63 4.64 3.63	0.297 .297 .297	0.325 .246 .166	Addition of side-edge/trailing-edge area to ED 13 strake	

[a]Strakes reported on in this paper.
[b]Analytically designed strake from which empirical variations are made.

TABLE III.- STRAKE PLANFORM PERIMETER POINTS

AD 9

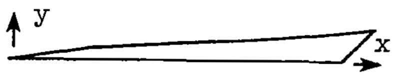

x		y	
cm	in.	cm	in.
0.000	0.000	0.000	0.000
0.919	0.362	0.201	0.079
2.169	0.854	0.401	0.158
3.665	1.443	0.599	0.236
5.367	2.113	0.800	0.315
7.242	2.851	1.001	0.394
9.268	3.649	1.201	0.473
13.724	5.403	1.600	0.630
18.626	7.333	2.002	0.788
23.891	9.406	2.400	0.945
29.385	11.569	2.802	1.103
34.557	13.605	3.200	1.260
39.119	15.401	3.602	1.418
42.606	16.774	4.001	1.575

AD 14

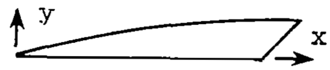

x		y	
cm	in.	cm	in.
0.000	0.000	0.000	0.000
0.325	0.128	0.229	0.090
0.818	0.322	0.457	0.180
1.433	0.564	0.686	0.270
2.154	0.848	0.914	0.360
2.974	1.171	1.143	0.450
3.886	1.530	1.374	0.541
5.982	2.355	1.831	0.721
8.440	3.323	2.289	0.901
11.298	4.448	2.746	1.081
14.623	5.757	3.203	1.261
18.590	7.319	3.660	1.441
23.589	9.287	4.120	1.622
31.991	12.595	4.577	1.802

AD 17

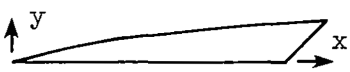

x		y	
cm	in.	cm	in.
0.000	0.000	0.000	0.000
0.693	0.273	0.229	0.090
1.473	0.580	0.457	0.180
2.334	0.919	0.686	0.270
3.274	1.289	0.914	0.360
4.290	1.689	1.143	0.450
5.385	2.120	1.374	0.541
7.813	3.076	1.831	0.721
10.577	4.164	2.289	0.901
13.721	5.402	2.746	1.081
17.328	6.822	3.203	1.261
21.560	8.488	3.660	1.441
26.817	10.558	4.120	1.622
35.550	13.996	4.577	1.802

AD 19

x		y	
cm	in.	cm	in.
0.000	0.000	0.000	0.000
0.455	0.179	0.229	0.090
1.115	0.439	0.457	0.180
1.935	0.762	0.686	0.270
2.893	1.139	0.914	0.360
3.980	1.567	1.143	0.450
5.189	2.043	1.374	0.541
7.968	3.137	1.831	0.721
11.247	4.428	2.289	0.901
15.085	5.939	2.746	1.081
19.558	7.700	3.203	1.261
24.491	9.642	3.660	1.441
30.170	11.878	4.120	1.622
38.892	15.312	4.577	1.802

TABLE III.- Continued

AD 22

x		y	
cm	in.	cm	in.
0.000	0.000	0.000	0.000
0.318	0.125	0.155	0.061
0.721	0.284	0.312	0.123
1.201	0.473	0.467	0.184
1.748	0.688	0.622	0.245
2.357	0.928	0.780	0.307
3.028	1.192	0.935	0.368
4.552	1.792	1.247	0.491
6.327	2.491	1.557	0.613
8.387	3.302	1.869	0.736
10.777	4.243	2.182	0.859
13.477	5.306	2.492	0.981
16.693	6.572	2.804	1.104
21.836	8.597	3.117	1.227

AD 23

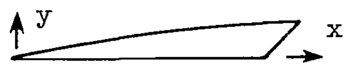

x		y	
cm	in.	cm	in.
0.000	0.000	0.000	0.000
0.465	0.183	0.229	0.090
1.062	0.418	0.457	0.180
1.763	0.694	0.686	0.270
2.565	1.010	0.914	0.360
3.459	1.362	1.143	0.450
4.445	1.750	1.374	0.541
6.683	2.631	1.831	0.721
9.291	3.658	2.289	0.901
12.319	4.850	2.746	1.081
15.827	6.231	3.203	1.261
19.792	7.792	3.660	1.441
24.514	9.651	4.120	1.622
32.070	12.626	4.577	1.802

AD 24

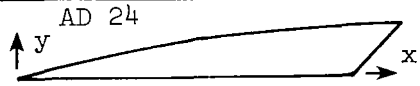

x		y	
cm	in.	cm	in.
0.000	0.000	0.000	0.000
0.653	0.257	0.320	0.126
1.486	0.585	0.643	0.253
2.471	0.973	0.963	0.379
3.597	1.416	1.283	0.505
4.849	1.909	1.603	0.631
6.231	2.453	1.925	0.758
9.365	3.687	2.565	1.010
13.023	5.127	3.208	1.263
17.262	6.796	3.848	1.515
22.179	8.732	4.491	1.768
27.739	10.921	5.131	2.020
34.356	13.526	5.773	2.273
44.943	17.694	6.414	2.525

TABLE III.- Continued

ED 2

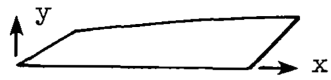

x		y	
cm	in.	cm	in.
0.000	0.000	0.000	0.000
6.985	2.750	4.034	1.588
7.041	2.772	4.041	1.591
8.270	3.256	4.491	1.768
16.114	6.344	5.131	2.020
22.730	8.949	5.773	2.273
25.977	10.227	6.030	2.374
33.320	13.118	6.414	2.525

ED 4

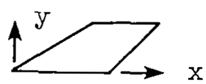

x		y	
cm	in.	cm	in.
0.000	0.000	0.000	0.000
10.437	4.109	6.025	2.372
10.478	4.125	6.030	2.374
17.821	7.016	6.414	2.525

TABLE III.- Continued

ED 5 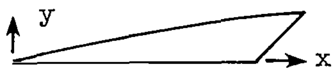

x		y	
cm	in.	cm	in.
0.000	0.000	0.000	0.000
0.653	0.257	0.320	0.126
1.486	0.585	0.643	0.253
2.471	0.973	0.963	0.379
3.597	1.416	1.283	0.505
4.849	1.909	1.603	0.631
6.231	2.453	1.925	0.758
9.365	3.687	2.565	1.010
13.023	5.127	3.208	1.263
17.262	6.796	3.848	1.515
22.179	8.732	4.491	1.768
25.425	10.010	4.874	1.919
28.953	11.399	5.260	2.071
33.142	13.048	5.667	2.231

ED 6 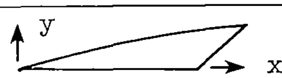

x		y	
cm	in.	cm	in.
0.000	0.000	0.000	0.000
0.653	0.257	0.320	0.126
1.486	0.585	0.643	0.253
2.471	0.973	0.963	0.379
3.597	1.416	1.287	0.505
4.849	1.909	1.603	0.631
6.231	2.453	1.925	0.758
9.365	3.687	2.565	1.010
13.023	5.127	3.208	1.263
17.262	6.796	3.848	1.515
22.179	8.732	4.491	1.768
25.425	10.010	4.874	1.919

TABLE III.- Continued

ED 9

x		y	
cm	in.	cm	in.
0.000	0.000	0.000	0.000
1.124	0.442	0.321	0.126
2.378	0.936	0.641	0.253
3.758	1.479	0.962	0.379
6.894	2.714	1.603	0.631
10.551	4.154	2.245	0.884
14.791	5.823	2.886	1.136
19.709	7.759	3.527	1.389
25.267	9.948	4.169	1.641
31.884	12.553	4.810	1.894
42.472	16.721	5.451	2.146

ED 10

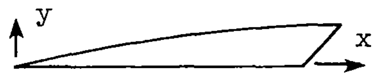

x		y	
cm	in.	cm	in.
0.000	0.000	0.000	0.000
1.505	0.592	0.321	0.126
3.136	1.235	0.641	0.253
6.793	2.674	1.283	0.505
11.033	4.344	1.924	0.758
15.951	6.280	2.565	1.010
21.509	8.468	3.207	1.263
28.126	11.073	3.848	1.515
38.714	15.242	4.489	1.768

ED 11

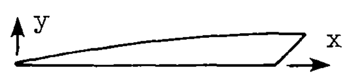

x		y	
cm	in.	cm	in.
0.000	0.000	0.000	0.000
1.896	0.747	0.321	0.126
6.137	2.416	0.962	0.379
11.054	4.352	1.603	0.631
16.613	6.540	2.245	0.884
23.230	9.146	2.886	1.136
33.817	13.314	3.527	1.389

TABLE III.- Concluded

ED 12 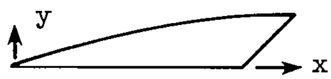			
x		y	
cm	in.	cm	in.
0.000	0.000	0.000	0.000
0.549	0.216	0.320	0.126
1.224	0.482	0.643	0.253
2.007	0.790	0.963	0.379
2.885	1.136	1.283	0.505
3.856	1.518	1.603	0.631
4.912	1.934	1.925	0.758
7.290	2.870	2.565	1.010
10.033	3.950	3.208	1.263
13.183	5.190	3.848	1.515
16.805	6.616	4.491	1.768
20.876	8.219	5.131	2.020
25.687	10.113	5.773	2.273
33.271	13.099	6.414	2.525

ED 13 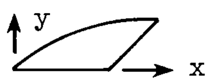			
x		y	
cm	in.	cm	in.
0.000	0.000	0.000	0.000
0.411	0.162	0.320	0.126
0.879	0.346	0.643	0.253
1.392	0.548	0.963	0.379
1.946	0.766	1.283	0.505
2.540	1.000	1.603	0.631
3.170	1.248	1.925	0.758
4.544	1.789	2.565	1.010
6.076	2.392	3.208	1.263
7.780	3.063	3.848	1.515
9.690	3.815	4.491	1.768
11.791	4.642	5.131	2.020
14.209	5.594	5.773	2.273
17.818	7.015	6.414	2.525

TABLE IV.- THEORETICAL LOADING FACTORS AND THEIR CENTROIDS FOR HIGH-ANGLE-OF-ATTACK AND LOW-ANGLE-OF-ATTACK SOLUTIONS AT M = 0.2

CONFIGURATION NO. AD 9

AERODYNAMIC PARAMETERS

INPUT KP, KV, AND CENTROIDS FOR RESPECTIVE COMPONENTS

		CENTER OF PRESSURE (CM.)	CENTER OF PRESSURE (IN.)
STRAKE			
KP=	.41229	27.58463	10.86009
KV LE=	1.57299	18.77365	7.39120
WING			
KP=	2.57992	-10.68390	-4.20626
KV LE=	2.20256	-8.61060	-3.39000
KV SE=	.48510	-21.12574	-8.31722

AUGMENTED KV AND RESPECTIVE CENTROID *

			CENTER OF PRESSURE (CM.)	CENTER OF PRESSURE (IN.)
LOW ALPHA				
STRAKE	----------------		-------	-------
WING	KV WS=	.94005	-13.34557	-5.25416
	KV WT=	.60981	-20.95048	-8.24822
HIGH ALPHA				
STRAKE	KV=	-.14224	.70822	.27883
WING	KV WR=	1.09716	-12.08363	-4.75734

TOTAL KV TERMS FOR RESPECTIVE COMPONENTS

	LOW ALPHA	HIGH ALPHA
STRAKE	1.57299	1.43075
WING	4.23752	1.09716
TOTAL	5.81051	2.52791

* WS - WING-STRAKE JUNCTURE, WT - WING TIP,
WR - WING ROOT AT BODY

NOTE: CENTROIDS POSITIVE AHEAD OF X SUB REF

TABLE IV.- Continued

CONFIGURATION NO. AD 14

AERODYNAMIC PARAMETEPS

INPUT KP, KV, AND CENTROIDS
FOR RESPECTIVE COMPONENTS

		CENTER OF PRESSURE (CM.)	CENTER OF PRESSURE (IN.)
STRAKE			
KP=	.51482	27.26040	10.73244
KV LE=	1.18831	20.79823	8.18828
WING			
KP=	2.47838	-6.95109	-2.73665
KV LE=	1.86479	-5.54965	-2.18490
KV SE=	.47626	-16.91000	-6.65748

AUGMENTED KV AND RESPECTIVE CENTROID *

			CENTER OF PRESSURE (CM.)	CENTER OF PRESSURE (IN.)
LOW ALPHA				
STRAKE		----------------	-------	-------
WING	KV WS=	.91187	-9.42461	-3.71047
	KV WT=	.53377	-16.78056	-6.60652
HIGH ALPHA				
STRAKE	KV=	-.16172	4.50743	1.77458
WING	KV WR=	1.09051	-8.04471	-3.16721

TOTAL KV TERMS FOR RESPECTIVE COMPONENTS

	LOW ALPHA	HIGH ALPHA
STRAKE	1.18831	1.02659
WING	3.78669	1.09051
TOTAL	4.97500	2.11709

* WS - WING-STRAKE JUNCTURE, WT - WING TIP,
WR - WING ROOT AT BODY

NOTE: CENTROIDS POSITIVE AHEAD OF X SUB REF

TABLE IV.- Continued

CONFIGURATION NO. AD 17

AERODYNAMIC PARAMETERS

INPUT KP, KV, AND CENTROIDS
FOR RESPECTIVE COMPONENTS

		CENTER OF PRESSURE (CM.)	CENTER OF PRESSURE (IN.)
STRAKE			
KP=	.51754	27.97658	11.01440
KV LE=	1.39443	23.46973	9.24005
WING			
KP=	2.47649	-6.95990	-2.74012
KV LE=	1.86658	-5.54805	-2.18427
KV SE=	.47651	-16.90997	-6.65747

AUGMENTED KV AND RESPECTIVE CENTROID *

			CENTER OF PRESSURE (CM.)	CENTER OF PRESSURE (IN.)
LOW ALPHA				
STRAKE		----------------	-------	-------
WING	KV WS=	.96713	-9.42461	-3.71047
	KV WT=	.53426	-16.78056	-6.60652
HIGH ALPHA				
STRAKE	KV=	-.17153	4.50743	1.77458
WING	KV WR=	1.15659	-8.04471	-3.16721

TOTAL KV TERMS FOR RESPECTIVE COMPONENTS

	LOW ALPHA	HIGH ALPHA
STRAKE	1.39443	1.22290
WING	3.84450	1.15659
TOTAL	5.23893	2.37950

* WS - WING-STRAKE JUNCTURE, WT - WING TIP,
WR - WING ROOT AT BODY

NOTE: CENTROIDS POSITIVE AHEAD OF X SUB REF

TABLE IV.- Continued

CONFIGURATION NO. AD 19

AERODYNAMIC PARAMETERS

INPUT KP, KV, AND CENTROIDS
FOR RESPECTIVE COMPONENTS

		CENTER OF PRESSURE (CM.)	(IN.)
STRAKE			
KP=	.51920	29.09821	11.45599
KV LE=	1.52509	24.71550	9.73051
WING			
KP=	2.47571	-6.96455	-2.74195
KV LE=	1.86943	-5.54314	-2.18234
KV SE=	.47676	-16.90992	-6.65745

AUGMENTED KV AND RESPECTIVE CENTROID *

			CENTER OF PRESSURE (CM.)	(IN.)
LOW ALPHA				
STRAKE	----------------		-------	-------
WING	KV WS=	.96788	-9.42461	-3.71047
	KV WT=	.53509	-16.78056	-6.60652
HIGH ALPHA				
STRAKE	KV=	-.17166	4.50743	1.77458
WING	KV WR=	1.15749	-8.04471	-3.16721

TOTAL KV TERMS FOR RESPECTIVE COMPONENTS

	LOW ALPHA	HIGH ALPHA
STRAKE	1.52509	1.35343
WING	3.84917	1.15749
TOTAL	5.37426	2.51092

* WS - WING-STRAKE JUNCTURE, WT - WING TIP,
WR - WING ROOT AT BODY

NOTE: CENTROIDS POSITIVE AHEAD OF X SUB REF

TABLE IV.- Continued

CONFIGURATION NO. AD 22

AERODYNAMIC PARAMETERS

INPUT KP, KV, AND CENTROIDS
FOR RESPECTIVE COMPONENTS

		CENTER OF PRESSURE (CM.)	(IN.)
STRAKE			
KP=	.36314	25.62949	10.09035
KV LE=	.84897	15.40152	6.06359
WING			
KP=	2.61135	-7.77578	-3.06133
KV LE=	1.92669	-6.56003	-2.58269
KV SE=	.46973	-18.16844	-7.15293

AUGMENTED KV AND RESPECTIVE CENTROID *

			CENTER OF PRESSURE (CM.)	(IN.)
LOW ALPHA				
STRAKE		----------------	-------	-------
WING	KV WS=	1.01560	-8.79326	-3.46191
	KV WT=	.50789	-16.78056	-6.60652
HIGH ALPHA				
STRAKE	KV=	-.11543	5.44753	2.14470
WING	KV WR=	1.14311	-7.86382	-3.09599

TOTAL KV TERMS FOR RESPECTIVE COMPONENTS

	LOW ALPHA	HIGH ALPHA
STRAKE	.84897	.73354
WING	3.91992	1.14311
TOTAL	4.76889	1.87664

* WS - WING-STRAKE JUNCTURE, WT - WING TIP,
WR - WING ROOT AT BODY

NOTE: CENTROIDS POSITIVE AHEAD OF X SUB REF

TABLE IV.- Continued

CONFIGURATION NO. AD 23

AERODYNAMIC PARAMETERS

INPUT KP, KV, AND CENTROIDS
FOR RESPECTIVE COMPONENTS

		CENTER OF PRESSURE (CM.)	CENTER OF PRESSURE (IN.)
STRAKE			
KP=	.51110	25.71595	10.12439
KV LE=	1.23796	19.06619	7.50637
WING			
KP=	2.45116	-8.19130	-3.22492
KV LE=	1.86461	-6.80517	-2.67920
KV SE=	.47797	-18.16710	-7.15240

AUGMENTED KV AND RESPECTIVE CENTROID*

			CENTER OF PRESSURE (CM.)	CENTER OF PRESSURE (IN.)
LOW ALPHA				
STRAKE		----------------	-------	-------
WING	KV WS=	.94890	-9.42461	-3.71047
	KV WT=	.53371	-16.78056	-6.60652
HIGH ALPHA				
STRAKE	KV=	-.16829	4.50743	1.77458
WING	KV WR=	1.13479	-8.04471	-3.16721

TOTAL KV TERMS FOR RESPECTIVE COMPONENTS

	LOW ALPHA	HIGH ALPHA
STRAKE	1.23796	1.06967
WING	3.82520	1.13479
TOTAL	5.06316	2.20446

* WS - WING-STRAKE JUNCTURE, WT - WING TIP,
WR - WING ROOT AT BODY

NOTE: CENTROIDS POSITIVE AHEAD OF X SUB REF

TABLE IV.- Continued

CONFIGURATION NO. AD 24

AERODYNAMIC PARAMETERS

INPUT KP, KV, AND CENTROIDS
FOR RESPECTIVE COMPONENTS

		CENTER OF PRESSURE (CM.)	(IN.)
STRAKE			
KP=	.71047	26.07958	10.26755
KV LE=	2.58358	20.79943	8.18875
WING			
KP=	2.29250	-11.45504	-4.50986
KV LE=	2.12844	-9.21863	-3.62938
KV SE=	.49145	-21.05914	-8.29100

AUGMENTED KV AND RESPECTIVE CENTROID *

			CENTER OF PRESSURE (CM.)	(IN.)
LOW ALPHA				
STRAKE		----------------	-------	-------
WING	KV WS=	1.30214	-14.38884	-5.66490
	KV WT=	.68298	-20.95048	-8.24822
HIGH ALPHA				
STRAKE	KV=	-.35128	-.84525	-.33278
WING	KV WR=	1.69015	-12.32460	-4.85220

TOTAL KV TERMS FOR RESPECTIVE COMPONENTS

	LOW ALPHA	HIGH ALPHA
STRAKE	2.58358	2.23230
WING	4.60502	1.69015
TOTAL	7.18860	3.92245

* WS - WING-STRAKE JUNCTURE, WT - WING TIP,
WR - WING ROOT AT BODY

NOTE: CENTROIDS POSITIVE AHEAD OF X SUB REF

TABLE IV.- Continued

CONFIGURATION NO. ED 2

AERODYNAMIC PARAMETERS

INPUT KP, KV, AND CENTROIDS
FOR RESPECTIVE COMPONENTS

		CENTER OF PRESSURE (CM.)	CENTER OF PRESSURE (IN.)
STRAKE			
KP=	.72502	26.38064	10.38608
KV LE=	2.05003	21.64301	8.52087
WING			
KP=	2.27735	-7.47824	-2.94419
KV LE=	2.13085	-5.05516	-1.99022
KV SE=	.48447	-16.91069	-6.65783

AUGMENTED KV AND RESPECTIVE CENTROID *

			CENTER OF PRESSURE (CM.)	CENTER OF PRESSURE (IN.)
LOW ALPHA				
STRAKE	----------------		-------	-------
WING	KV WS=	1.40750	-10.21892	-4.02320
	KV WT=	.68376	-16.78056	-6.60652
HIGH ALPHA				
STRAKE	KV=	-.37970	3.32467	1.30892
WING	KV WR=	1.82690	-8.25705	-3.25081

TOTAL KV TERMS FOR RESPECTIVE COMPONENTS

	LOW ALPHA	HIGH ALPHA
STRAKE	2.05003	1.67033
WING	4.70657	1.82690
TOTAL	6.75660	3.49723

* WS - WING-STRAKE JUNCTURE, WT - WING TIP,
WR - WING ROOT AT BODY

NOTE: CENTROIDS POSITIVE AHEAD OF X SUB REF

TABLE IV.- Continued

CONFIGURATION NO. ED 4

AERODYNAMIC PARAMETERS

INPUT KP, KV, AND CENTROIDS
FOR RESPECTIVE COMPONENTS

		CENTER OF PRESSURE (CM.)	(IN.)
STRAKE			
KP=	.63951	19.13682	7.53418
KV LE=	.81712	13.03442	5.13166
WING			
KP=	2.36253	-7.16318	-2.82015
KV LE=	2.07982	-5.13568	-2.02192
KV SE=	.48295	-16.90952	-6.65729

AUGMENTED KV AND RESPECTIVE CENTROID *

			CENTER OF PRESSURE (CM.)	(IN.)
LOW ALPHA				
STRAKE		----------------	-------	-------
WING	KV WS=	1.05164	-10.21892	-4.02320
	KV WT=	.66738	-16.78056	-6.60652
HIGH ALPHA				
STRAKE	KV=	-.28370	3.32467	1.30892
WING	KV WR=	1.36501	-8.25705	-3.25081

TOTAL KV TERMS FOR RESPECTIVE COMPONENTS

	LOW ALPHA	HIGH ALPHA
STRAKE	.81712	.53342
WING	4.28179	1.36501
TOTAL	5.09891	1.89843

* WS - WING-STRAKE JUNCTURE, WT - WING TIP,
WR - WING ROOT AT BODY

NOTE: CENTROIDS POSITIVE AHEAD OF X SUB REF

TABLE IV.- Continued

CONFIGURATION NO. ED 5

AERODYNAMIC PARAMETERS

INPUT KP, KV, AND CENTROIDS
FOR RESPECTIVE COMPONENTS

		CENTER OF PRESSURE (CM.)	(IN.)
STRAKE			
KP=	.61122	25.27465	9.95065
KV LE=	1.81488	17.78000	7.00000
WING			
KP=	2.39163	-7.17987	-2.82672
KV LE=	2.14088	-4.92785	-1.94010
KV SE=	.48347	-16.91074	-6.65777

AUGMENTED KV AND RESPECTIVE CENTROID *

			CENTER OF PRESSURE (CM.)	(IN.)
LOW ALPHA				
STRAKE		----------------	-------	-------
WING	KV WS=	1.27772	-9.89606	-3.89608
	KV WT=	.65476	-16.78056	-6.60652
HIGH ALPHA				
STRAKE	KV=	-.29434	3.80543	1.49820
WING	KV WR=	1.60284	-8.17290	-3.21768

TOTAL KV TERMS FOR RESPECTIVE COMPONENTS

	LOW ALPHA	HIGH ALPHA
STRAKE	1.81488	1.52054
WING	4.55683	1.60284
TOTAL	6.37171	3.12338

* WS - WING-STRAKE JUNCTURE, WT - WING TIP,
WR - WING ROOT AT BODY

NOTE: CENTROIDS POSITIVE AHEAD OF X SUB REF

TABLE IV.- Continued

CONFIGURATION NO. ED 6

AERODYNAMIC PARAMETERS

INPUT KP, KV, AND CENTROIDS
FOR RESPECTIVE COMPONENTS

		CENTER OF PRESSURE (CM.)	(IN.)
STRAKE			
KP=	.51109	23.90473	9.41131
KV LE=	1.28527	15.71219	6.18590
WING			
KP=	2.47902	-6.92226	-2.72530
KV LE=	2.24632	-4.38198	-1.72519
KV SE=	.47872	-16.91109	-6.65791

AUGMENTED KV AND RESPECTIVE CENTROID *

			CENTER OF PRESSURE (CM.)	(IN.)
LOW ALPHA				
STRAKE	----------------		-------	-------
WING	KV WS=	1.21764	-9.55342	-3.76119
	KV WT=	.65443	-16.78056	-6.60652
HIGH ALPHA				
STRAKE	KV=	-.23299	4.31562	1.69906
WING	KV WR=	1.47499	-8.08034	-3.18124

TOTAL KV TERMS FOR RESPECTIVE COMPONENTS

	LOW ALPHA	HIGH ALPHA
STRAKE	1.28527	1.05228
WING	4.59711	1.47499
TOTAL	5.88238	2.52727

* WS - WING-STRAKE JUNCTURE, WT - WING TIP,
WR - WING ROOT AT BODY

NOTE: CENTROIDS POSITIVE AHEAD OF X SUR REF

TABLE IV.- Continued

CONFIGURATION NO. ED 9

AERODYNAMIC PARAMETERS

INPUT KP, KV, AND CENTROIDS
FOR RESPECTIVE COMPONENTS

		CENTER OF PRESSURE (CM.)	CENTER OF PRESSURE (IN.)
STRAKE			
KP=	.58661	26.20599	10.31732
KV LE=	2.17464	19.57205	7.70553
WING			
KP=	2.42399	-11.11763	-4.37702
KV LE=	1.76518	-10.23904	-4.03112
KV SE=	.49116	-21.12429	-8.31665

AUGMENTED KV AND RESPECTIVE CENTROID *

			CENTER OF PRESSURE (CM.)	CENTER OF PRESSURE (IN.)
LOW ALPHA				
STRAKE		----------------	-------	-------
WING	KV WS=	1.21596	-13.97296	-5.50116
	KV WT=	.53266	-20.95048	-8.24822
HIGH ALPHA				
STRAKE	KV=	-.26690	-.22599	-.08897
WING	KV WR=	1.51077	-12.23265	-4.81601

TOTAL KV TERMS FOR RESPECTIVE COMPONENTS

	LOW ALPHA	HIGH ALPHA
STRAKE	2.17464	1.90774
WING	4.00496	1.51077
TOTAL	6.17960	3.41851

* WS - WING-STRAKE JUNCTURE, WT - WING TIP,
WR - WING ROOT AT BODY

NOTE: CENTROIDS POSITIVE AHEAD OF X SUB REF

TABLE IV.- Continued

CONFIGURATION NO. ED 10

AERODYNAMIC PARAMETERS

INPUT KP, KV, AND CENTROIDS
FOR RESPECTIVE COMPONENTS

			CENTER OF PRESSURE (CM.)	(IN.)
STRAKE				
	KP=	.50546	28.50904	11.22403
	KV LE=	1.77967	22.76328	8.96192
WING				
	KP=	2.48890	-6.92711	-2.72721
	KV LE=	1.80450	-5.75122	-2.26426
	KV SE=	.47589	-16.91475	-6.65935

AUGMENTED KV AND RESPECTIVE CENTROID*

			CENTER OF PRESSURE (CM.)	(IN.)
LOW ALPHA				
STRAKE		----------------	-------	-------
WING	KV WS=	1.14091	-9.38705	-3.69569
	KV WT=	.51389	-16.78056	-6.60652
HIGH ALPHA				
STRAKE	KV=	-.19777	4.56336	1.79660
WING	KV WR=	1.35936	-8.03424	-3.16309

TOTAL KV TERMS FOR RESPECTIVE COMPONENTS

	LOW ALPHA	HIGH ALPHA
STRAKE	1.77967	1.58190
WING	3.93519	1.35936
TOTAL	5.71486	2.94126

* WS - WING-STRAKE JUNCTURE, WT - WING TIP,
WR - WING ROOT AT BODY

NOTE: CENTROIDS POSITIVE AHEAD OF X SUB REF

TABLE IV.- Continued

CONFIGURATION NO. ED 11

AERODYNAMIC PARAMETERS

INPUT KP, KV, AND CENTROIDS
FOR RESPECTIVE COMPONENTS

		CENTER OF PRESSURE (CM.)	CENTER OF PRESSURE (IN.)
STRAKE			
KP=	.40680	28.47213	11.20950
KV LE=	1.44936	21.37585	8.41569
WING			
KP=	2.57467	-6.64505	-2.61616
KV LE=	2.00681	-4.90713	-1.93194
KV SE=	.47403	-16.91361	-6.65890

AUGMENTED KV AND RESPECTIVE CENTROID *

			CENTER OF PRESSURE (CM.)	CENTER OF PRESSURE (IN.)
LOW ALPHA				
STRAKE	----------------		--------	-------
WING	KV WS=	1.10913	-8.97117	-3.53196
	KV WT=	.54106	-16.78056	-6.60652
HIGH ALPHA				
STRAKE	KV=	-.14511	5.18262	2.04040
WING	KV WR=	1.26942	-7.91582	-3.11646

TOTAL KV TERMS FOR RESPECTIVE COMPONENTS

	LOW ALPHA	HIGH ALPHA
STRAKE	1.44936	1.30425
WING	4.13104	1.26942
TOTAL	5.58040	2.57367

* WS - WING-STRAKE JUNCTURE, WT - WING TIP,
WR - WING ROOT AT BODY

NOTE: CENTROIDS POSITIVE AHEAD OF X SUB REF

TABLE IV.- Continued

CONFIGURATION NO. ED 12

AERODYNAMIC PARAMETERS

INPUT KP, KV, AND CENTROIDS
FOR RESPECTIVE COMPONENTS

		Center of pressure (CM.)	Center of pressure (IN.)
STRAKE			
KP=	.70071	24.62352	9.69430
KV LE=	1.85714	17.32354	6.82029
WING			
KP=	2.31505	-7.40247	-2.91436
KV LE=	2.12297	-5.09212	-2.00477
KV SE=	.48518	-16.91343	-6.65883

AUGMENTED KV AND RESPECTIVE CENTROID *

			Center of pressure (CM.)	Center of pressure (IN.)
LOW ALPHA				
STRAKE		----------------	-------	-------
WING	KV WS=	1.25039	-10.21892	-4.02320
	KV WT=	.68123	-16.78056	-6.60652
HIGH ALPHA				
STRAKE	KV=	-.33732	3.32467	1.30892
WING	KV WR=	1.62298	-8.25705	-3.25081

TOTAL KV TERMS FOR RESPECTIVE COMPONENTS

	LOW ALPHA	HIGH ALPHA
STRAKE	1.85714	1.51982
WING	4.53976	1.62298
TOTAL	6.39690	3.14280

* WS - WING-STRAKE JUNCTURE, WT - WING TIP,
WR - WING ROOT AT BODY

NOTE: CENTROIDS POSITIVE AHEAD OF X SUB REF

TABLE IV.- Concluded

CONFIGURATION NO. ED 13

AERODYNAMIC PARAMETERS

INPUT KP, KV, AND CENTROIDS
FOR RESPECTIVE COMPONENTS

		CENTER OF PRESSURE (CM.)	(IN.)
STRAKE			
KP=	.60003	19.20697	7.56180
KV LE=	1.29273	10.49254	4.13092
WING			
KP=	2.39464	-7.08858	-2.79078
KV LE=	2.04864	-5.18236	-2.04030
KV SE=	.47730	-16.91452	-6.65926

AUGMENTED KV AND RESPECTIVE CENTROID *

			CENTER OF PRESSURE (CM.)	(IN.)
LOW ALPHA				
STRAKE		----------------	-------	-------
WING	KV WS=	1.55413	-10.21892	-4.02320
	KV WT=	.65738	-16.78056	-6.60652
HIGH ALPHA				
STRAKE	KV=	-.41926	3.32467	1.30892
WING	KV WR=	2.01723	-8.25705	-3.25081

TOTAL KV TERMS FOR RESPECTIVE COMPONENTS

	LOW ALPHA	HIGH ALPHA
STRAKE	1.29273	.87347
WING	4.73744	2.01723
TOTAL	6.03017	2.89070

* WS - WING-STRAKE JUNCTURE, WT - WING TIP,
WR - WING ROOT AT BODY

NOTE: CENTROIDS POSITIVE AHEAD OF X SUB REF

TABLE V.- THEORETICAL LOADING FACTORS AND THEIR CENTROIDS FOR HIGH-ANGLE-OF-ATTACK AND LOW-ANGLE-OF-ATTACK SOLUTIONS FOR AD 19 CONFIGURATION AT M = 0.2, 0.5, AND 0.7

CONFIGURATION NO. AD19, M=0.2

AERODYNAMIC PARAMETERS

INPUT KP, KV, AND CENTROIDS
FOR RESPECTIVE COMPONENTS

		CENTER OF PRESSURE (CM.)	(IN.)
STRAKE			
KP=	.51920	29.09821	11.45599
KV LE=	1.52509	24.71550	9.73051
WING			
KP=	2.47571	-6.96455	-2.74195
KV LE=	1.86943	-5.54314	-2.18234
KV SE=	.47676	-16.90992	-6.65745

AUGMENTED KV AND RESPECTIVE CENTROID*

			CENTER OF PRESSURE (CM.)	(IN.)
LOW ALPHA				
STRAKE	----------------		-------	-------
WING	KV WS=	.96788	-9.42461	-3.71047
	KV WT=	.53509	-16.78056	-6.60652
HIGH ALPHA				
STRAKE	KV=	-.17166	4.50743	1.77458
WING	KV WR=	1.15749	-8.04471	-3.16721

TOTAL KV TERMS FOR RESPECTIVE COMPONENTS

	LOW ALPHA	HIGH ALPHA
STRAKE	1.52509	1.35343
WING	3.84917	1.15749
TOTAL	5.37426	2.51092

* WS - WING-STRAKE JUNCTURE, WT - WING TIP,
WR - WING ROOT AT BODY

NOTE: CENTROIDS POSITIVE AHEAD OF X SUB REF

TABLE V.- Continued

CONFIGURATION NO. AD19, M=0.5

AERODYNAMIC PARAMETERS

INPUT KP, KV, AND CENTROIDS
FOR RESPECTIVE COMPONENTS

		CENTER OF PRESSURE (CM.)	(IN.)
STRAKE			
KP=	.51203	29.20243	11.49702
KV LE=	1.28436	24.71052	9.72855
WING			
KP=	2.60191	-6.94693	-2.73501
KV LE=	1.91991	-5.70278	-2.24519
KV SE=	.52424	-16.90406	-6.65514

AUGMENTED KV AND RESPECTIVE CENTROID *

			CENTER OF PRESSURE (CM.)	(IN.)
LOW ALPHA				
STRAKE	----------------		-------	-------
WING	KV WS=	.81510	-9.42461	-3.71047
	KV WT=	.54954	-16.78056	-6.60652
HIGH ALPHA				
STRAKE	KV=	-.14456	4.50743	1.77458
WING	KV WR=	.97478	-8.04471	-3.16721

TOTAL KV TERMS FOR RESPECTIVE COMPONENTS

	LOW ALPHA	HIGH ALPHA
STRAKE	1.28436	1.13980
WING	3.80880	.97478
TOTAL	5.09316	2.11458

* WS - WING-STRAKE JUNCTURE, WT - WING TIP,
WR - WING ROOT AT BODY

NOTE: CENTROIDS POSITIVE AHEAD OF X SUB REF

TABLE V.- Concluded

CONFIGURATION NO. AD19, M=0.7

AERODYNAMIC PARAMETERS

INPUT KP, KV, AND CENTROIDS
FOR RESPECTIVE COMPONENTS

		CENTER OF PRESSURE (CM.)	CENTER OF PRESSURE (IN.)
STRAKE			
KP=	.49980	29.42991	11.58658
KV LE=	1.00813	24.90026	9.80325
WING			
KP=	2.78608	-6.93080	-2.72866
KV LE=	1.98825	-5.94225	-2.33947
KV SE=	.59649	-16.89273	-6.65068

AUGMENTED KV AND RESPECTIVE CENTROID *

			CENTER OF PRESSURE (CM.)	CENTER OF PRESSURE (IN.)
LOW ALPHA				
STRAKE		----------------	-------	-------
WING	KV WS=	.63980	-9.42461	-3.71047
	KV WT=	.56910	-16.78056	-6.60652
HIGH ALPHA				
STRAKE	KV=	-.11347	4.50743	1.77458
WING	KV WR=	.76514	-8.04471	-3.16721

TOTAL KV TERMS FOR RESPECTIVE COMPONENTS

	LOW ALPHA	HIGH ALPHA
STRAKE	1.00813	.89466
WING	3.79364	.76514
TOTAL	4.80177	1.65979

* WS - WING-STRAKE JUNCTURE, WT - WING TIP,
WR - WING ROOT AT BODY

NOTE: CENTROIDS POSITIVE AHEAD OF X SUB REF

TABLE VI.- THEORETICAL LOADING FACTORS FOR BASIC WING-BODY CONFIGURATION, FORWARD AND AFT WING POSITIONS, AT $M = 0.2, 0.5,$ AND 0.7

CONFIGURATION NO. WB (FORWARD), M=0.2

AERODYNAMIC PARAMETERS

INPUT KP, KV, AND CENTROIDS FOR RESPECTIVE COMPONENTS

		CENTER OF PRESSURE (CM.)	(IN.)
FOREBODY			
KP=	.14528	40.60881	15.98772
KV LE=	.79525	25.53876	10.05463
WING			
KP=	2.82136	-5.86677	-2.30975
KV LE=	2.08937	-4.50195	-1.77242
KV SE=	.47270	-16.89933	-6.65328

CONFIGURATION NO. WB (AFT), M=0.2

AERODYNAMIC PARAMETERS

INPUT KP, KV, AND CENTROIDS FOR RESPECTIVE COMPONENTS

		CENTER OF PRESSURE (CM.)	(IN.)
FOREBODY			
KP=	.12428	44.15490	17.38382
KV LE=	.71655	26.26426	10.34026
WING			
KP=	2.68387	-12.27110	-4.83114
KV LE=	1.88166	-10.26772	-4.04241
KV SE=	.44007	-21.12594	-8.31730

NOTE: CENTROIDS POSITIVE AHEAD OF X SUB REF

TABLE VI.- Continued

CONFIGURATION NO. WB (FORWARD), M=0.5

AERODYNAMIC PARAMETERS

INPUT KP, KV, AND CENTROIDS
FOR RESPECTIVE COMPONENTS

		CENTER OF PRESSURE (CM.)	CENTER OF PRESSURE (IN.)
FOREBODY			
KP=	.14084	41.23959	16.23606
KV LE=	.77081	25.69708	10.11696
WING			
KP=	2.95294	-5.87690	-2.31374
KV LE=	2.13494	-4.74203	-1.86694
KV SE=	.52153	-16.89377	-6.65109

CONFIGURATION NO. WB (AFT), M=0.5

AERODYNAMIC PARAMETERS

INPUT KP, KV, AND CENTROIDS
FOR RESPECTIVE COMPONENTS

		CENTER OF PRESSURE (CM.)	CENTER OF PRESSURE (IN.)
FOREBODY			
KP=	.12237	44.55653	17.54194
KV LE=	.70601	26.33711	10.36894
WING			
KP=	2.82370	-12.27750	-4.83366
KV LE=	1.92481	-10.46036	-4.11825
KV SE=	.48500	-21.12427	-8.31664

NOTE: CENTROIDS POSITIVE AHEAD OF X SUB REF

TABLE VI.- Concluded

CONFIGURATION NO. WB (FORWARD), M=0.7

AERODYNAMIC PARAMETERS

INPUT KP, KV, AND CENTROIDS
FOR RESPECTIVE COMPONENTS

		CENTER OF PRESSURE (CM.)	(IN.)
FOREBODY			
KP=	.13443	42.25679	16.63653
KV LE=	.73947	25.93050	10.20886
WING			
KP=	3.14255	-5.90174	-2.32352
KV LE=	2.19310	-5.10675	-2.01053
KV SE=	.59623	-16.88247	-6.64664

CONFIGURATION NO. WB (AFT), M=0.7

AERODYNAMIC PARAMETERS

INPUT KP, KV, AND CENTROIDS
FOR RESPECTIVE COMPONENTS

		CENTER OF PRESSURE (CM.)	(IN.)
FOREBODY			
KP=	.11987	45.10319	17.75716
KV LE=	.69273	26.43553	10.40769
WING			
KP=	3.02807	-12.28616	-4.83707
KV LE=	1.97715	-10.77852	-4.24351
KV SE=	.55497	-21.11832	-8.31430

NOTE: CENTROIDS POSITIVE AHEAD OF X SUB REF

TABLE VII.- $\partial f/\partial R_a$ RESULTS AT $M = 0.2$

Strake designation	R_a	R_b	α^*, deg	$(C_{L,tot})_{wb}$ at α^*	$\left.\frac{\partial (C_{L,tot})_{swb}}{\partial R_a}\right\|_{\alpha^*}$	f at α^*	$\frac{\partial f}{\partial R_a}$
AD 9	0.183	0.197	26.8	0.87	Not available	1.50	----
AD 14	.172	.212	27.3	.86	≈5.0	1.62	3.58
AD 17	.185	.212	28.4	.88	≈5.0	1.63	3.42
AD 19	.205	.212	29.3	.90	≈5.0	1.64	3.25
AD 22	.077	.144	36.0	.97	≈3.5	1.19	2.25
AD 23	.166	.212	34.2	.96	≈4.0	1.44	2.34
AD 24	.325	.297	31.9	.92	≈3.0	1.63	1.23
ED 2	.266	.297	36.9	.96	≈3.5	1.55	1.66
ED 4	.114	.297	30.3	.91	≈3.5	1.34	2.25
ED 5	.188	.262	28.3	.88	≈5.0	1.65	3.39
ED 6	.124	.226	33.2	.95	≈3.0	1.32	1.64
ED 9	.259	.253	30.6	.91	≈3.5	1.63	1.76
ED 10	.192	.208	28.4	.88	≈5.0	1.59	3.43
ED 11	.131	.163	38.4	.95	≈3.5	1.31	2.10
ED 12	.227	.297	33.4	.95	≈3.0	1.53	1.33
ED 13	.098	.297	34.2	.96	≈4.0	1.26	2.65

Note: $\alpha^* = \alpha$ for $(C_{L,max})_{swb}$.

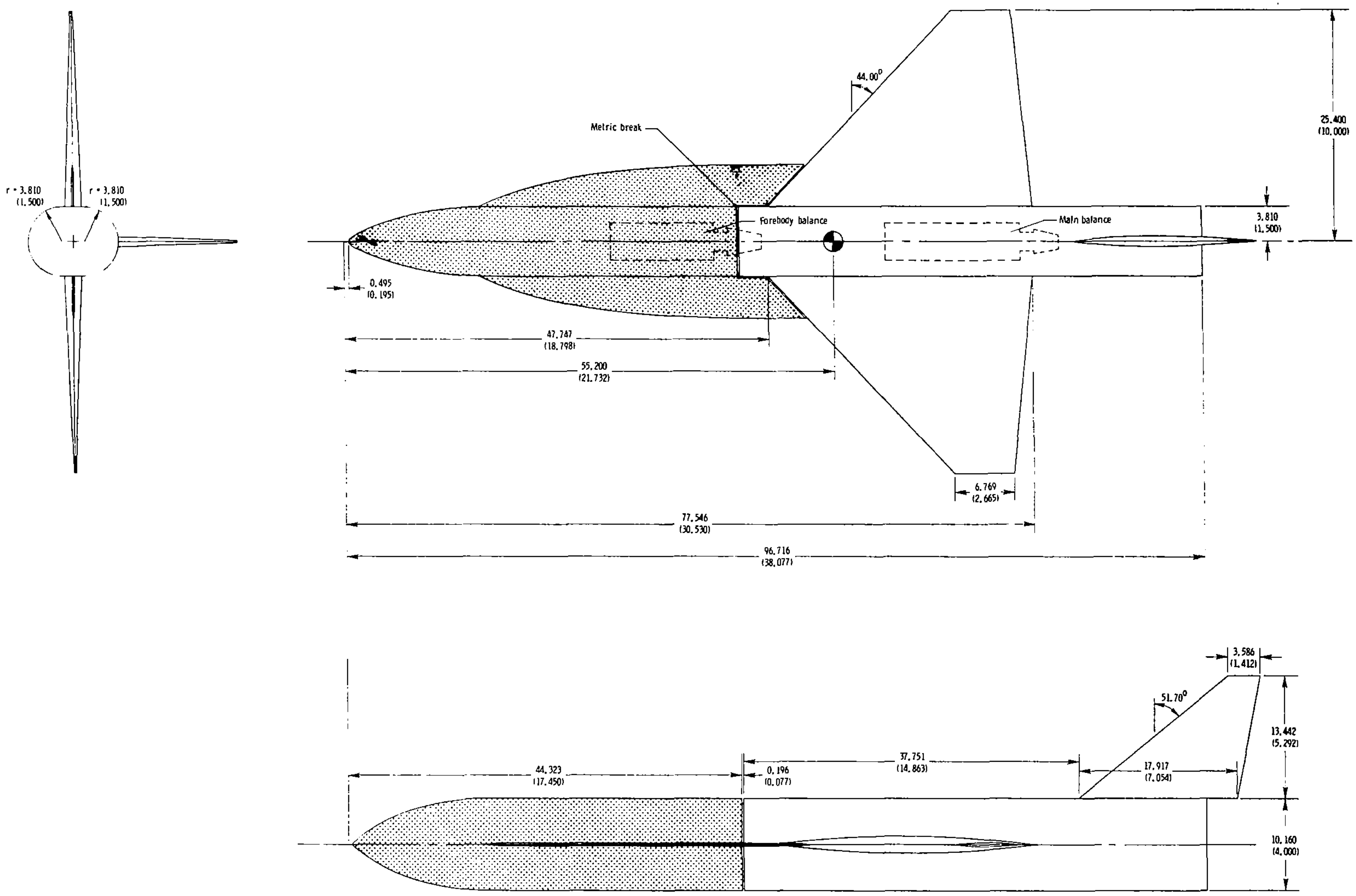

Figure 1.- Three-view drawing of typical wind-tunnel model. Shaded area is associated with forebody balance; linear dimensions are in centimeters (inches).

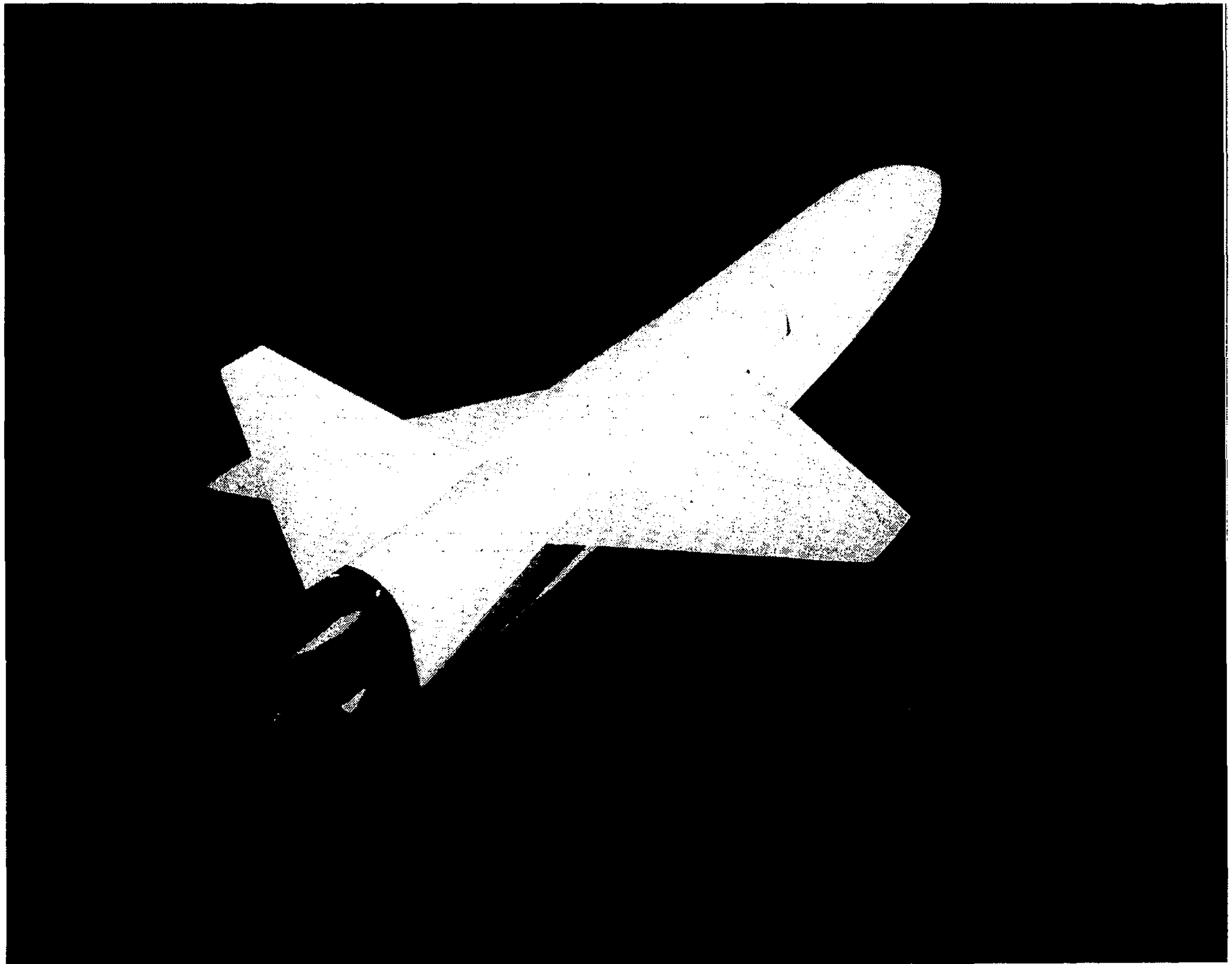

L-79-658

Figure 2.- Three-quarter rear view of typical configuration.

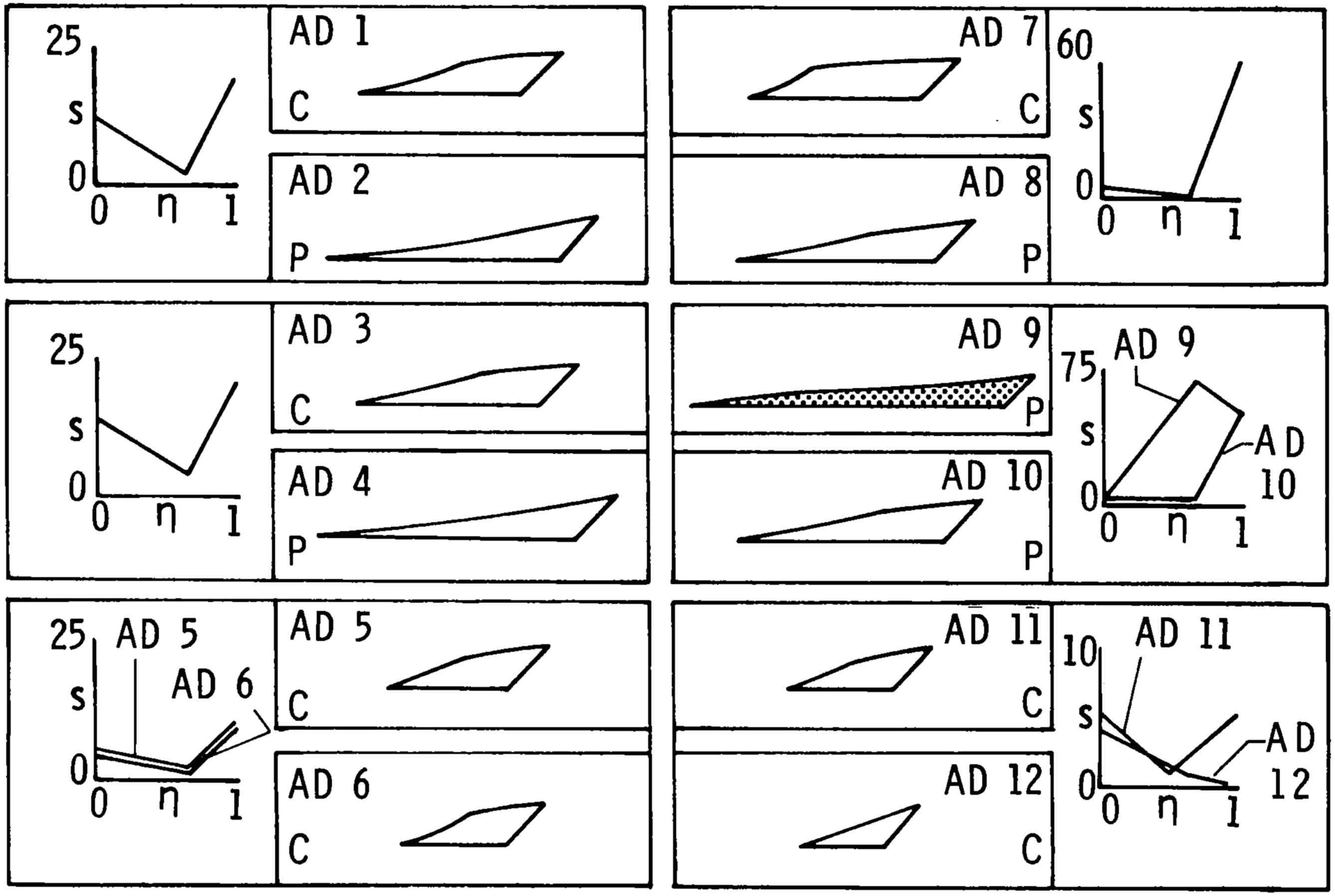

C - CONSTANT ΔC_p

P - 3-D OR POLYNOMIAL ΔC_p

$$s = \frac{c_s c}{\alpha^2 (b/2)}$$

(a) Analytical, reflexive group.

Figure 3.- Analytically and empirically designed strakes. (Shading indicates those strakes tested in wind tunnel.)

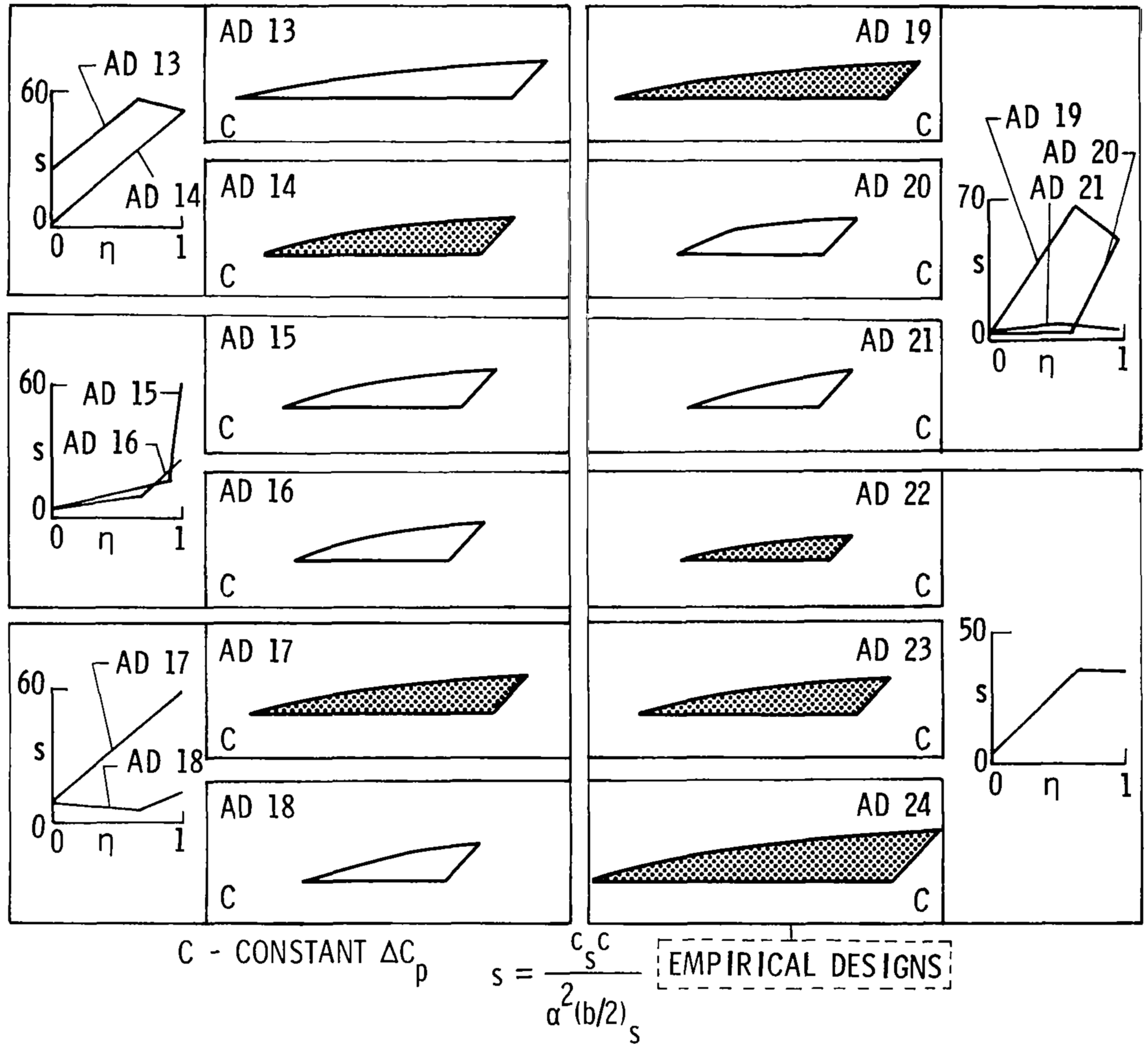

(b) Analytical, gothic group.

Figure 3.- Continued.

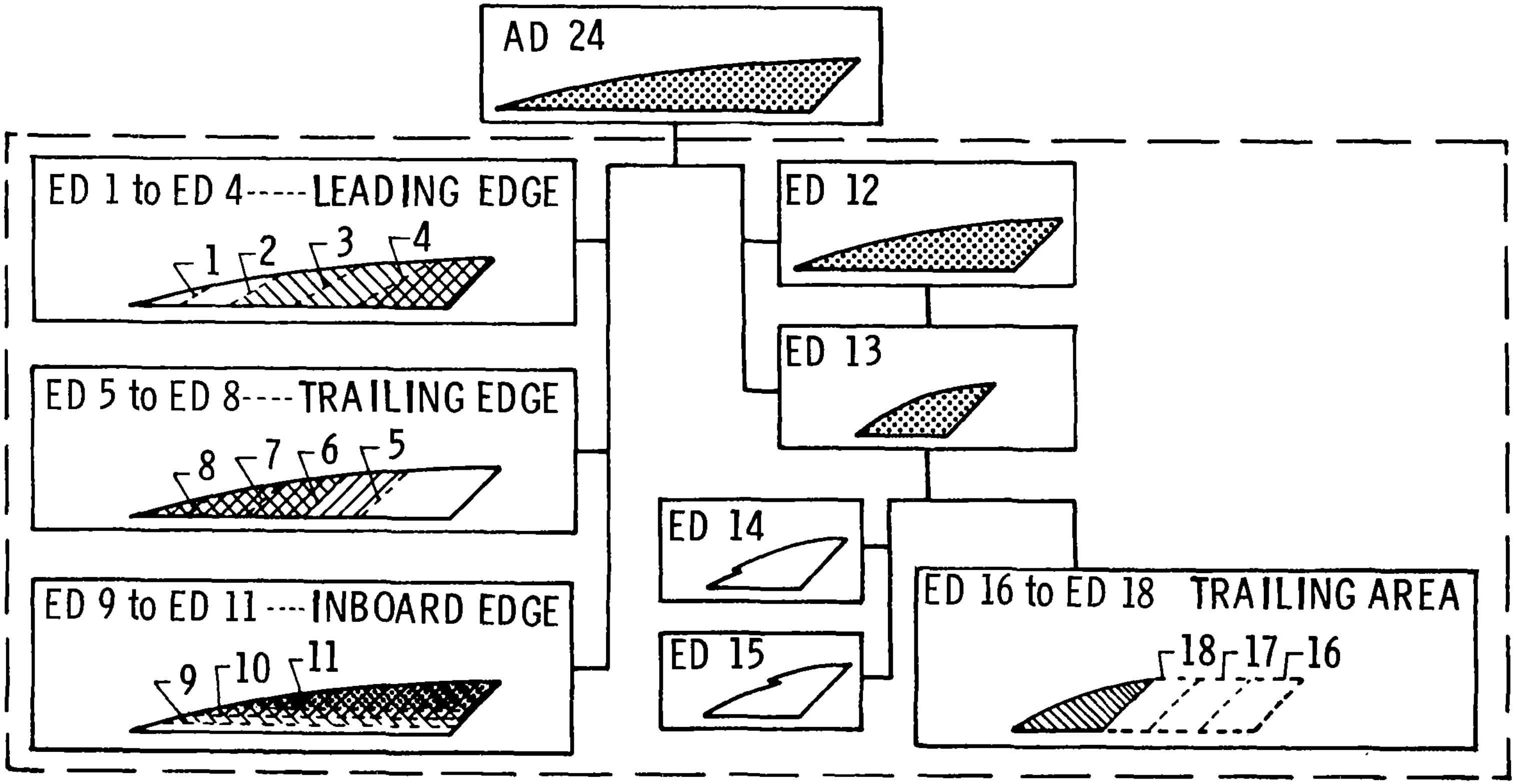

(c) Empirical group.

Figure 3.- Concluded.

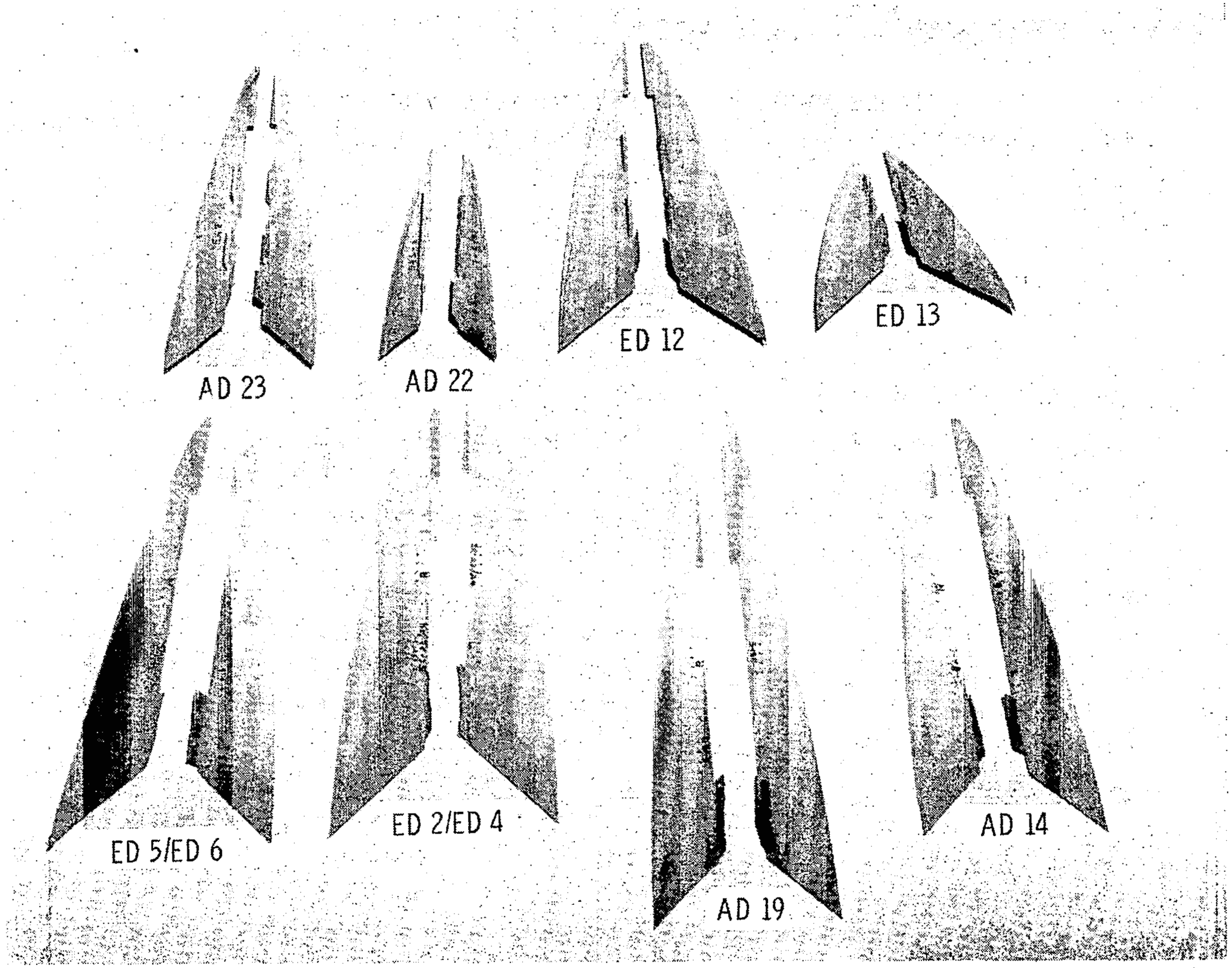

L-79-656

Figure 4.- Typical strakes.

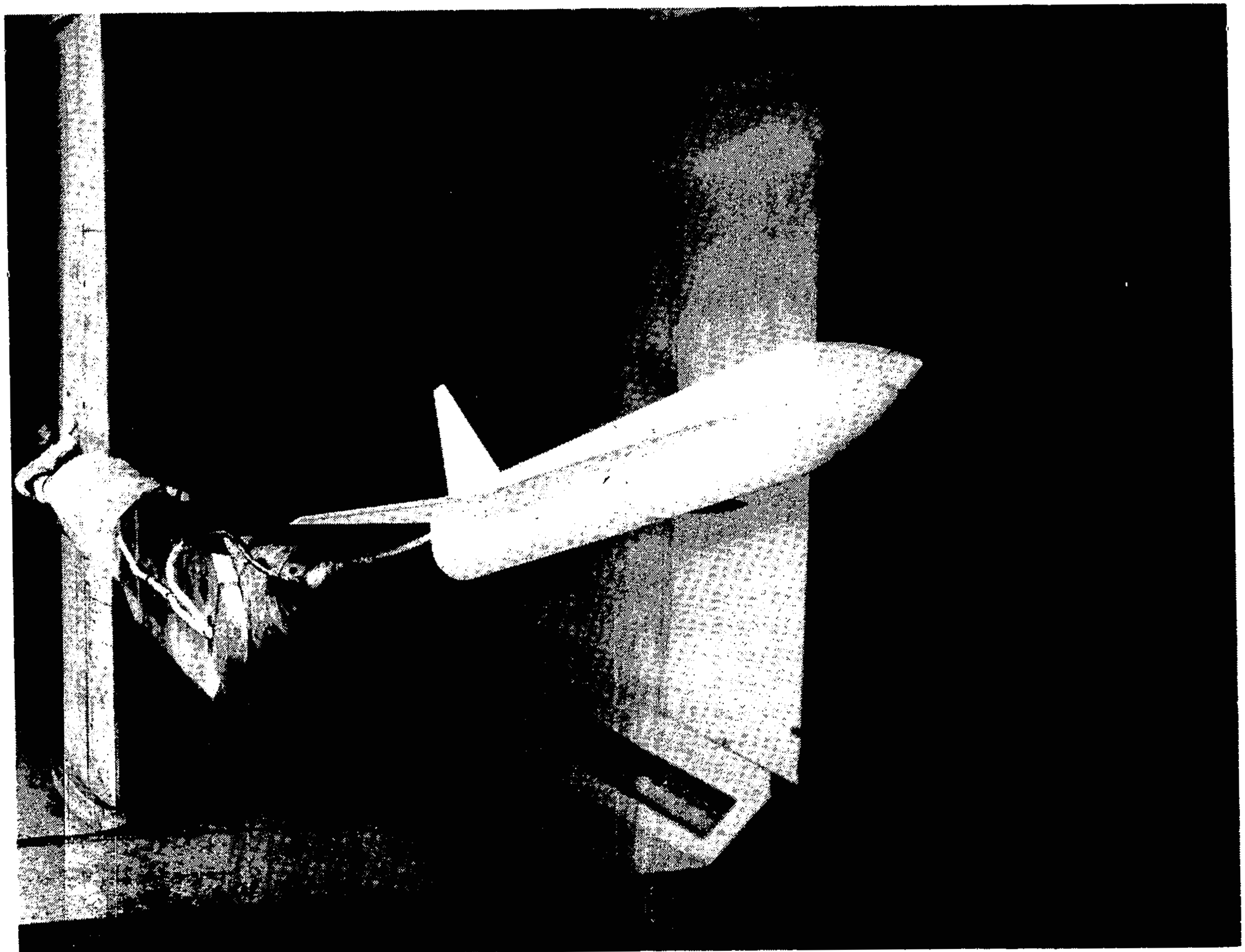

L-79-657

Figure 5.- Three-quarter front view of model mounted on high-angle-of-attack sting support in Langley High-Speed 7- by 10-Foot Tunnel.

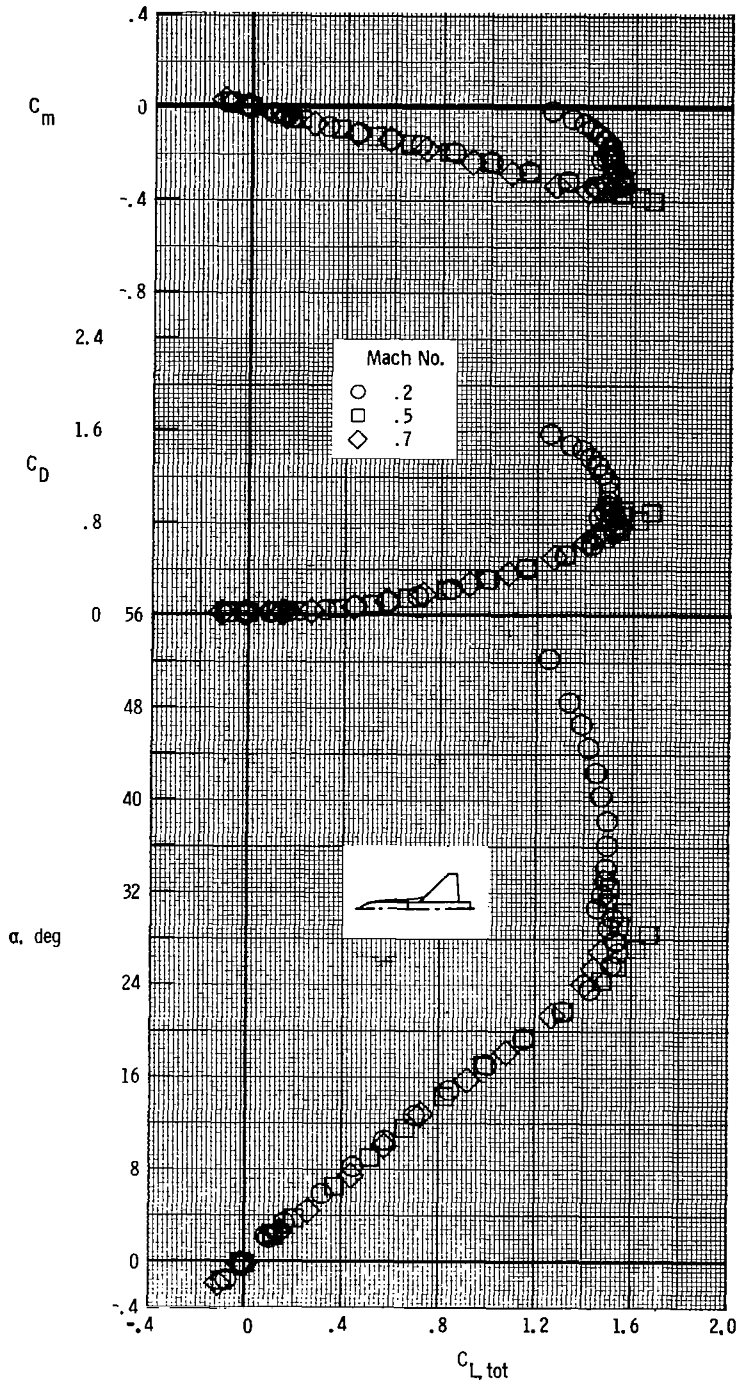

(a) AD 9.

Figure 6.- Effect of Mach number on basic longitudinal characteristics for complete configuration.

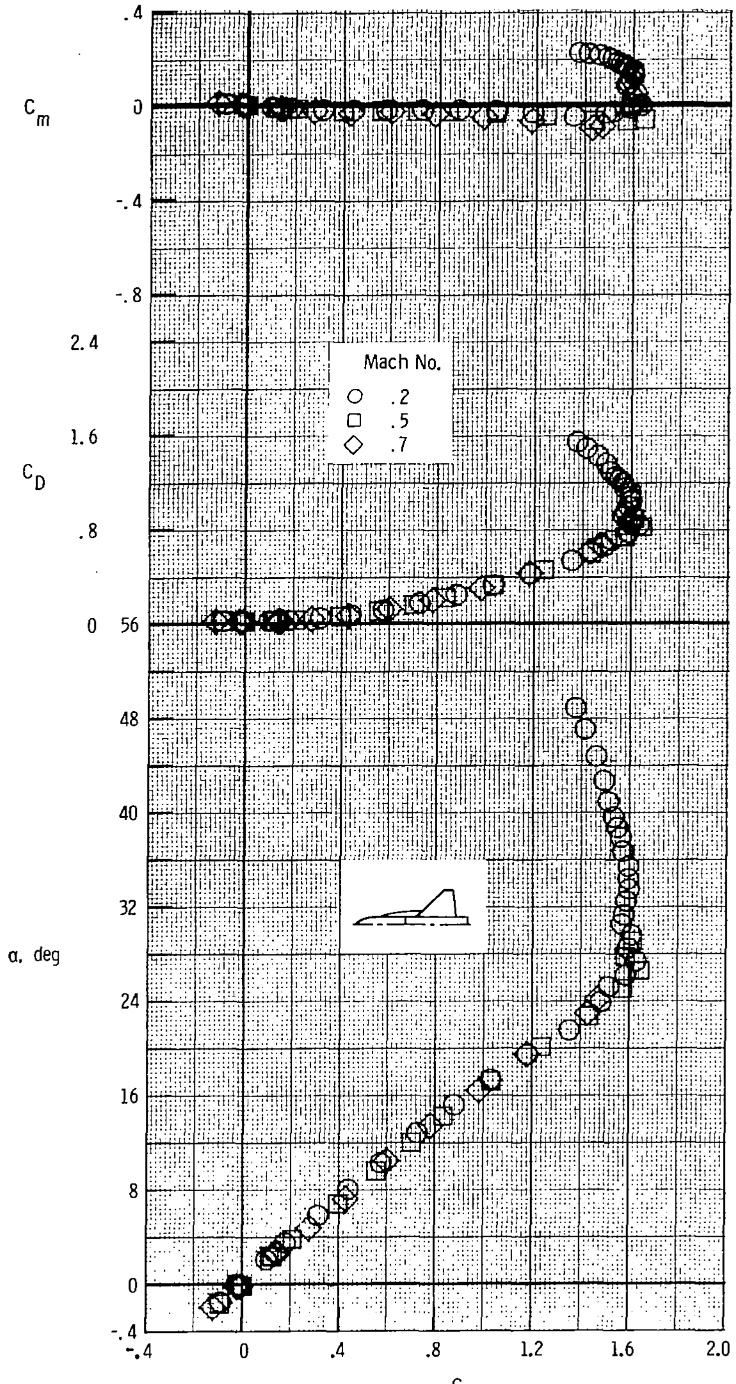

(b) AD 14.

Figure 6.- Continued.

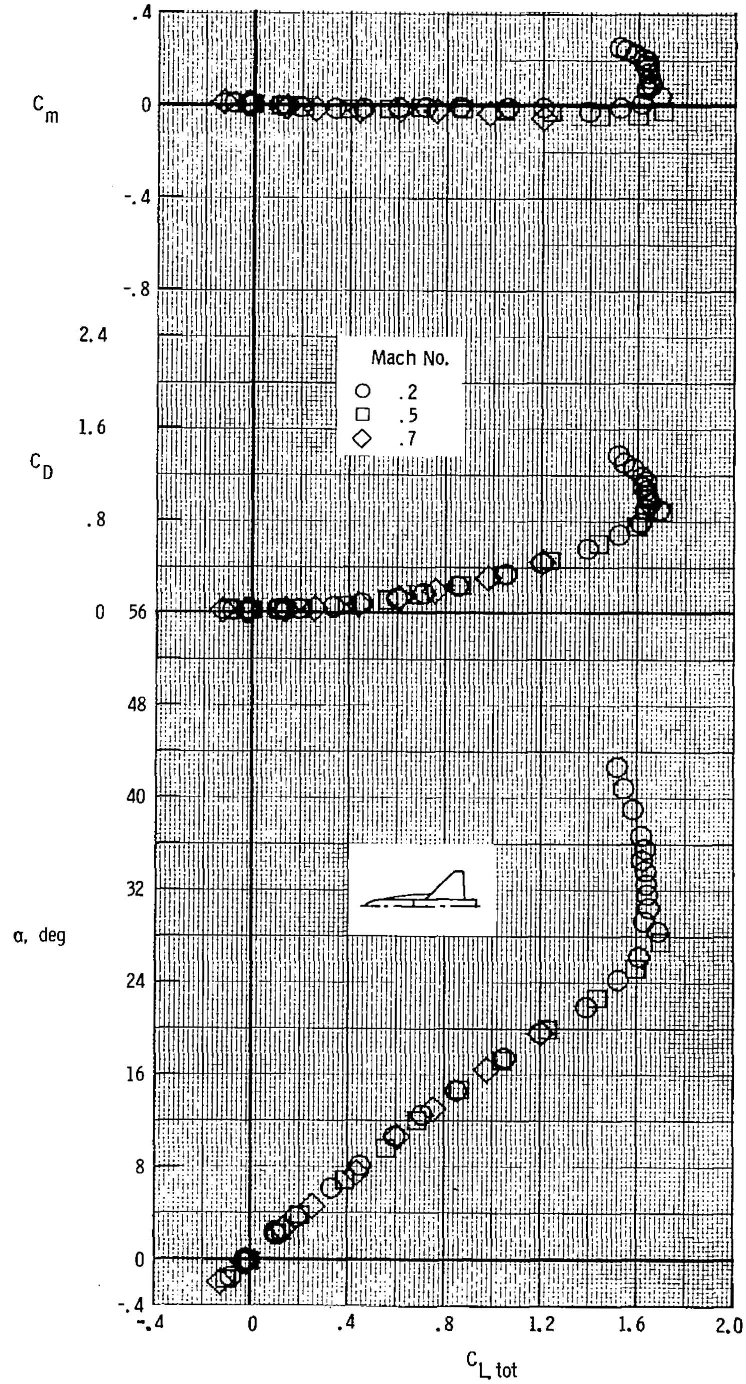

(c) AD 17.

Figure 6.- Continued.

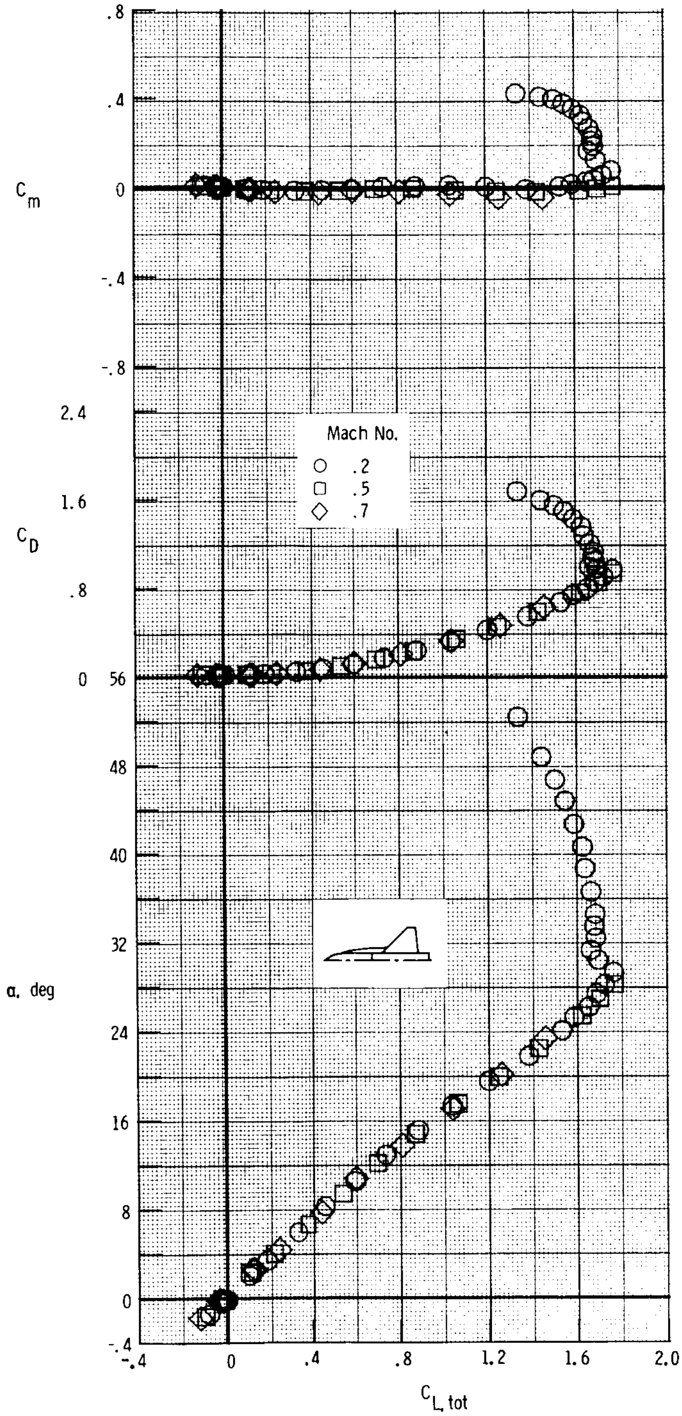

(d) AD 19.

Figure 6.- Continued.

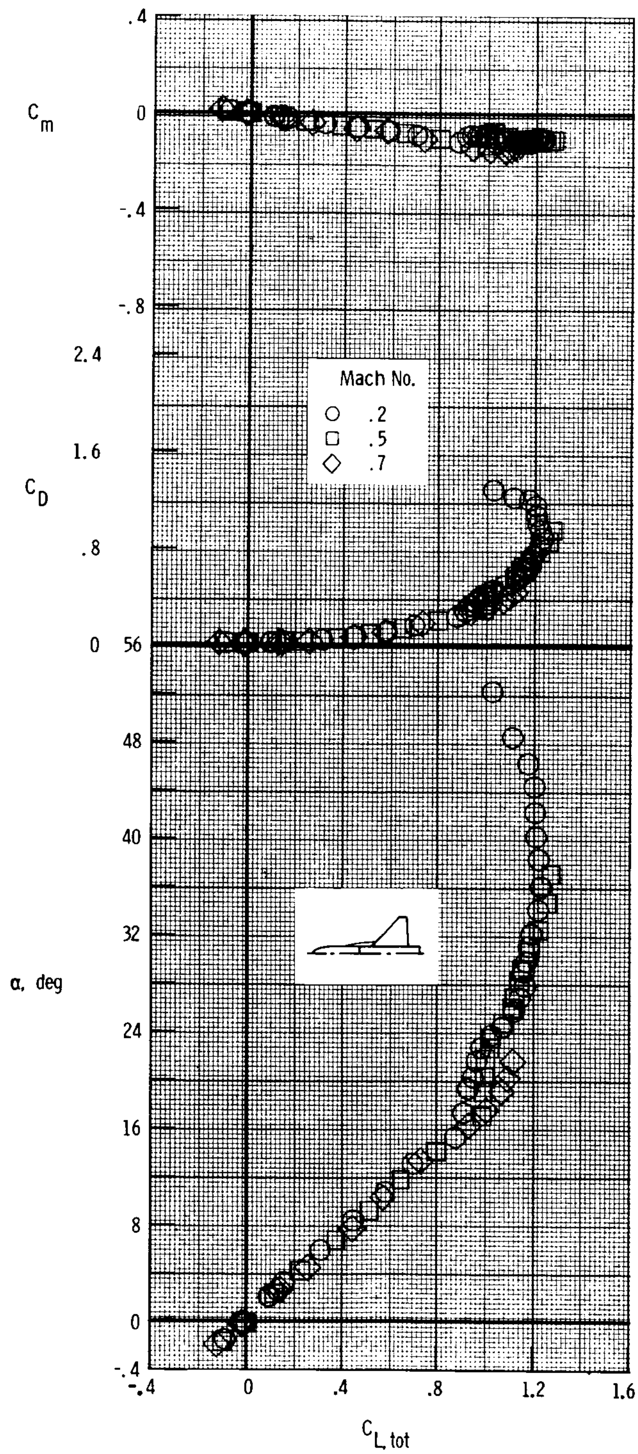

(e) AD 22.

Figure 6.- Continued.

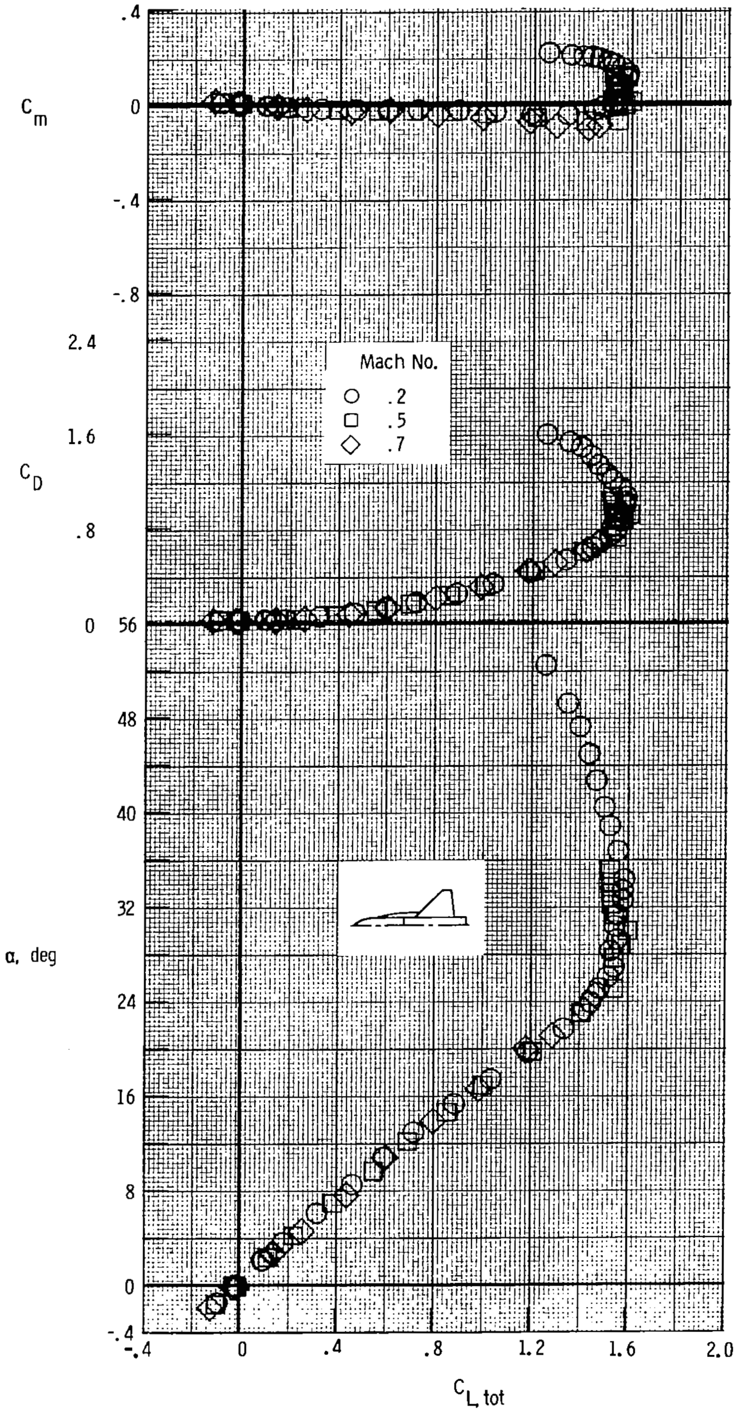

(f) AD 23.

Figure 6.- Continued.

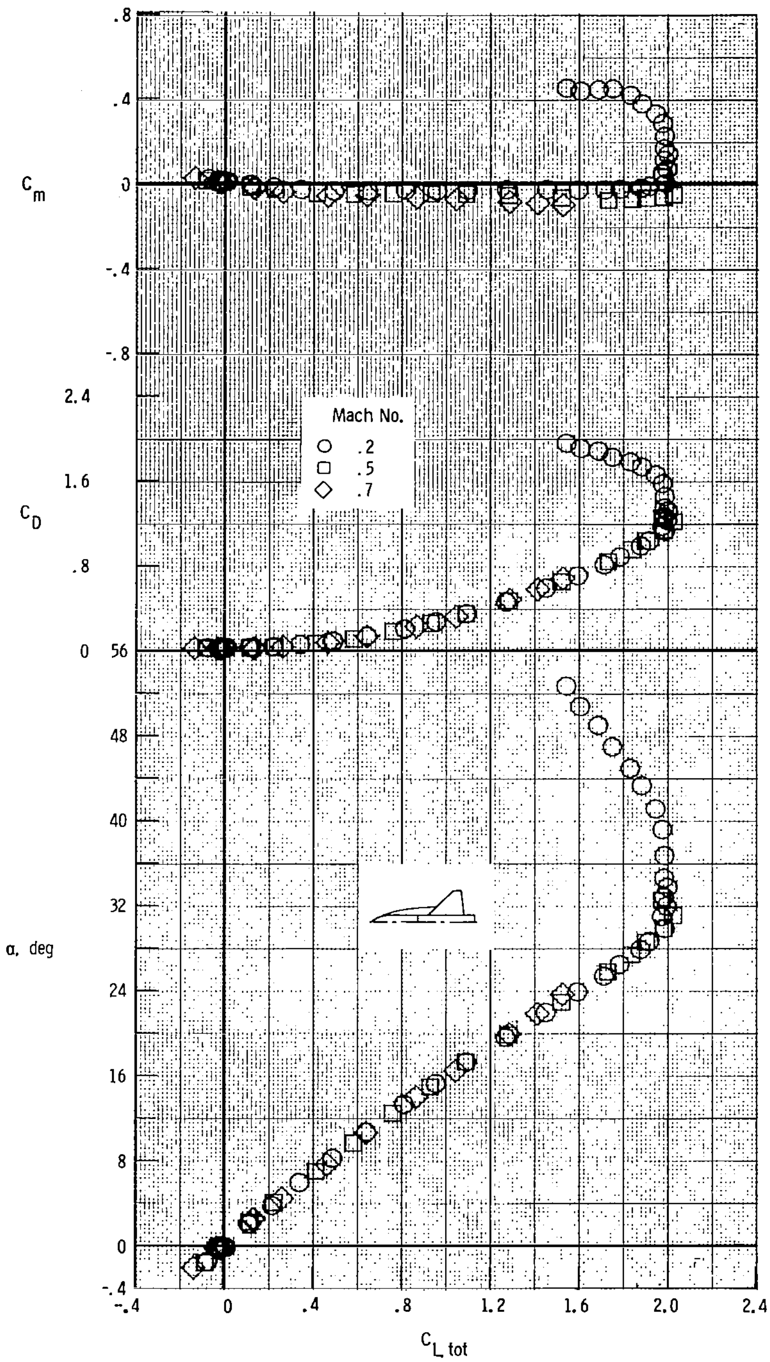

(g) AD 24.

Figure 6.- Continued.

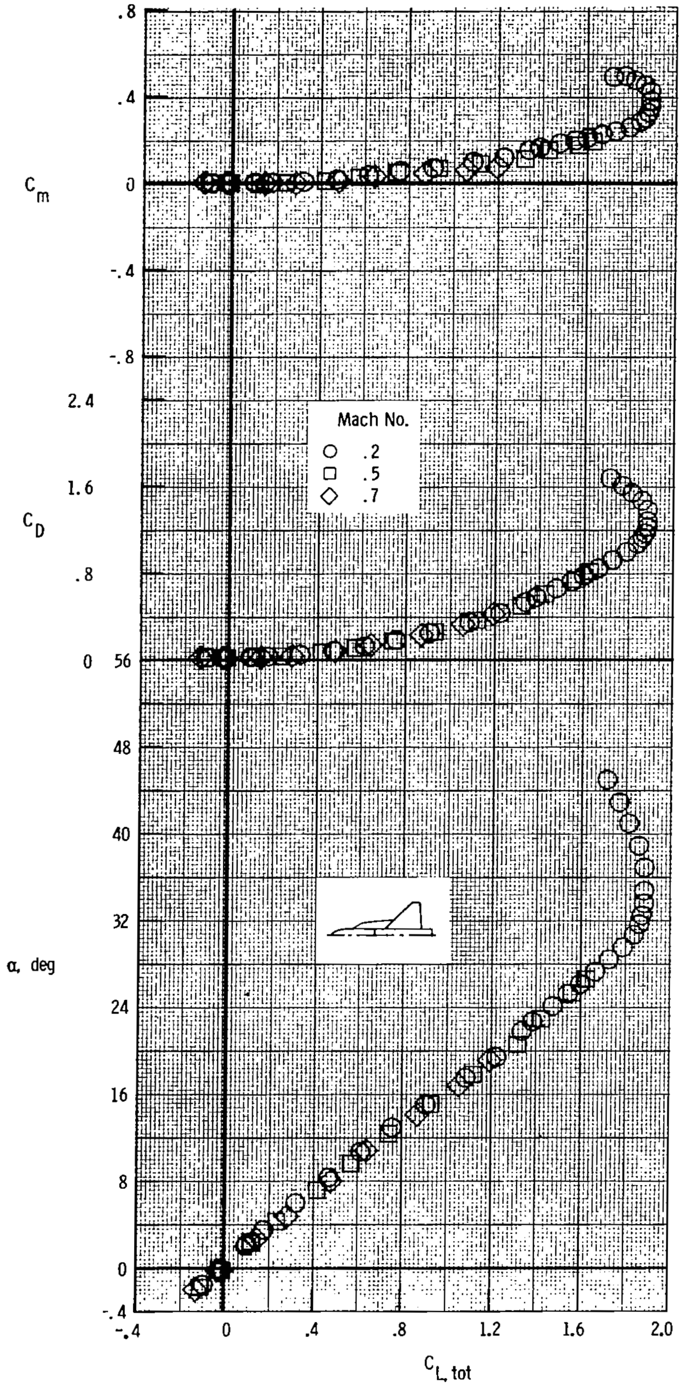

(h) ED 2.

Figure 6.- Continued.

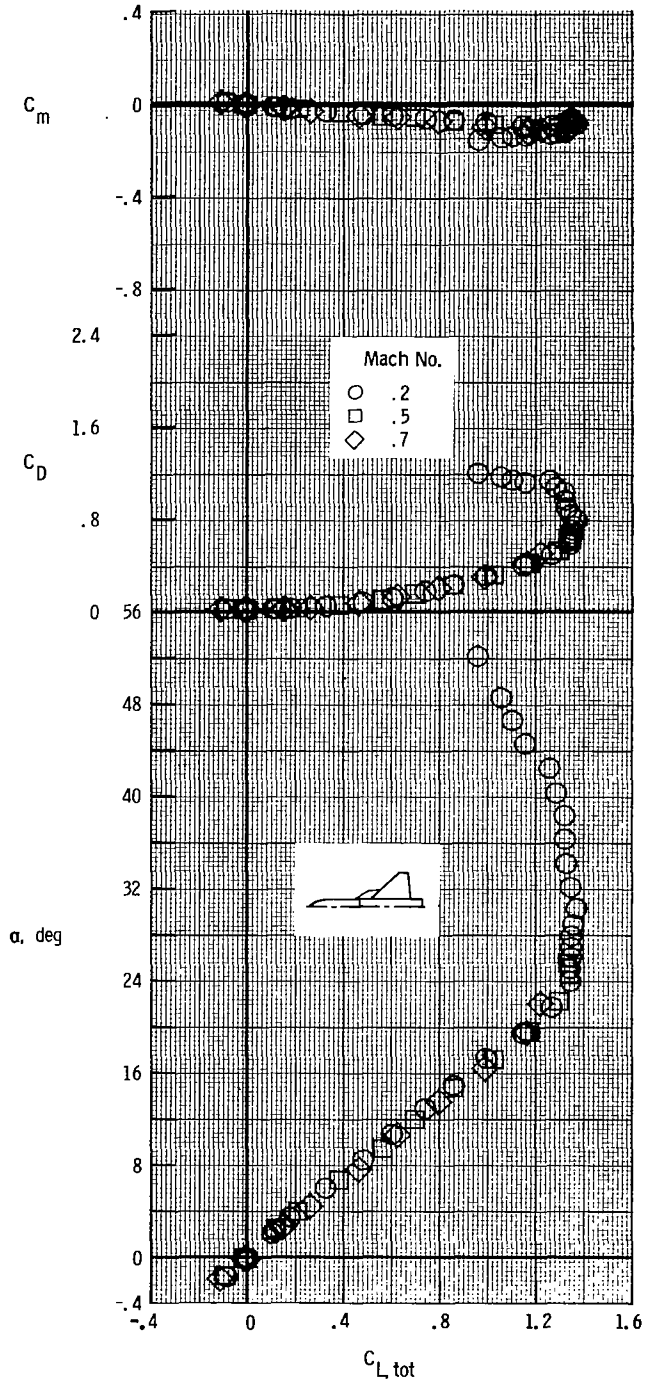

(i) ED 4.

Figure 6.- Continued.

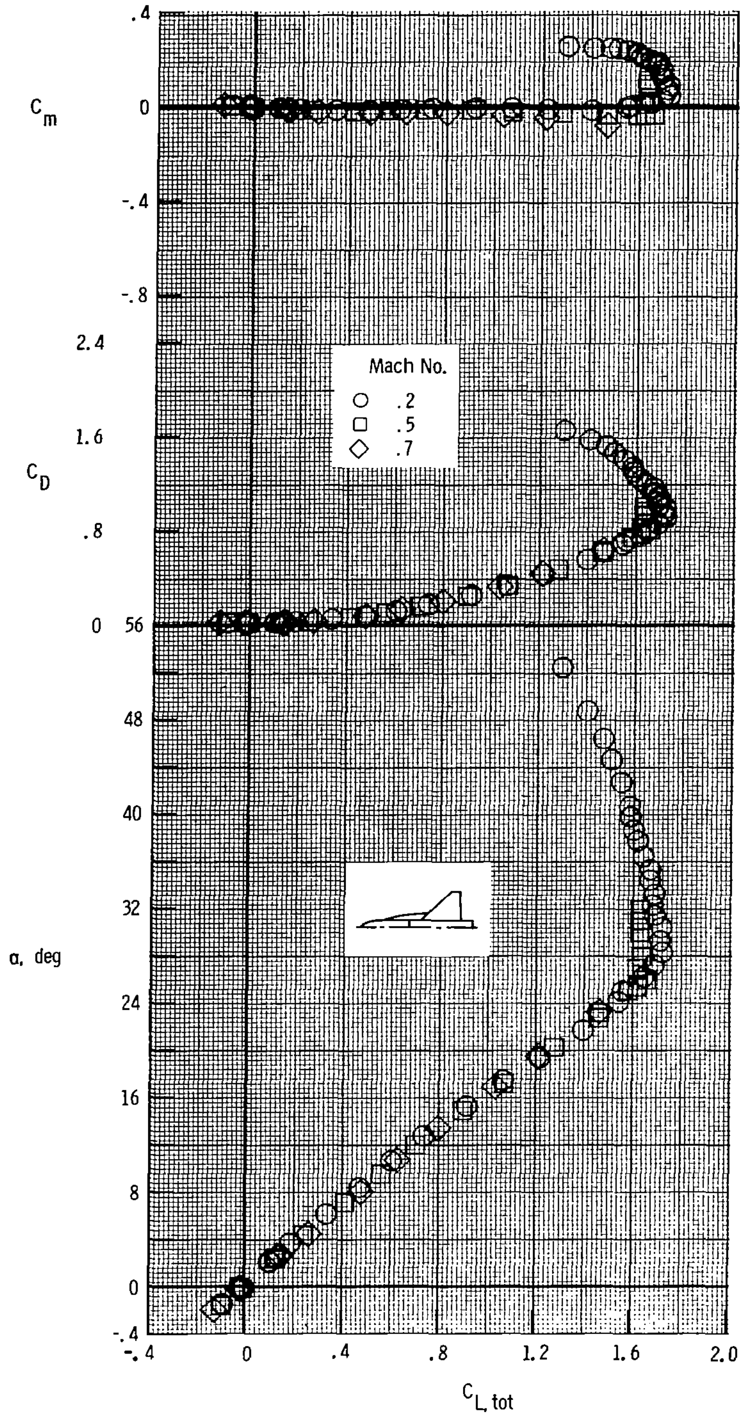

(j) ED 5.

Figure 6.- Continued.

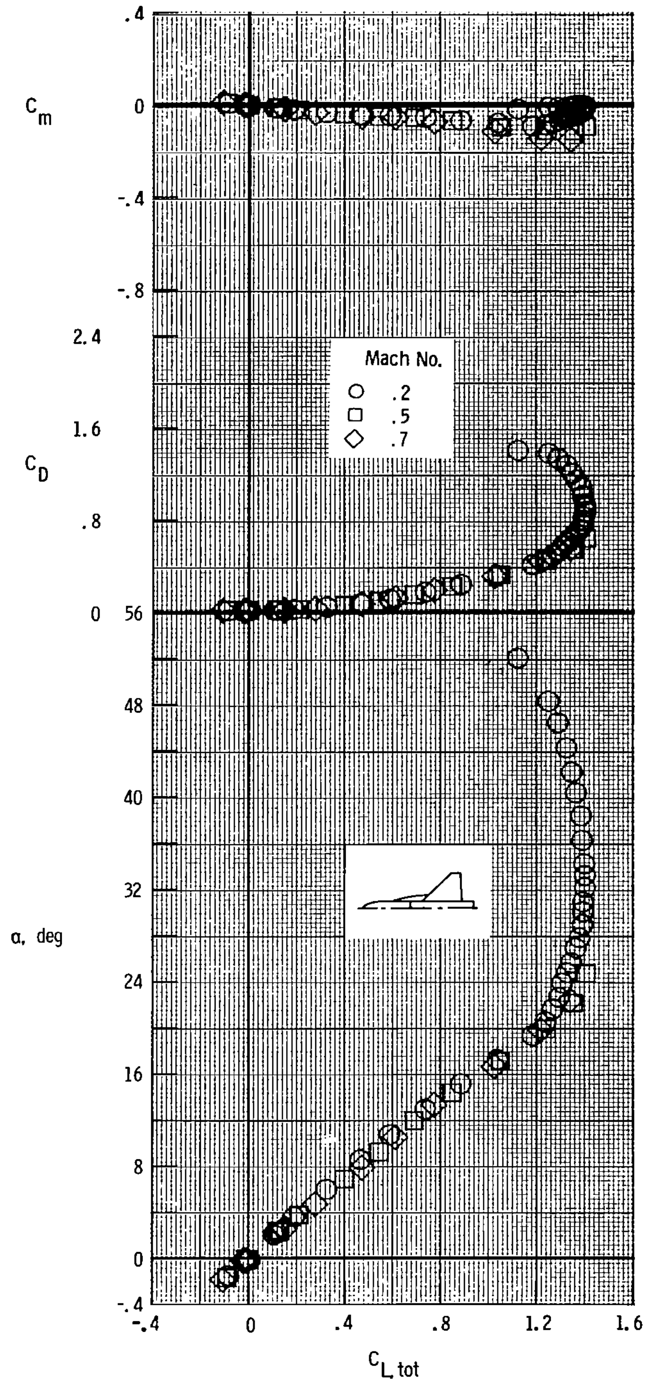

(k) ED 6.

Figure 6.- Continued.

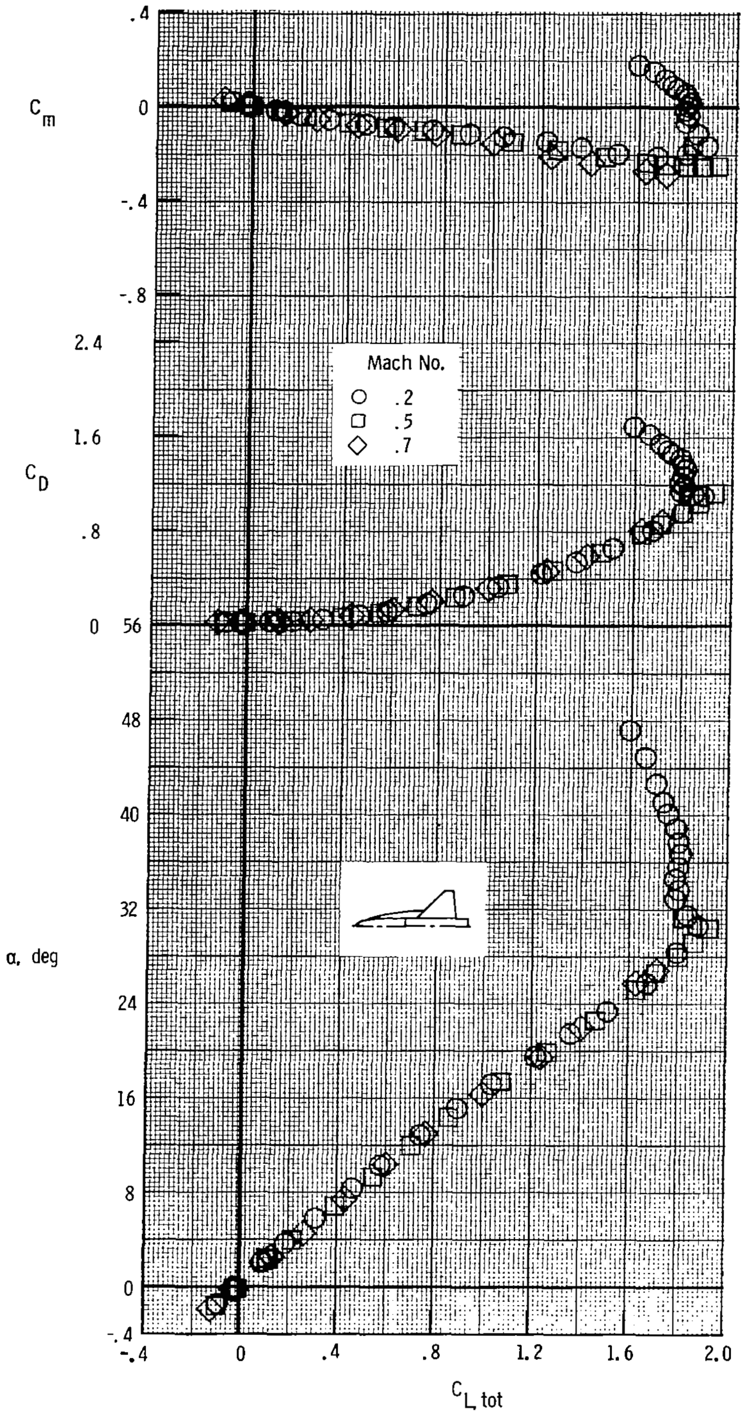

(l) ED 9.

Figure 6.- Continued.

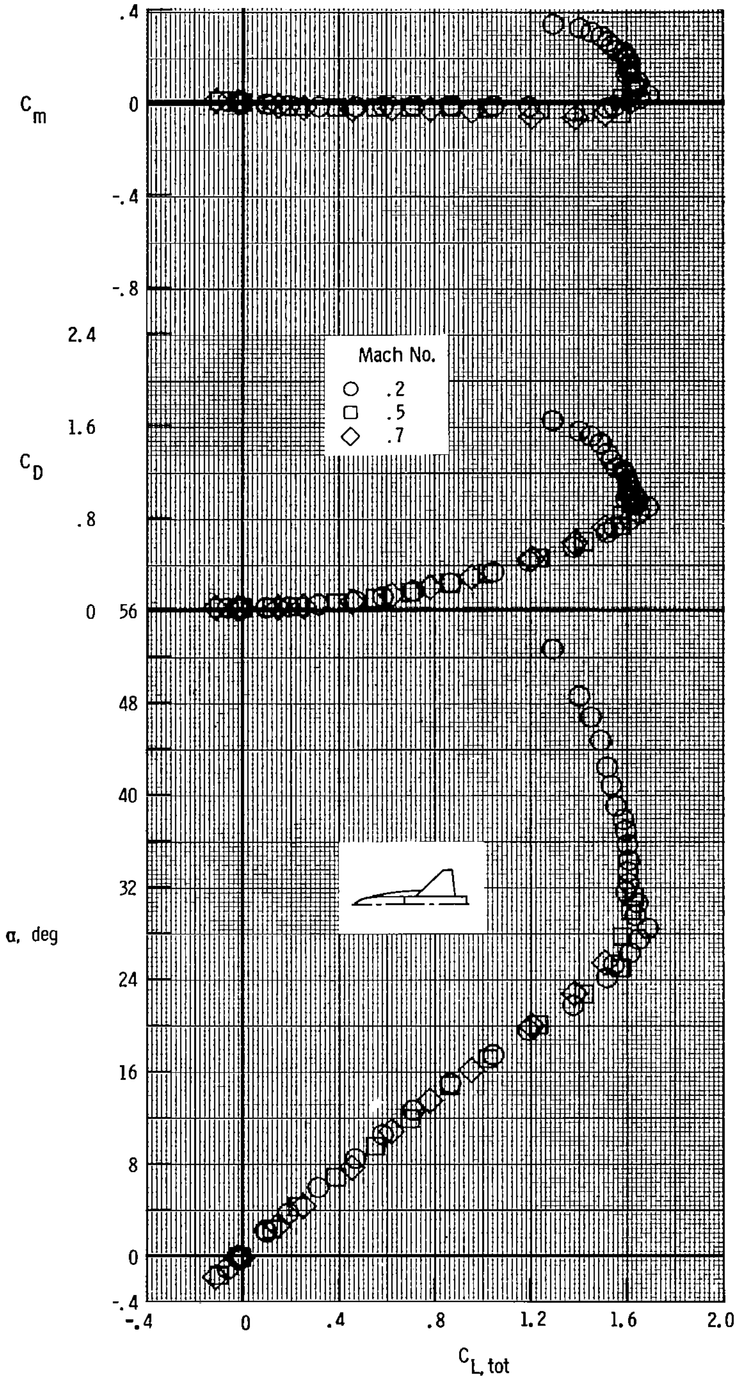

(m) ED 10.

Figure 6.- Continued.

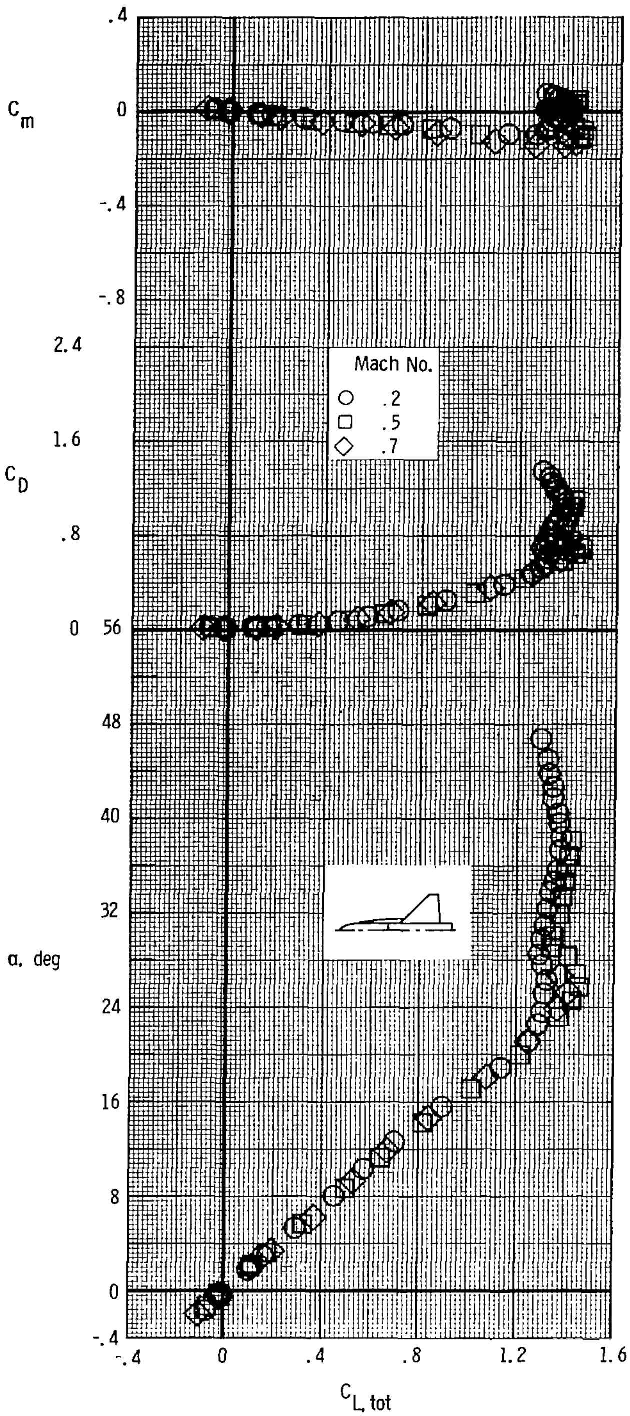

(n) ED 11.

Figure 6.- Continued.

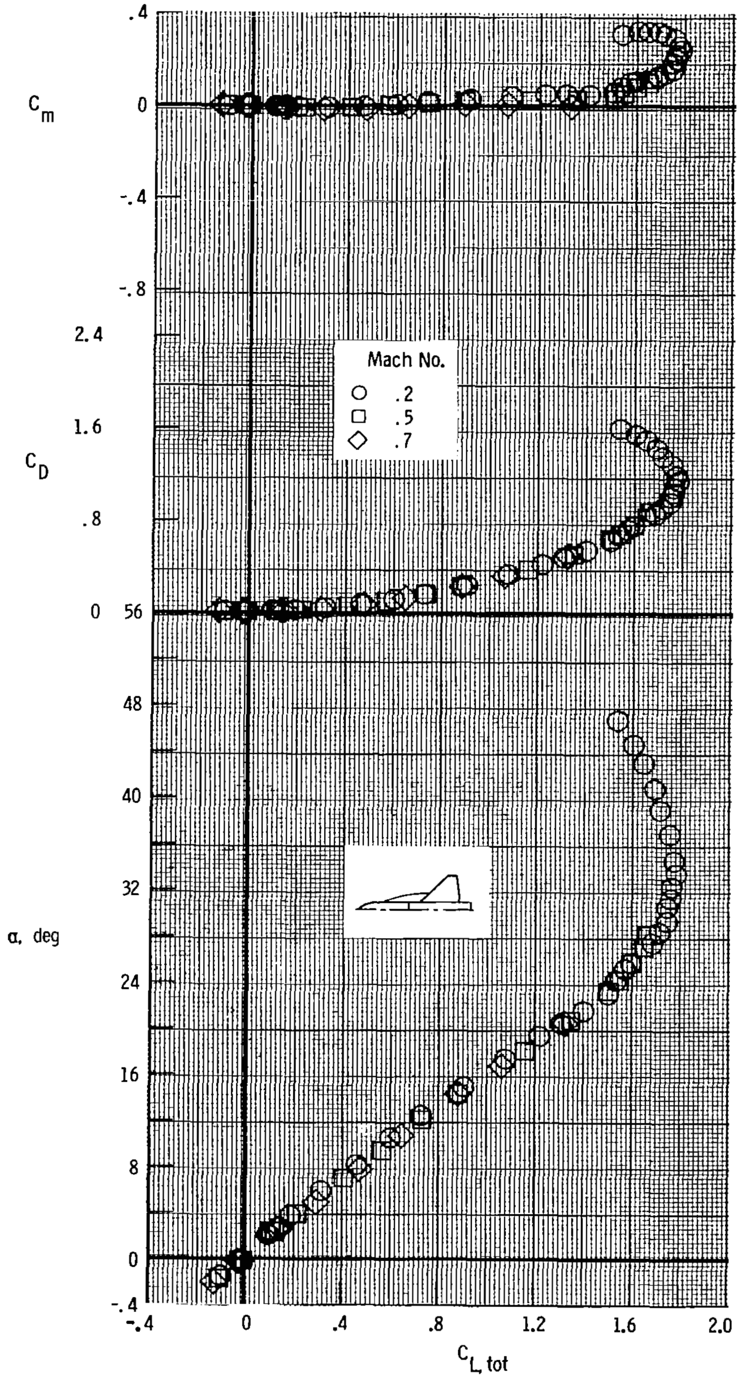

(o) ED 12.

Figure 6.- Continued.

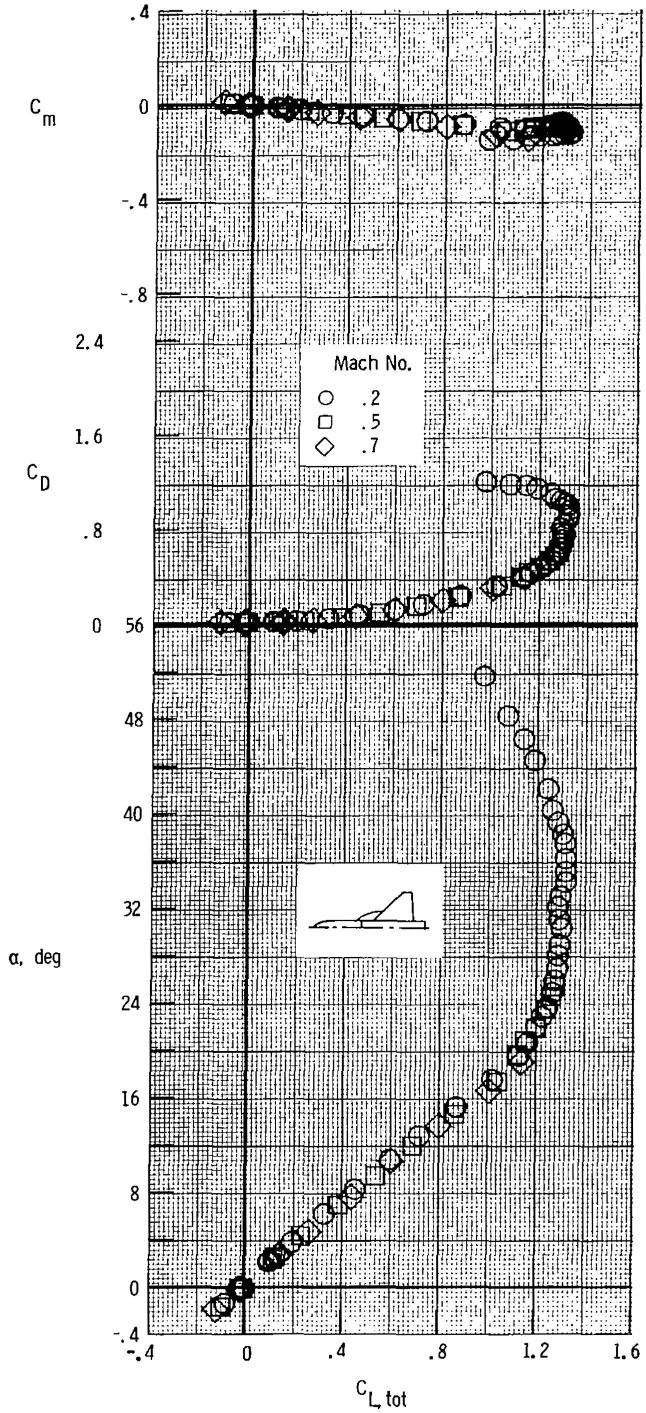

(p) ED 13.

Figure 6.- Concluded.

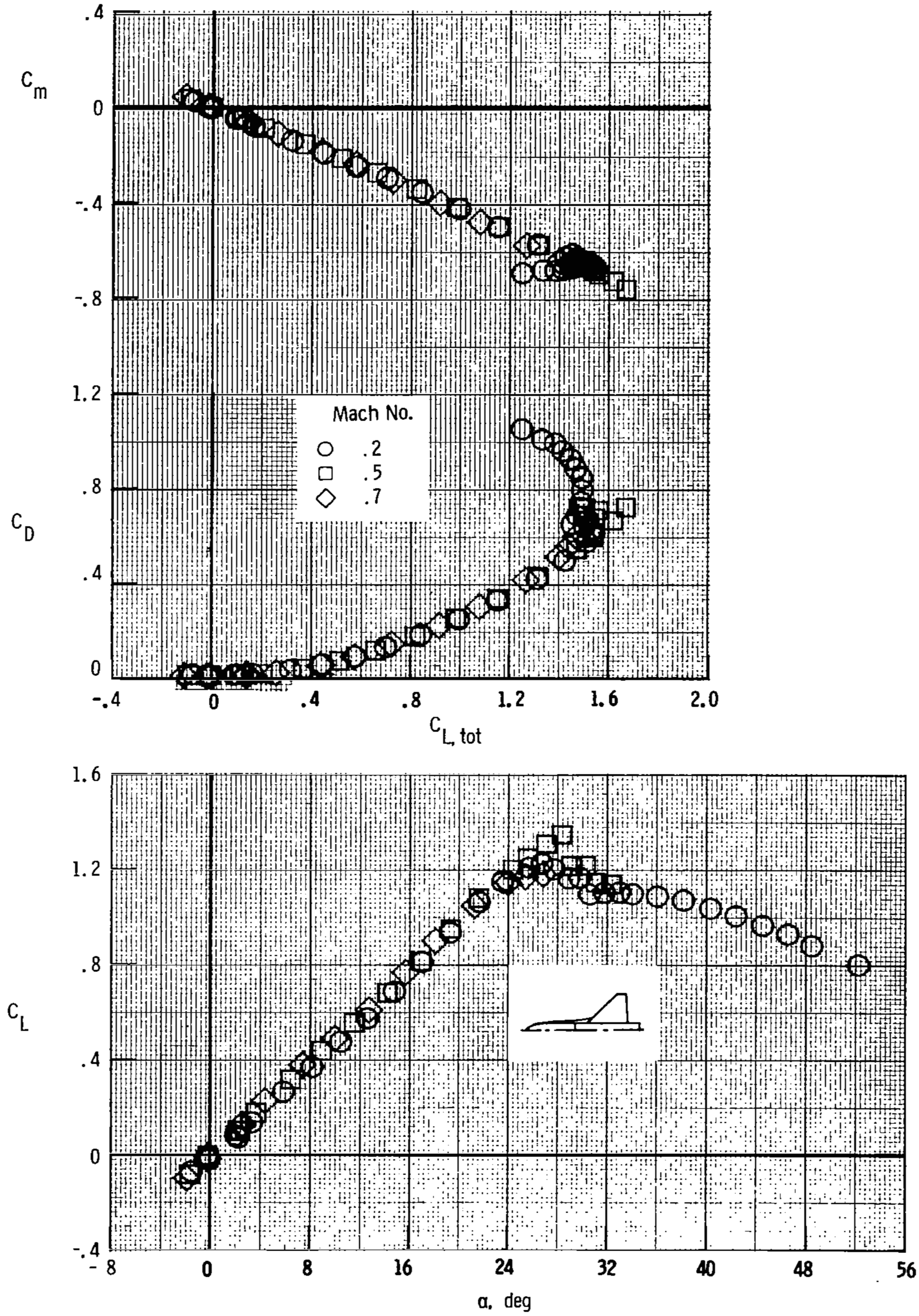

(a) AD 9.

Figure 7.- Effect of Mach number on basic longitudinal characteristics for wing-afterbody.

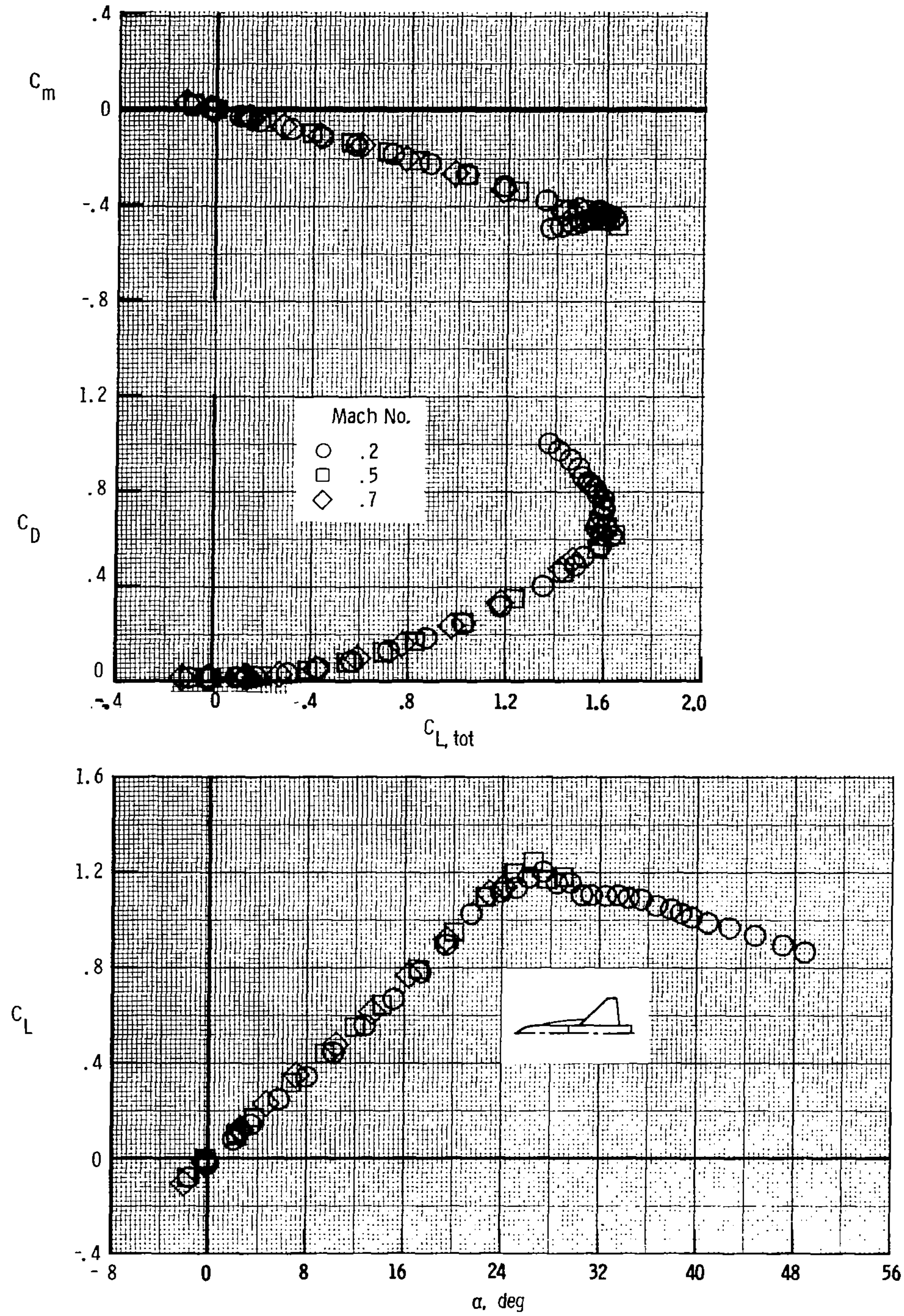

(b) AD 14.

Figure 7.- Continued.

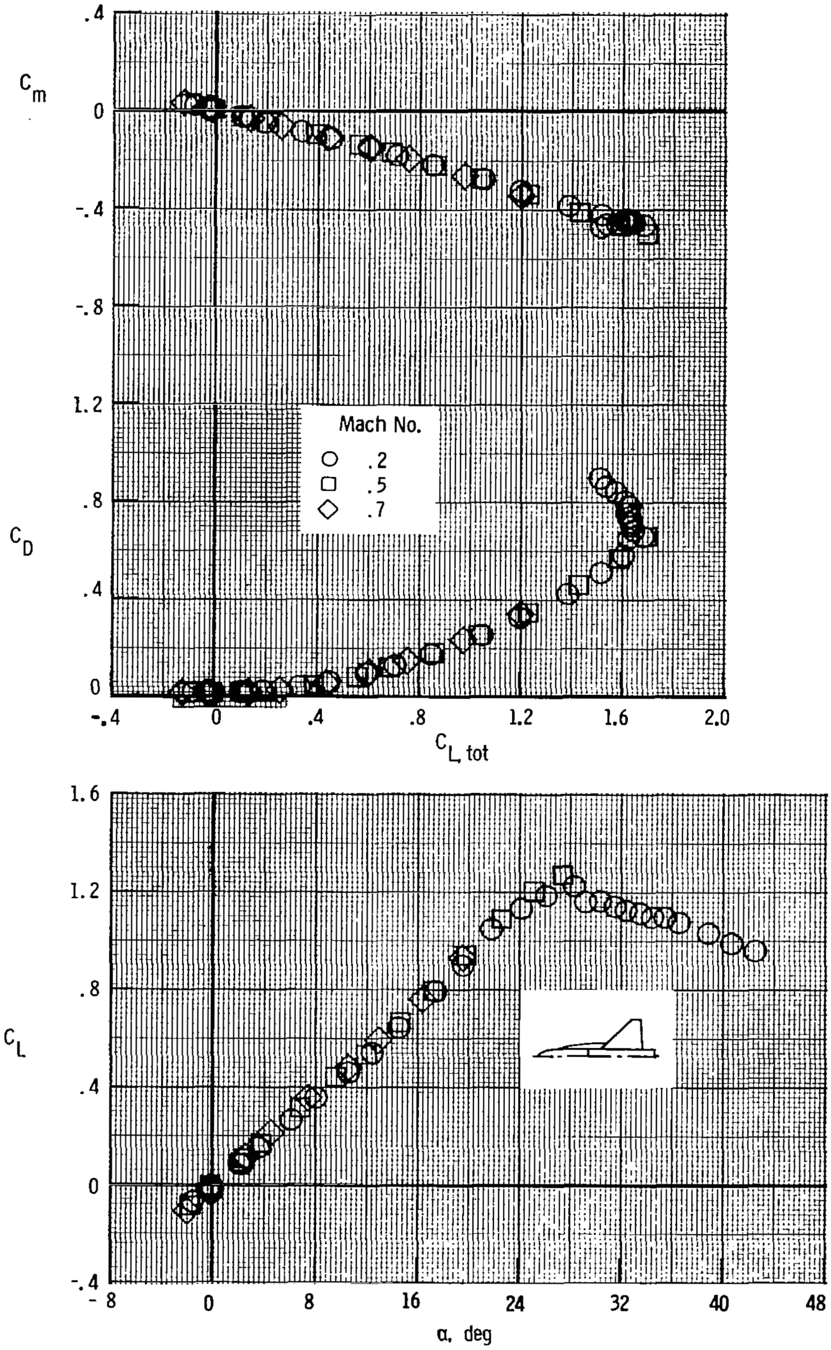

(c) AD 17.

Figure 7.- Continued.

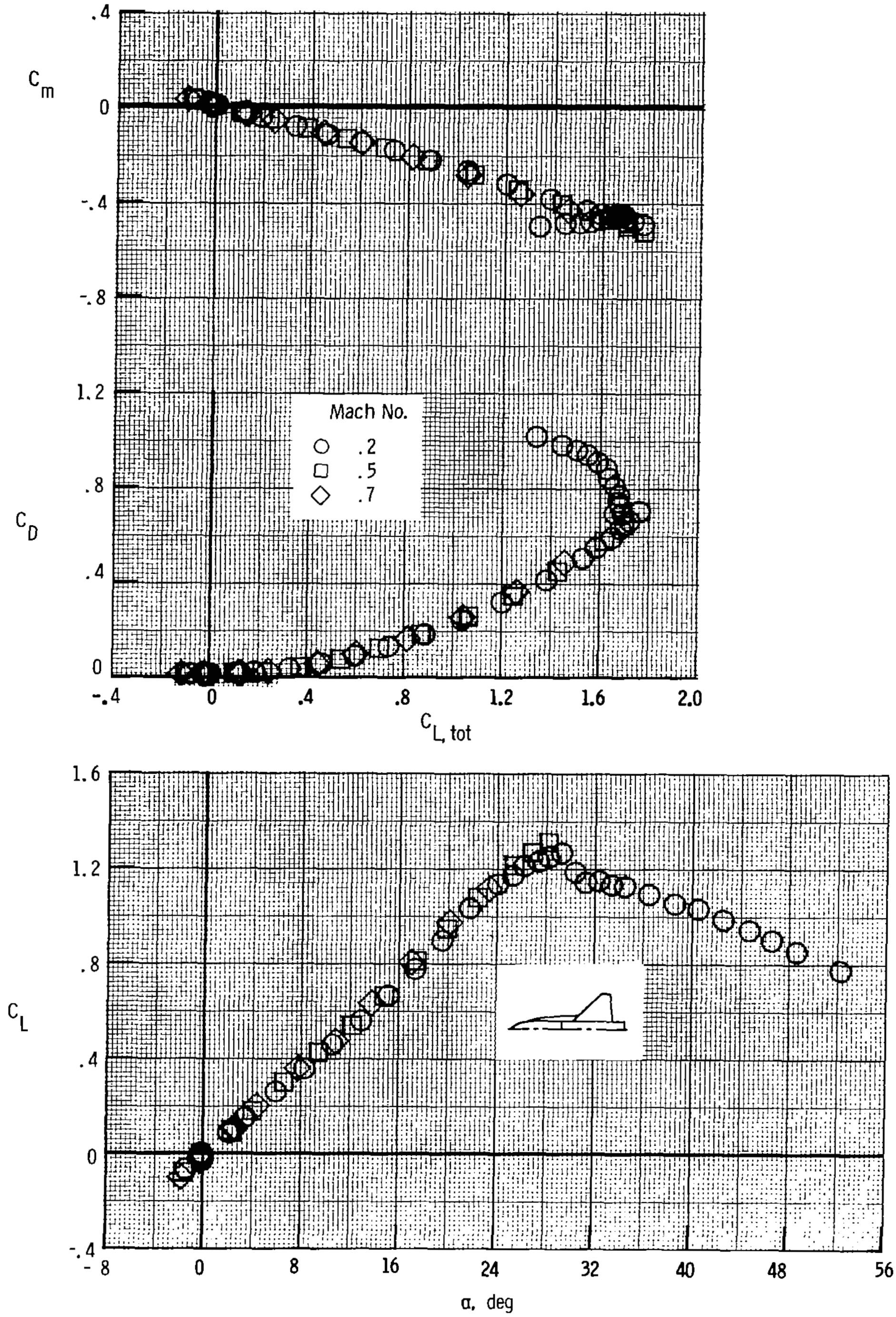

(d) AD 19.

Figure 7.- Continued.

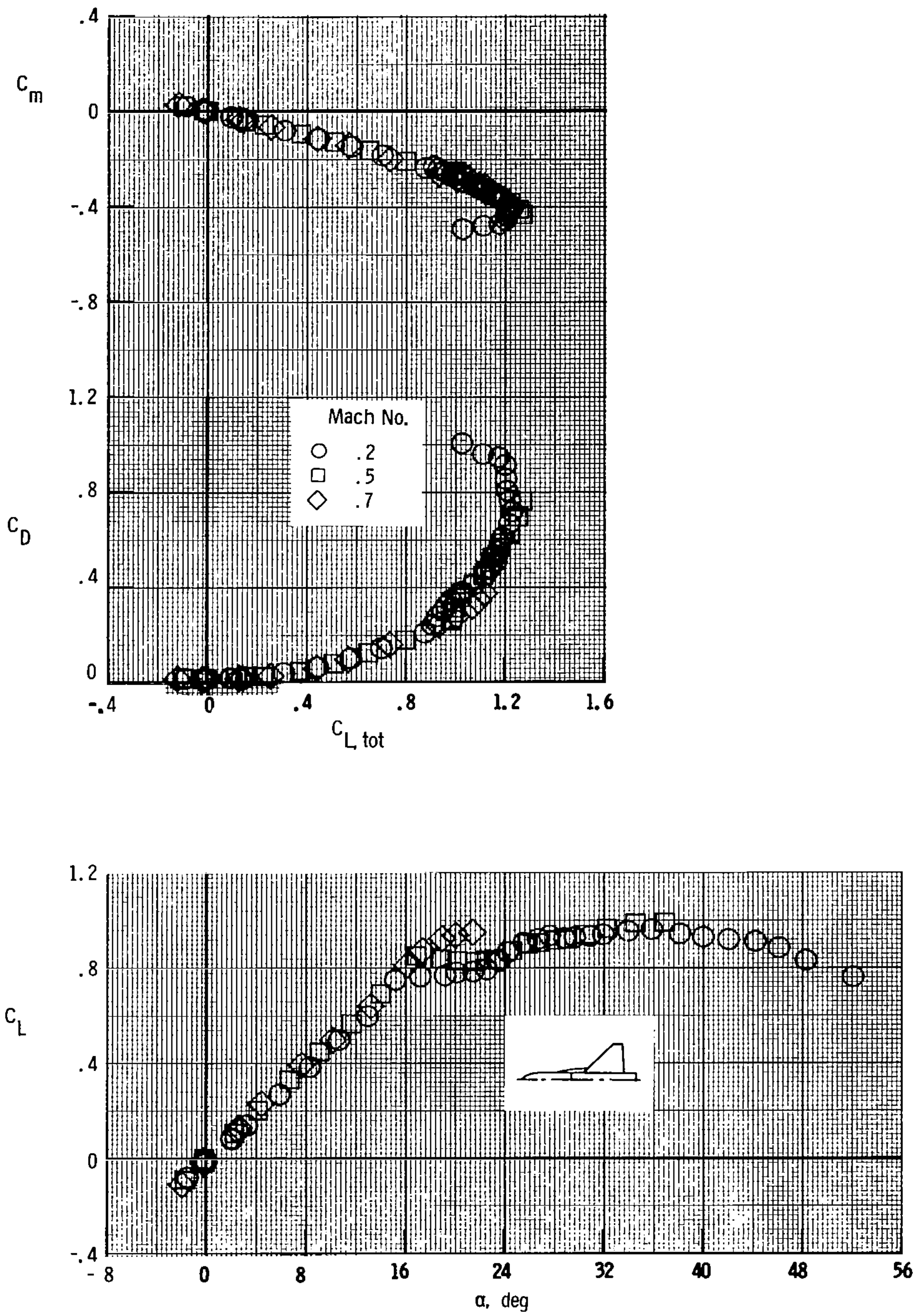

(e) AD 22.

Figure 7.- Continued.

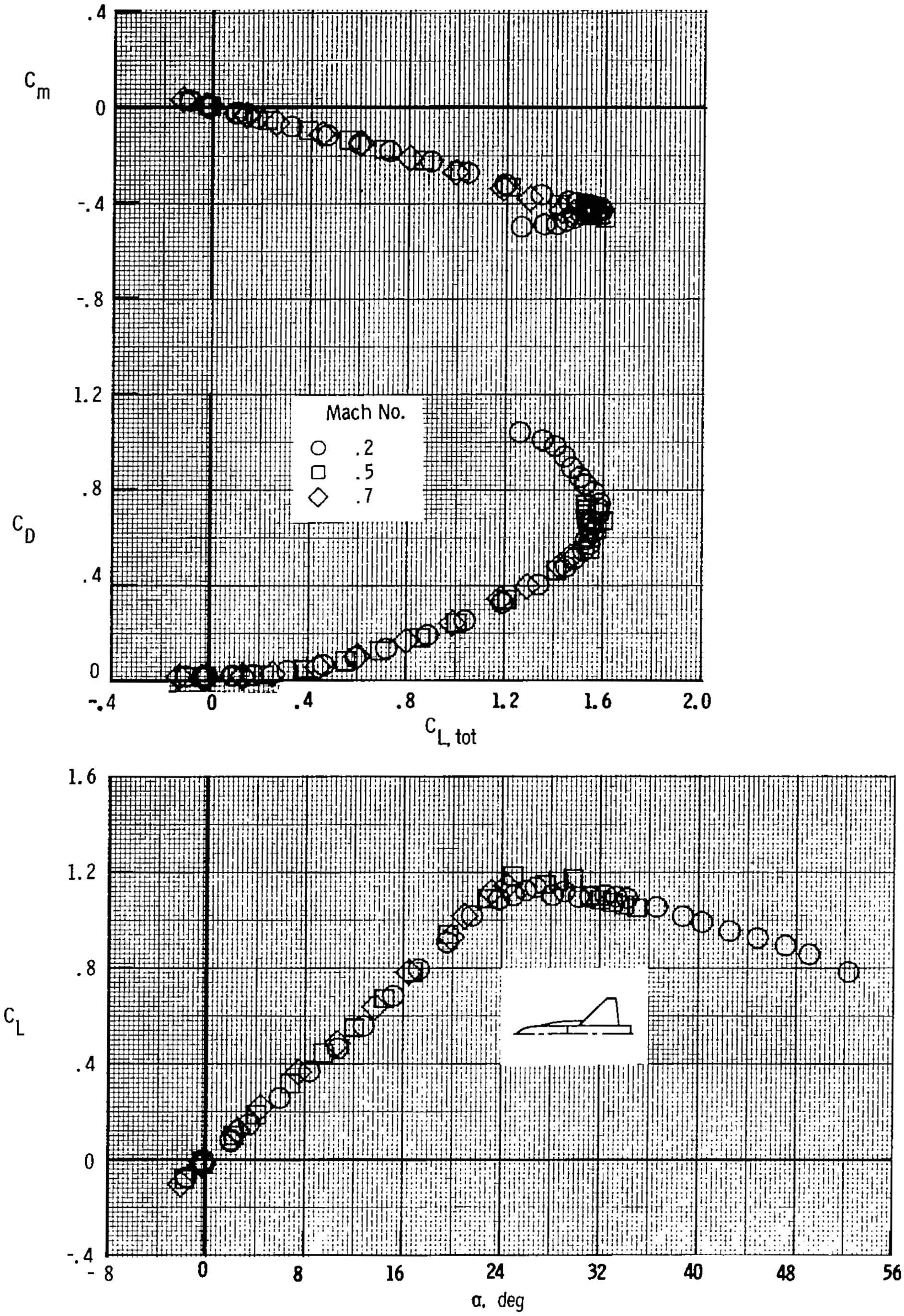

(f) AD 23.

Figure 7.- Continued.

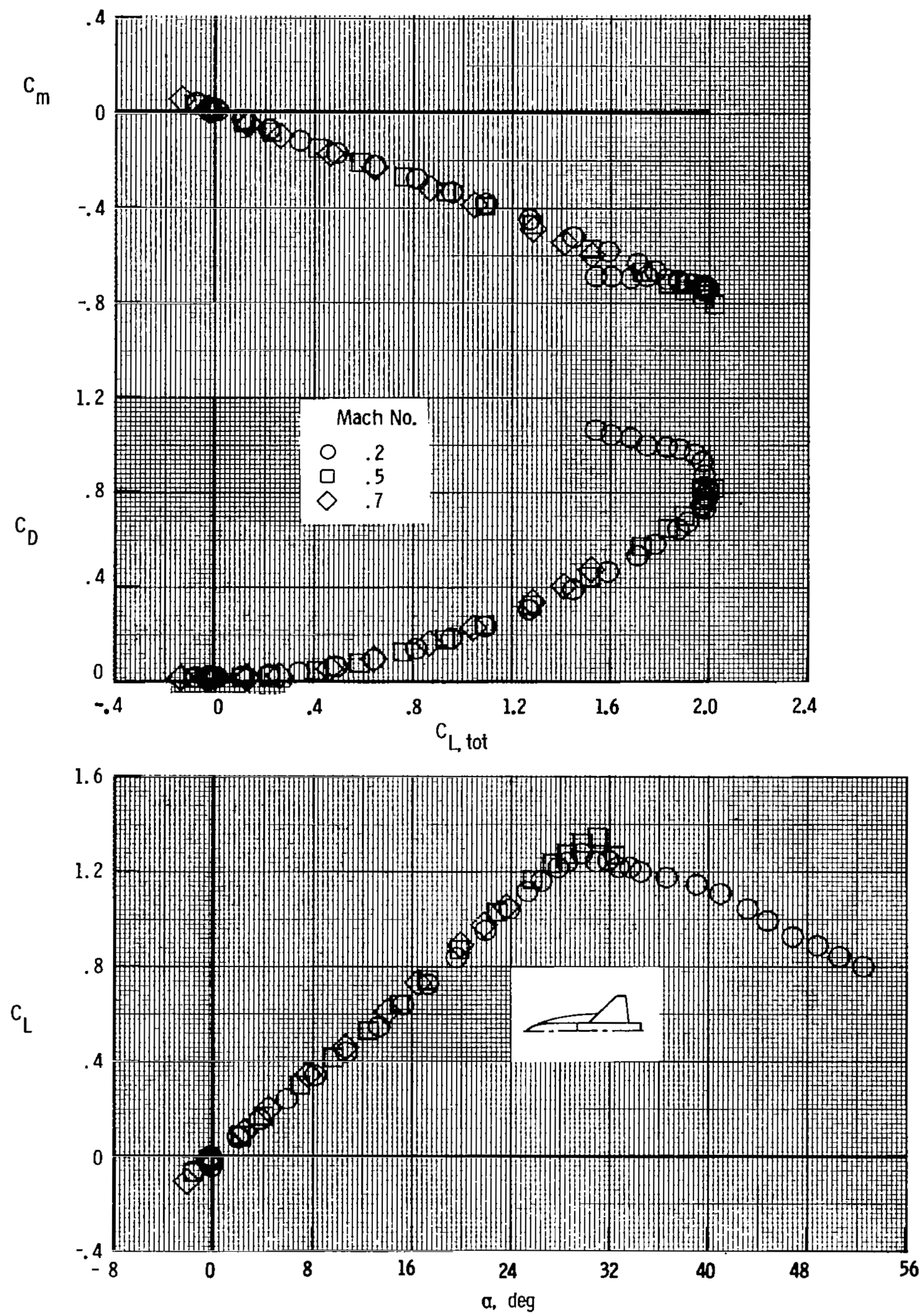

(g) AD 24.

Figure 7.- Continued.

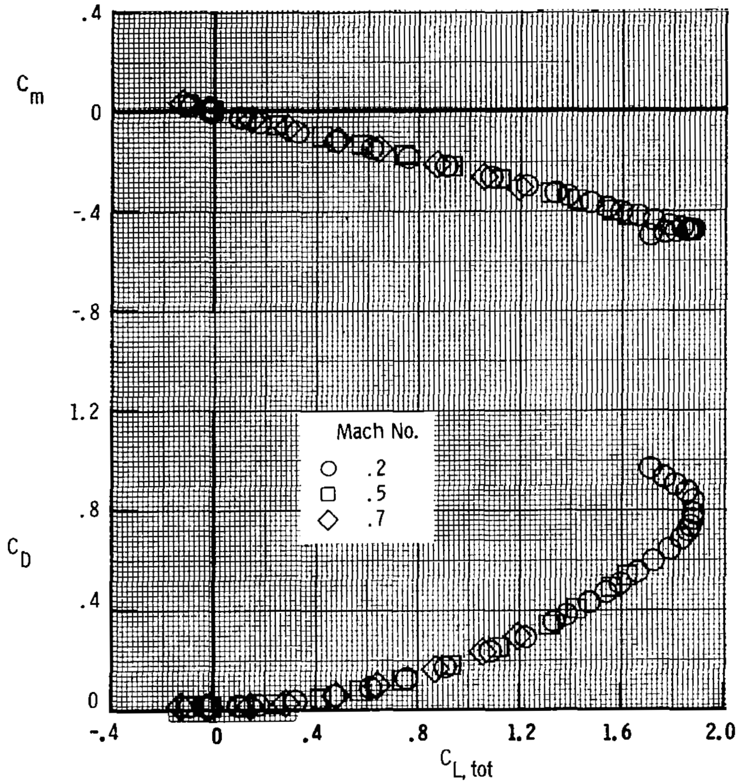

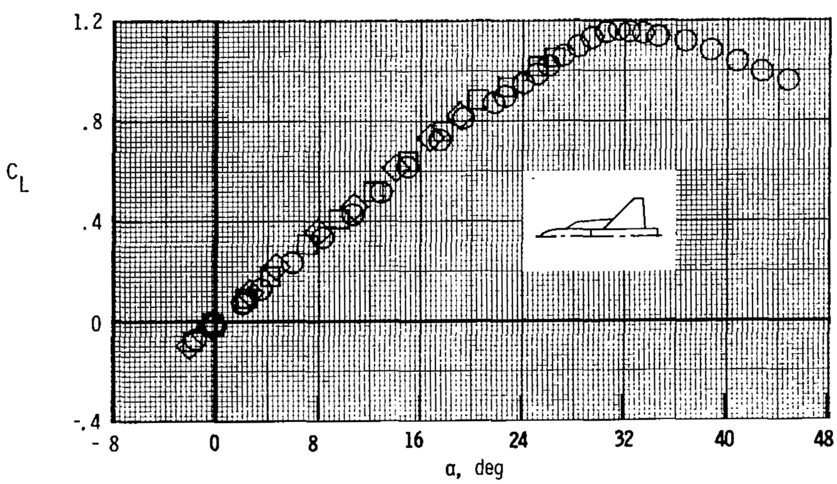

(h) ED 2.

Figure 7.- Continued.

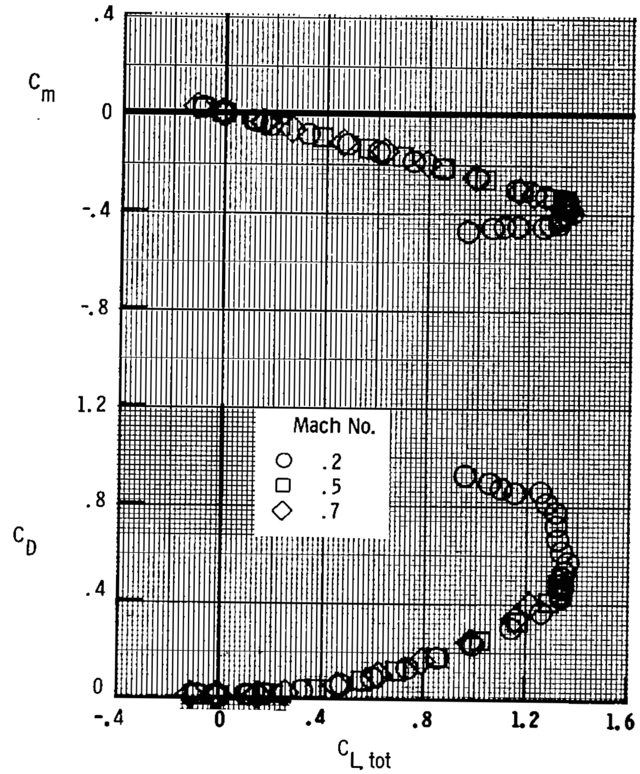

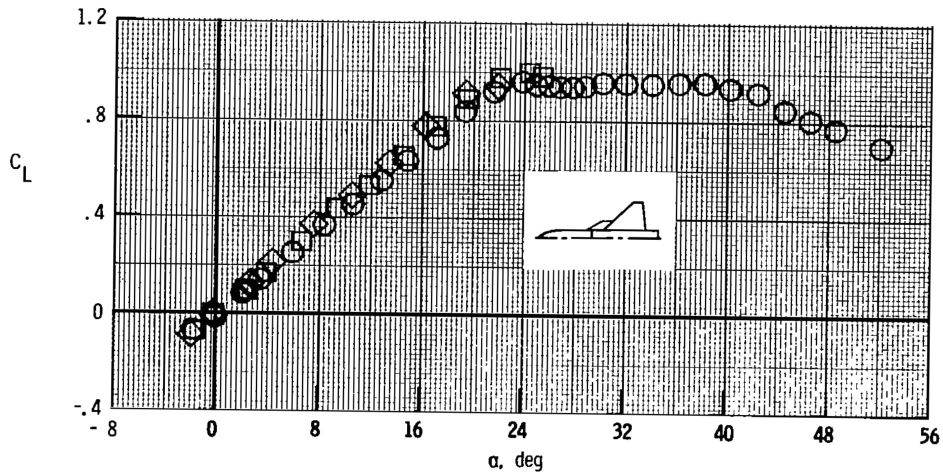

(i) ED 4.

Figure 7.- Continued.

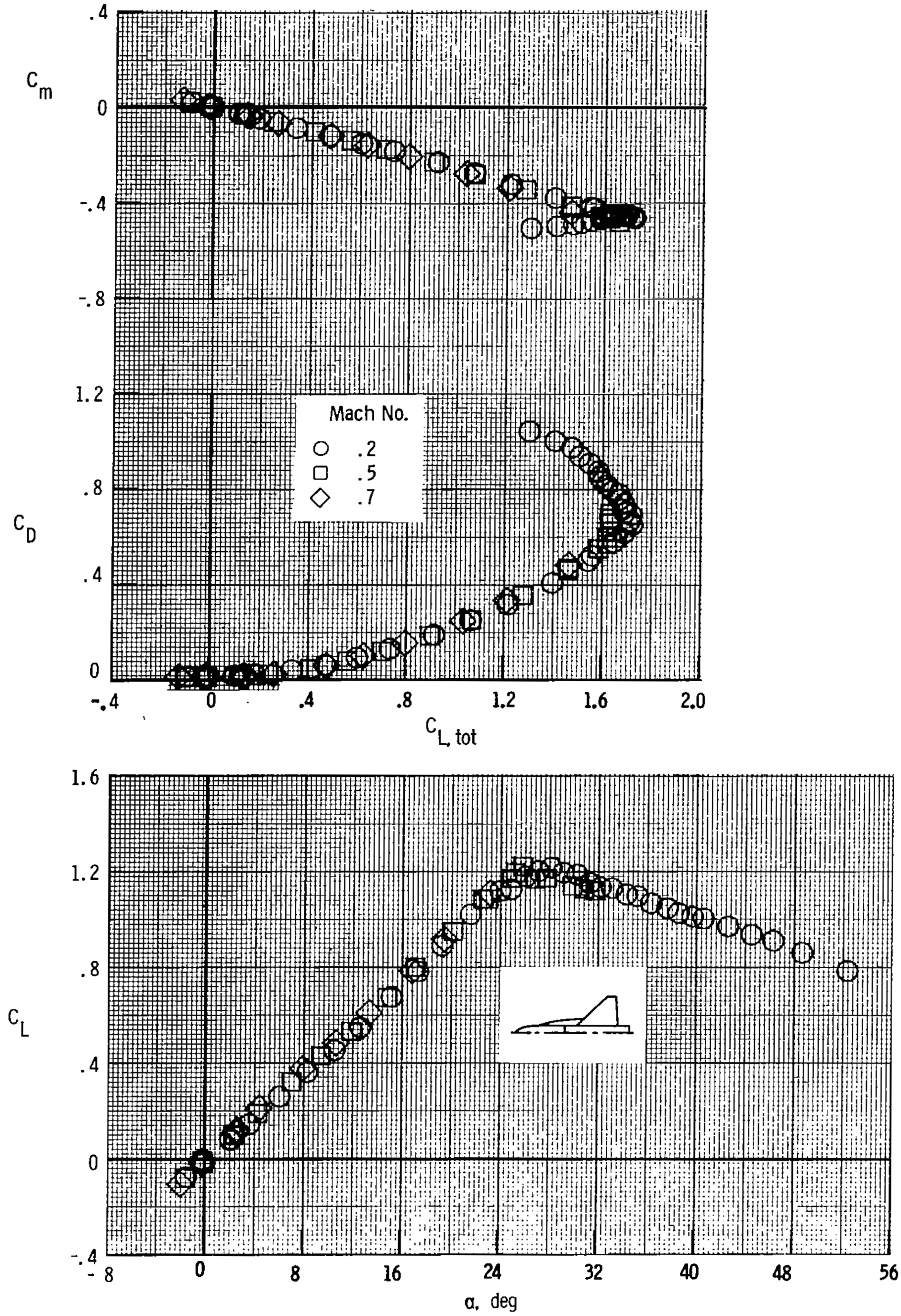

(j) ED 5.

Figure 7.- Continued.

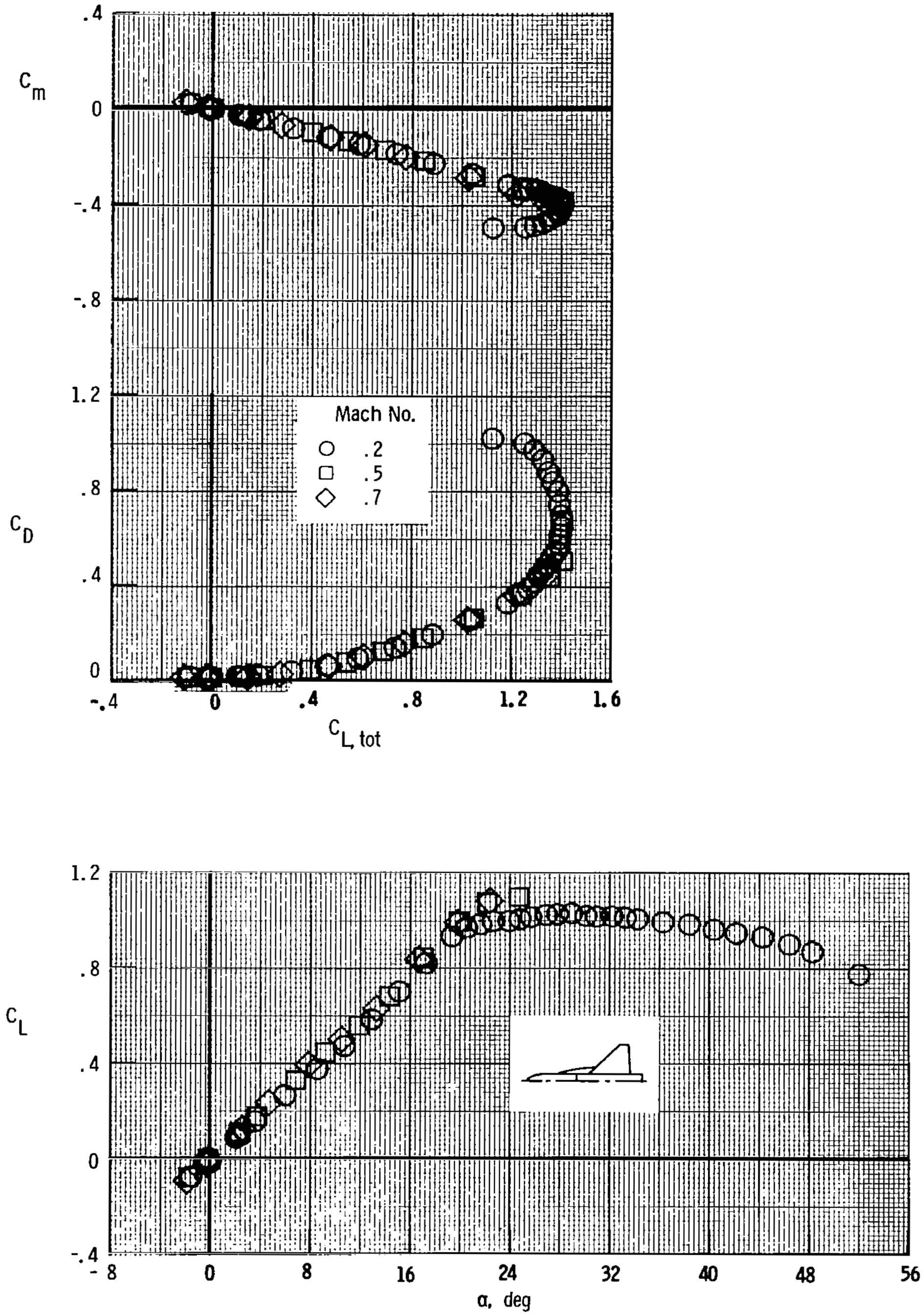

(k) ED 6.

Figure 7.- Continued.

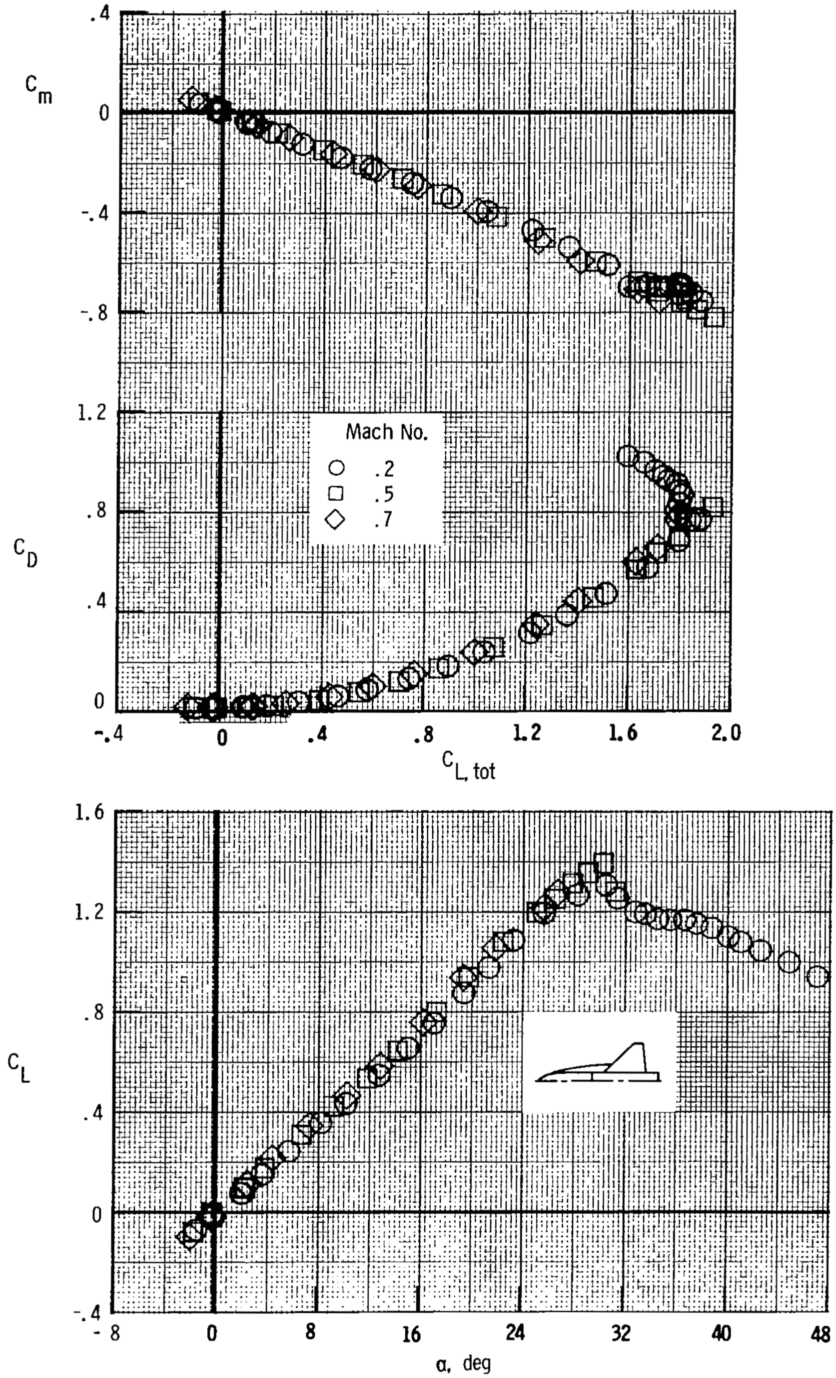

(l) ED 9.

Figure 7.- Continued.

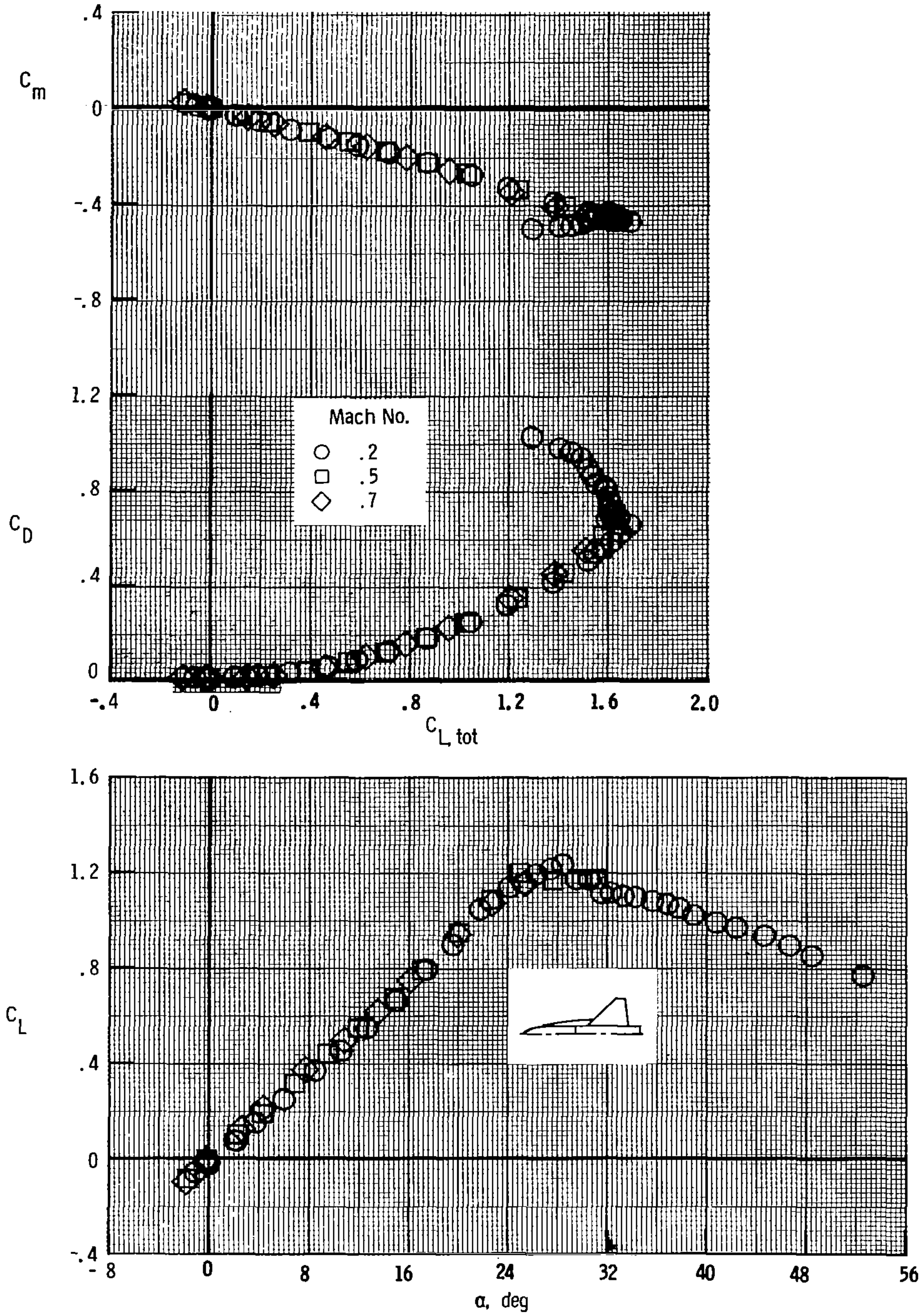

(m) ED 10.

Figure 7.- Continued.

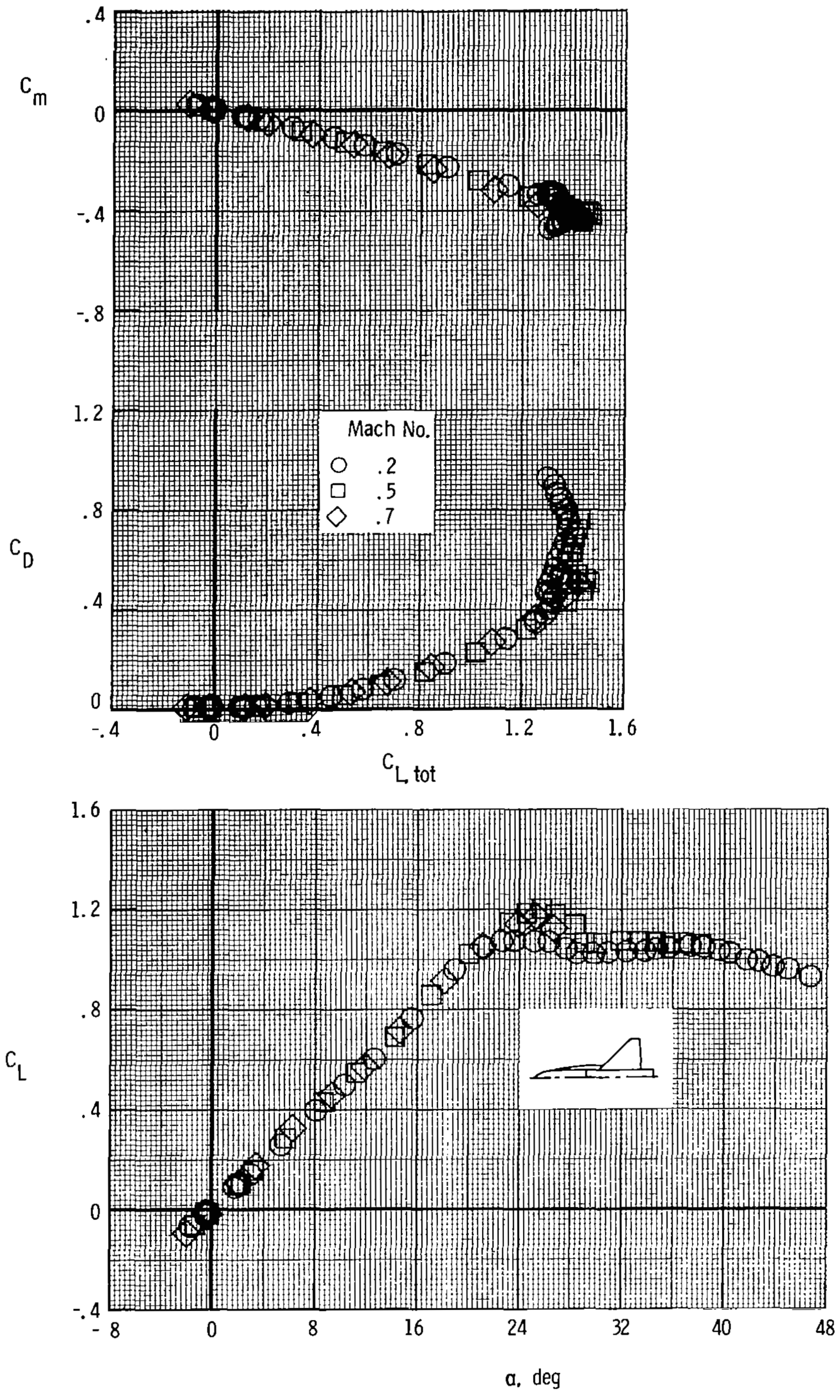

(n) ED 11.

Figure 7.- Continued.

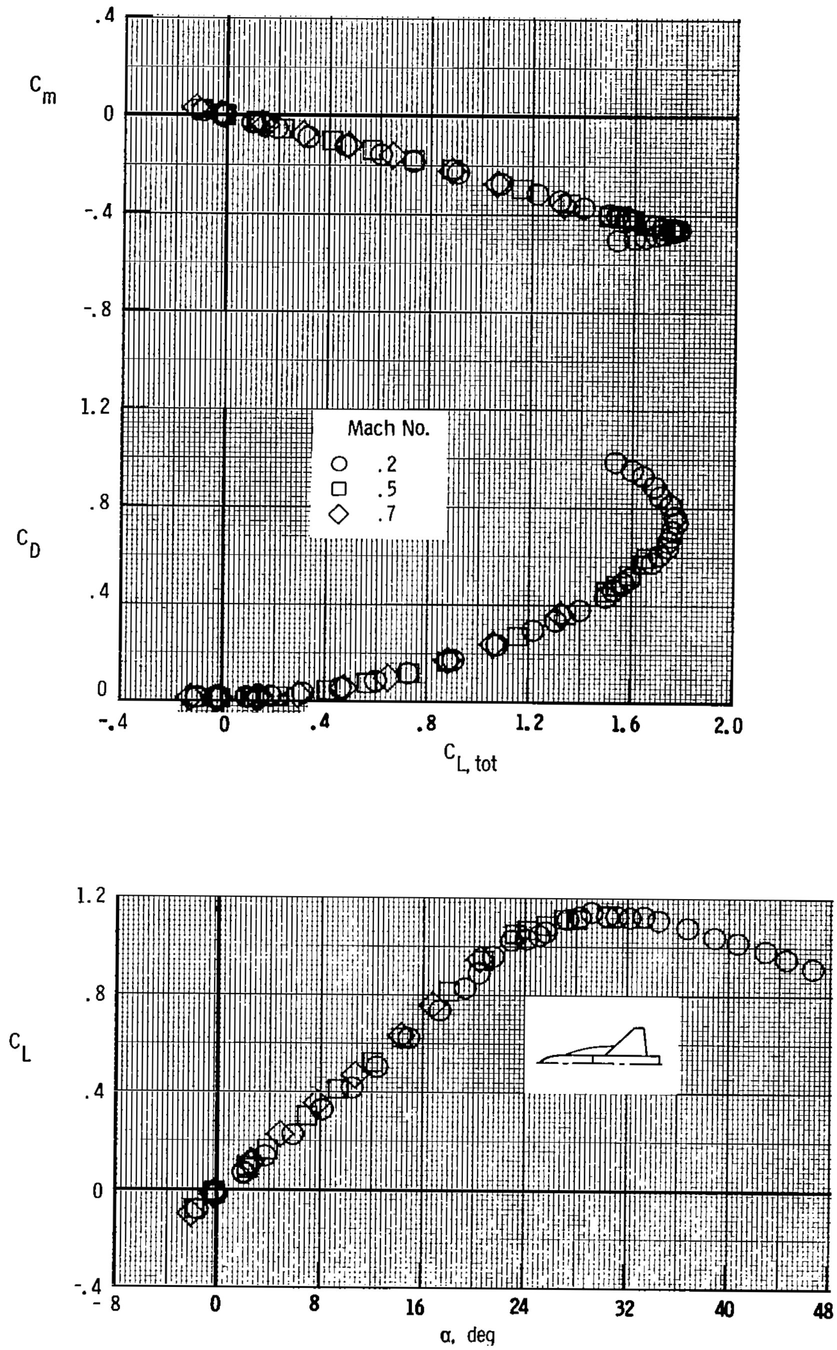

(o) ED 12.

Figure 7.- Continued.

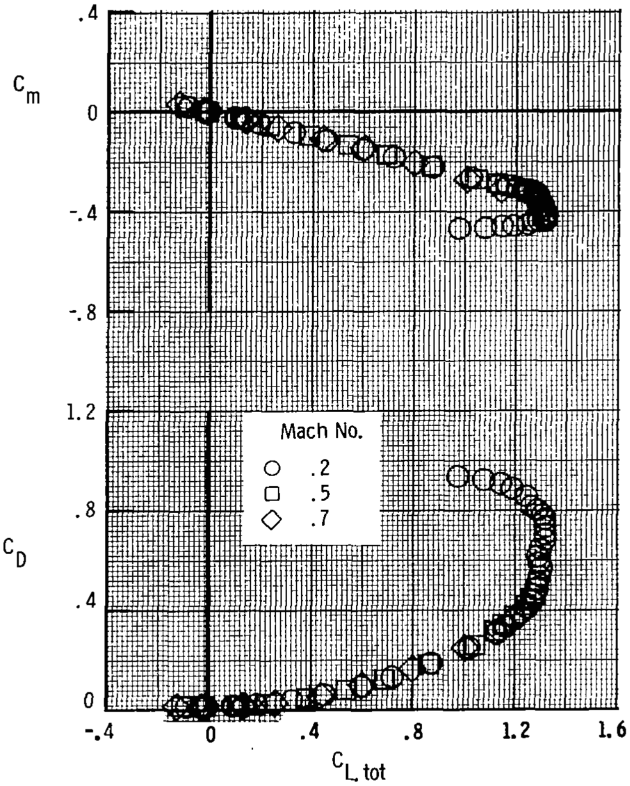

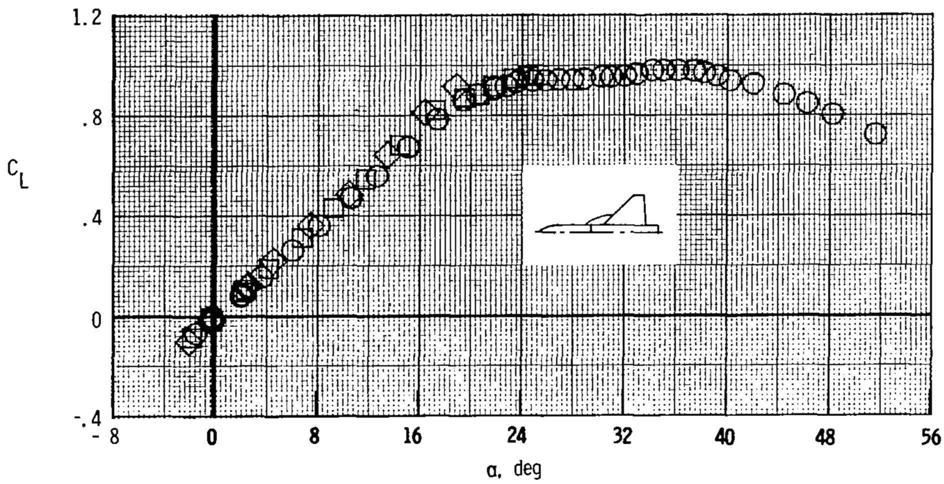

(p) ED 13.

Figure 7.- Concluded.

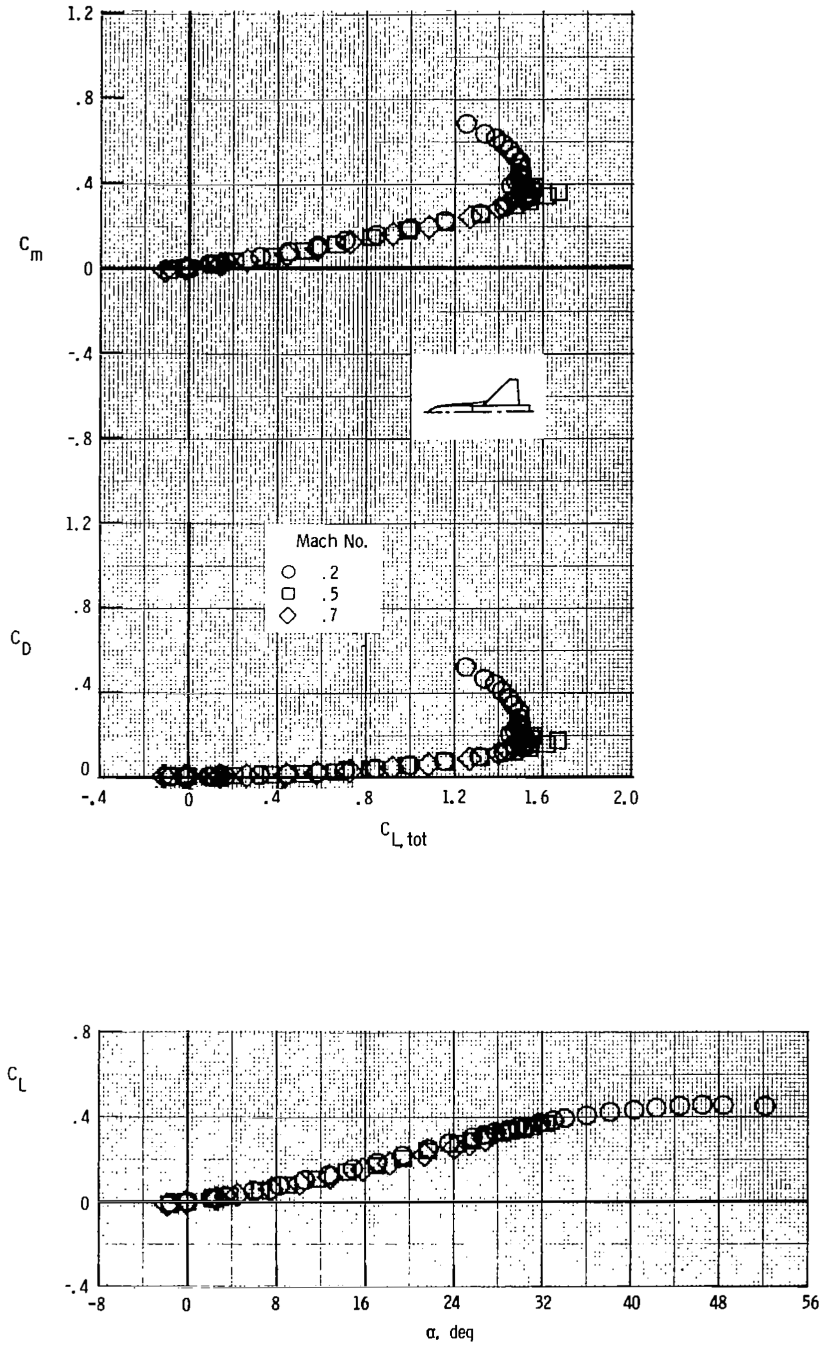

(a) AD 9.

Figure 8.- Effect of Mach number on basic longitudinal characteristics for strake-forebody.

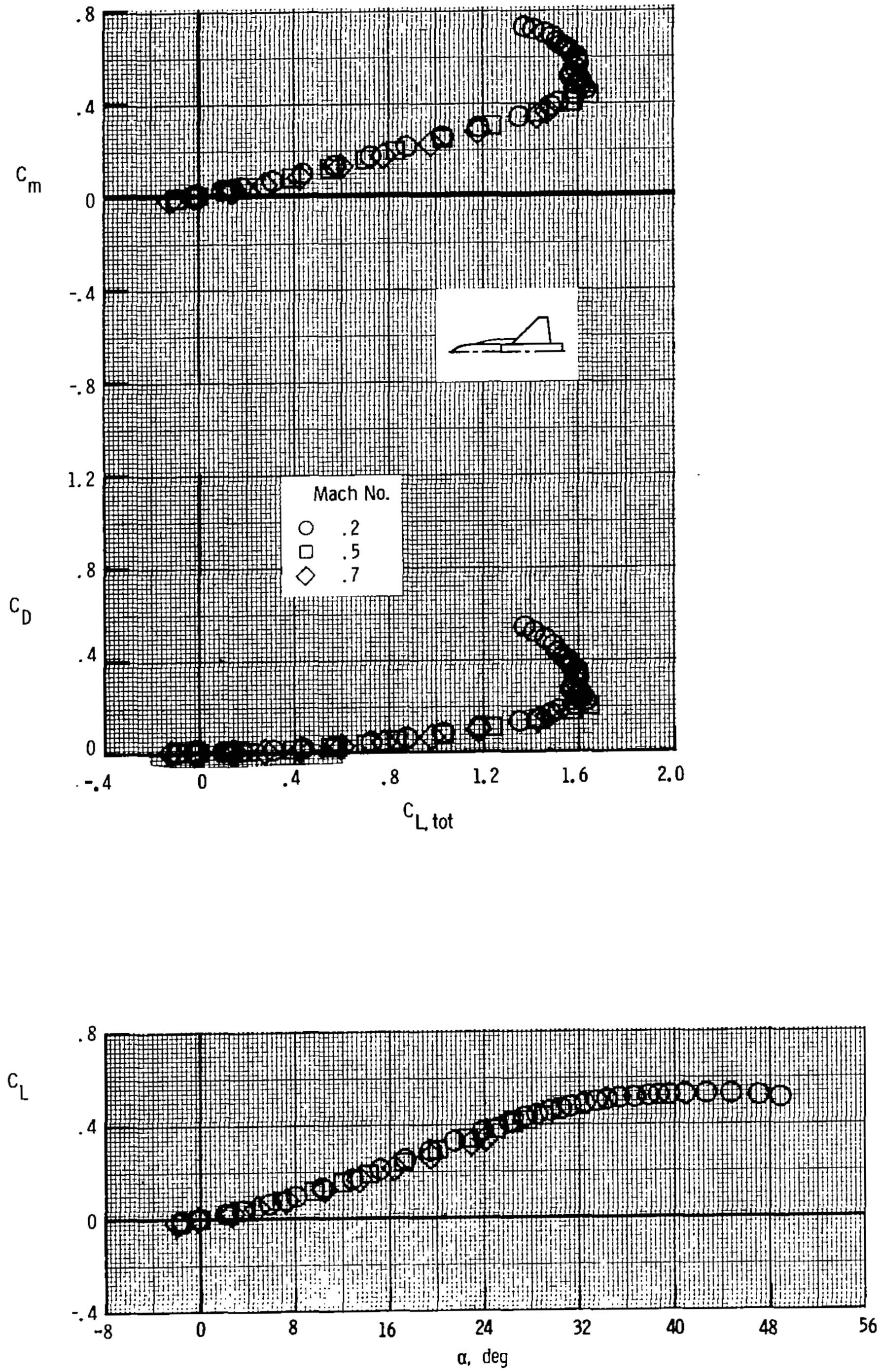

(b) AD 14.

Figure 8.- Continued.

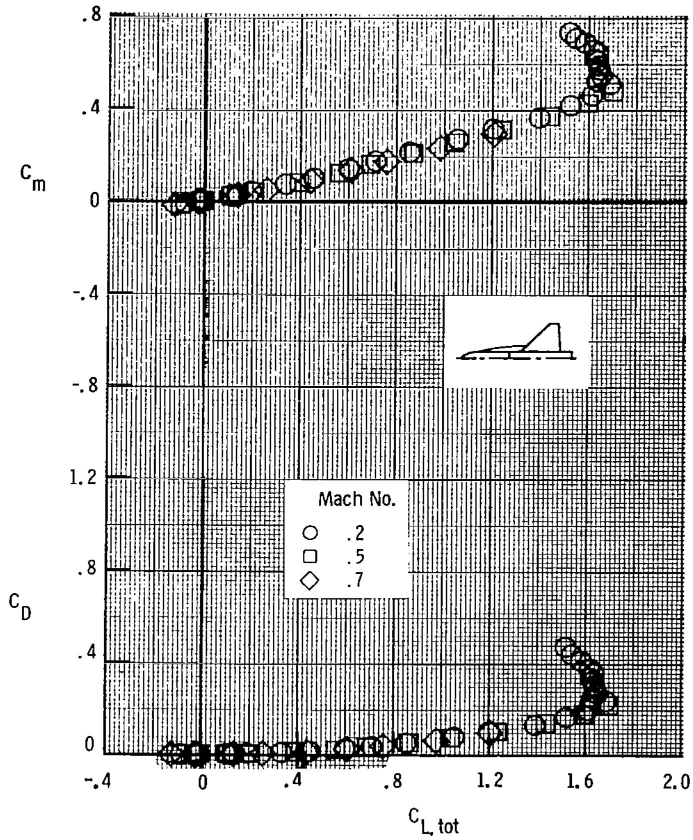

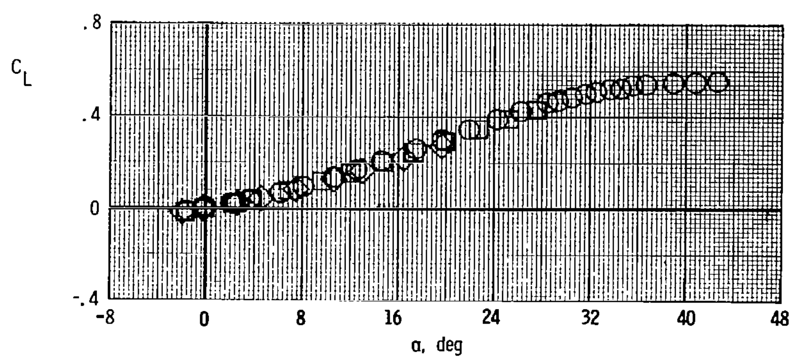

(c) AD 17.

Figure 8.- Continued.

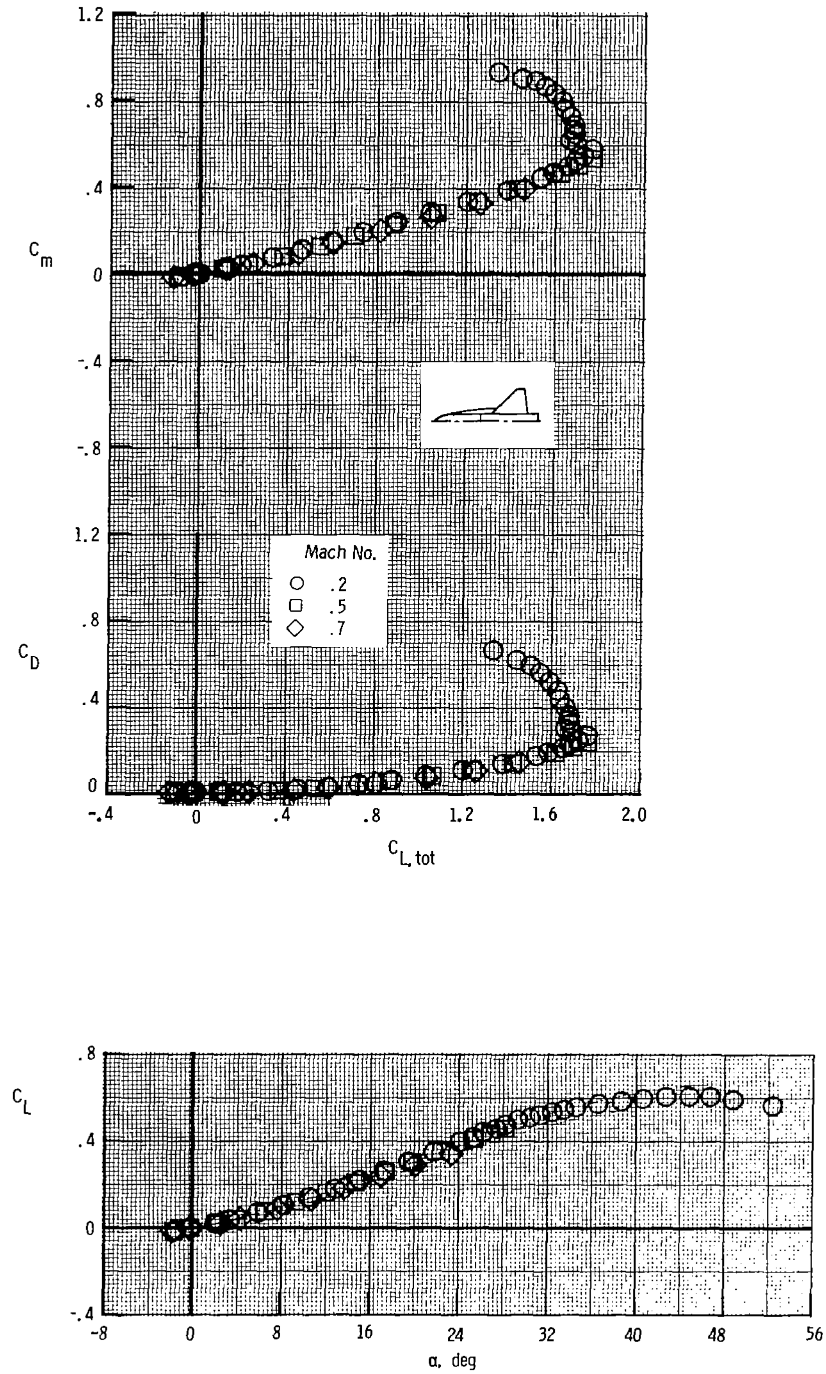

(d) AD 19.

Figure 8.- Continued.

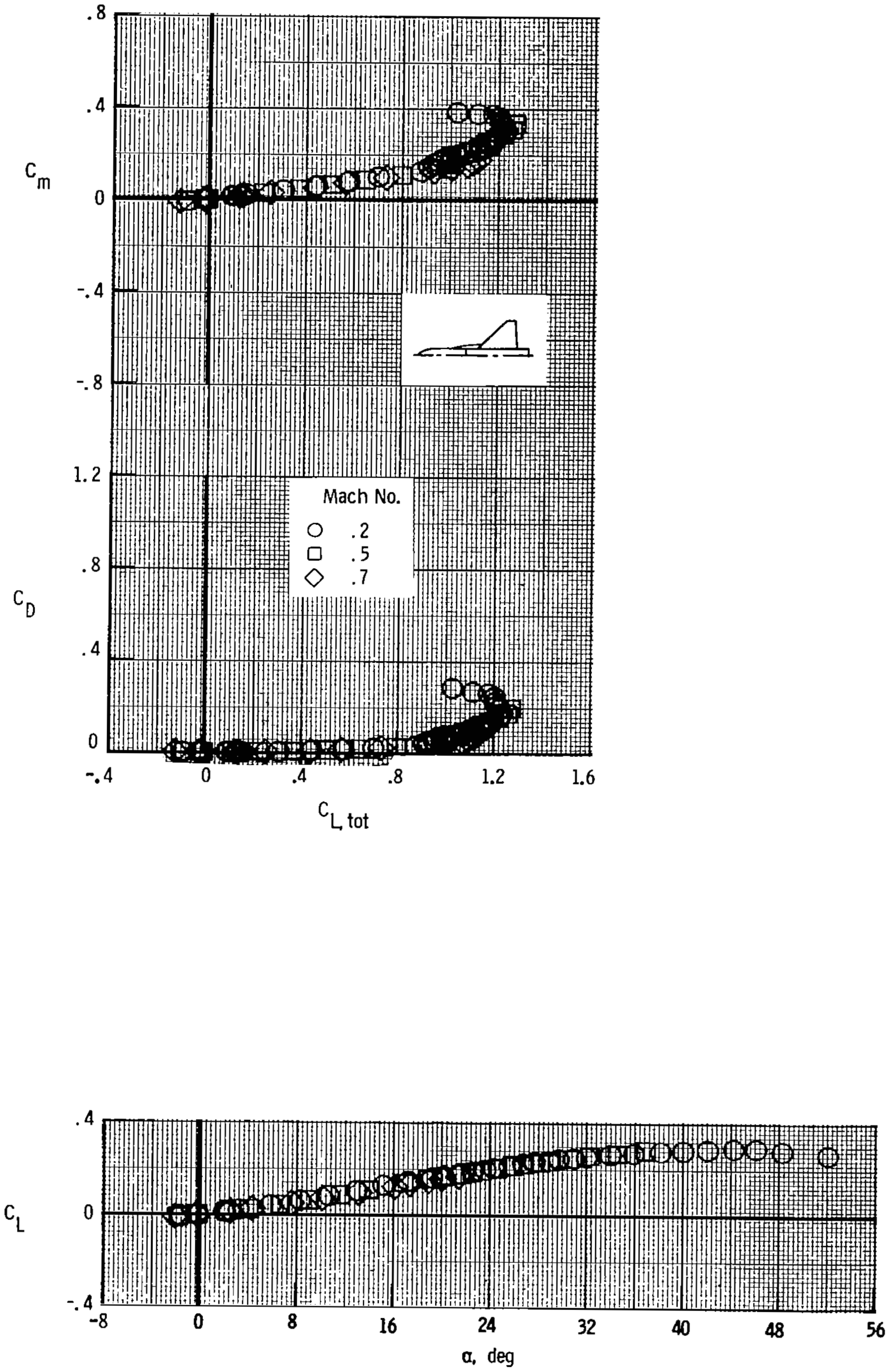

(e) AD 22.

Figure 8.- Continued.

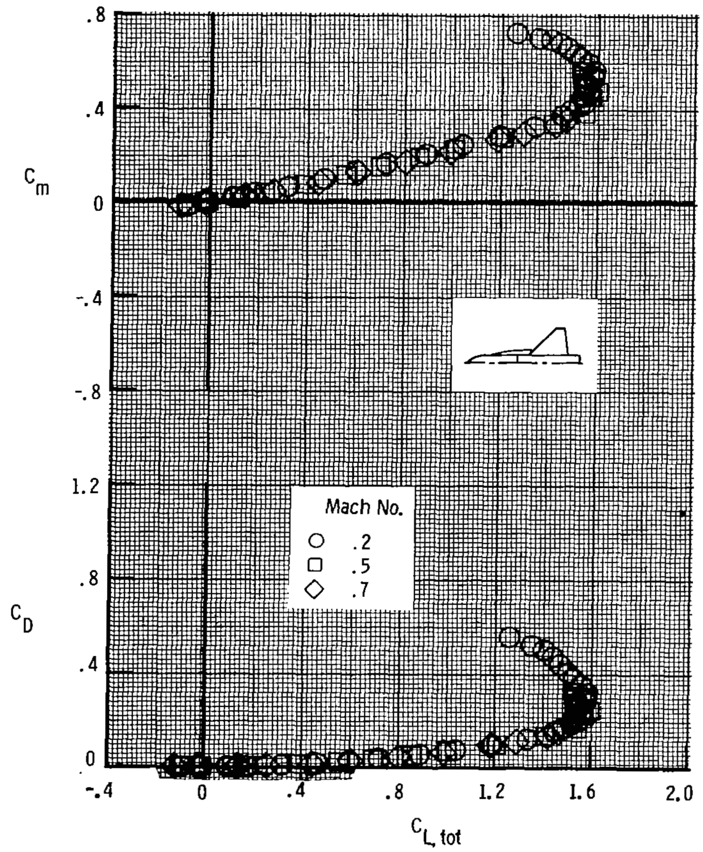

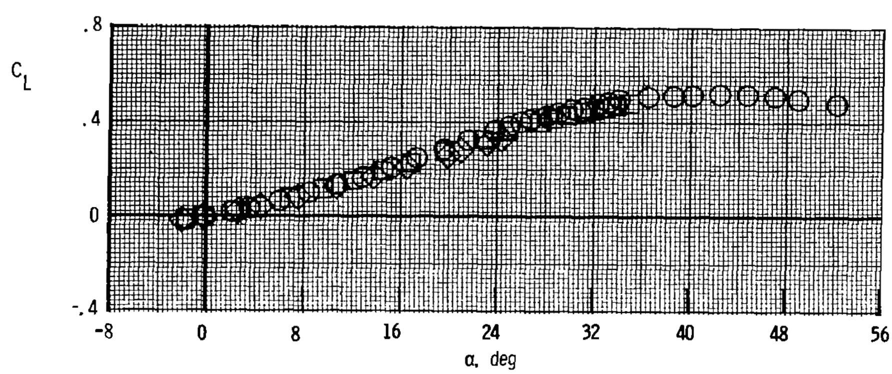

(f) AD 23.

Figure 8.- Continued.

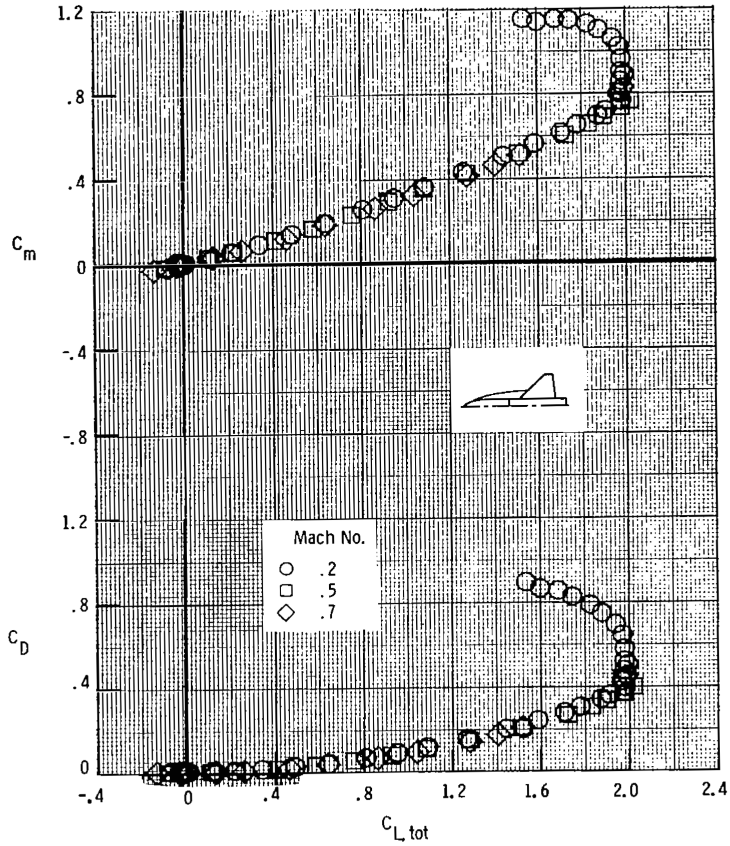

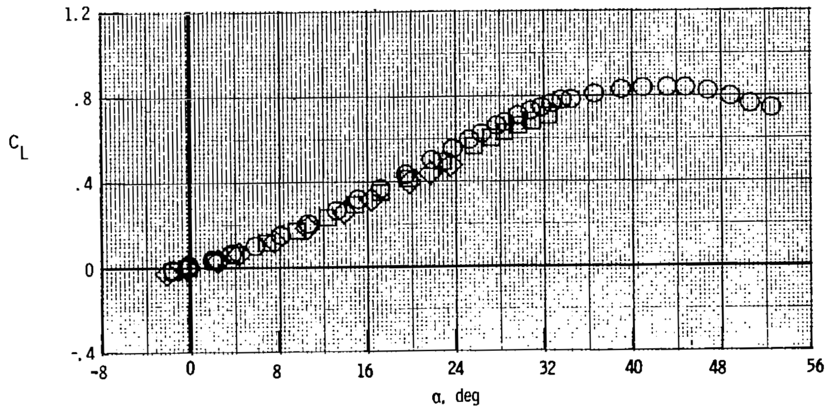

(g) AD 24.

Figure 8.- Continued.

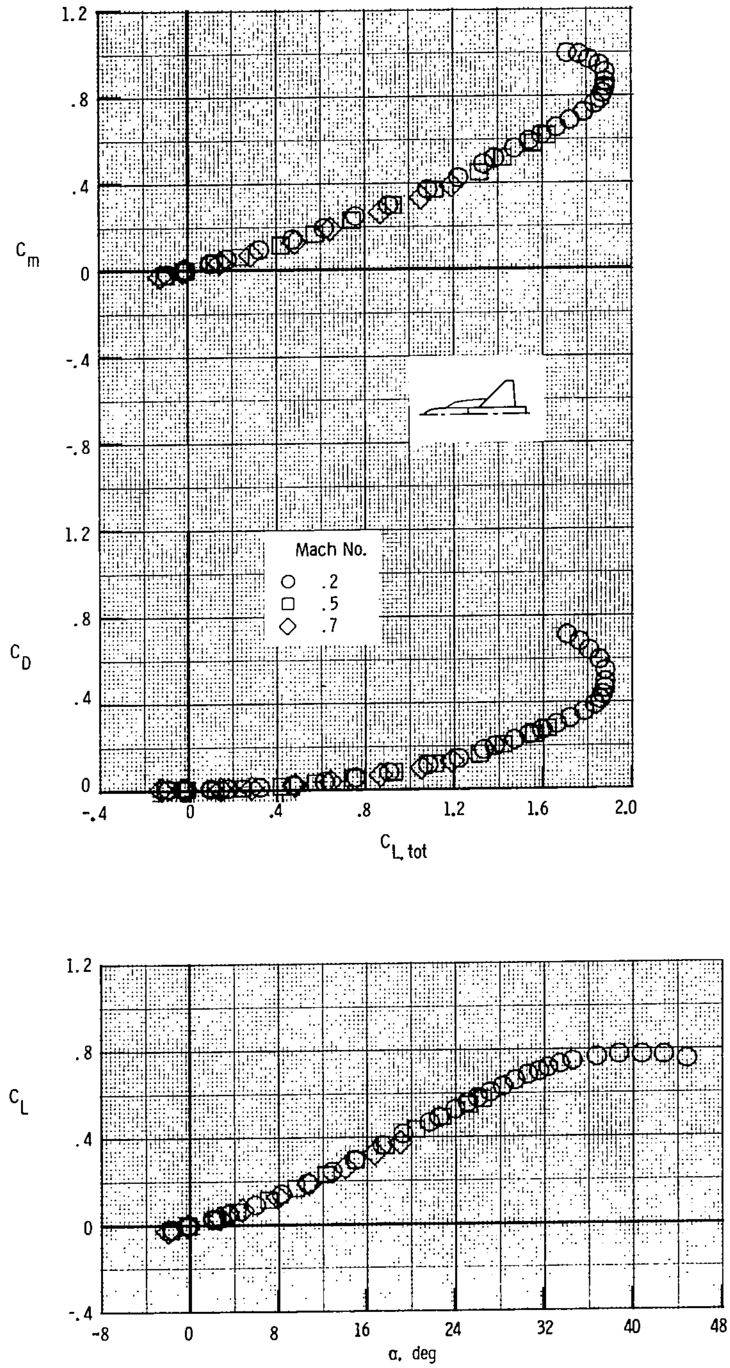

(h) ED 2.

Figure 8.- Continued.

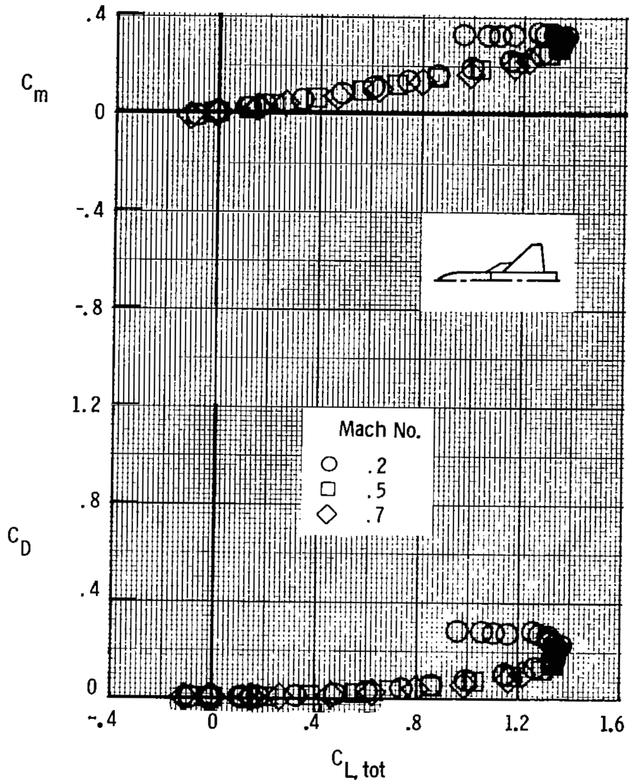

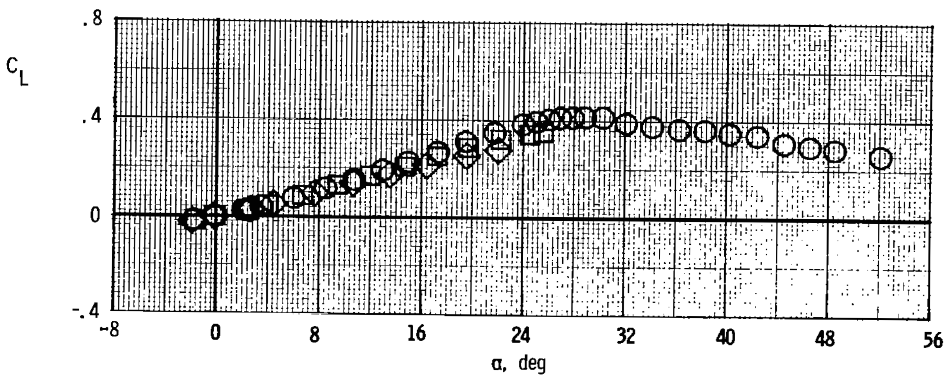

(i) ED 4.

Figure 8.- Continued.

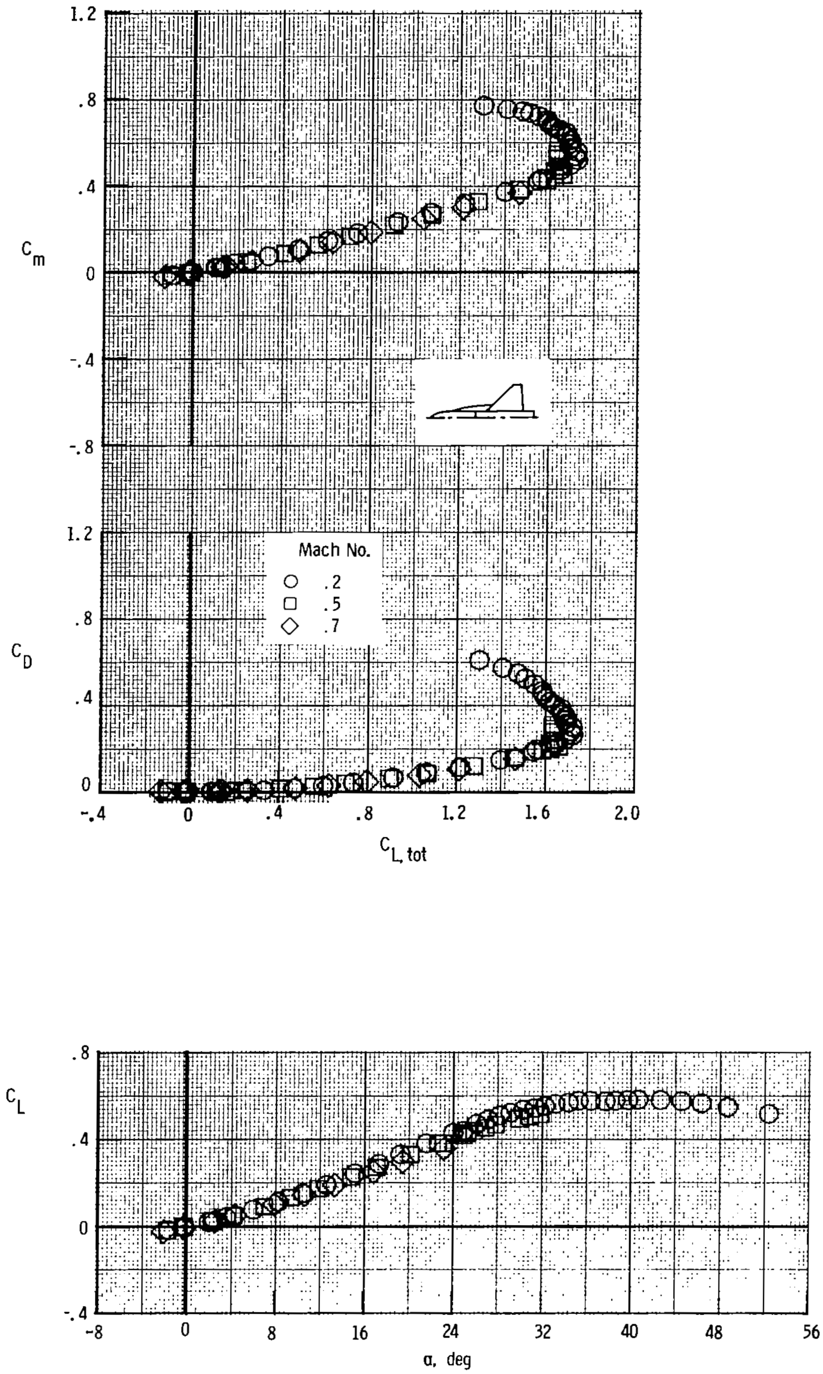

(j) ED 5.

Figure 8.- Continued.

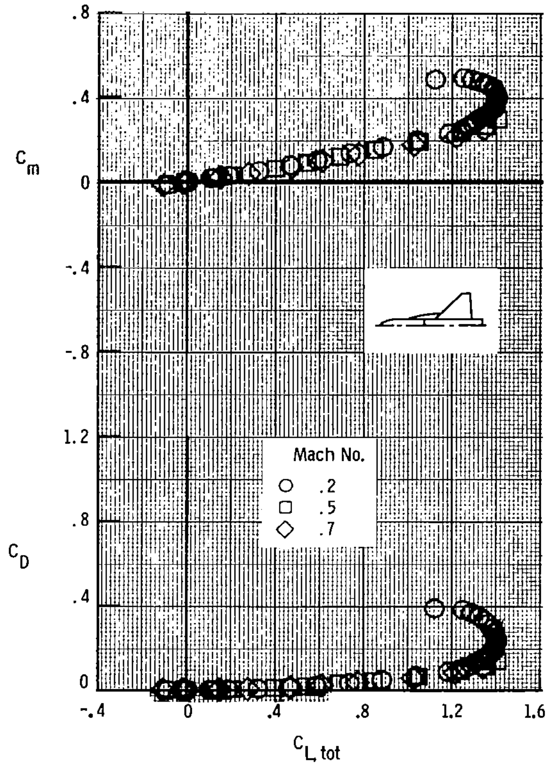

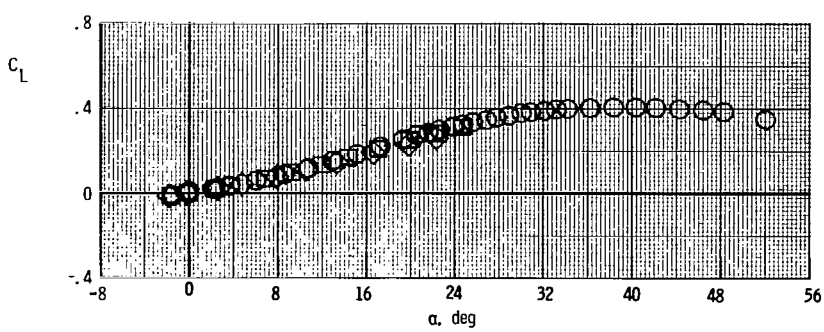

(k) ED 6.

Figure 8.- Continued.

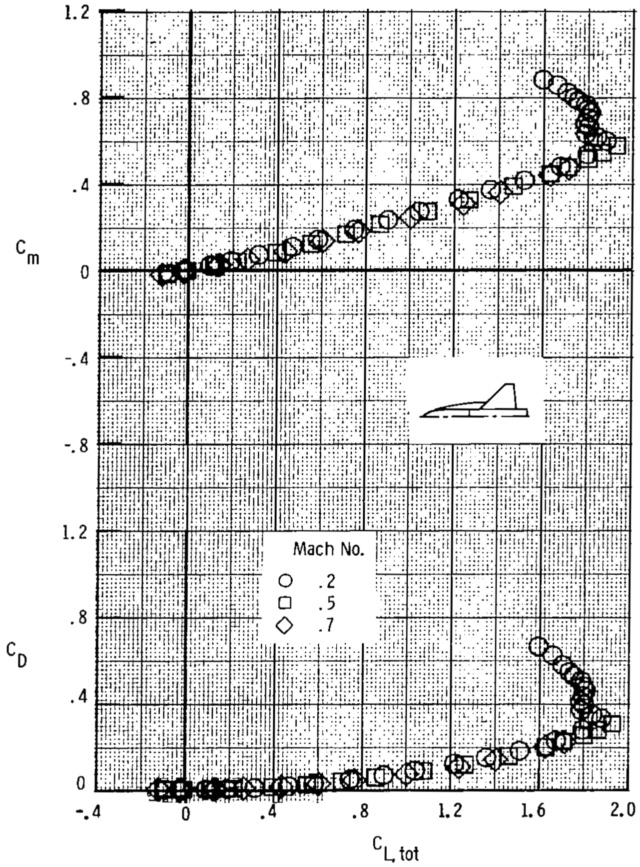

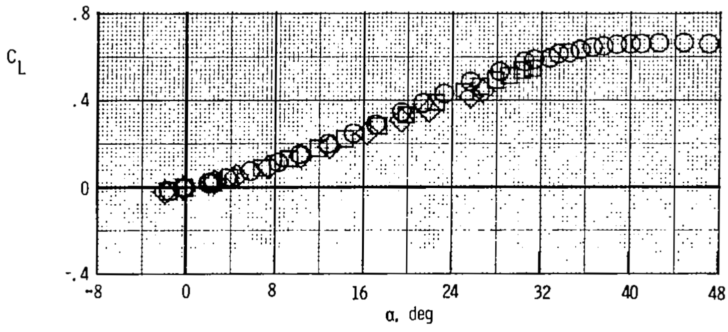

(l) ED 9.

Figure 8.- Continued.

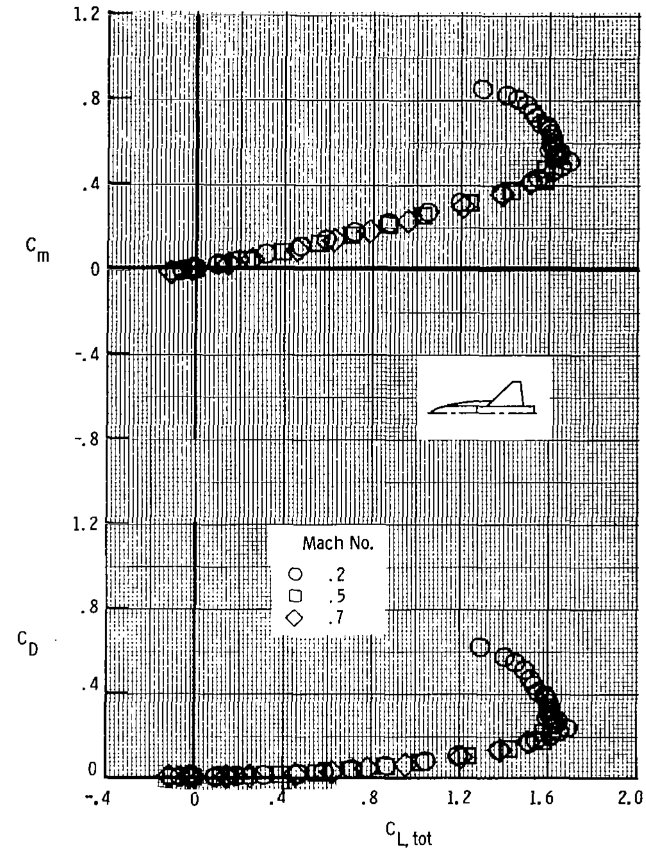

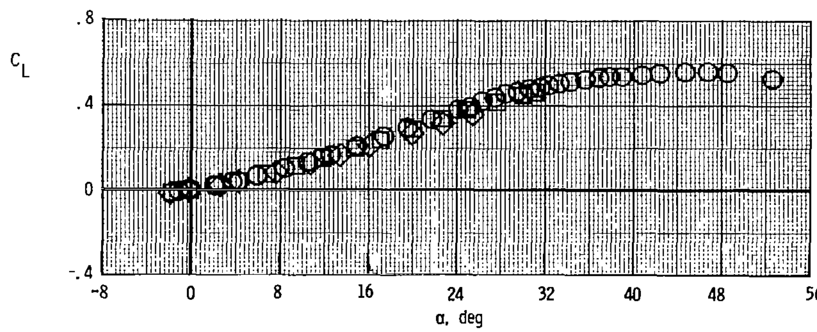

(m) ED 10.

Figure 8.- Continued.

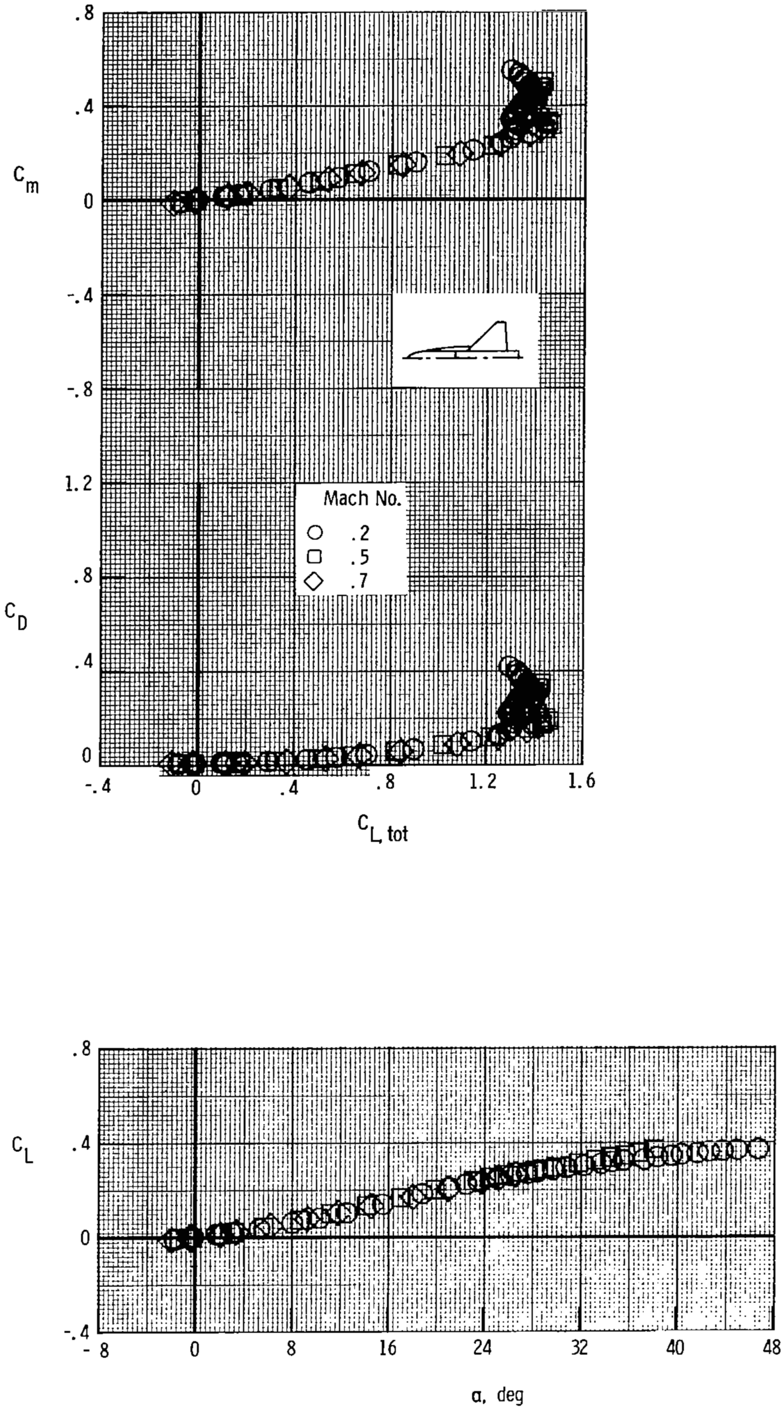

(n) ED 11.

Figure 8.- Continued.

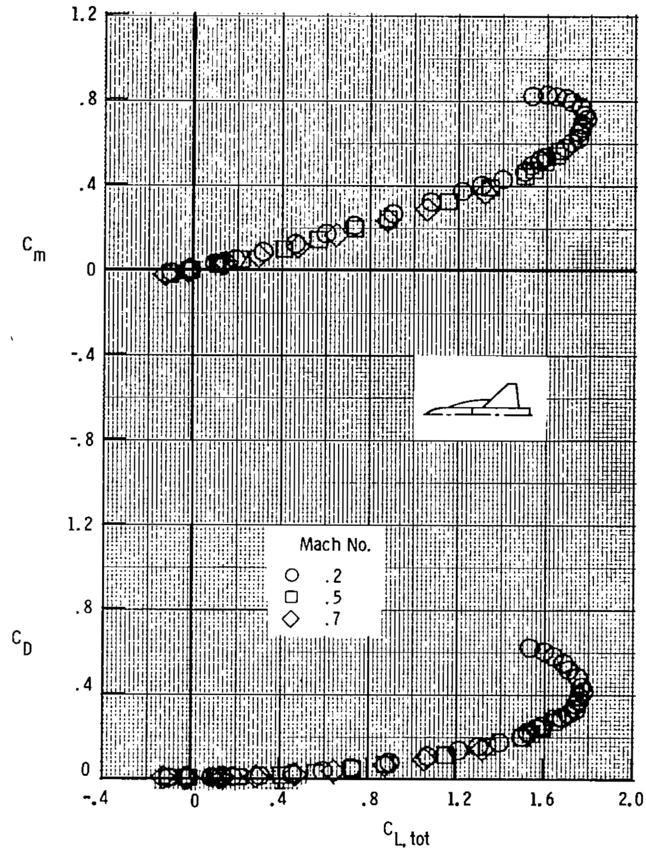

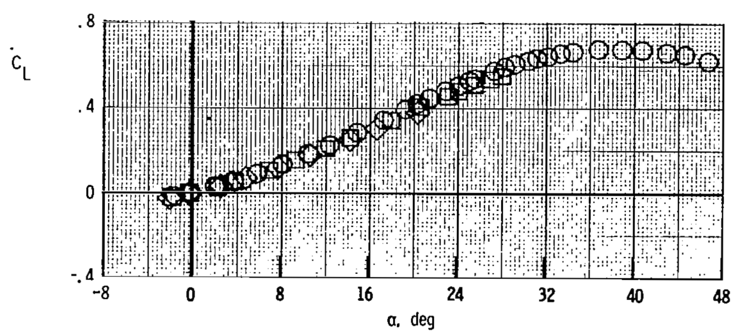

(o) ED 12.

Figure 8.- Continued.

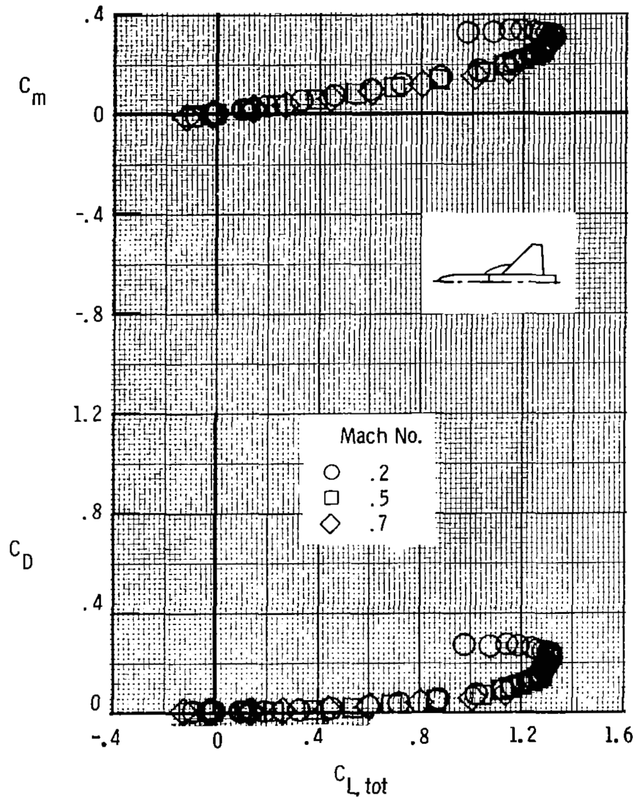

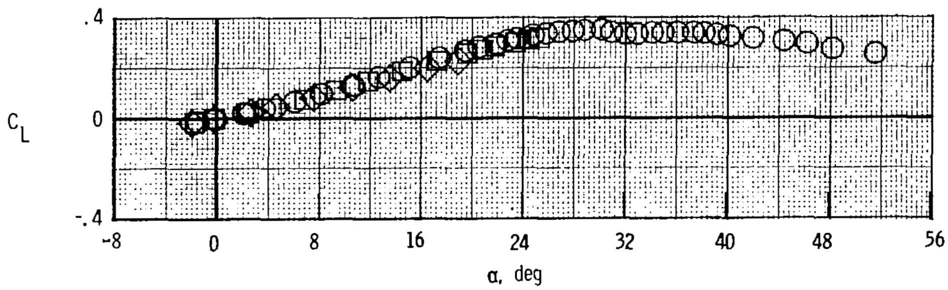

(p) ED 13.

Figure 8.- Concluded.

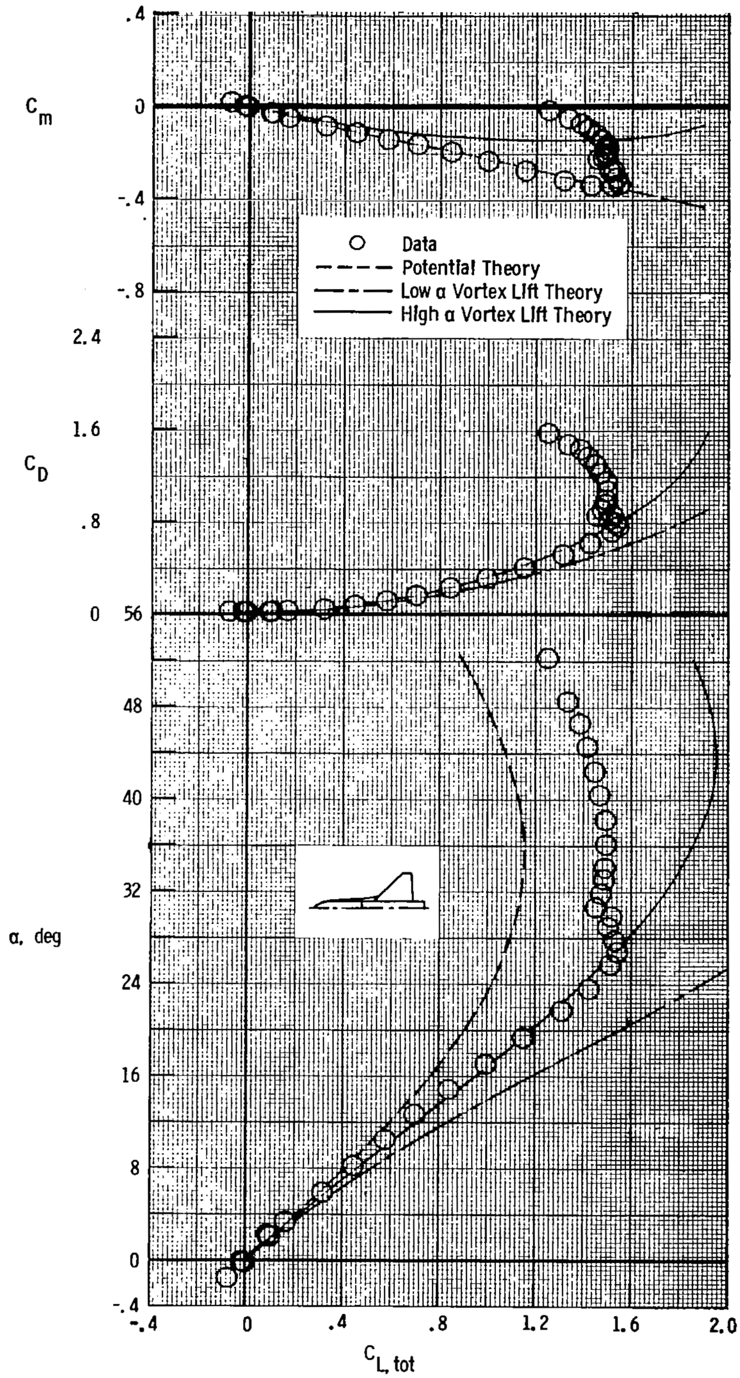

(a) AD 9.

Figure 9.- Complete-configuration longitudinal aerodynamic characteristics at $M = 0.2$; data and theoretical estimates.

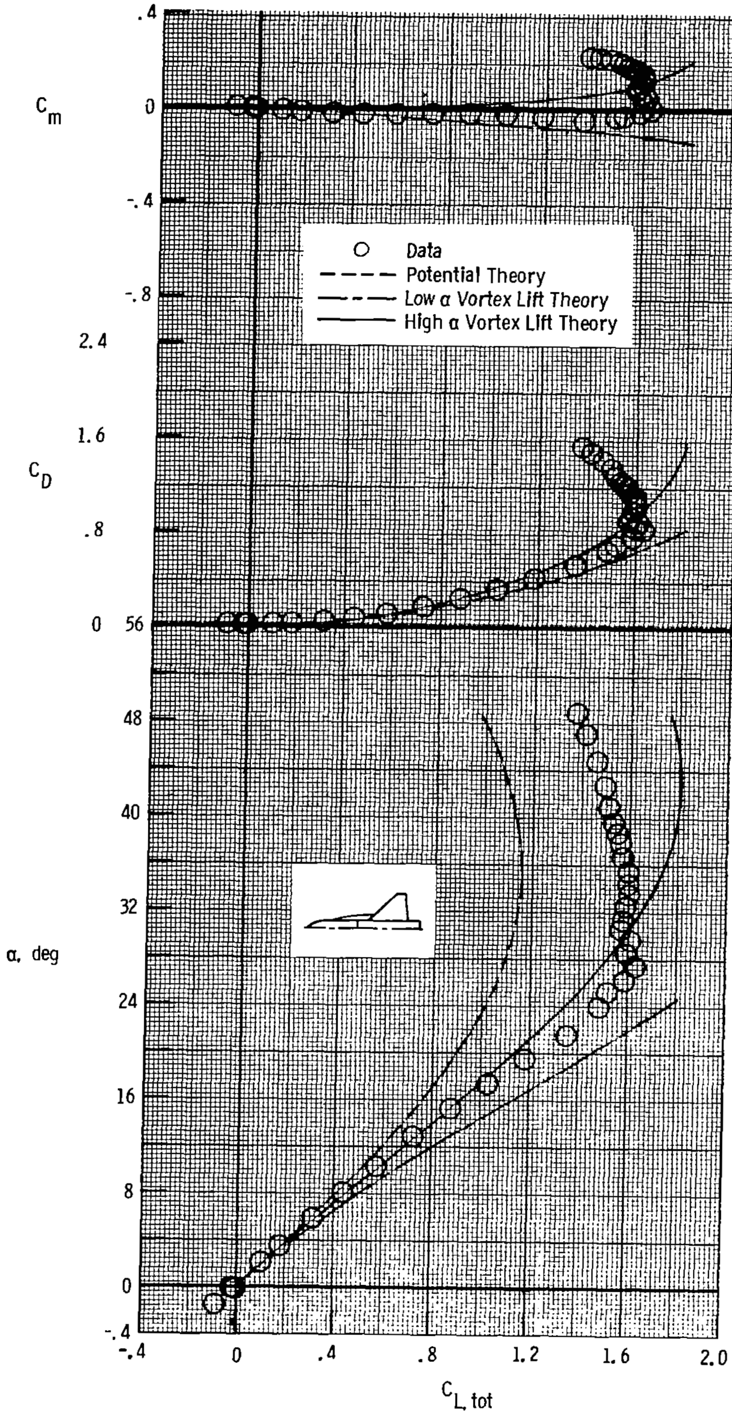

(b) AD 14.

Figure 9.- Continued.

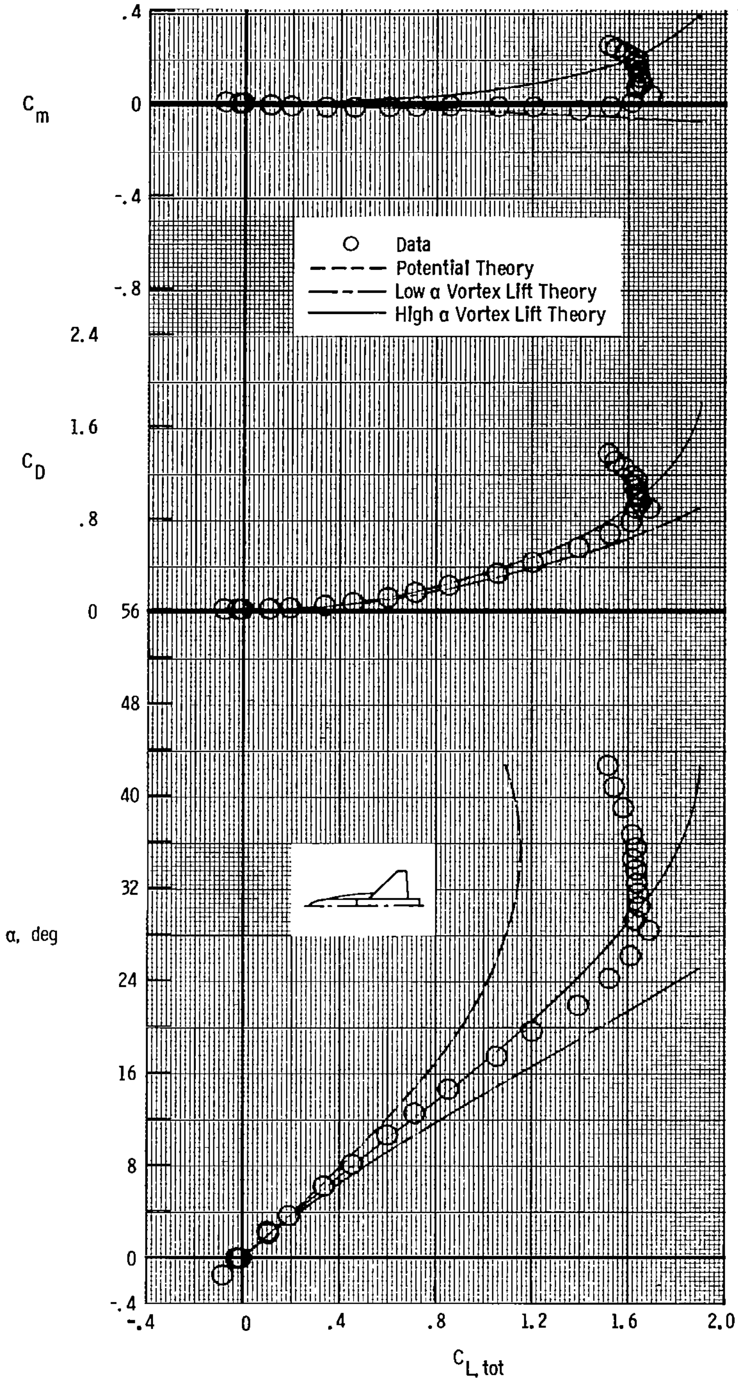

(c) AD 17.

Figure 9.- Continued.

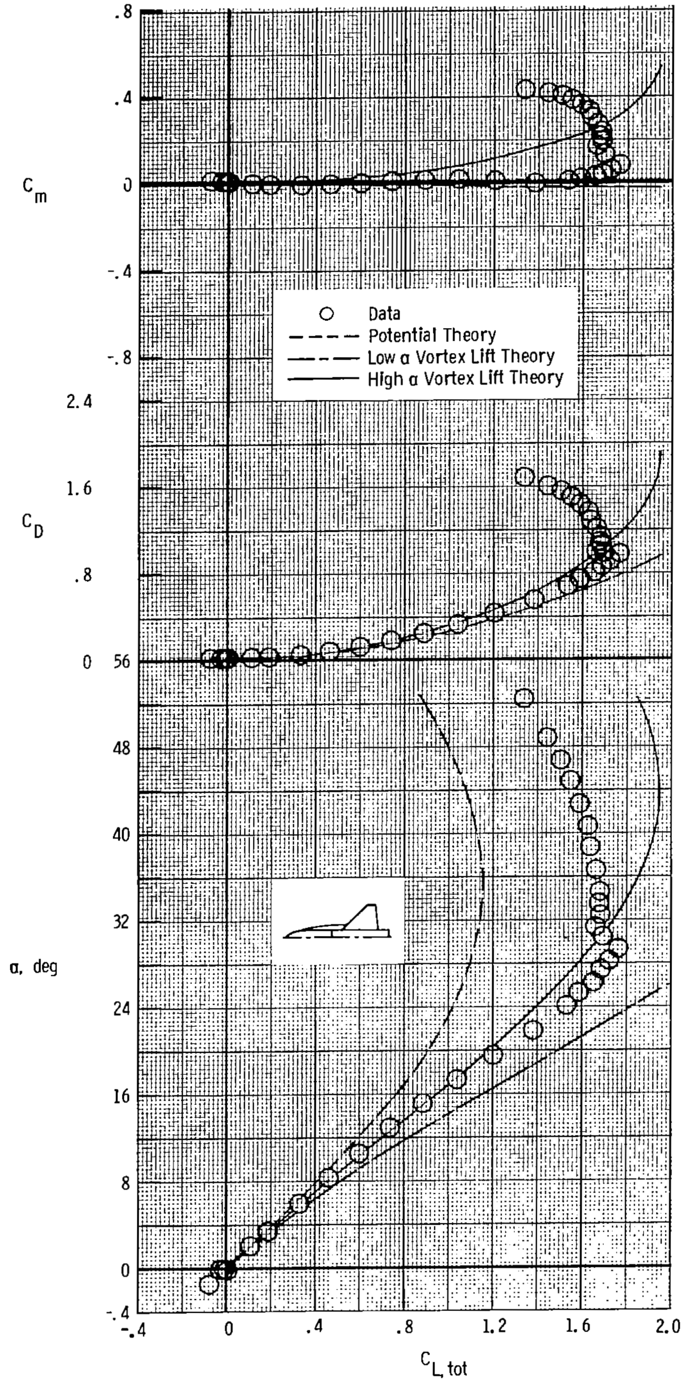

(d) AD 19.

Figure 9.- Continued.

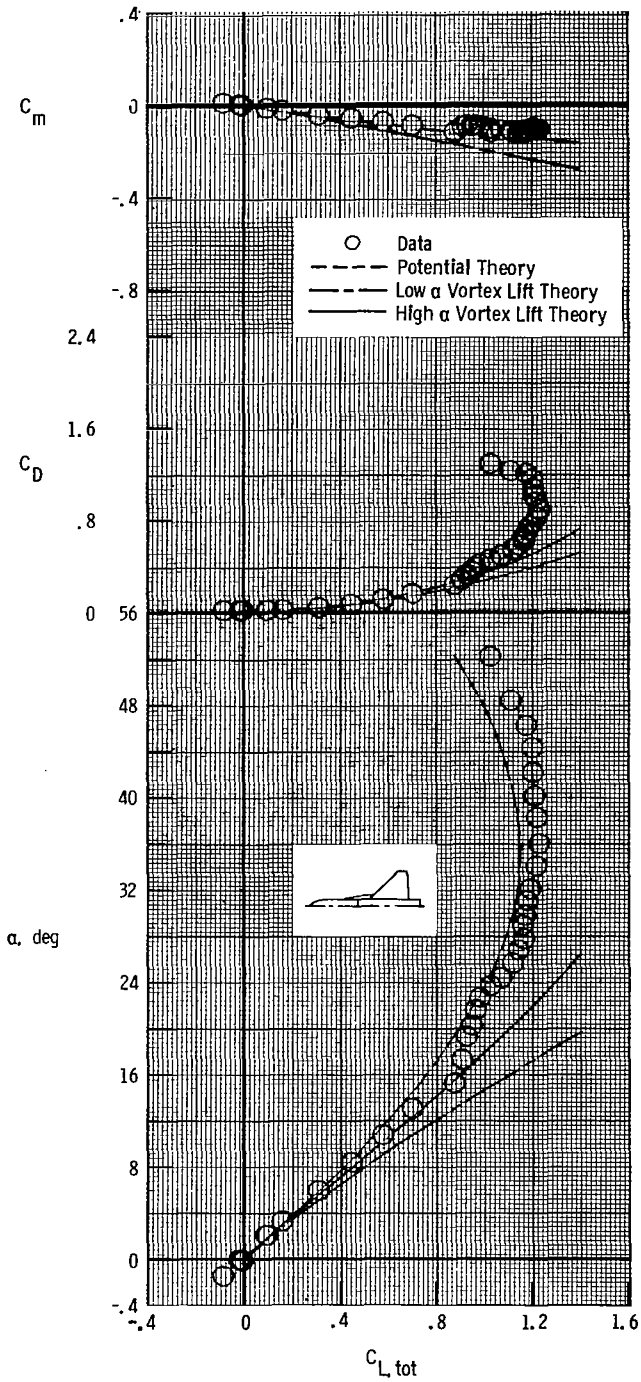

(e) AD 22.

Figure 9.- Continued.

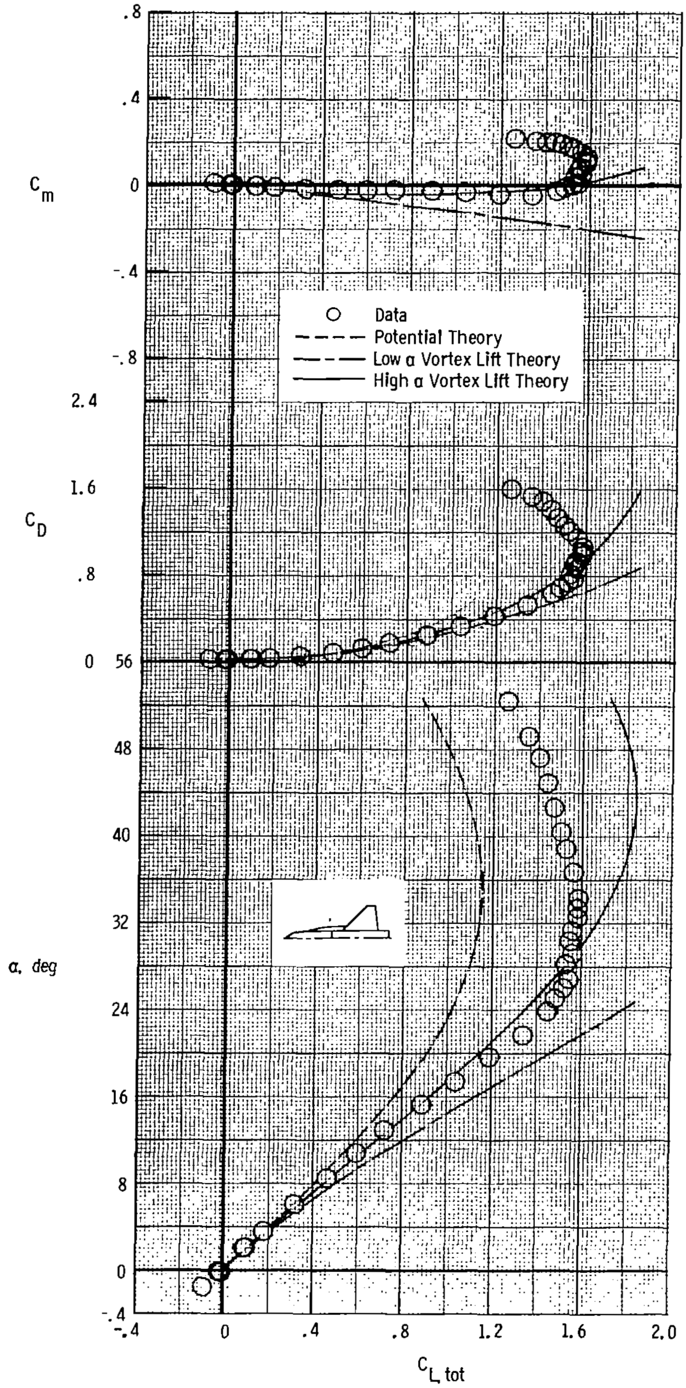

(f) AD 23.

Figure 9.- Continued.

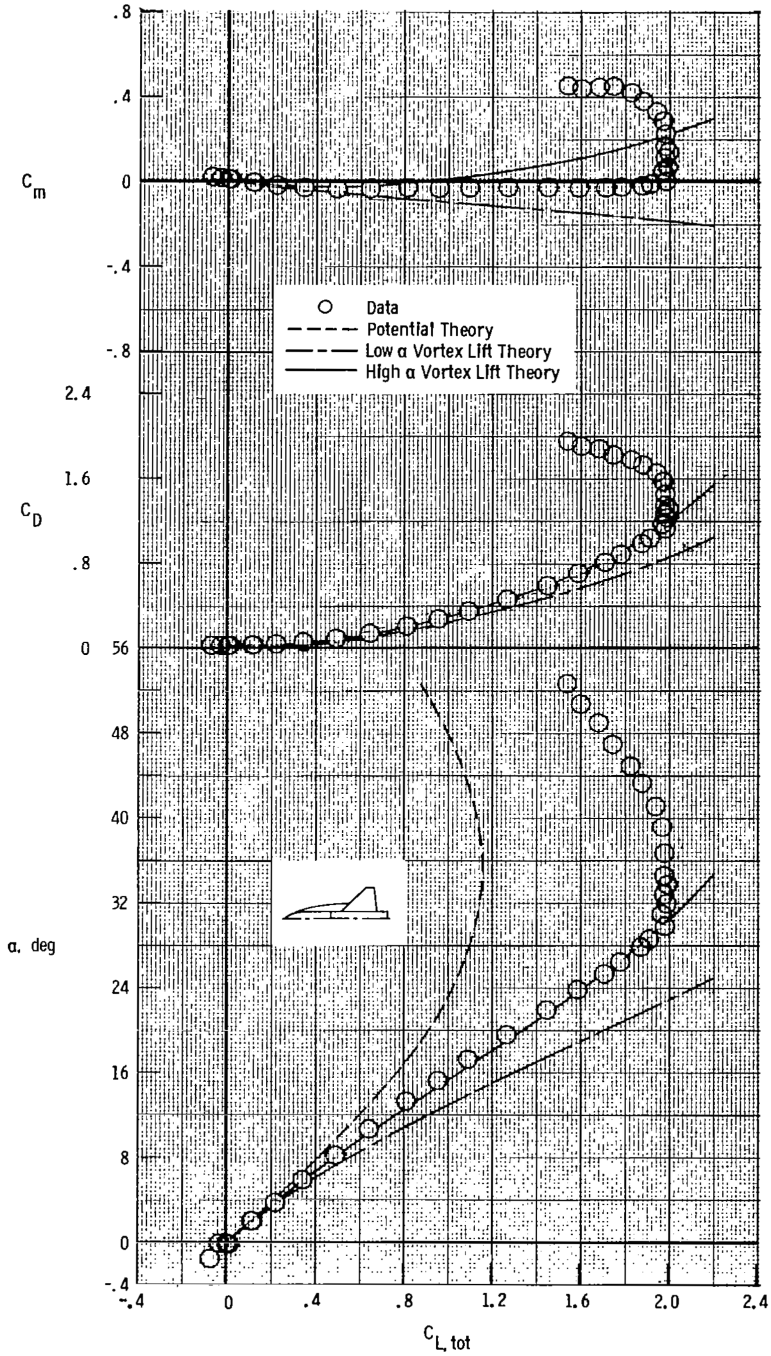

(g) AD 24.

Figure 9.- Continued.

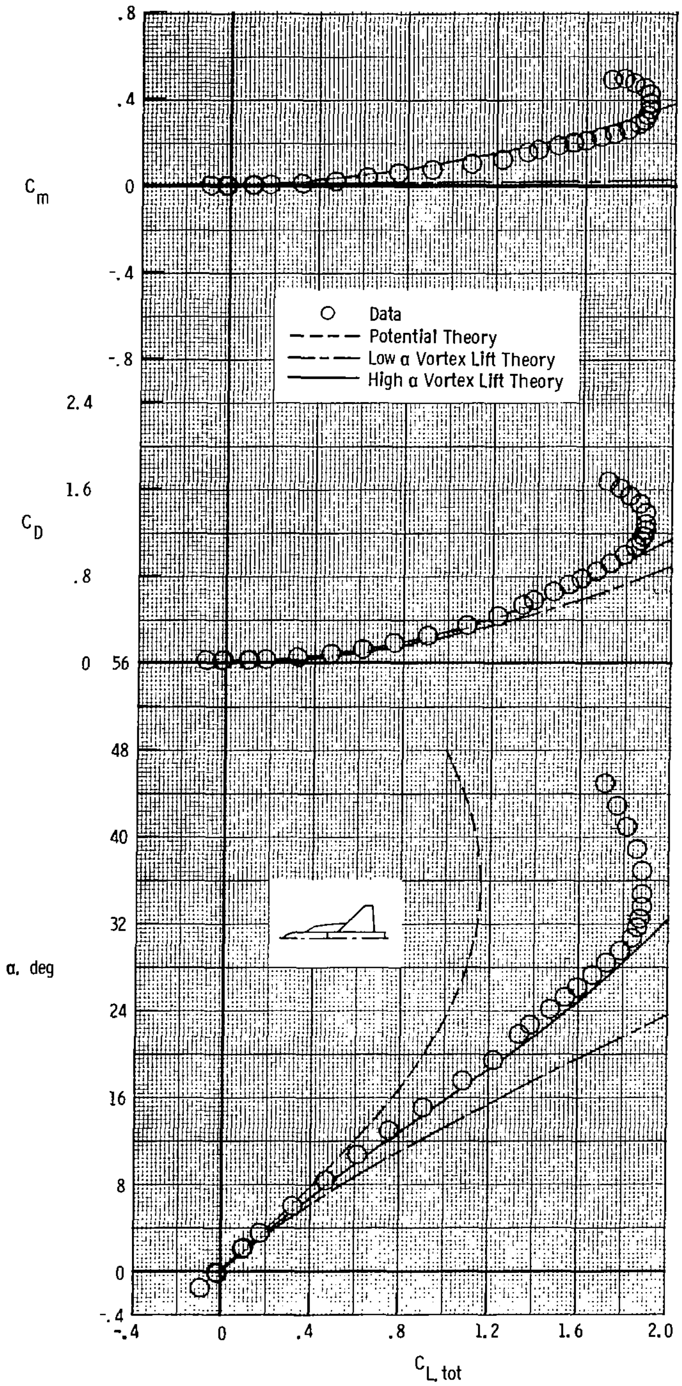

(h) ED 2.

Figure 9.- Continued.

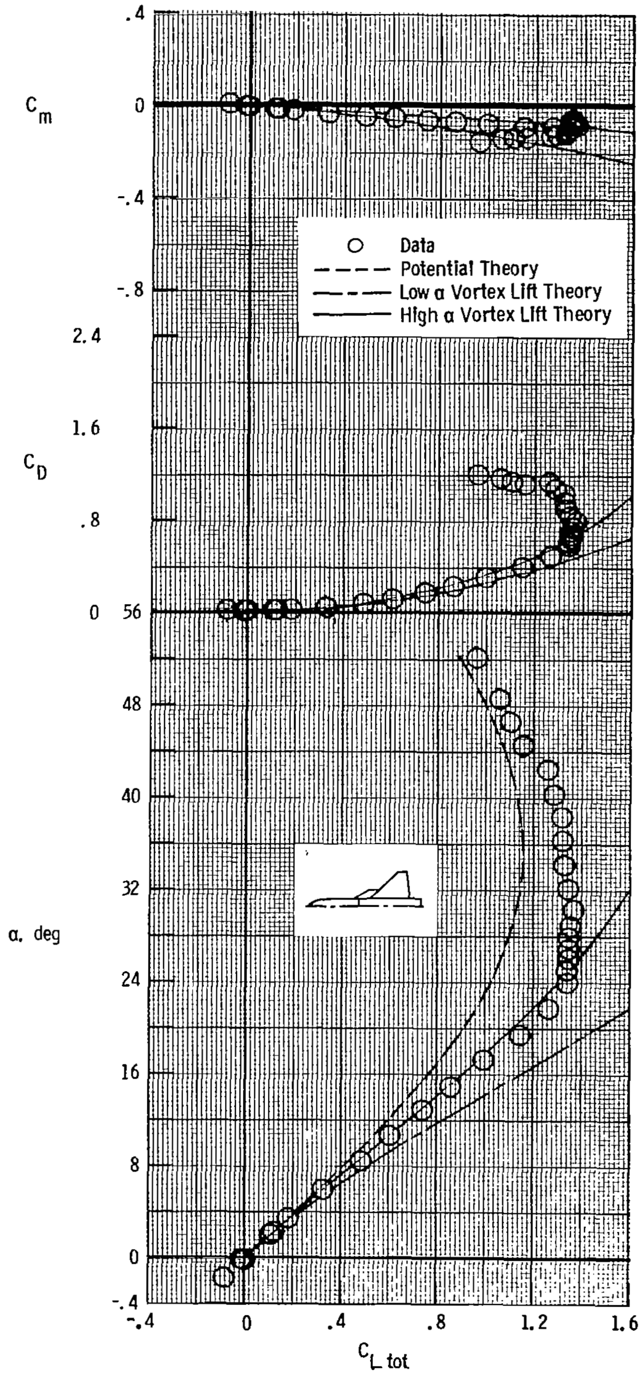

(i) ED 4.

Figure 9.- Continued.

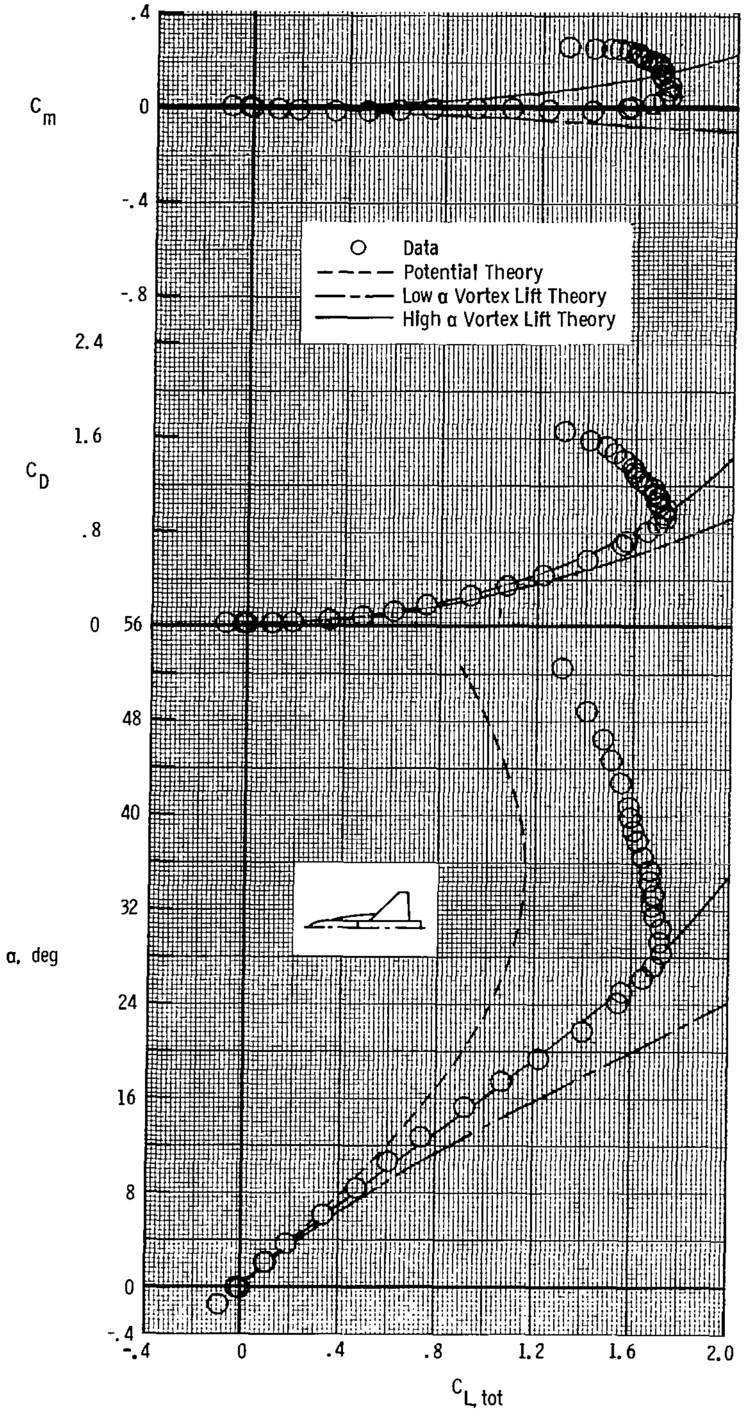

(j) ED 5.

Figure 9.- Continued.

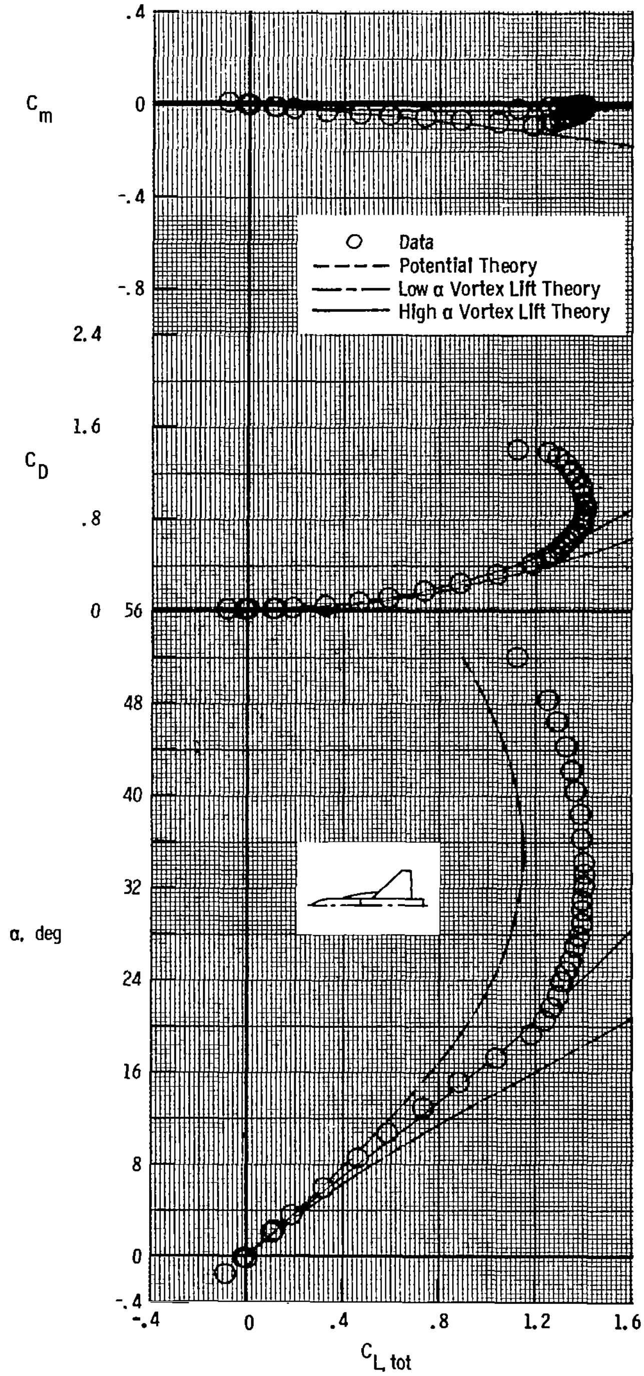

(k) ED 6.

Figure 9.- Continued.

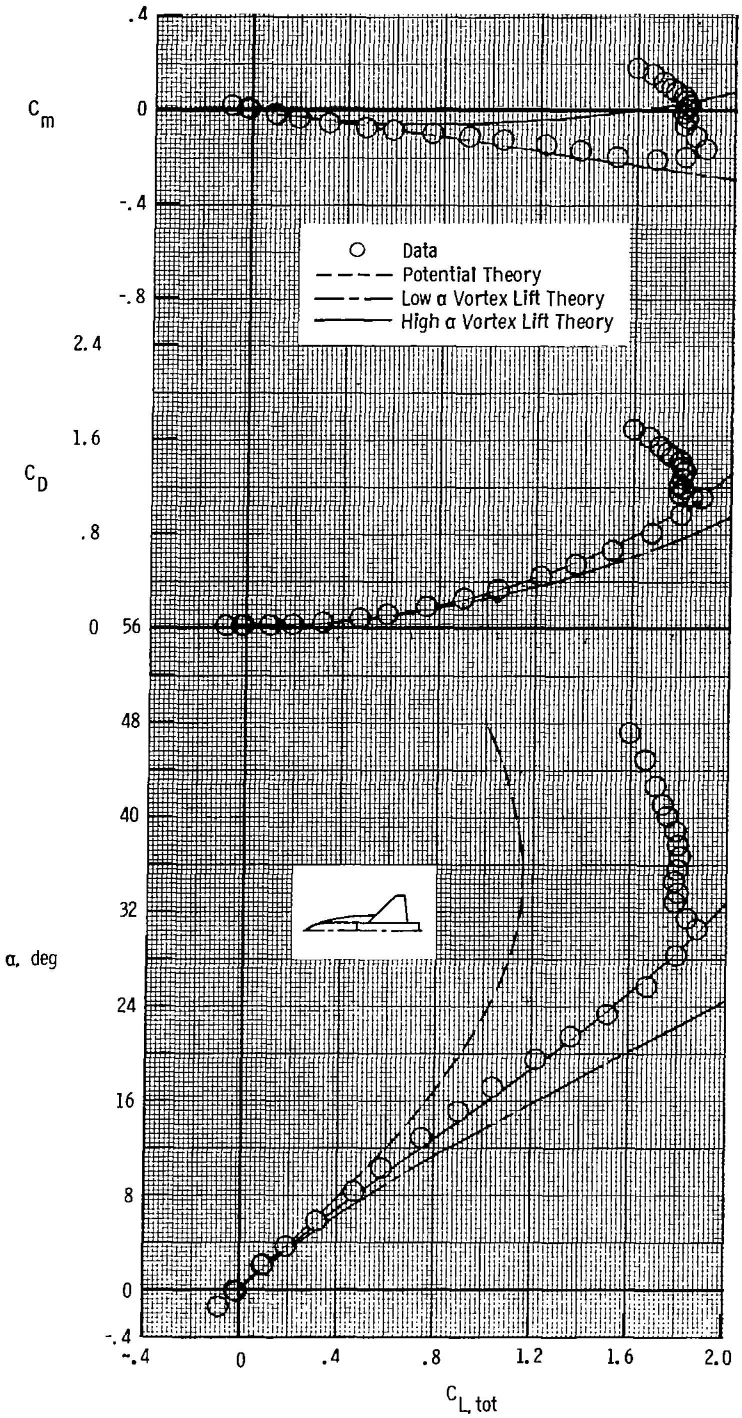

(l) ED 9.

Figure 9.- Continued.

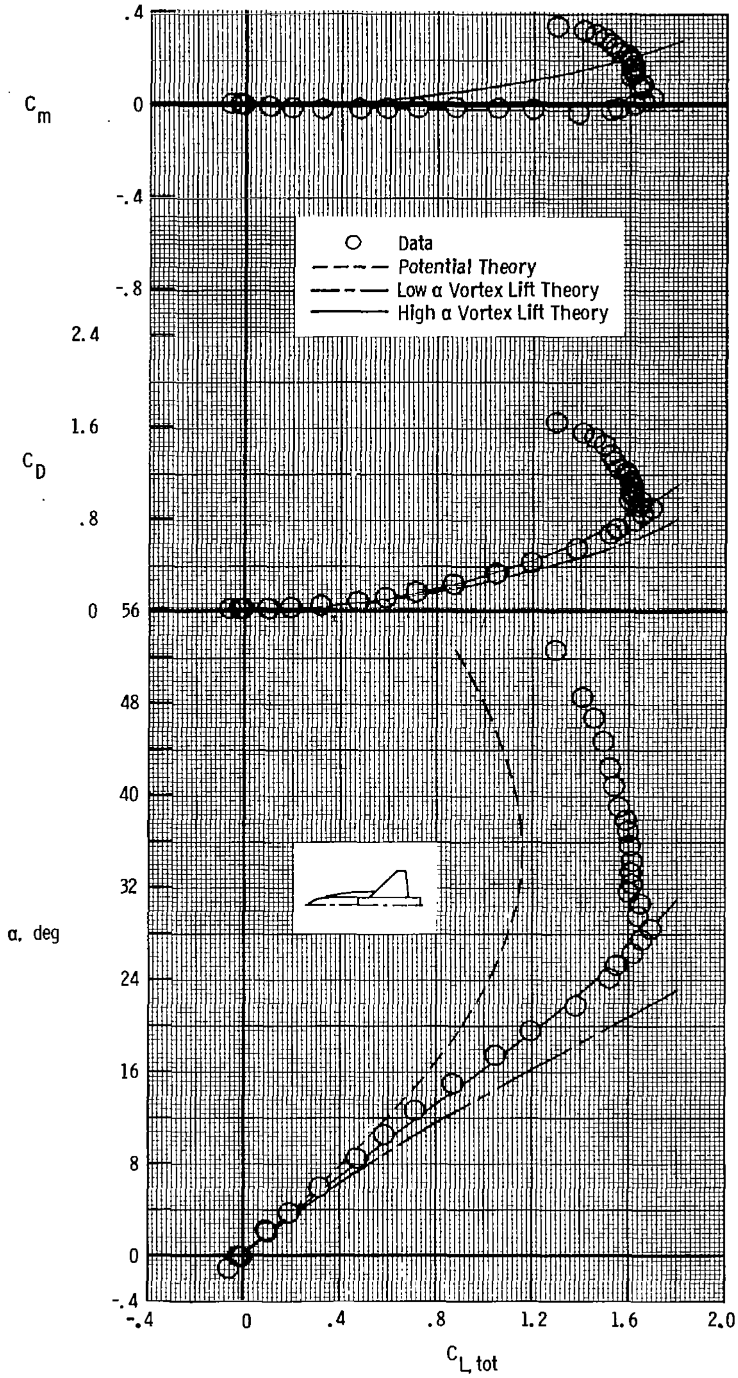

(m) ED 10.

Figure 9.- Continued.

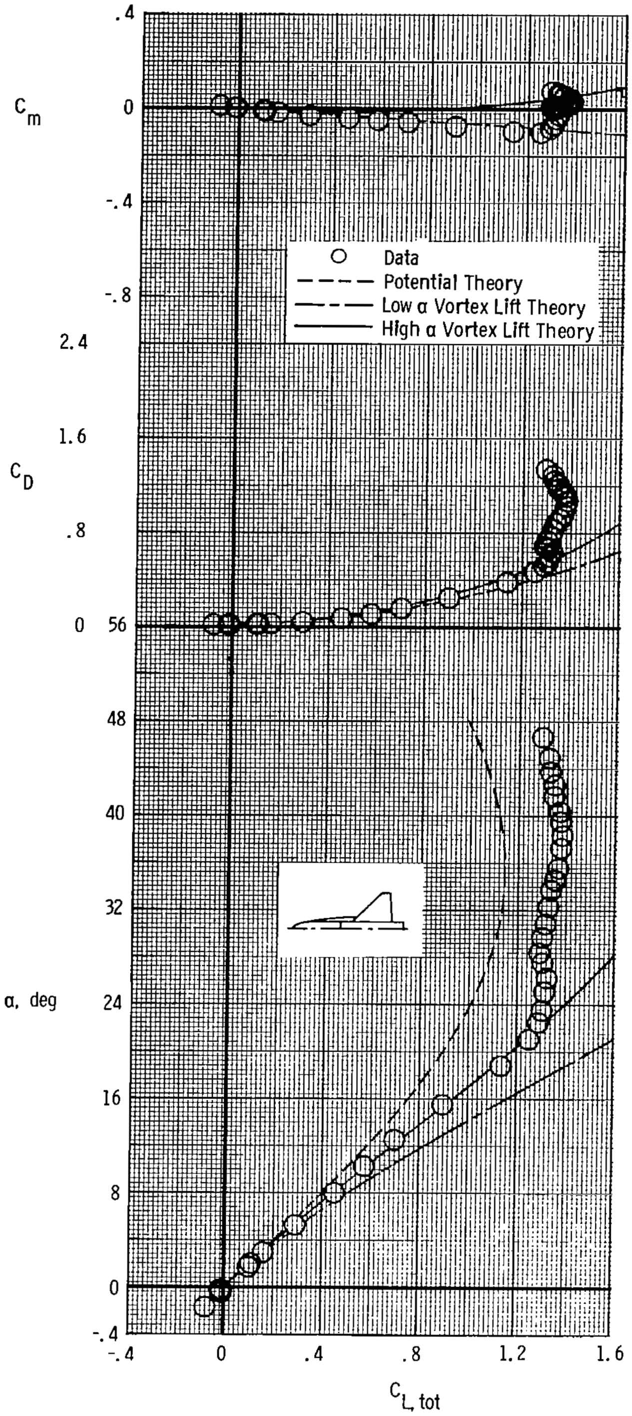

(n) ED 11.

Figure 9.- Continued.

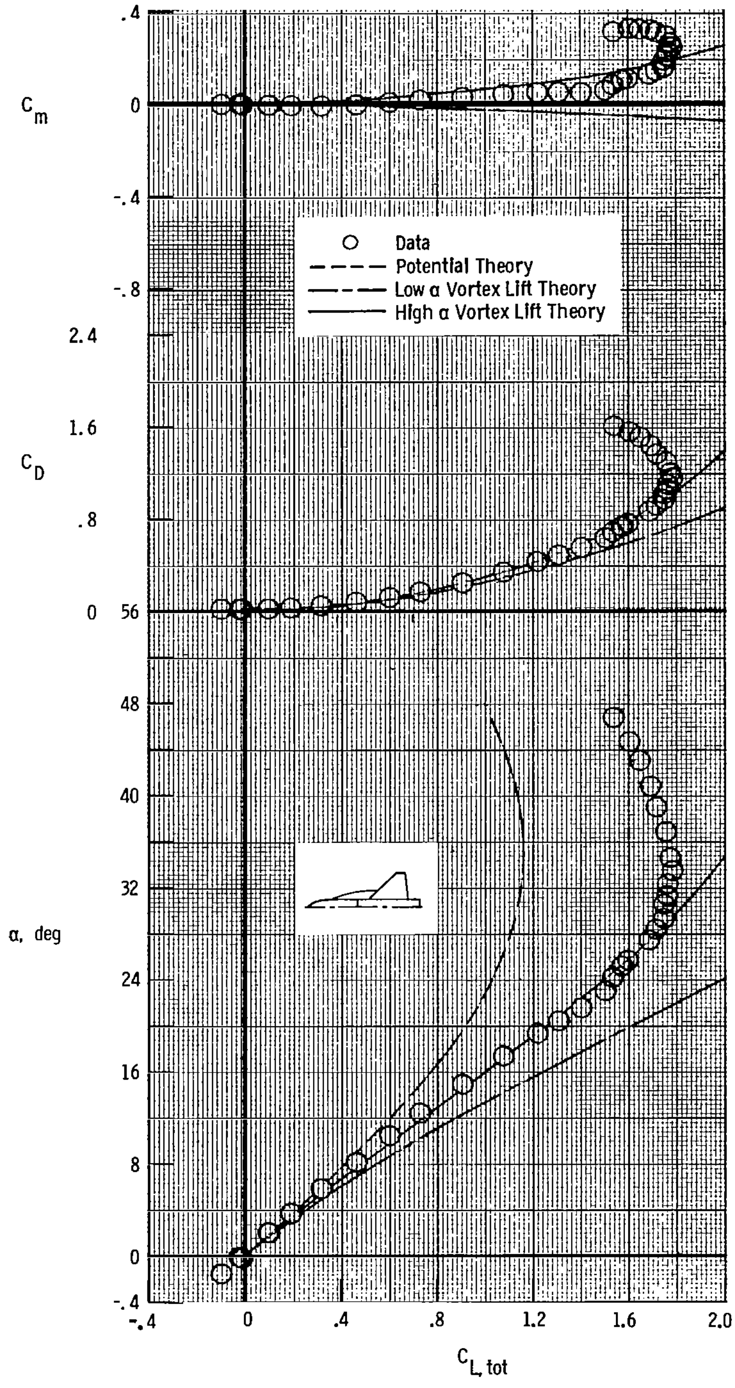

(o) ED 12.

Figure 9.- Continued.

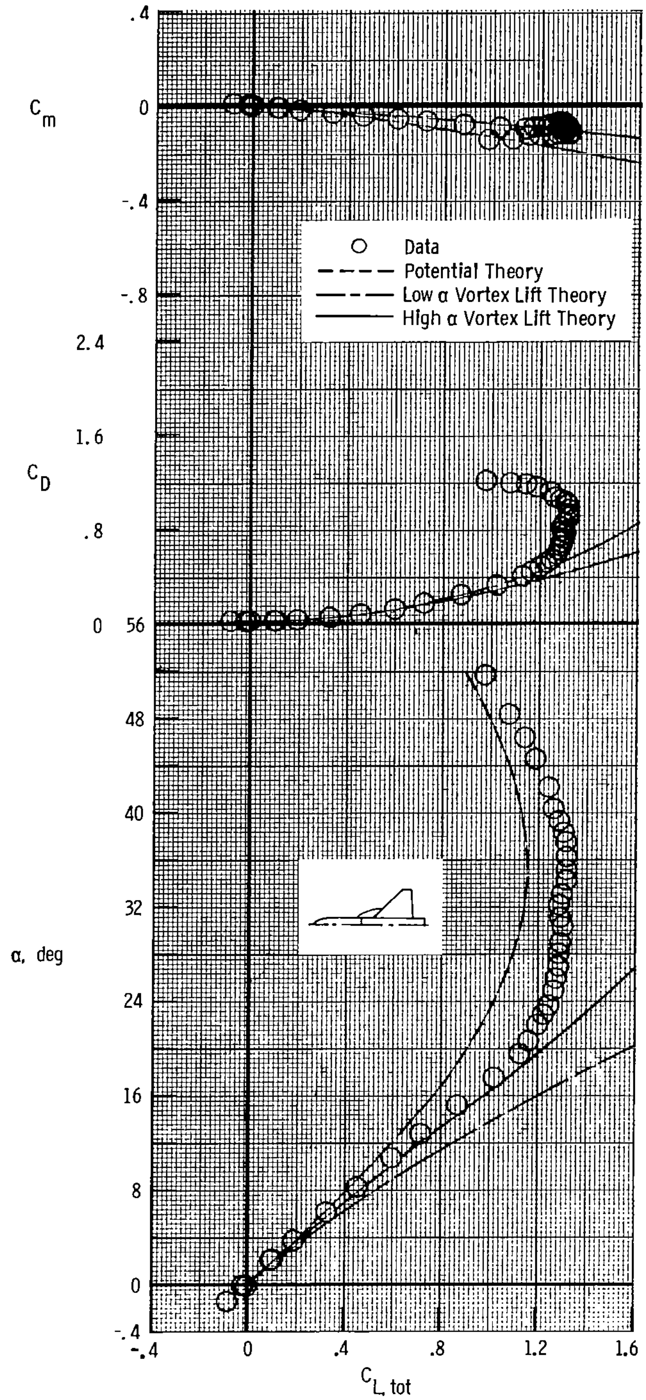

(p) ED 13.

Figure 9.- Concluded.

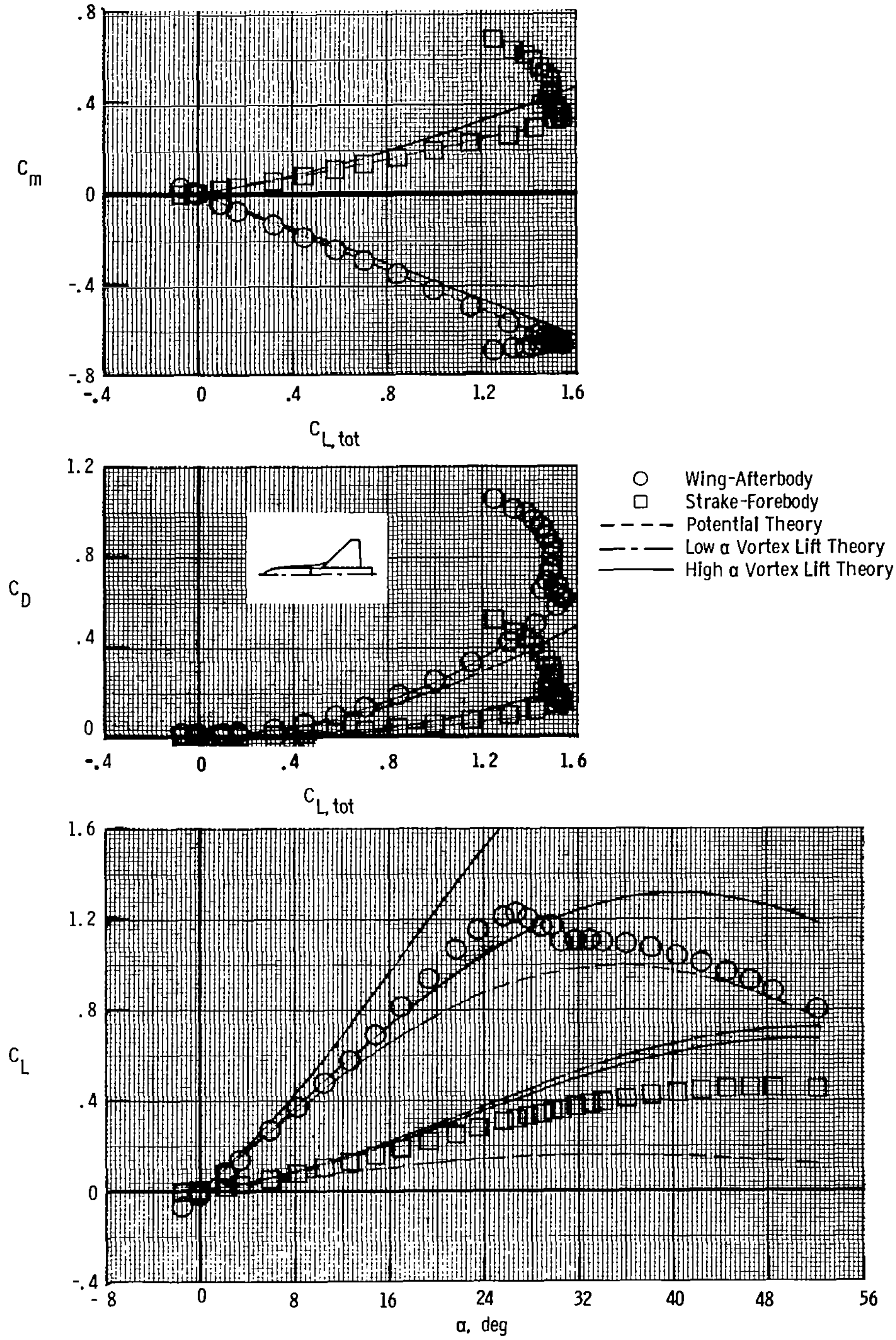

(a) AD 9.

Figure 10.- Component longitudinal aerodynamic characteristics at M = 0.2; data and theoretical estimates.

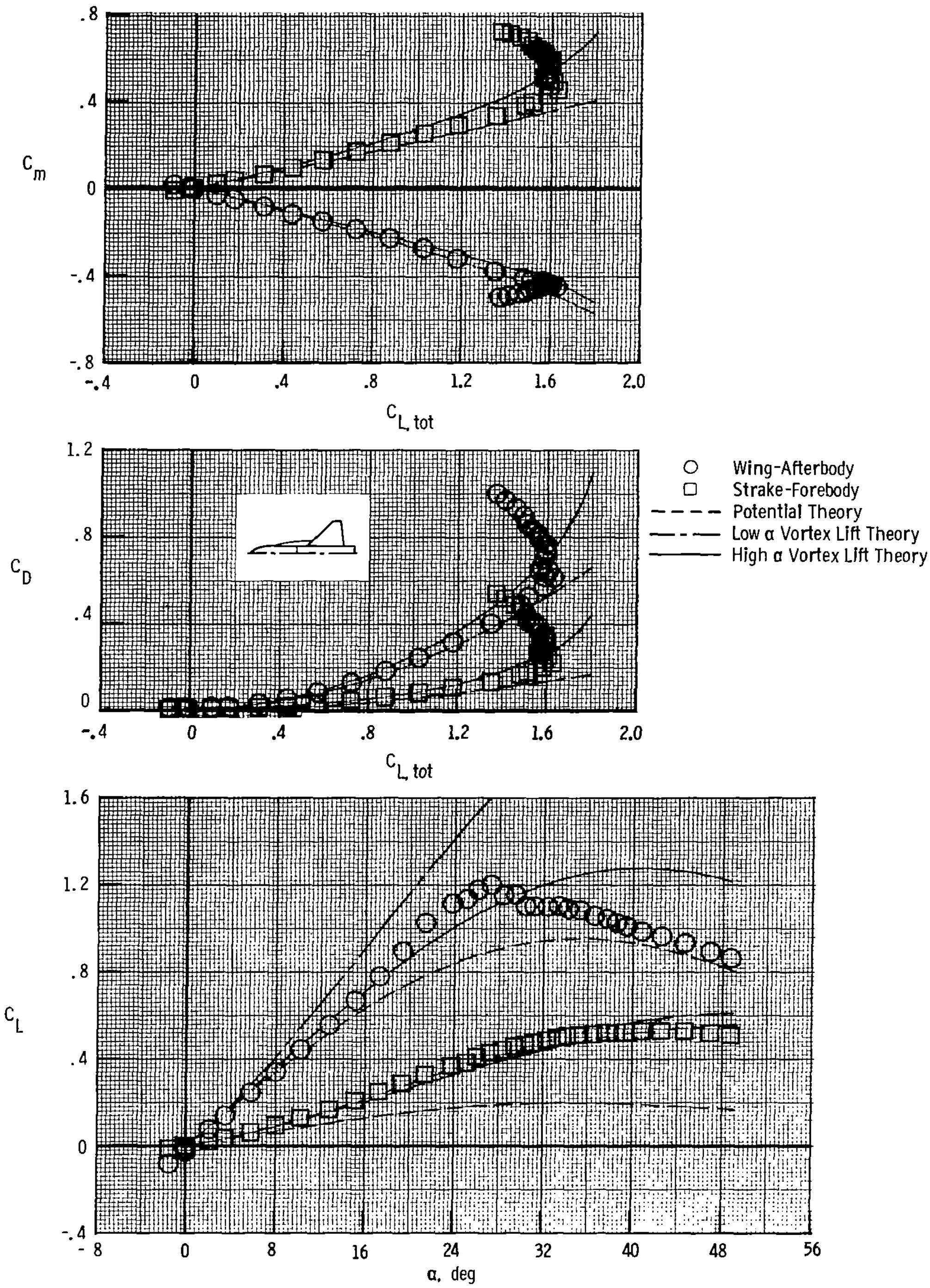

(b) AD 14.

Figure 10.- Continued.

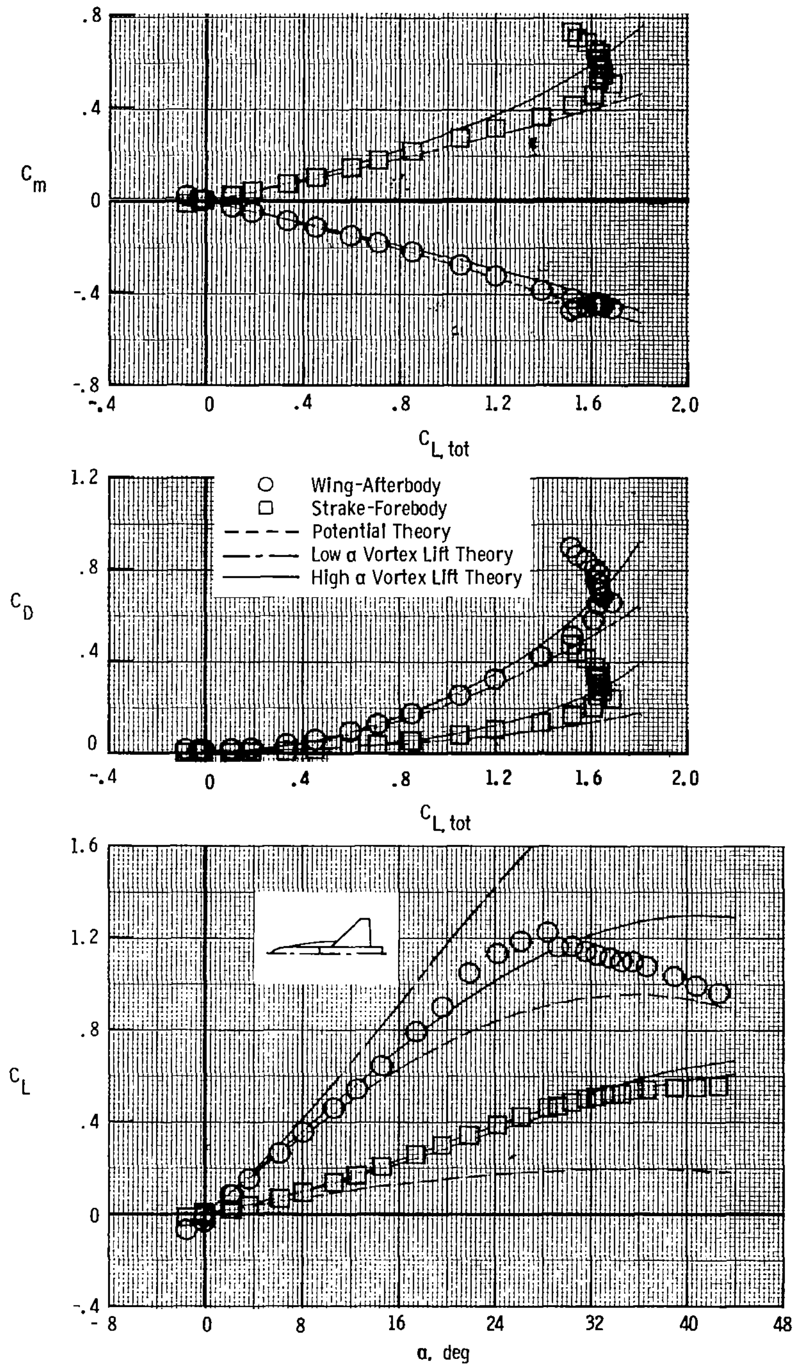

(c) AD 17.

Figure 10.- Continued.

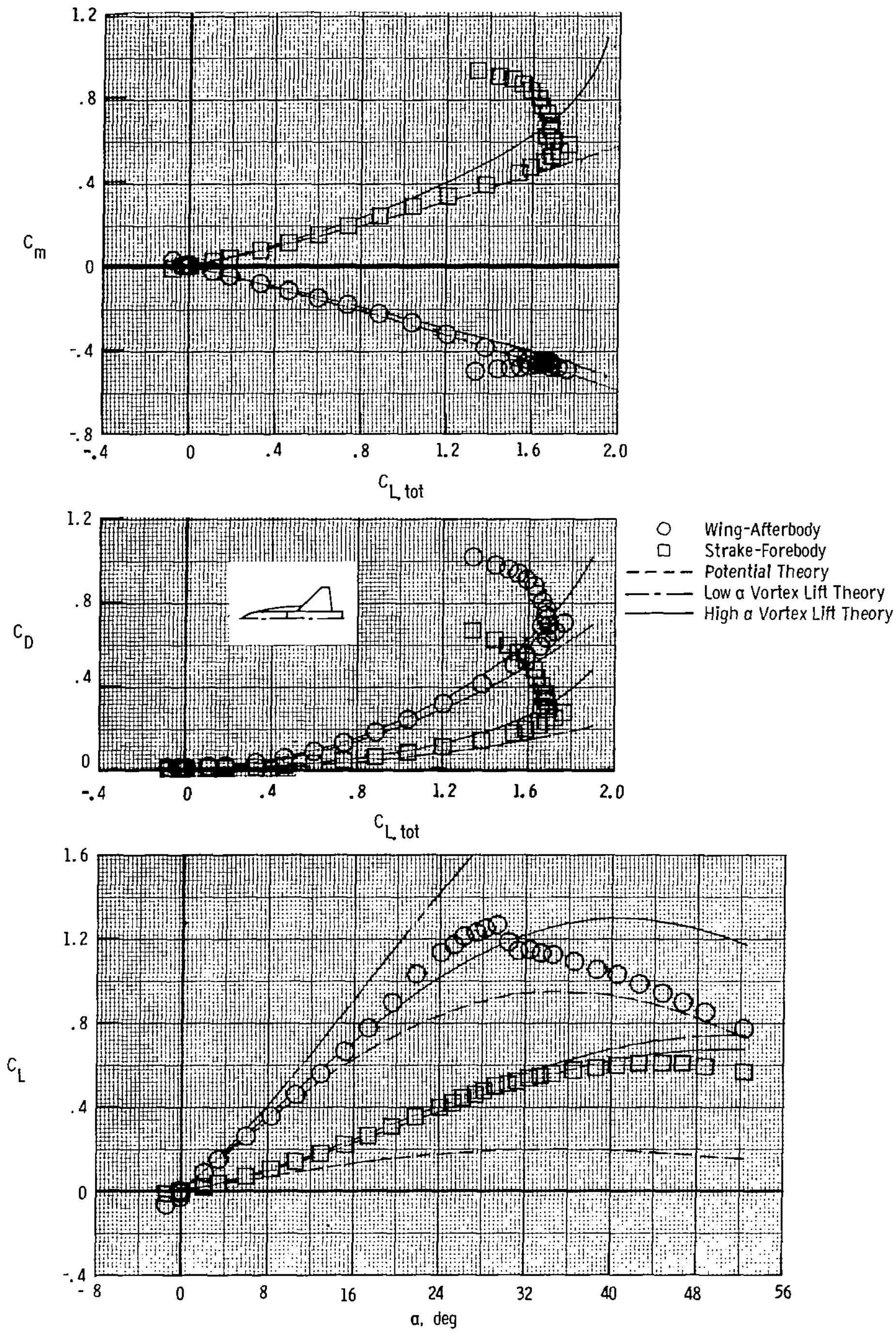

(d) AD 19.

Figure 10.- Continued.

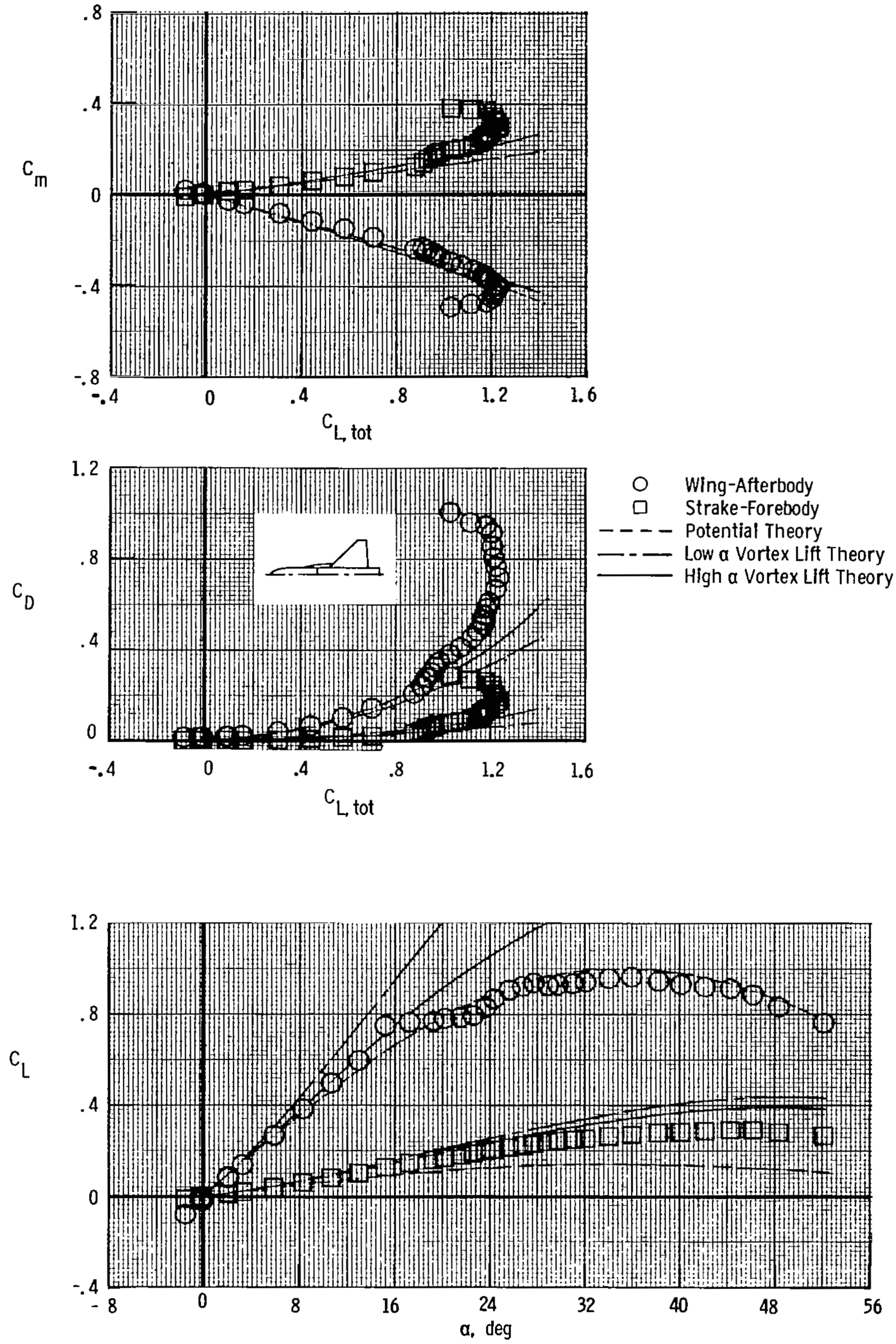

(e) AD 22.

Figure 10.- Continued.

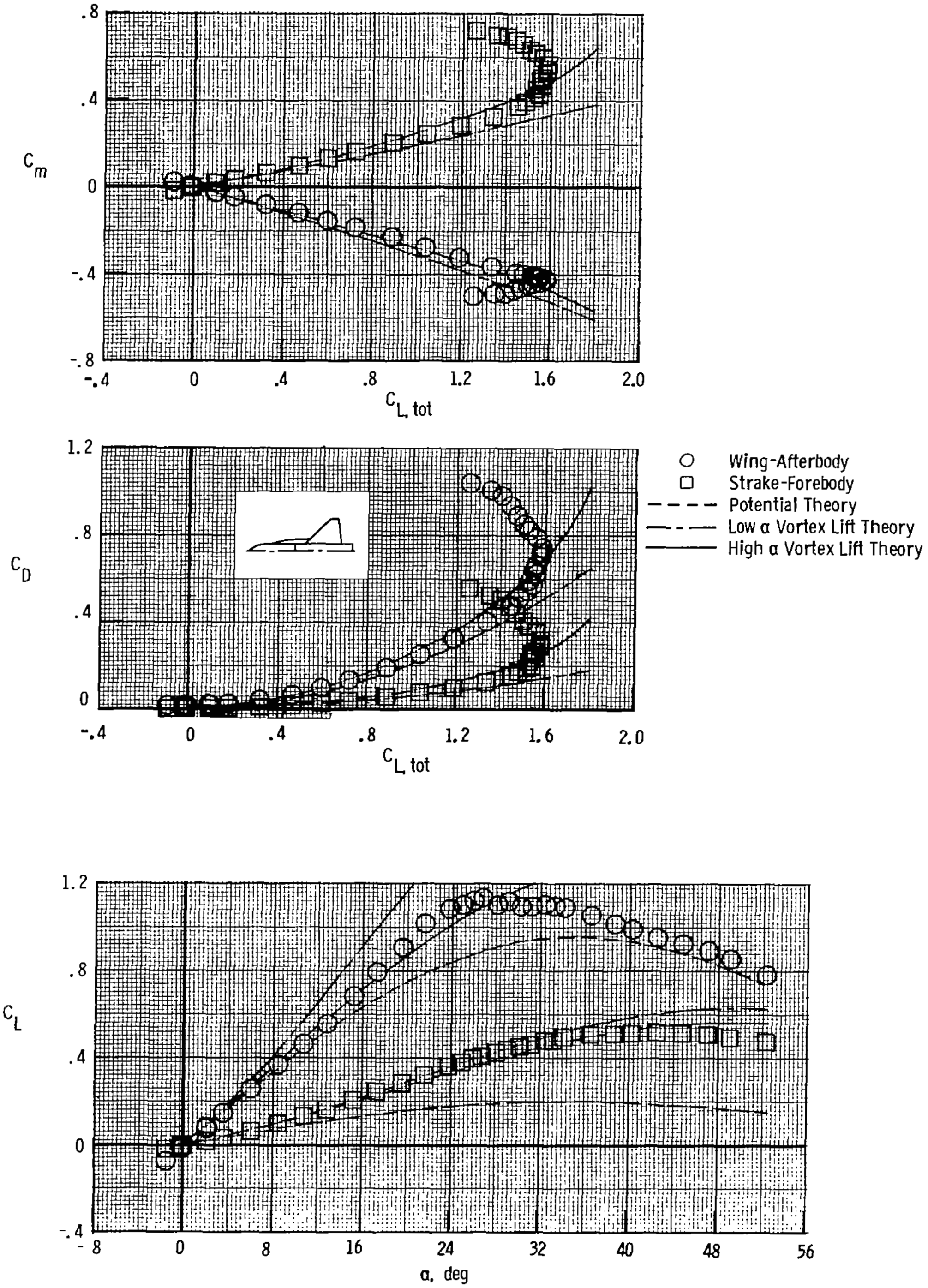

(f) AD 23.

Figure 10.- Continued.

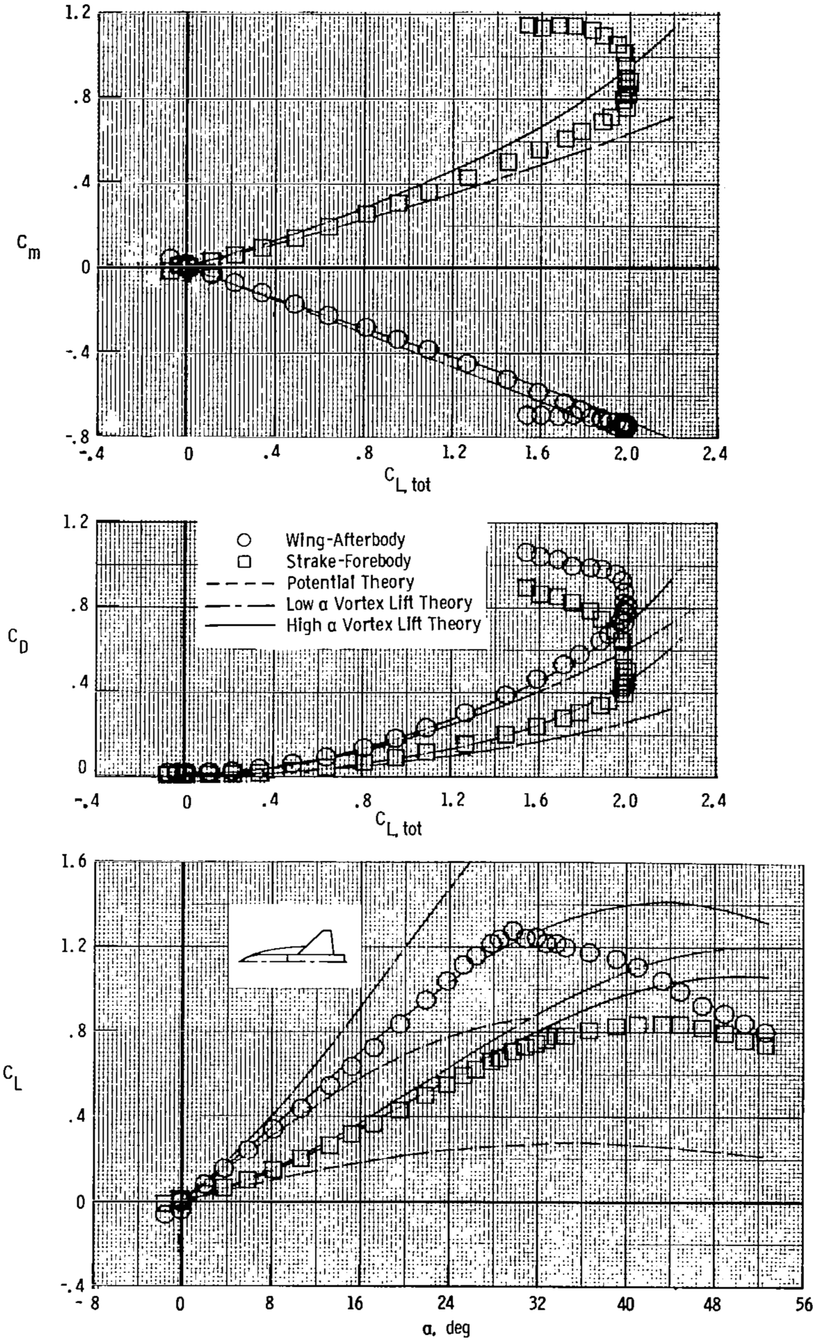

(g) AD 24.

Figure 10.- Continued.

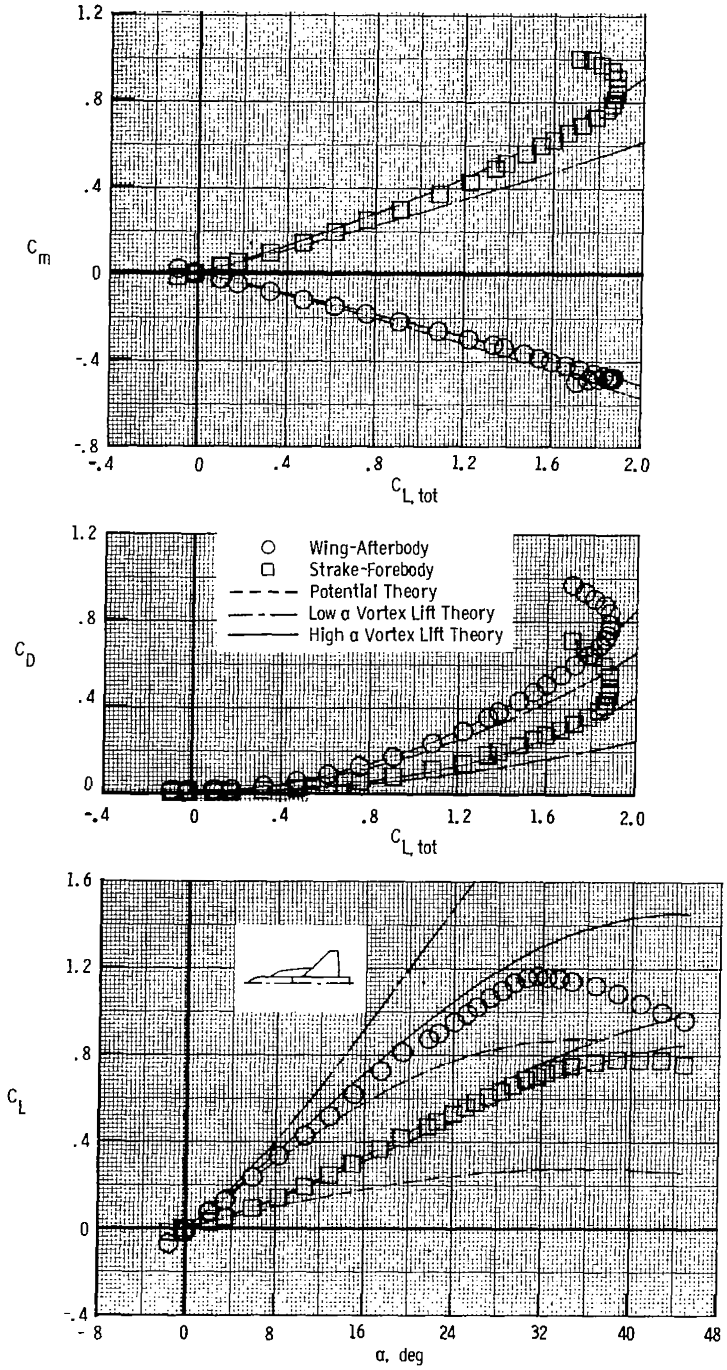

(h) ED 2.

Figure 10.- Continued.

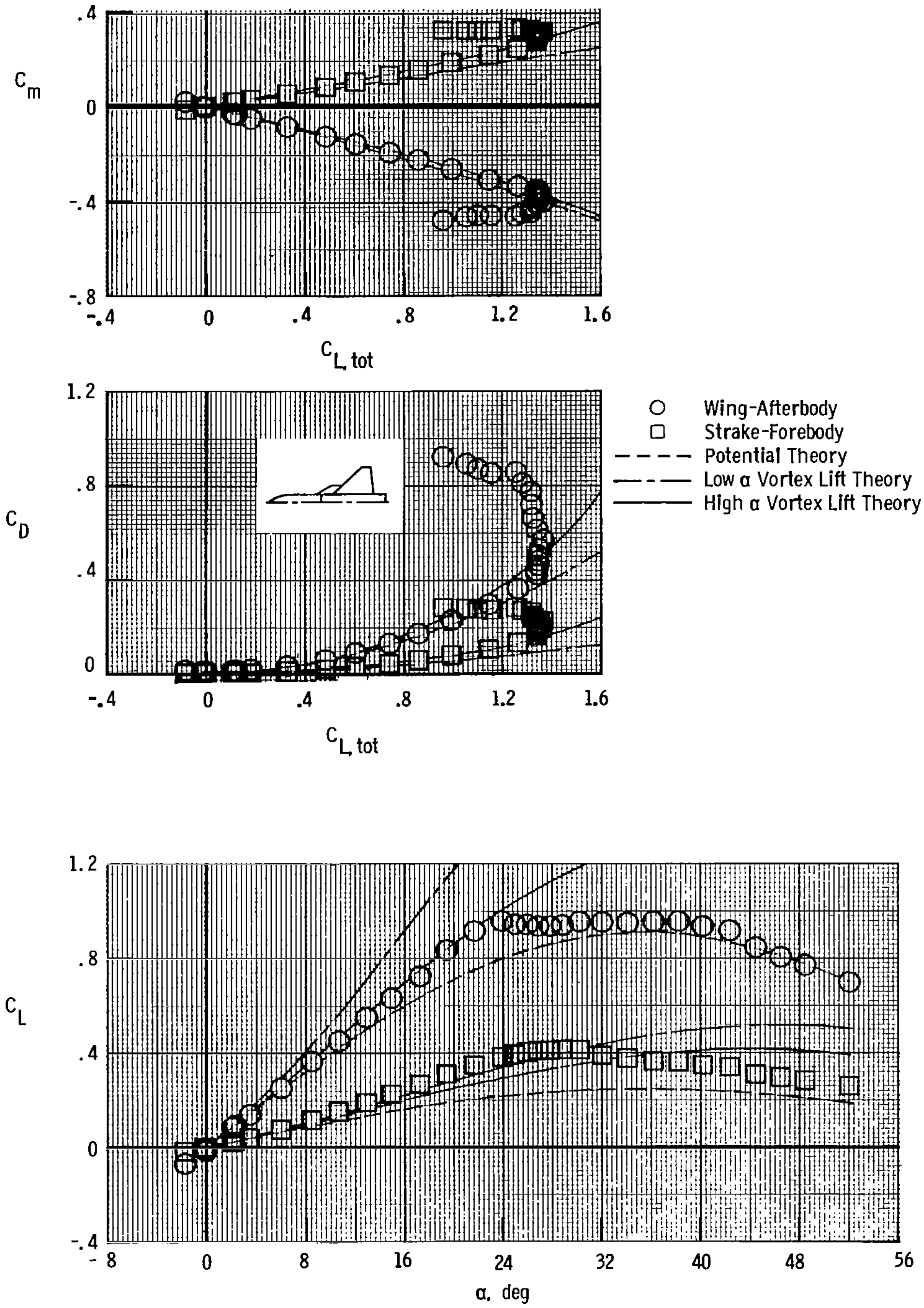

(i) ED 4.

Figure 10.- Continued.

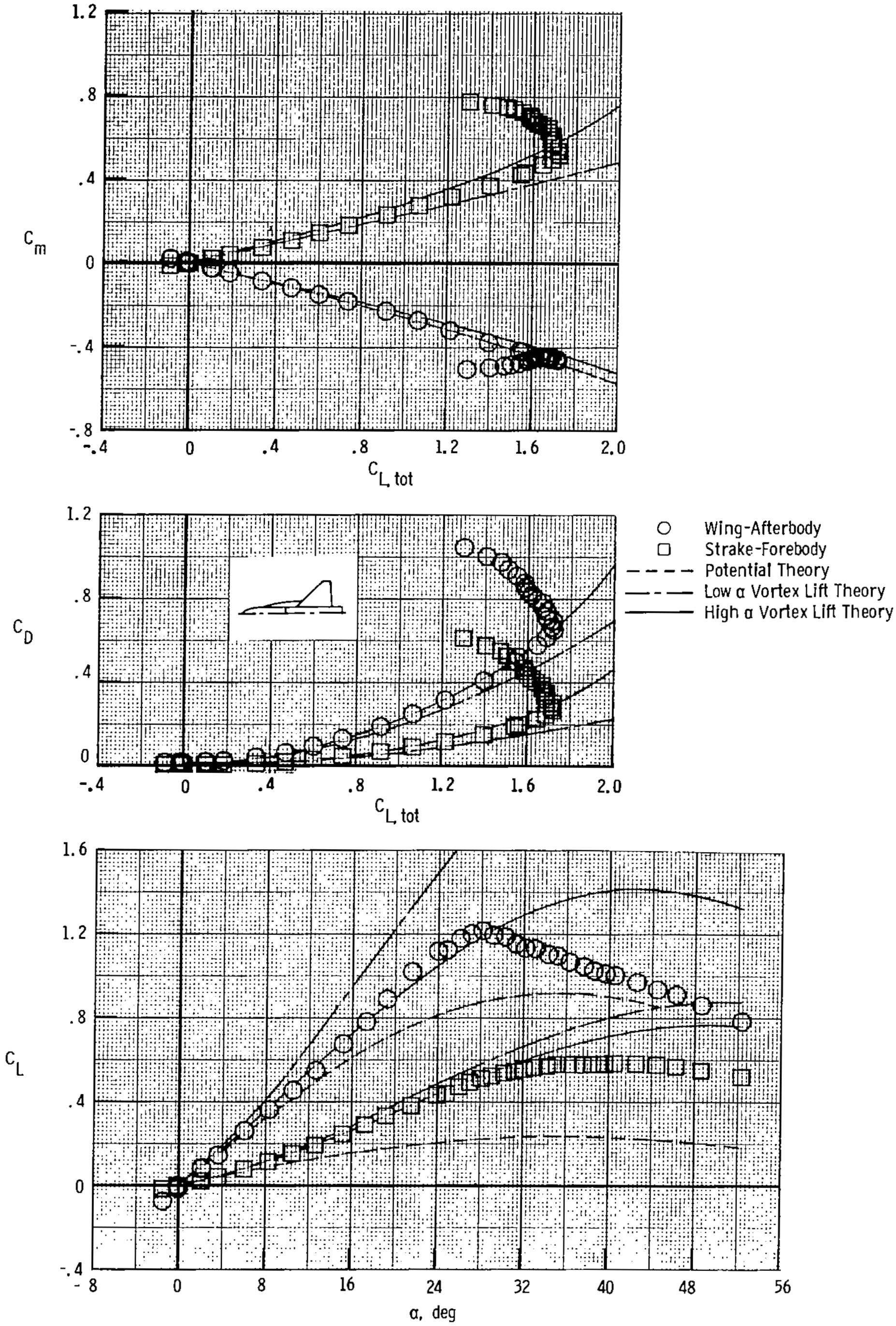

(j) ED 5.

Figure 10.- Continued.

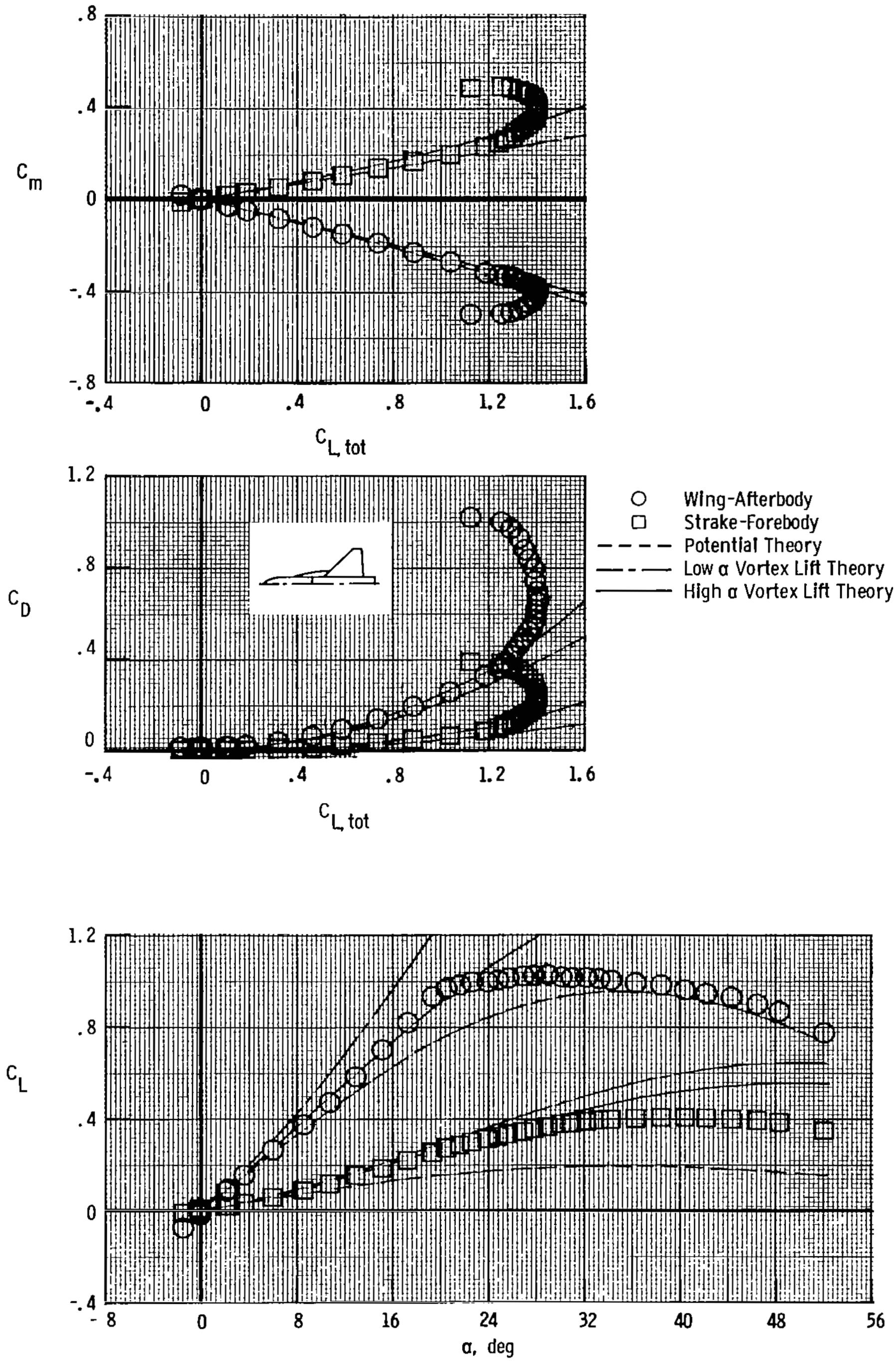

(k) ED 6.

Figure 10.- Continued.

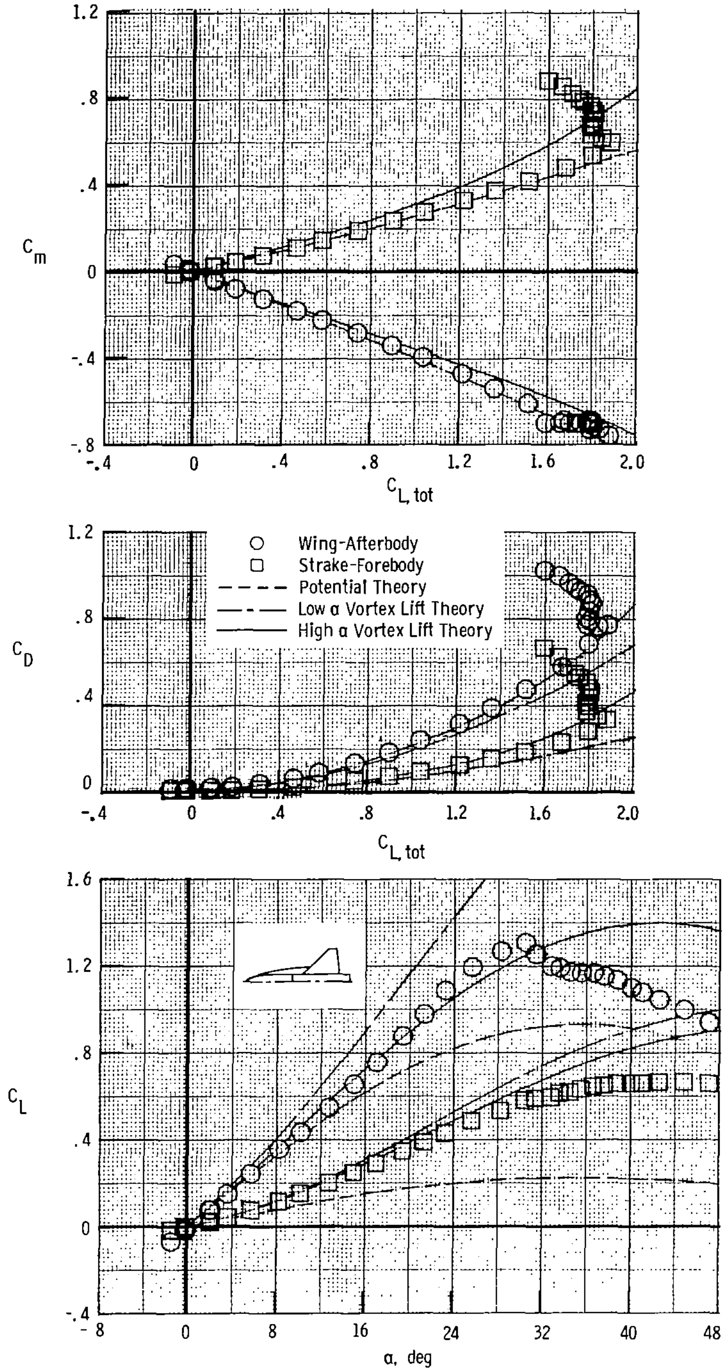

(l) ED 9.

Figure 10.- Continued.

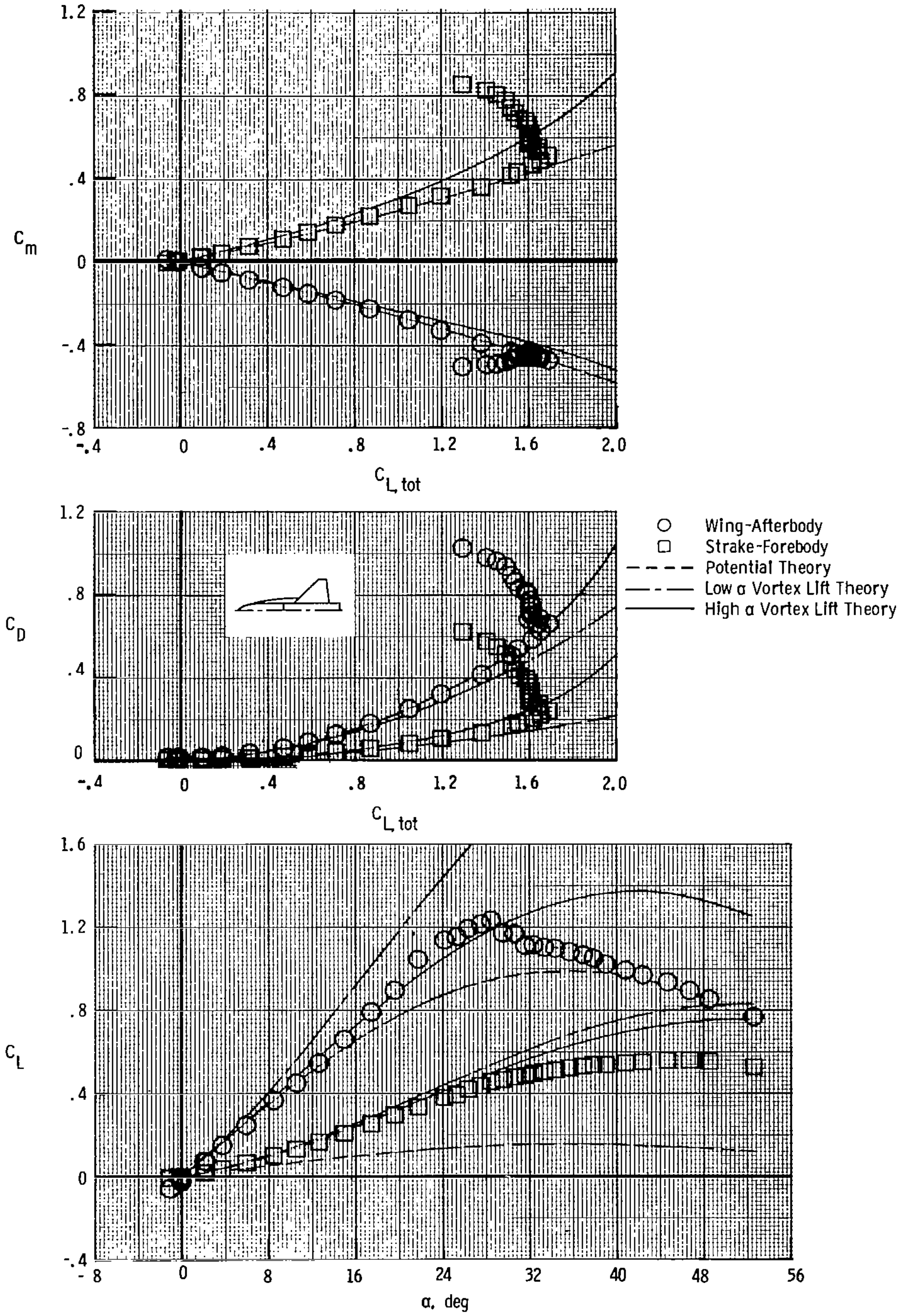

(m) ED 10.

Figure 10.- Continued.

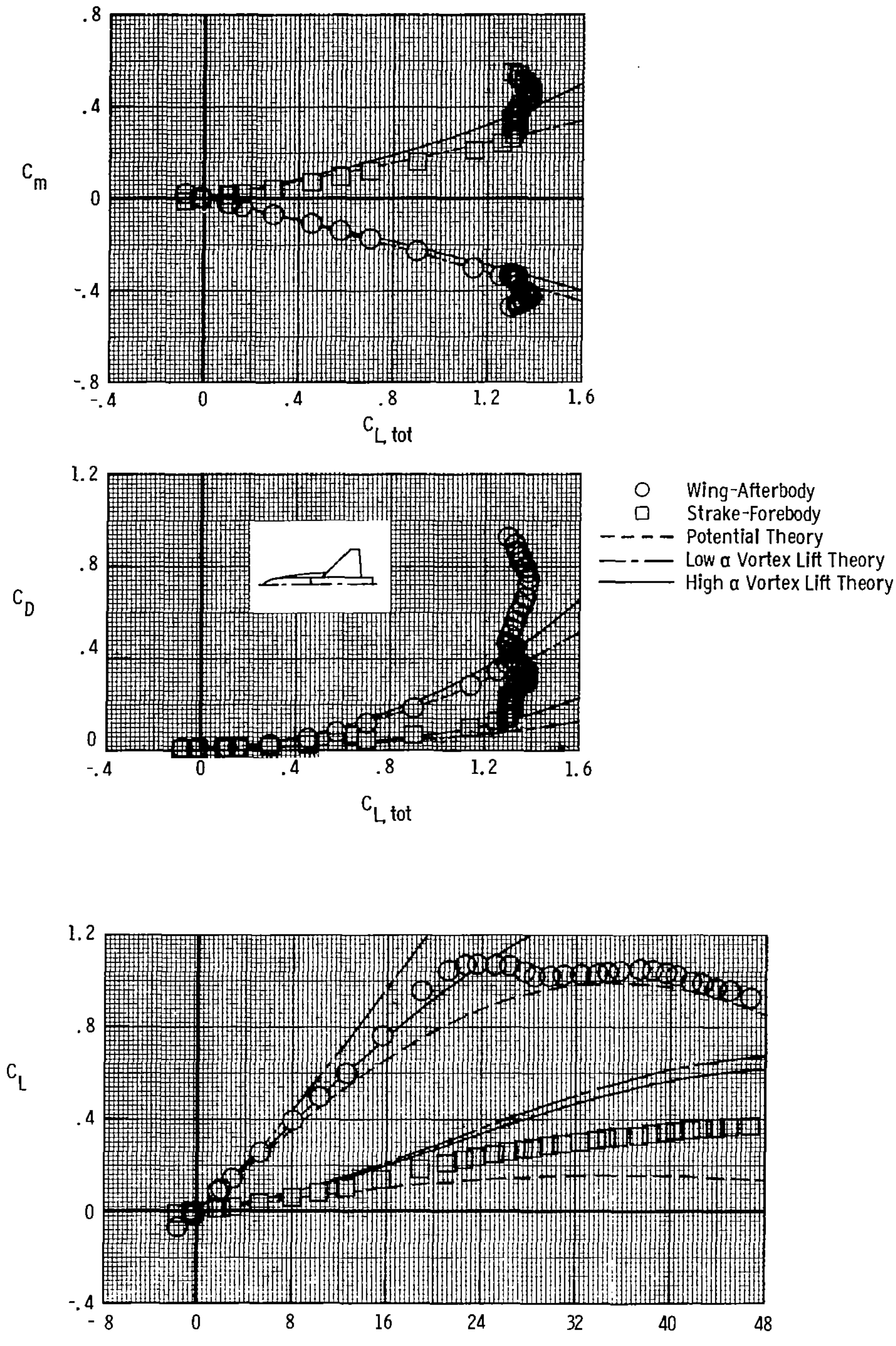

(n) ED 11.

Figure 10.- Continued.

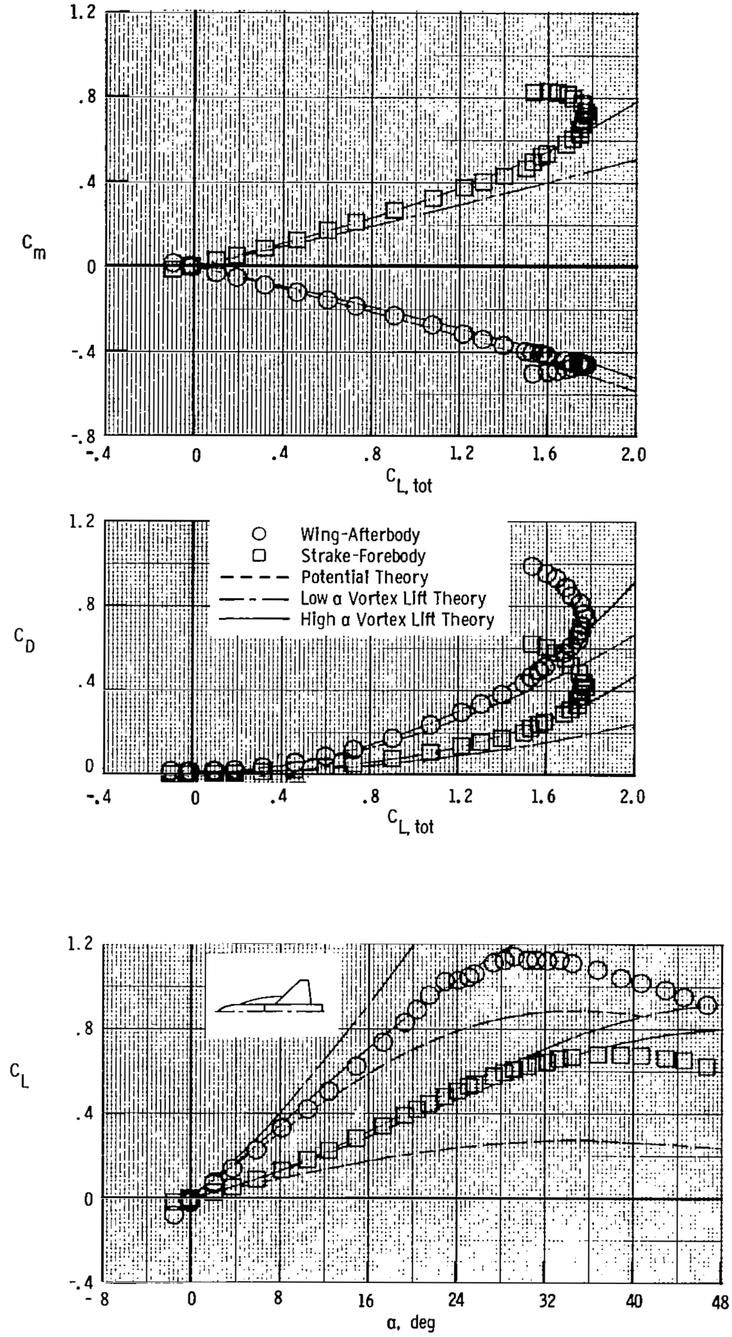

(o) ED 12.

Figure 10.- Continued.

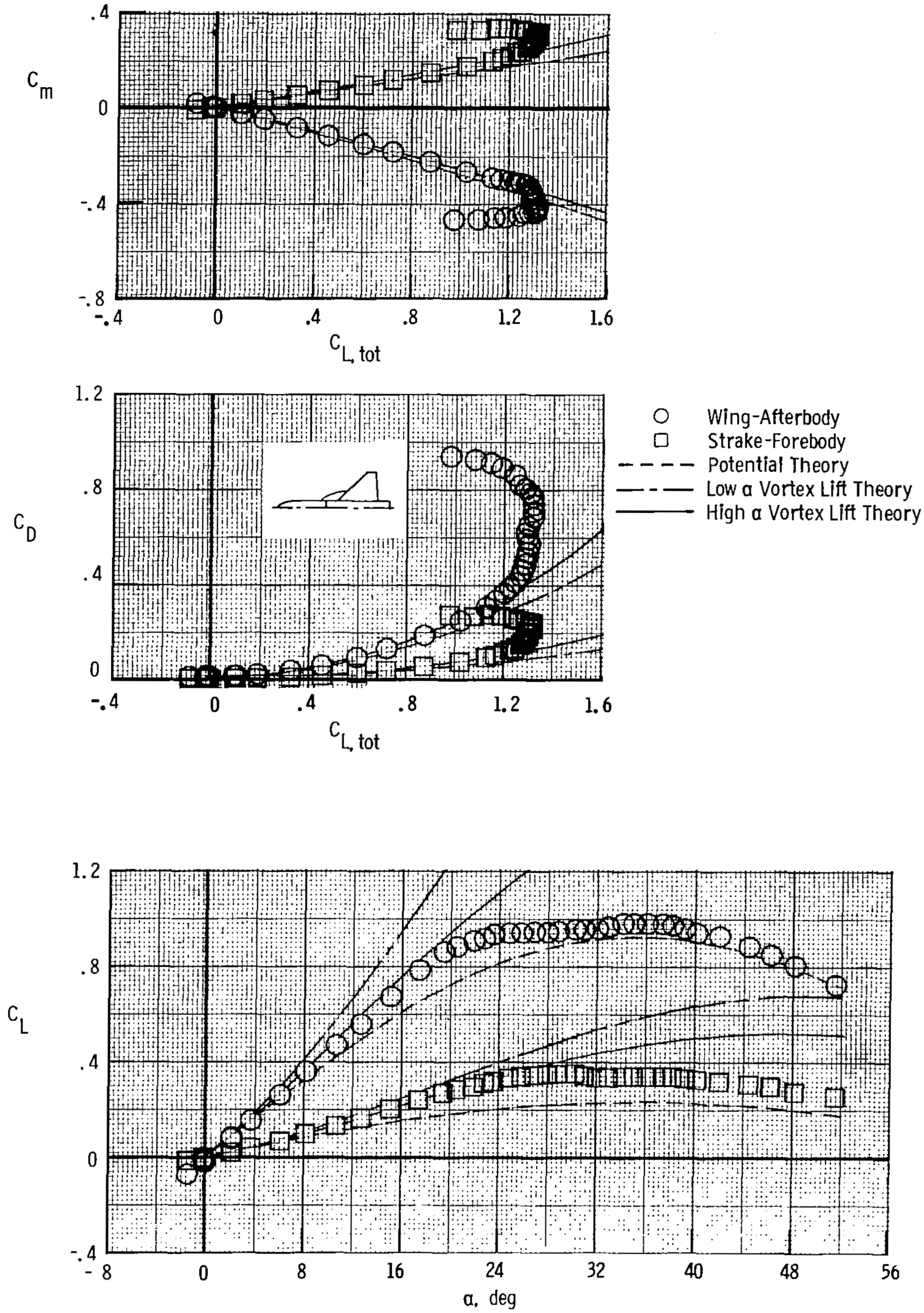

(p) ED 13.

Figure 10.- Concluded.

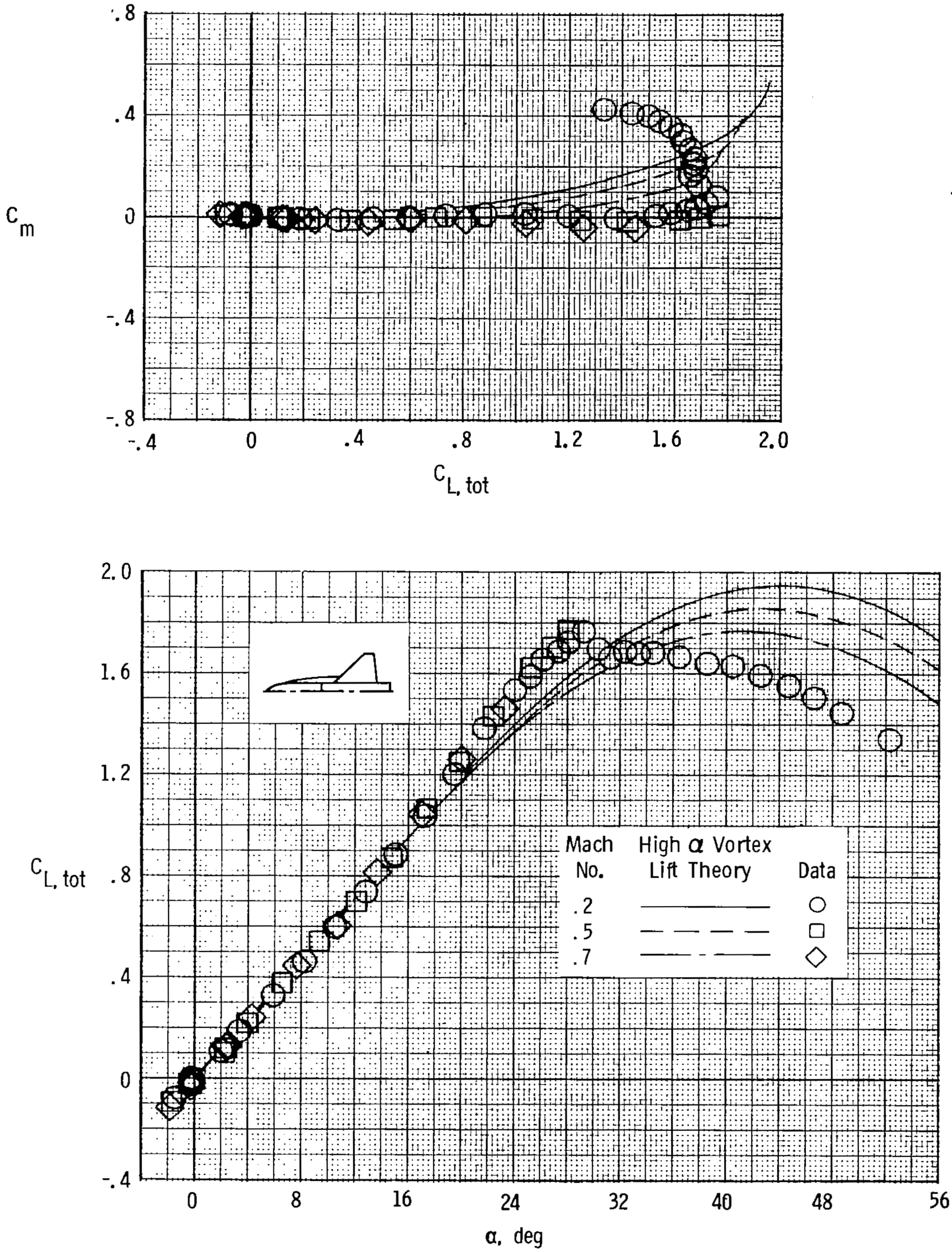

(a) Complete configuration.

Figure 11.- Effect of Mach number on lift and pitching-moment characteristics for AD 19 configuration; data and theoretical estimates.

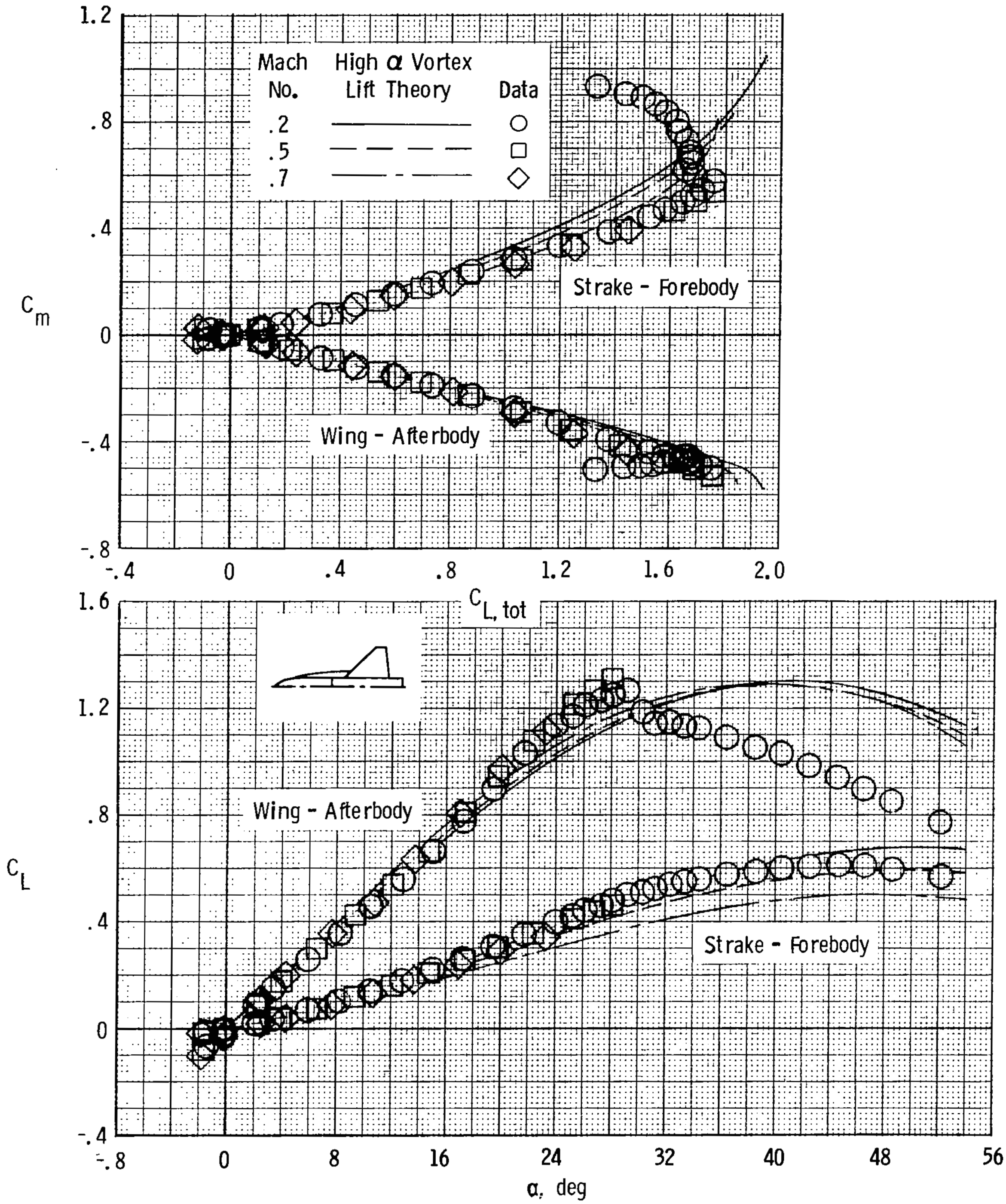

(b) Components.

Figure 11.- Concluded.

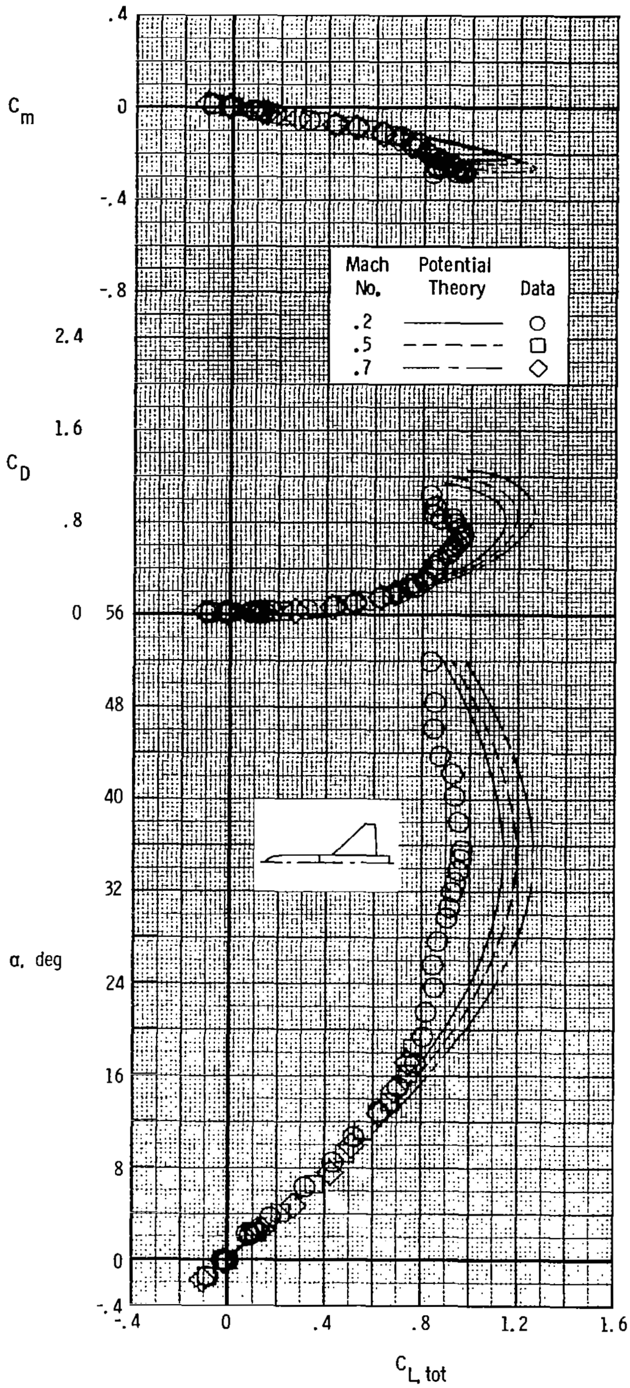

(a) Forward wing position.

Figure 12.- Effect of Mach number on longitudinal aerodynamic characteristics for basic wing-body configuration; data and theoretical estimates.

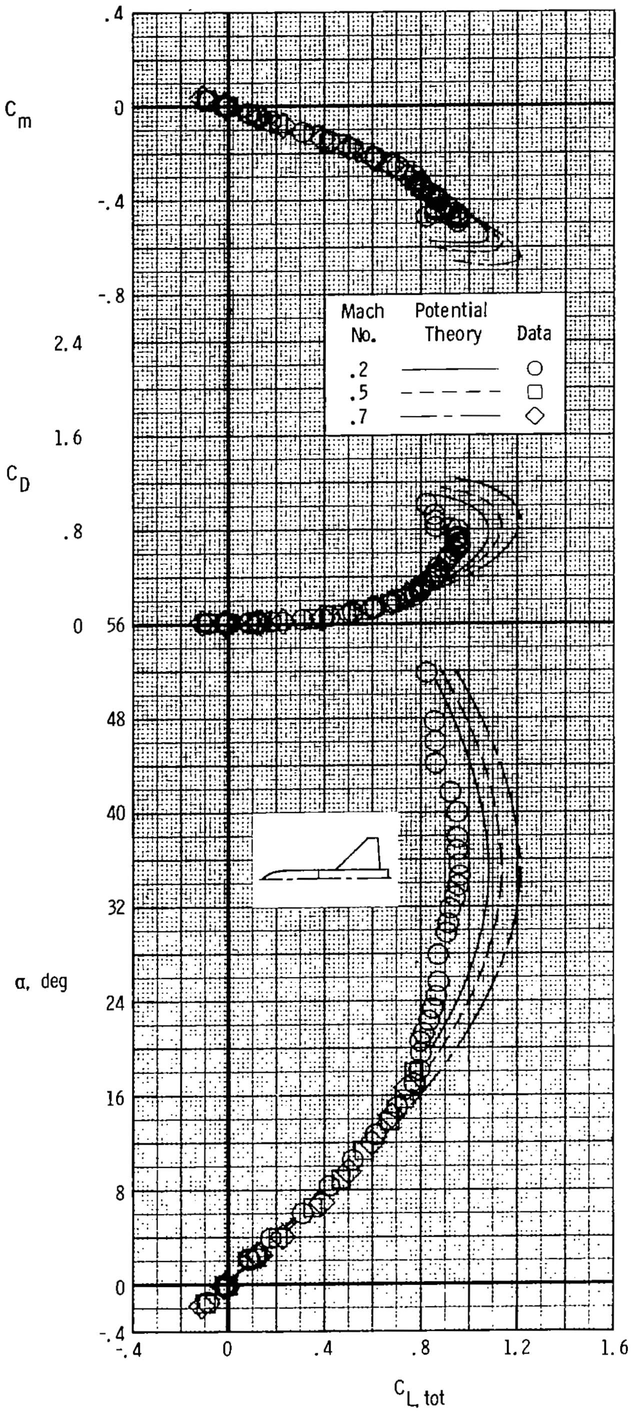

(b) Aft wing position.

Figure 12.- Concluded.

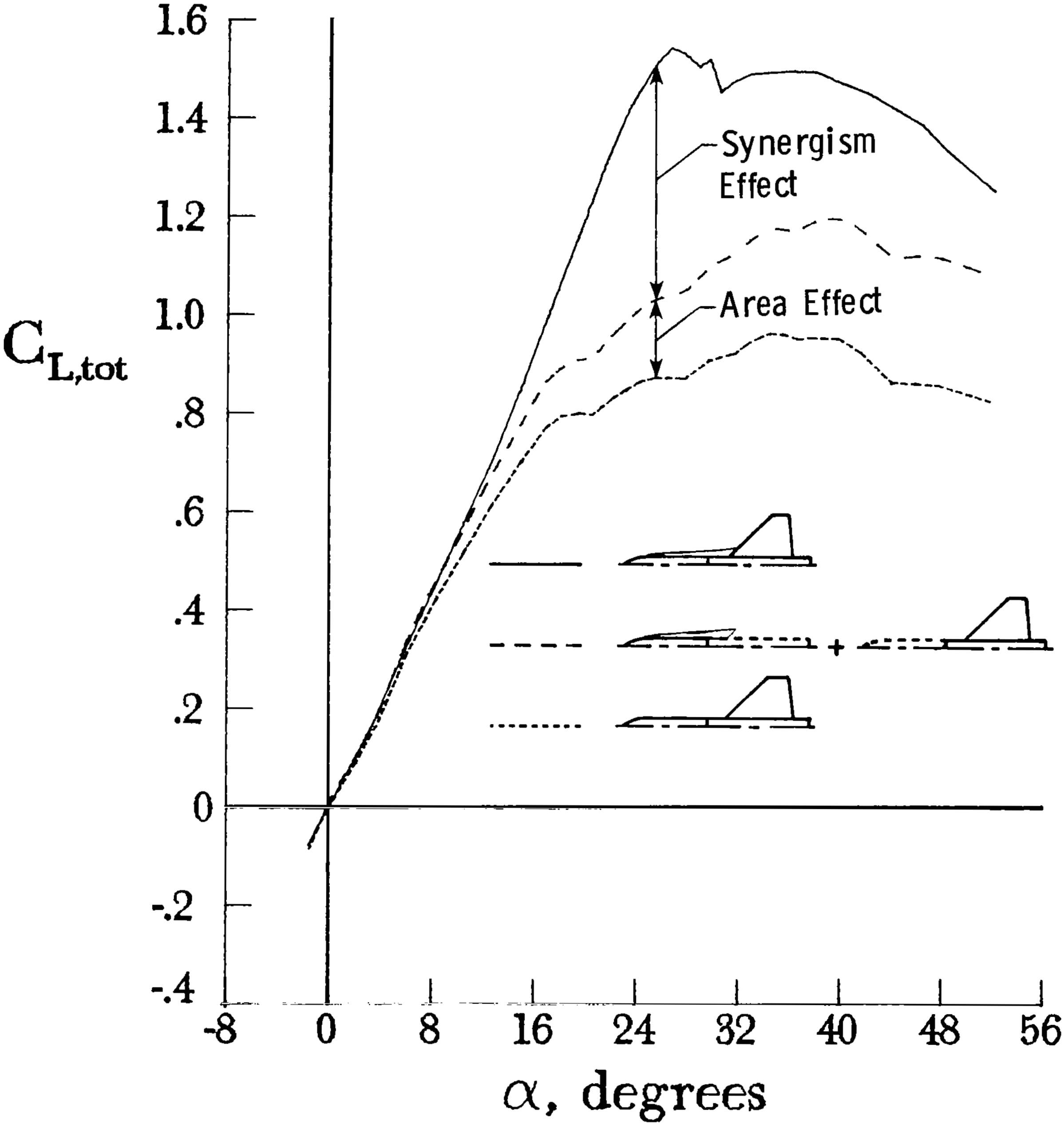

(a) AD 9.

Figure 13.- Aerodynamic synergism effect on configuration lift at M = 0.2.

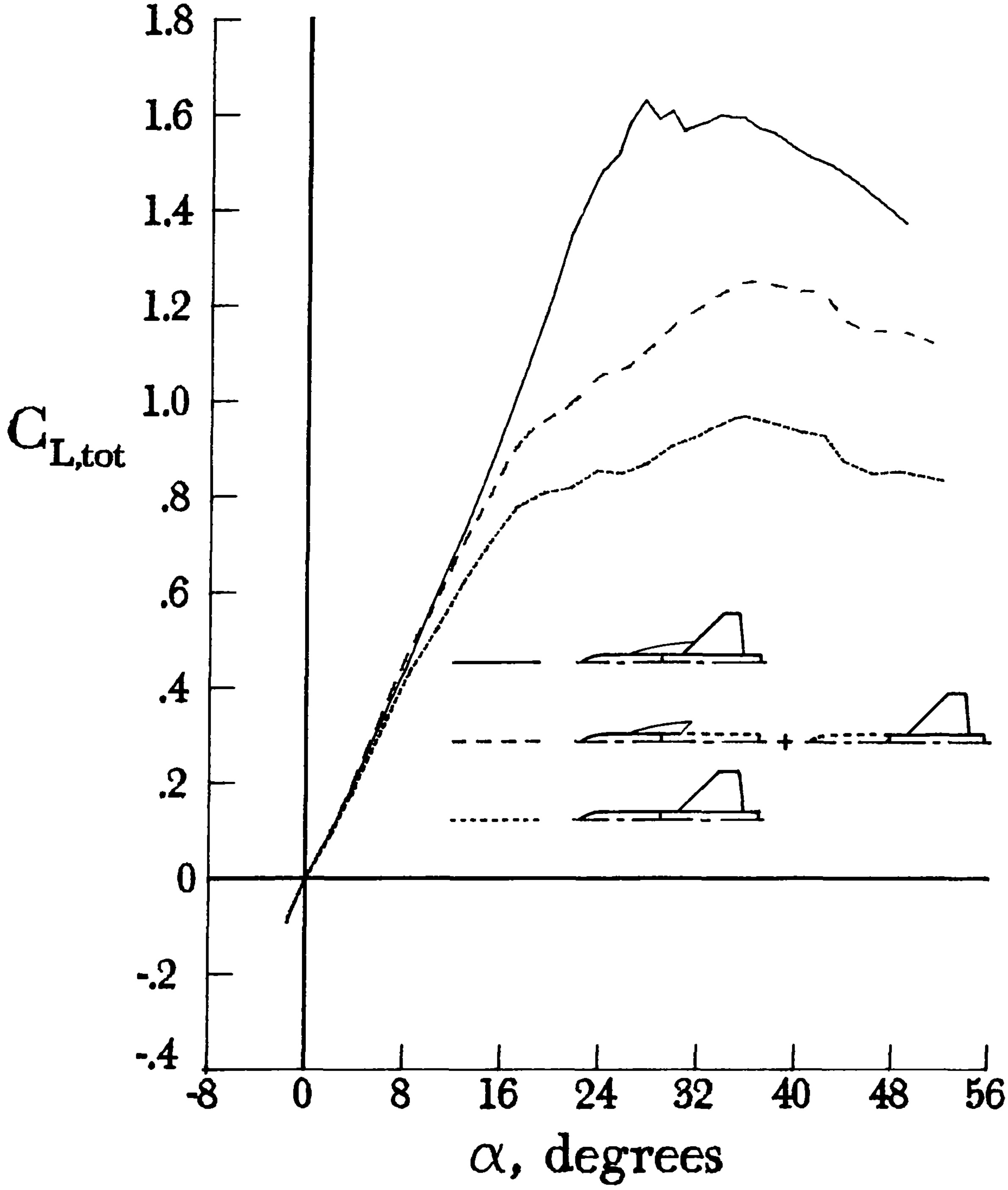

(b) AD 14.

Figure 13.- Continued.

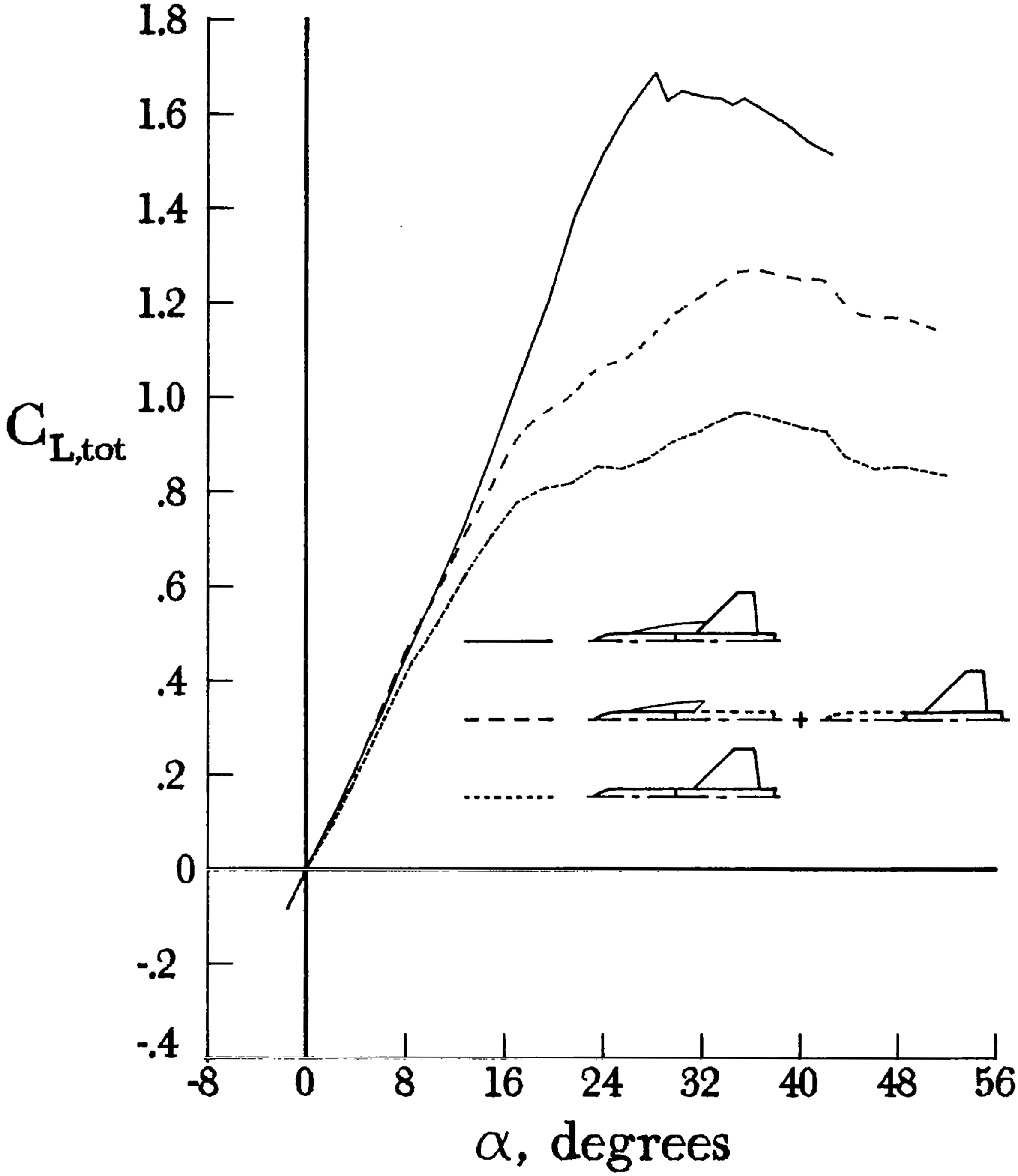

(c) AD 17.

Figure 13.- Continued.

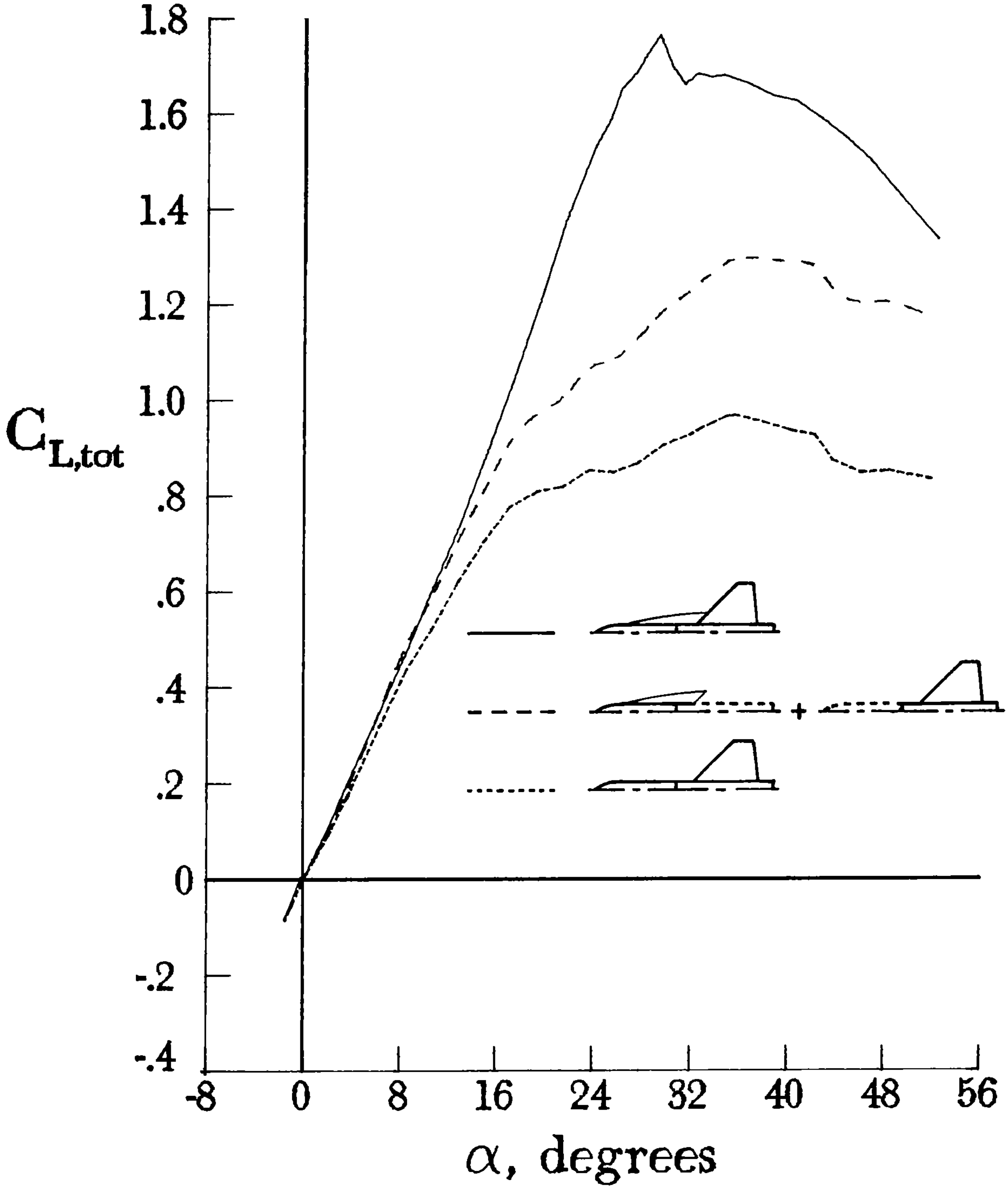

(d) AD 19.

Figure 13.- Continued.

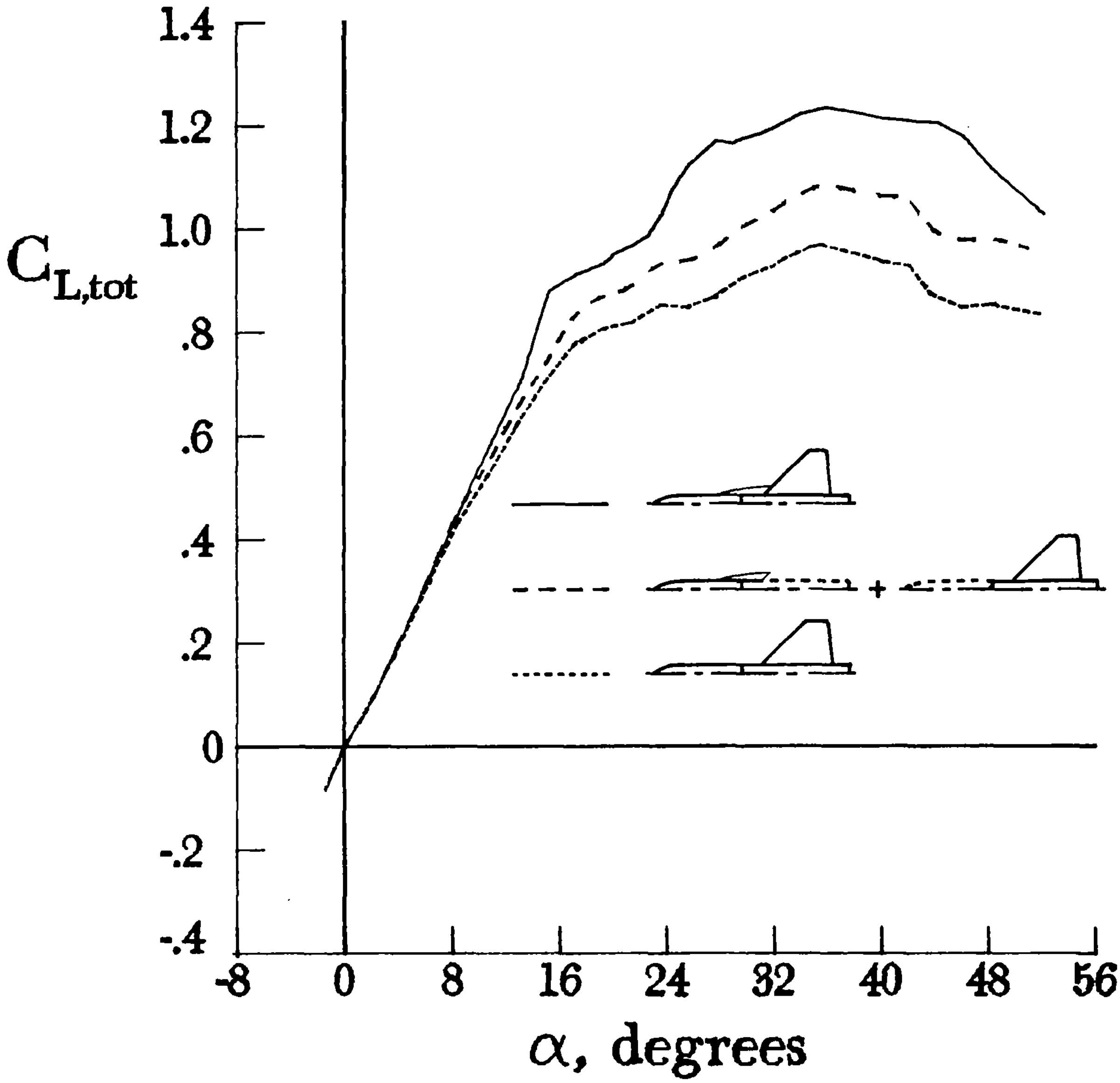

(e) AD 22.

Figure 13.- Continued.

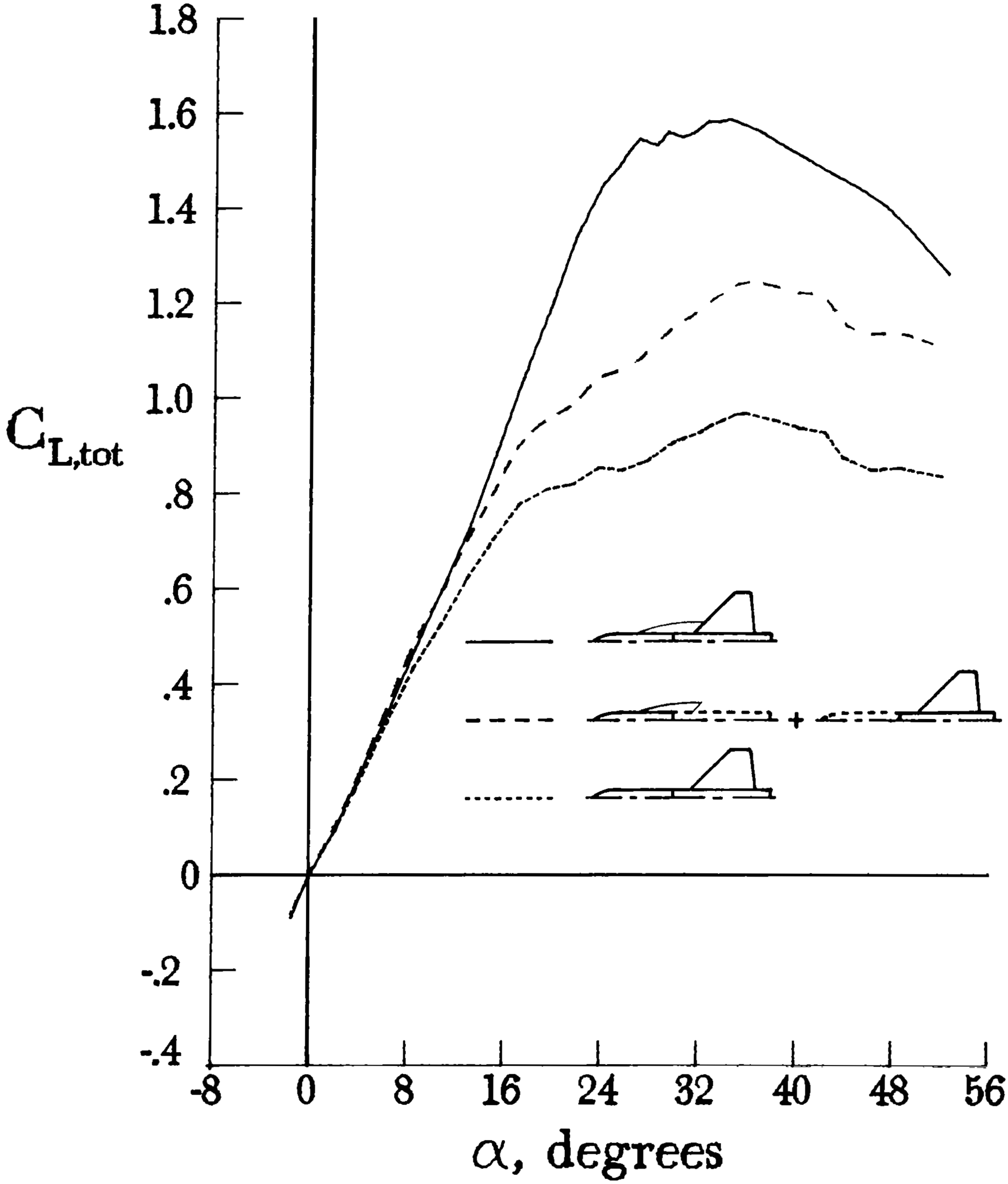

(f) AD 23.

Figure 13.- Continued.

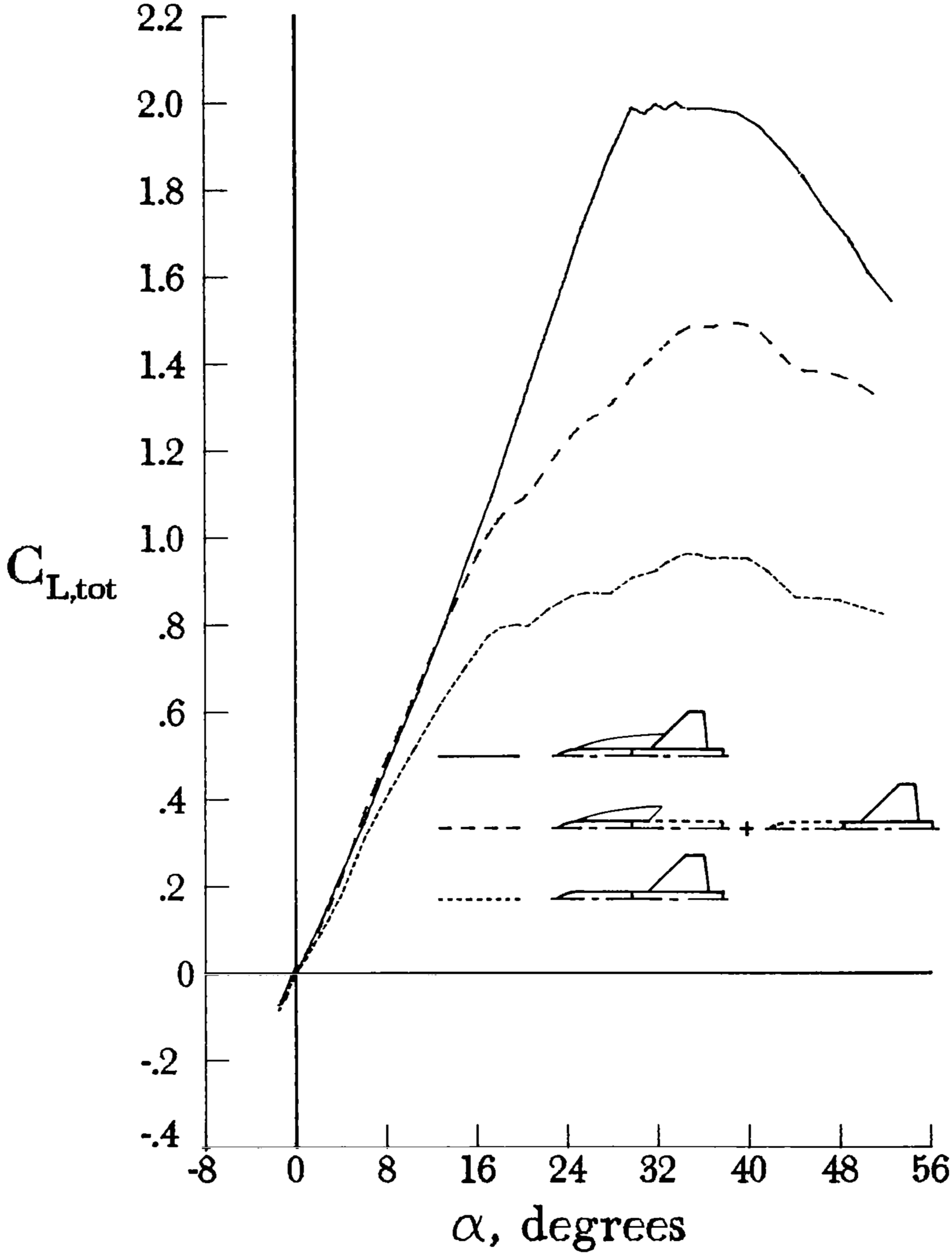

(g) AD 24.

Figure 13.- Continued.

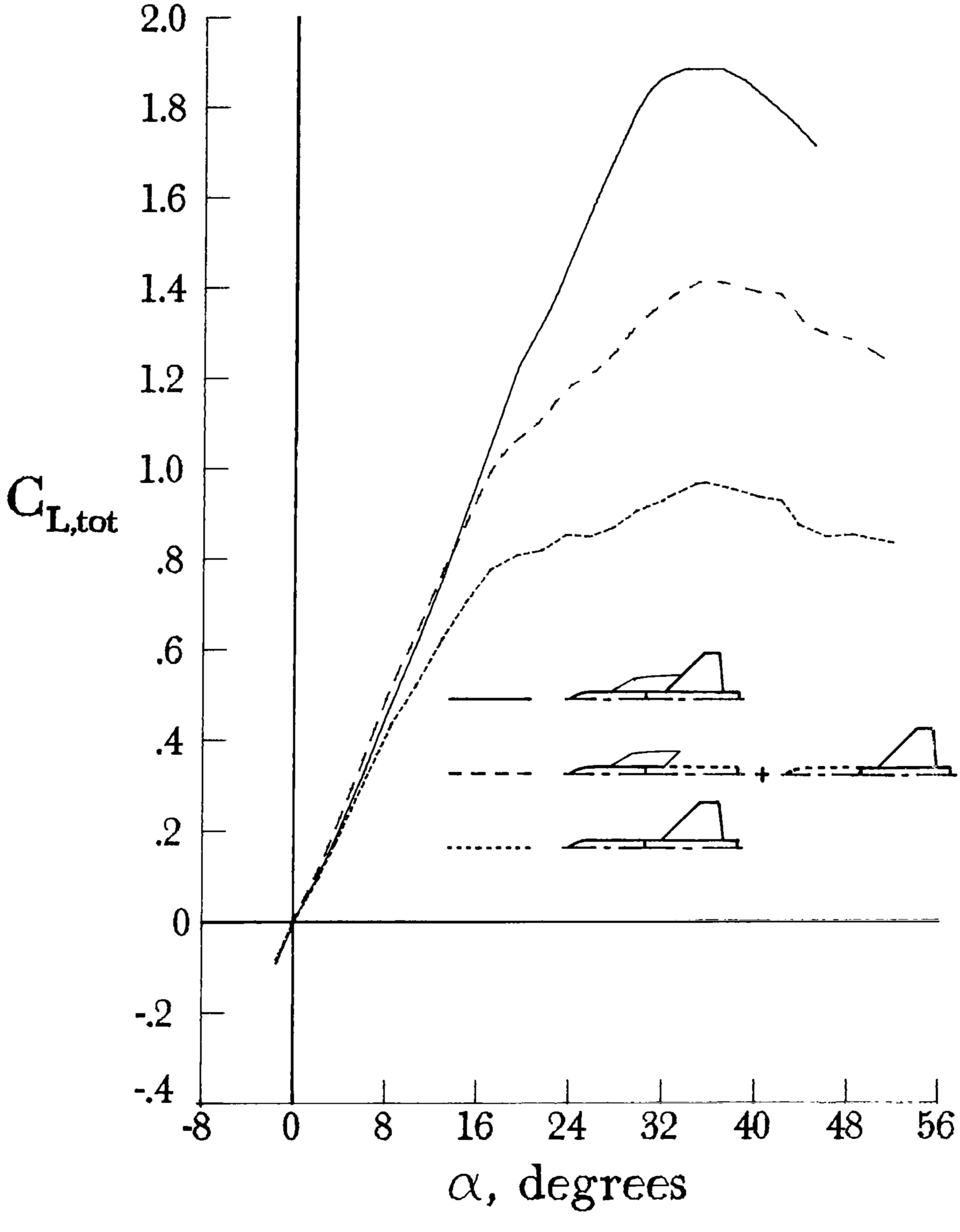

(h) ED 2.

Figure 13.- Continued.

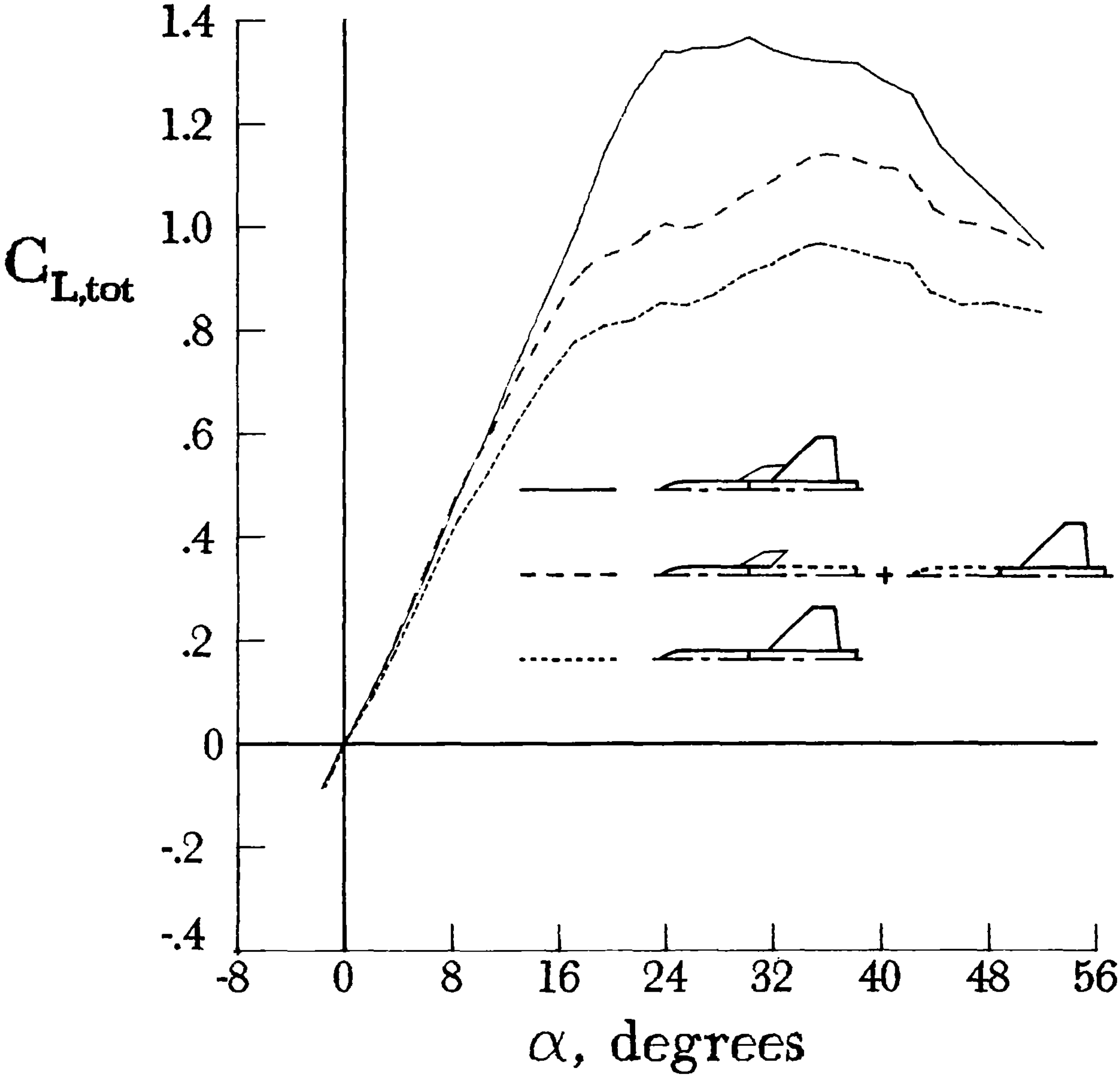

(i) ED 4.

Figure 13.- Continued.

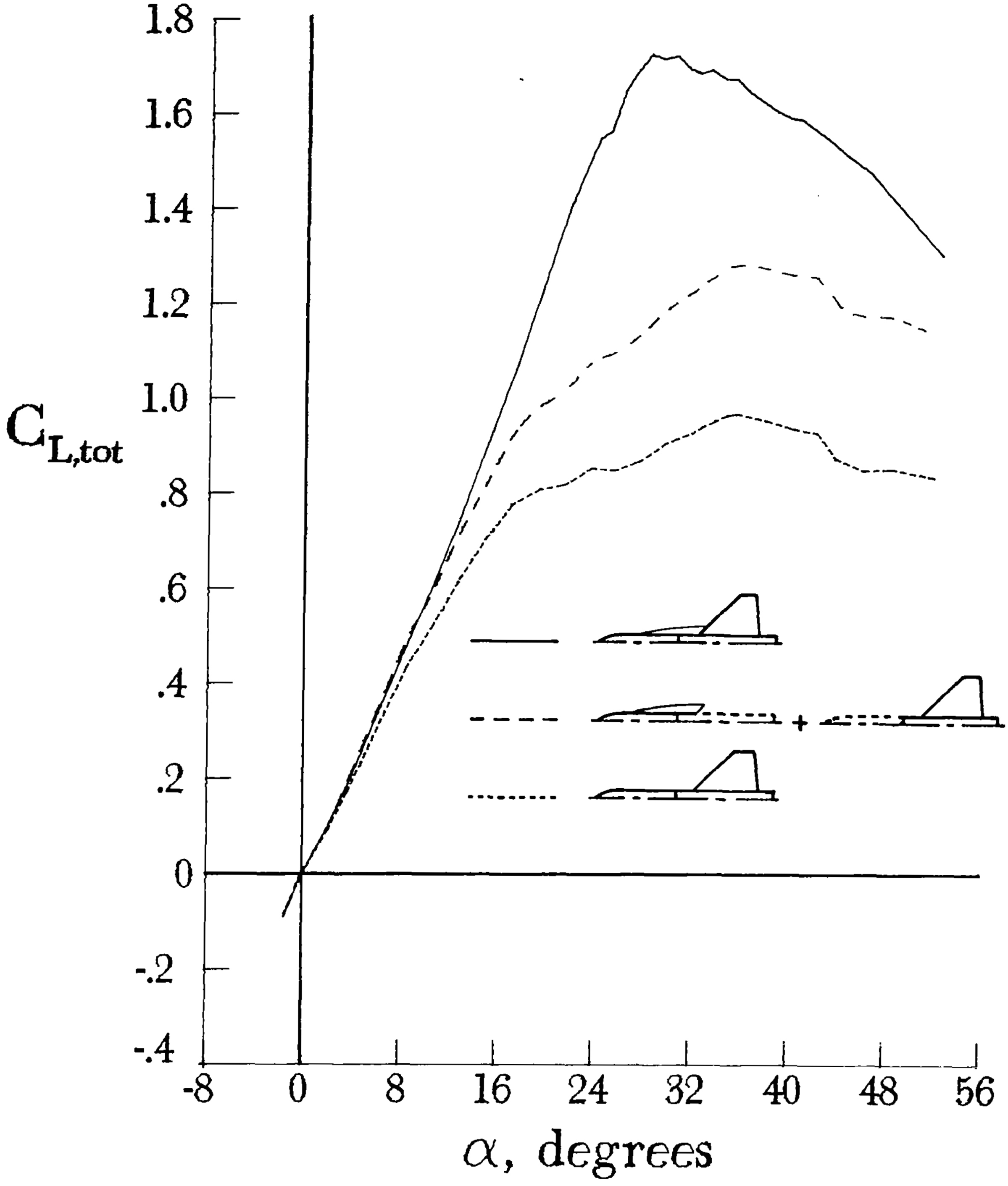

(j) ED 5.

Figure 13.- Continued.

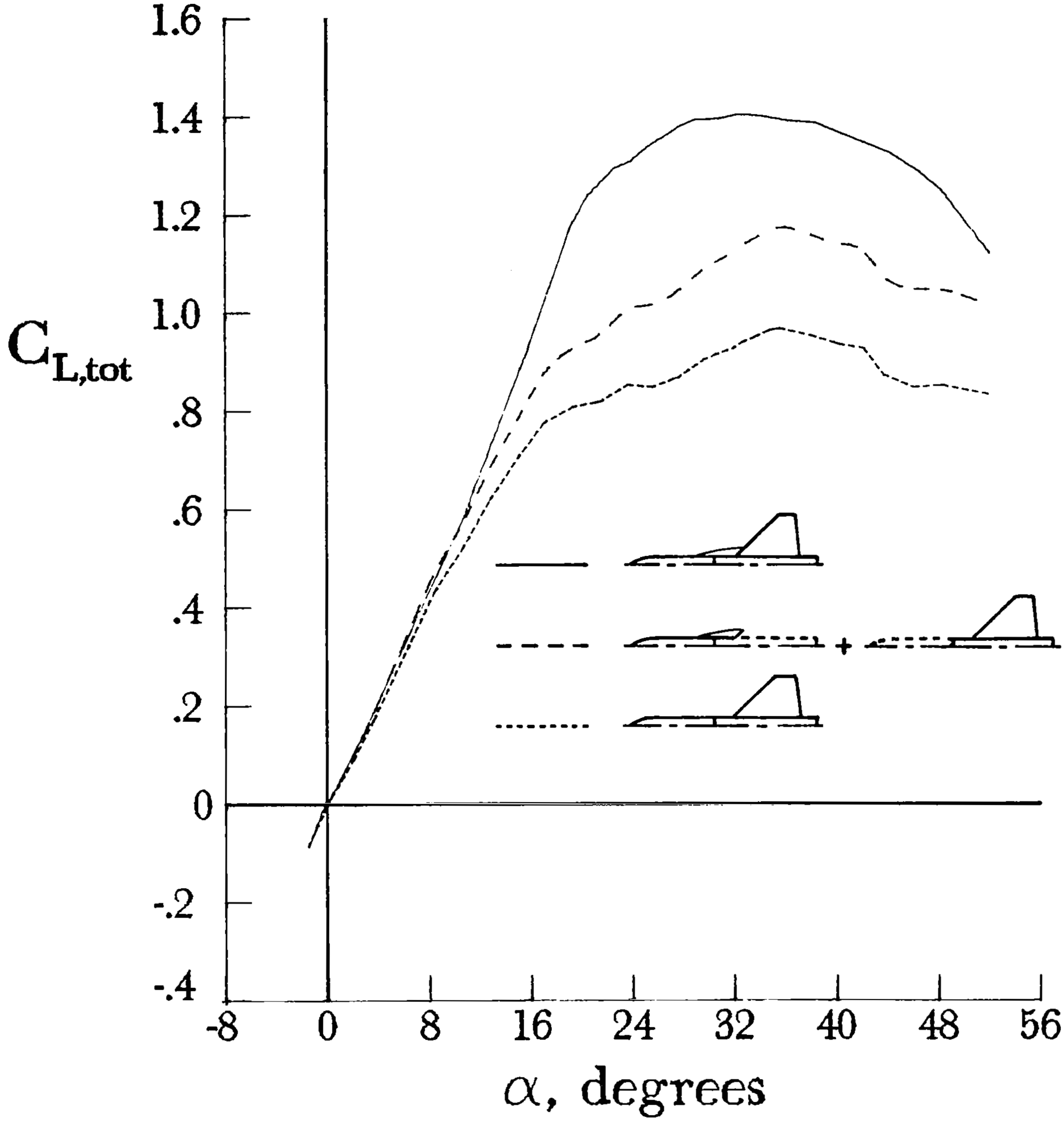

(k) ED 6.

Figure 13.- Continued.

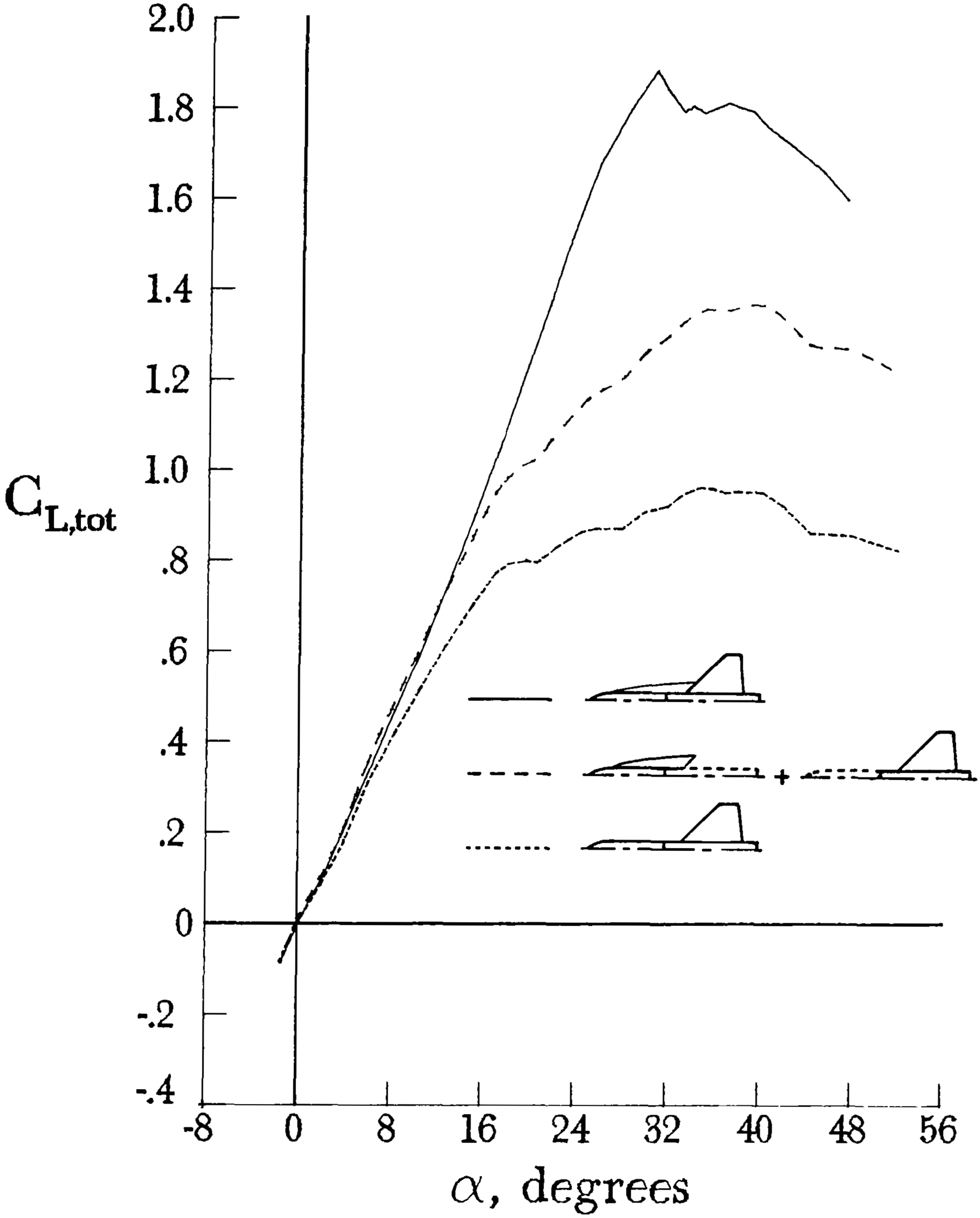

(l) ED 9.

Figure 13.- Continued.

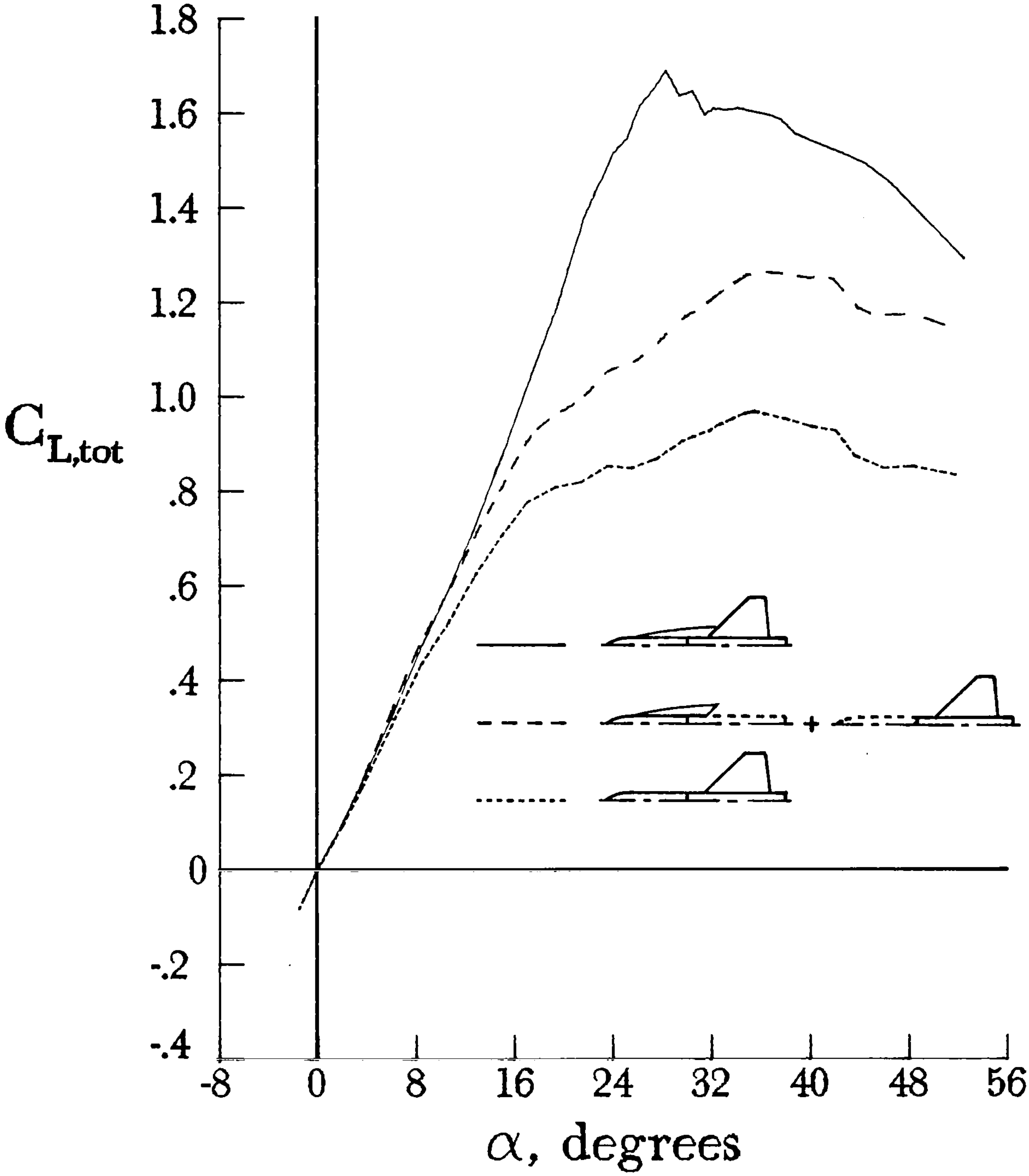

(m) ED 10.

Figure 13.- Continued.

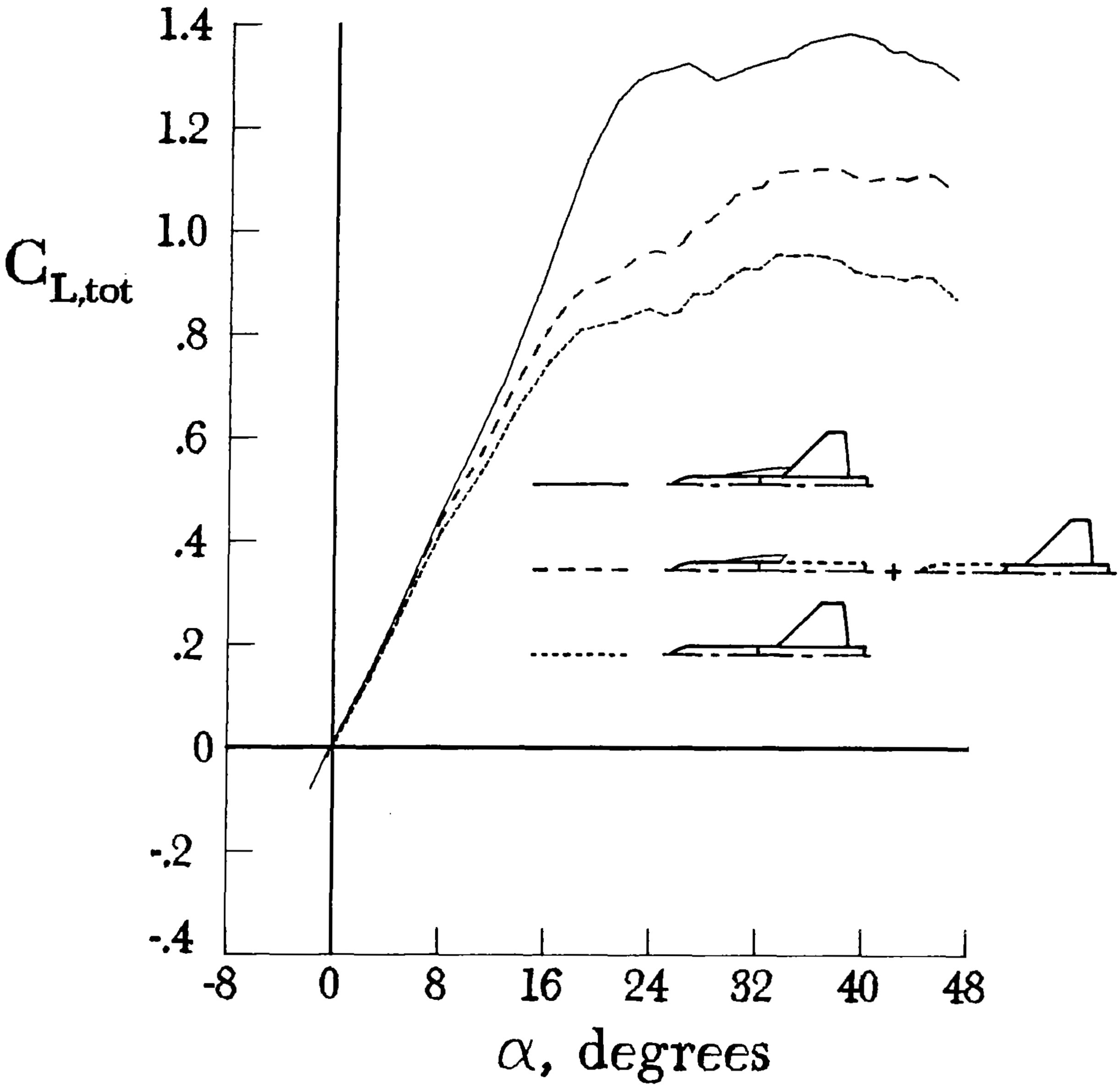

(n) ED 11.

Figure 13.- Continued.

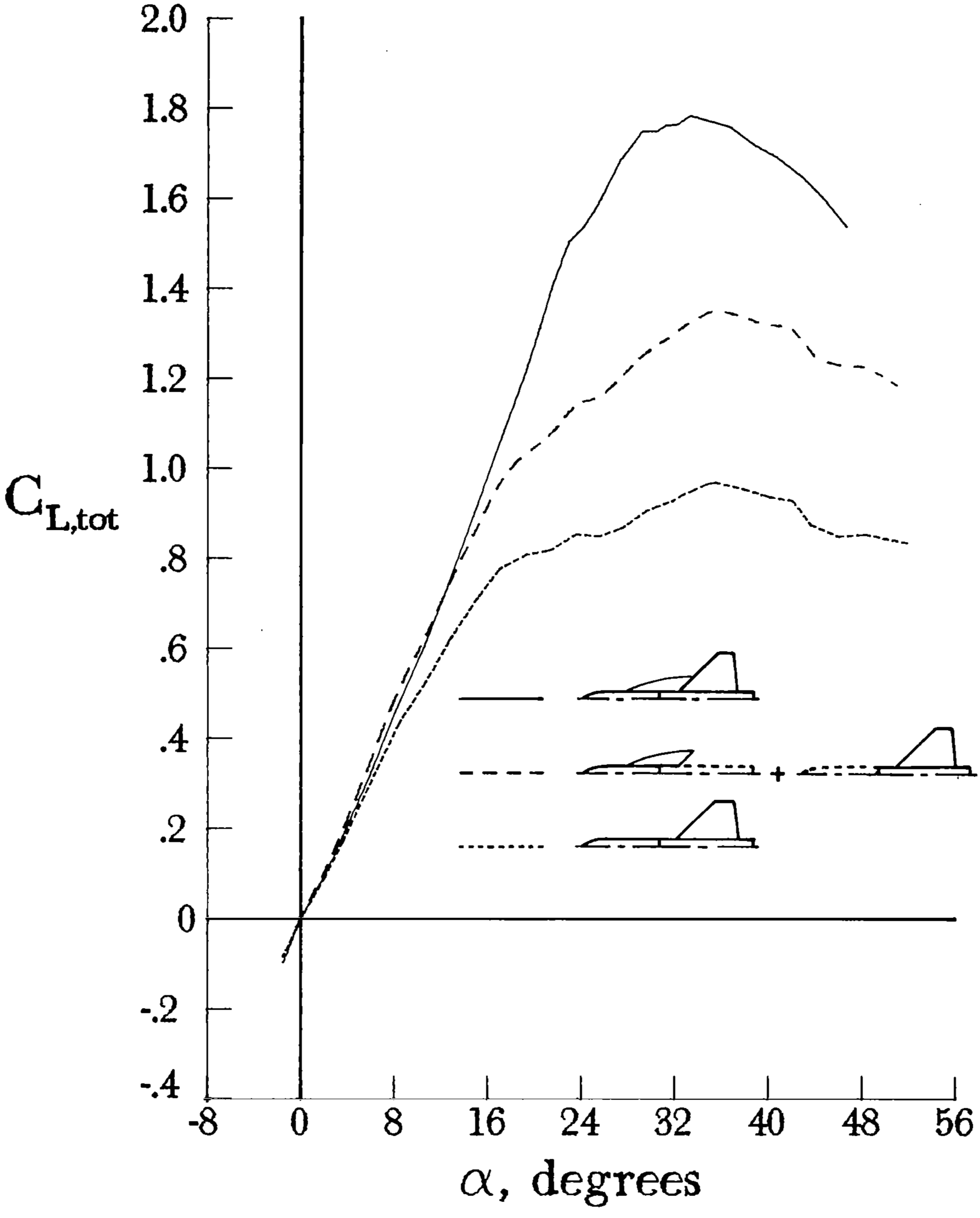

(o) ED 12.

Figure 13.- Continued.

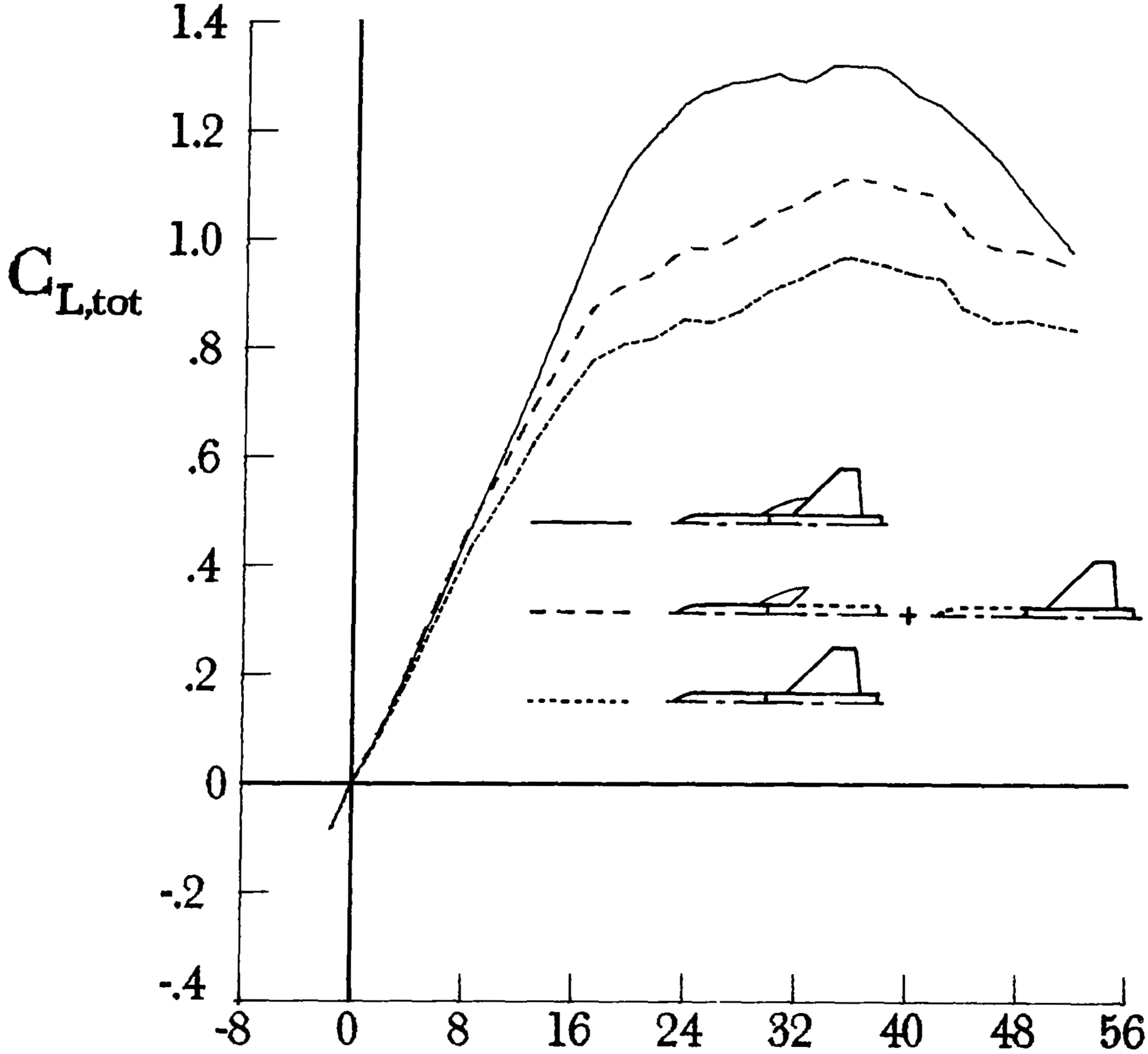

(p) ED 13.

Figure 13.- Concluded.

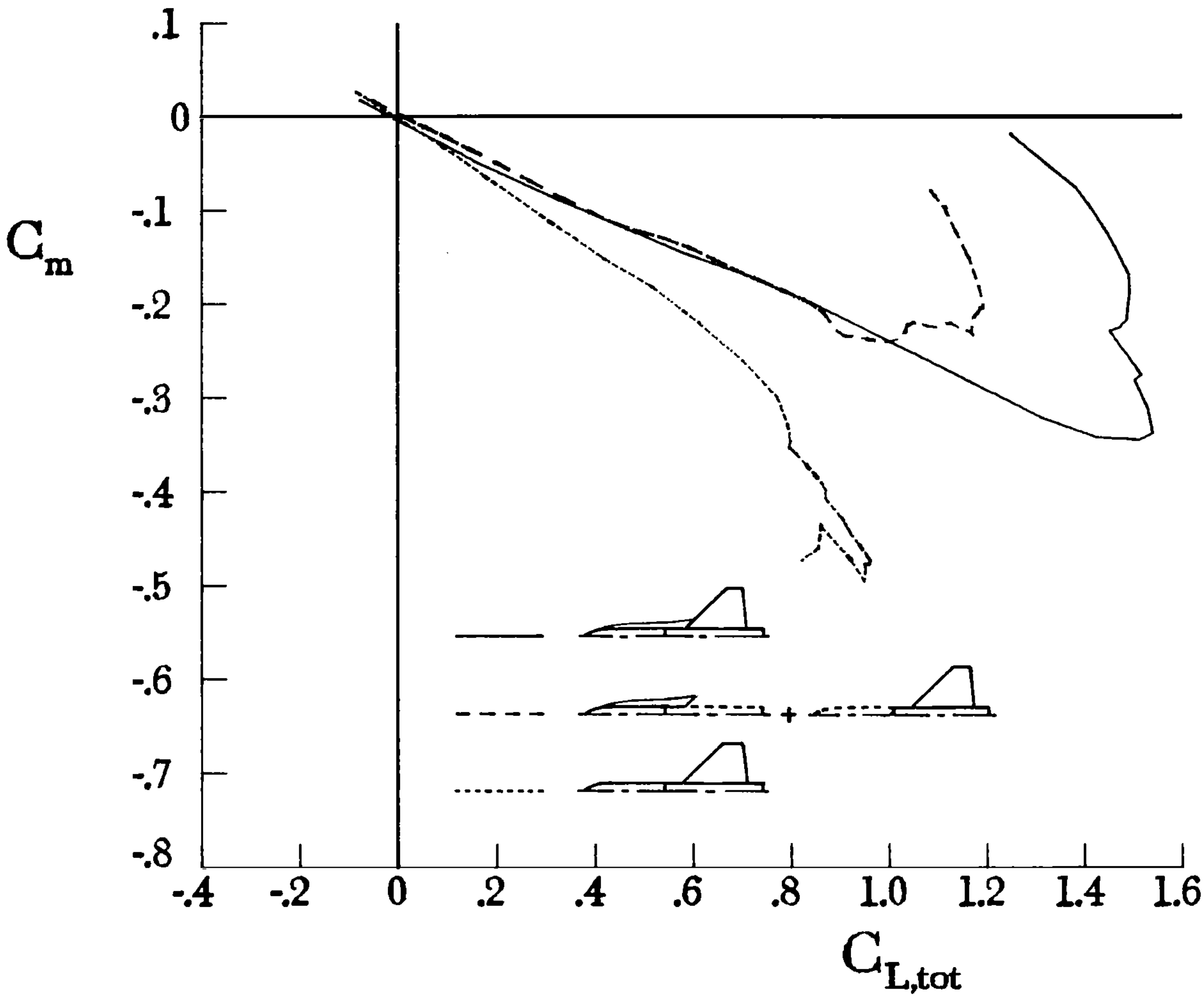

(a) AD 9.

Figure 14.- Aerodynamic synergistic effect on configuration pitching moment at M = 0.2.

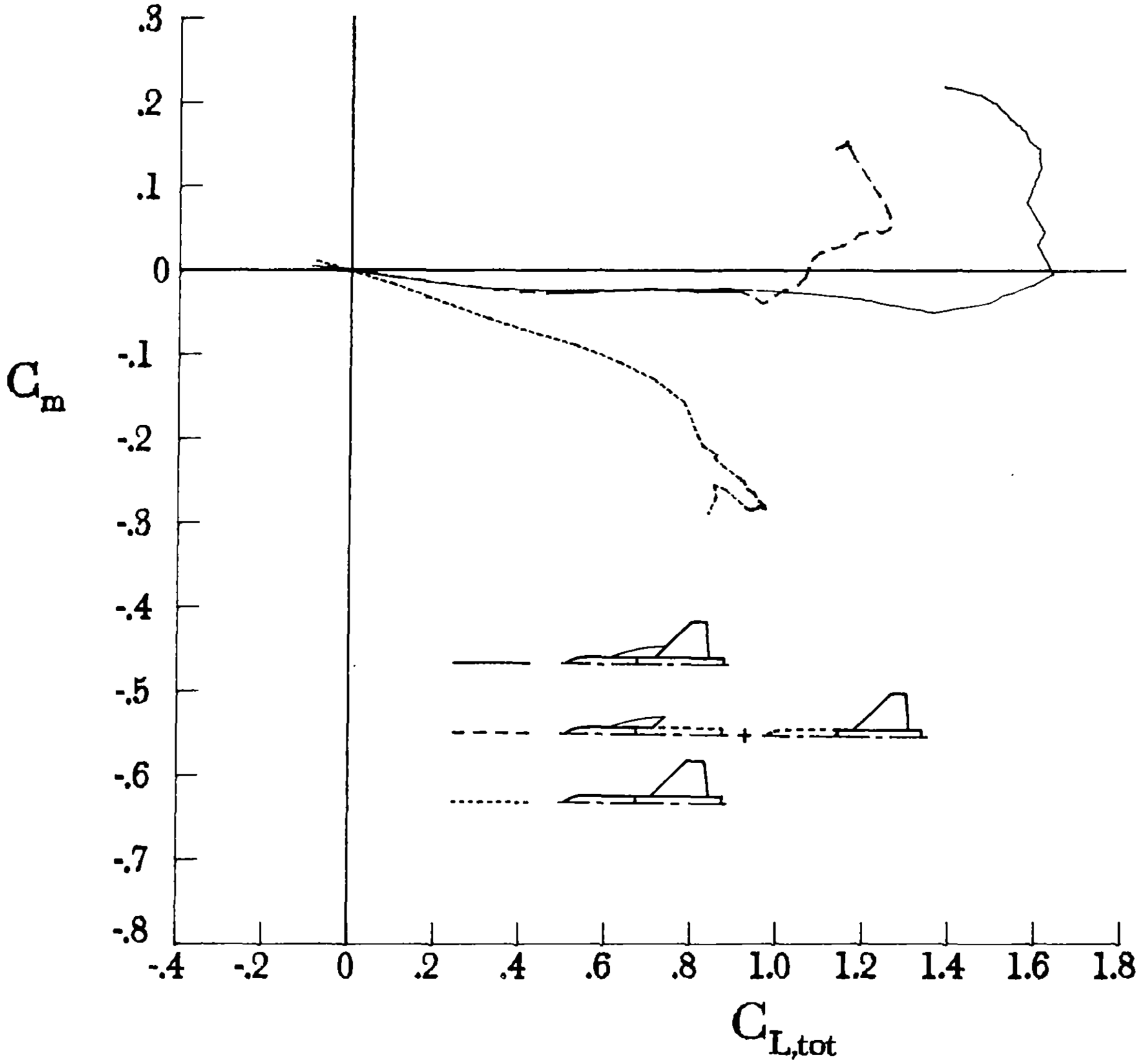

(b) AD 14.

Figure 14.- Continued.

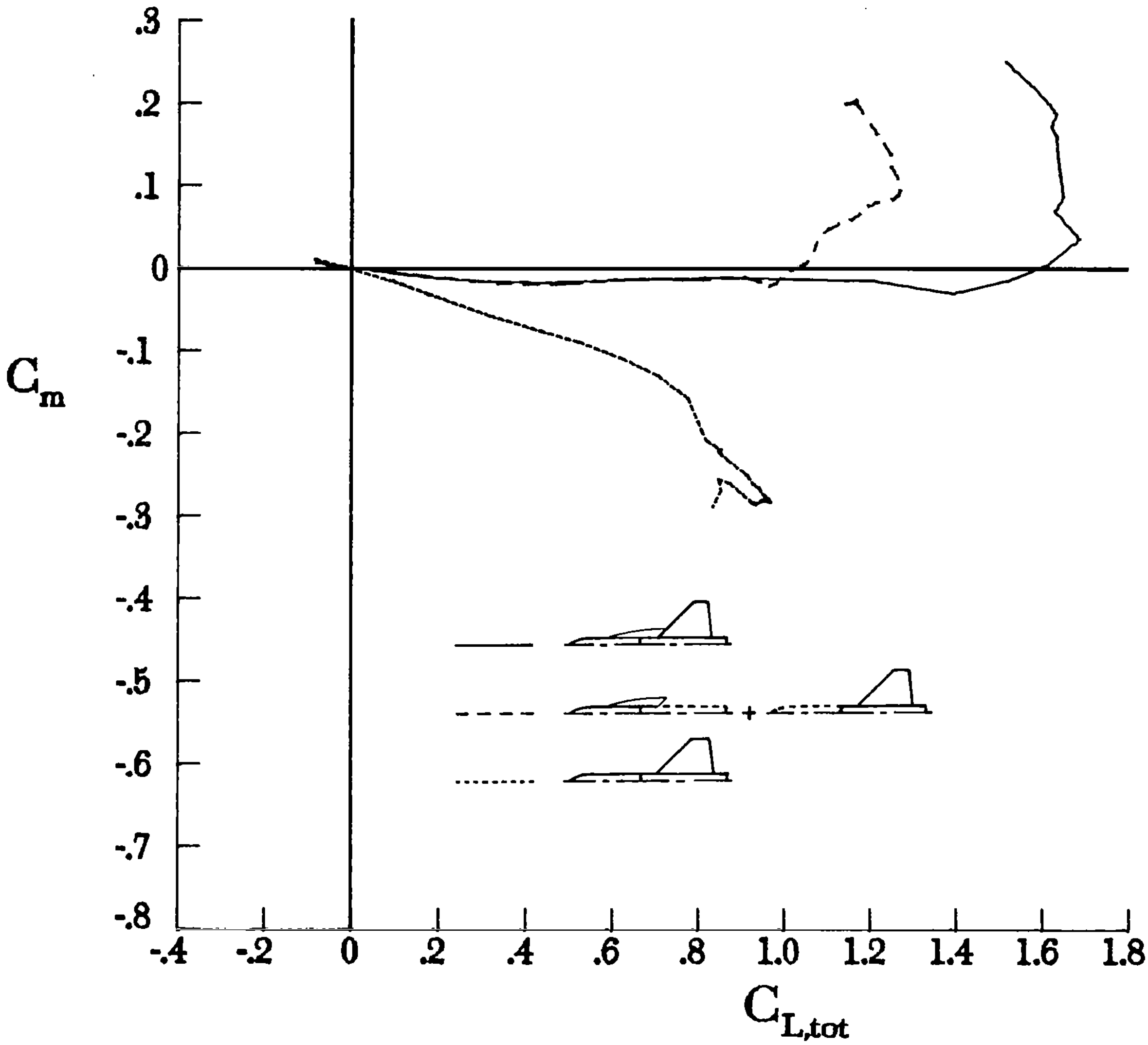

(c) AD 17.

Figure 14.- Continued.

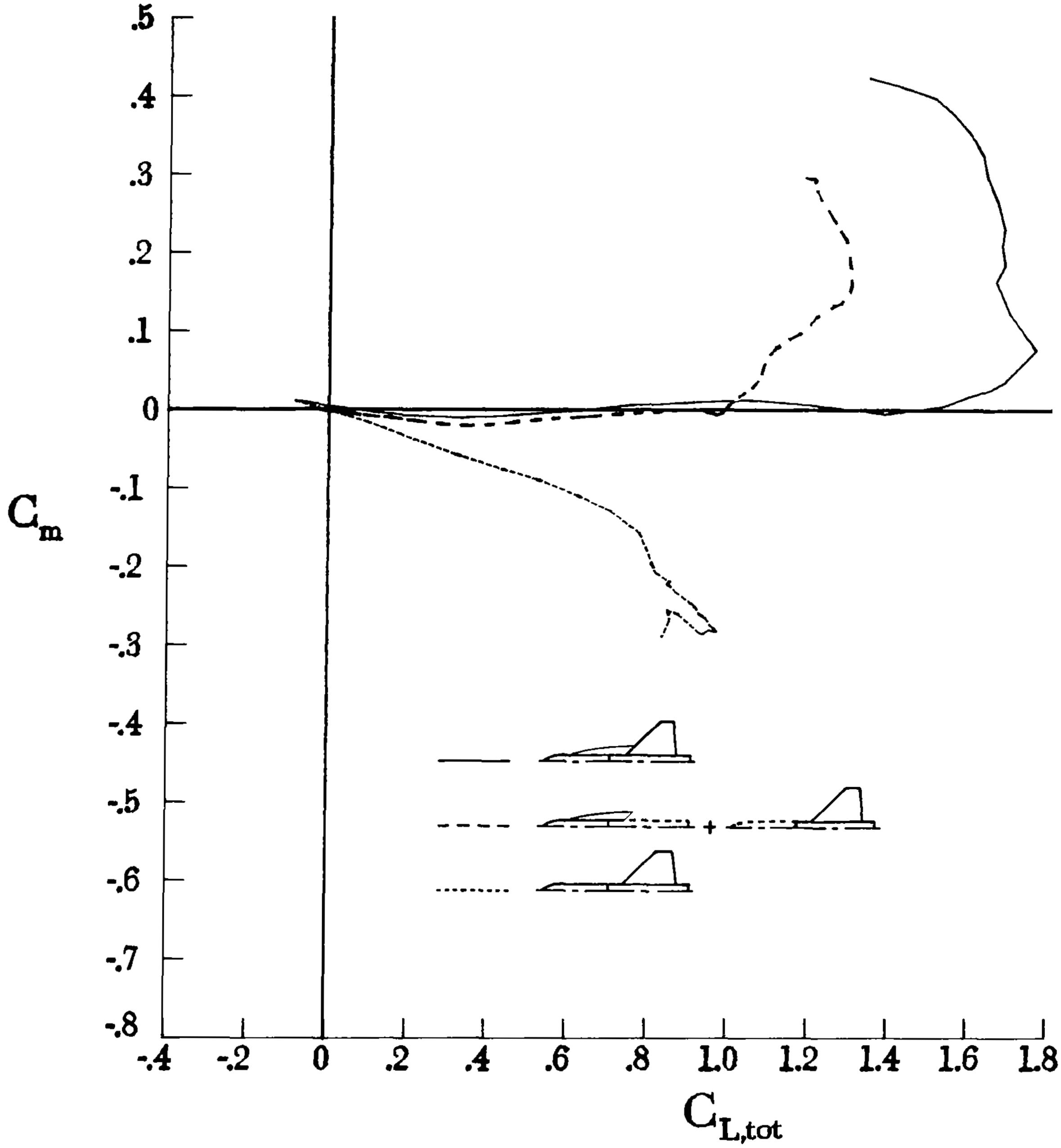

(d) AD 19.

Figure 14.- Continued.

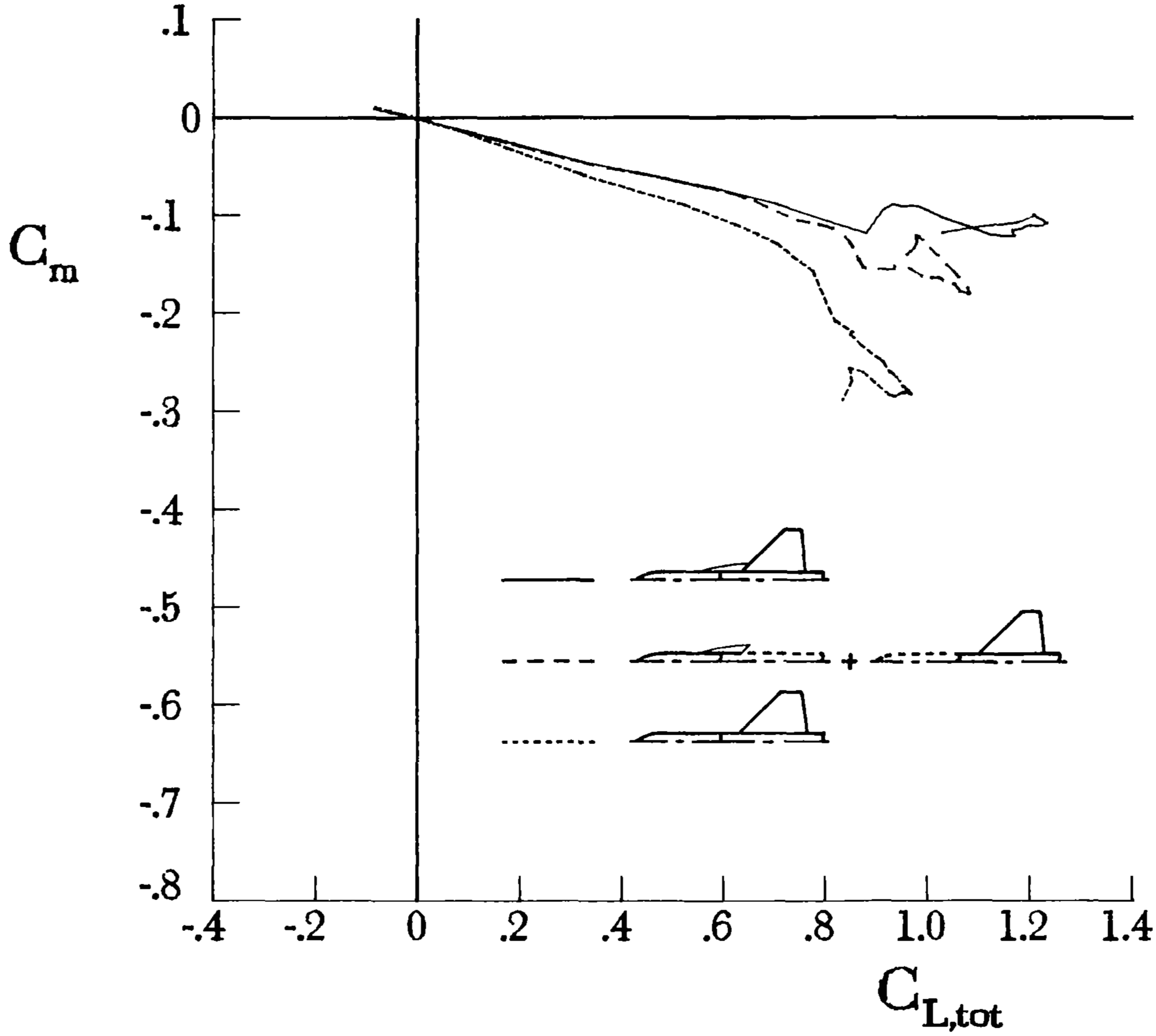

(e) AD 22.

Figure 14.- Continued.

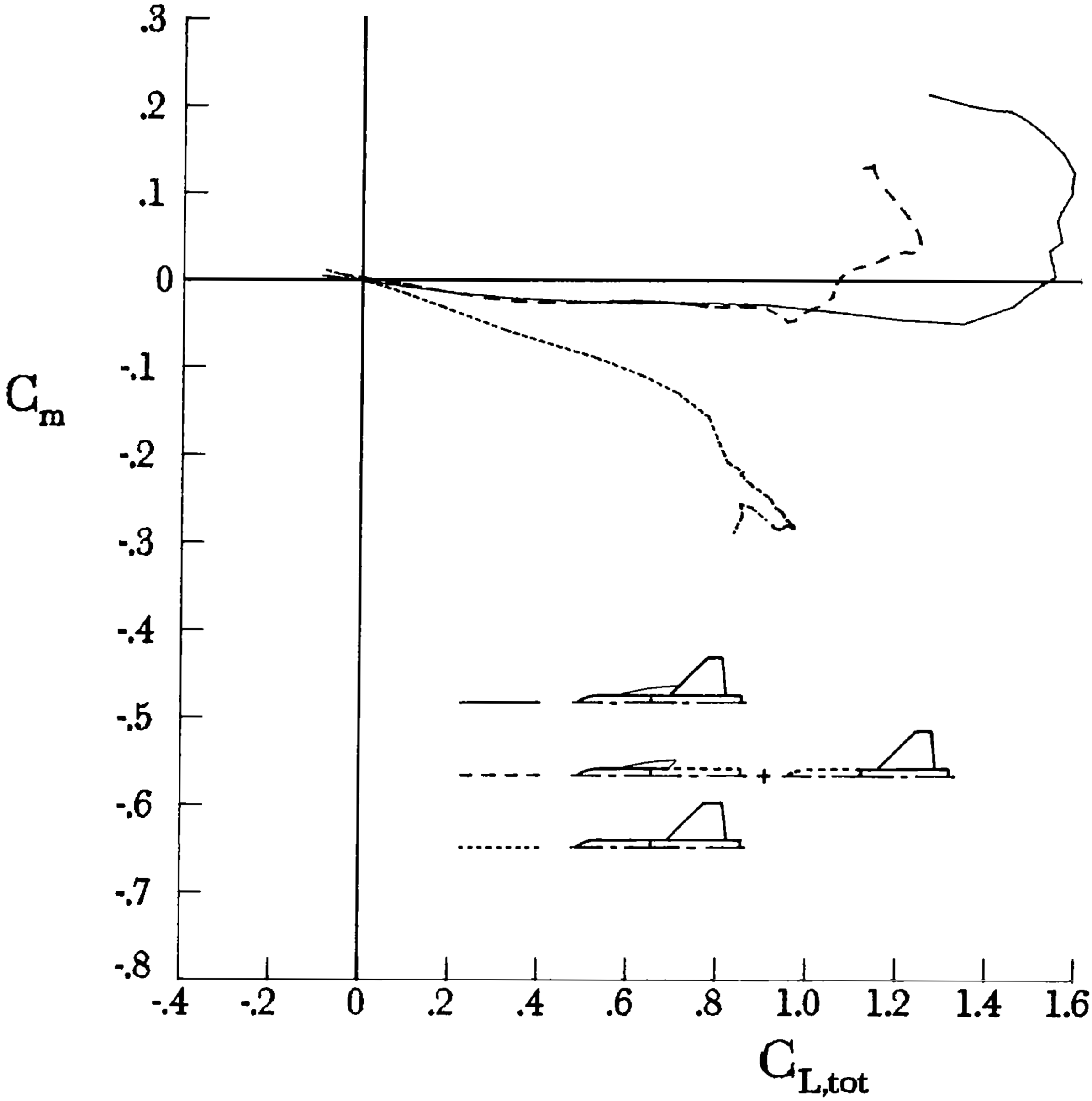

(f) AD 23.

Figure 14.- Continued.

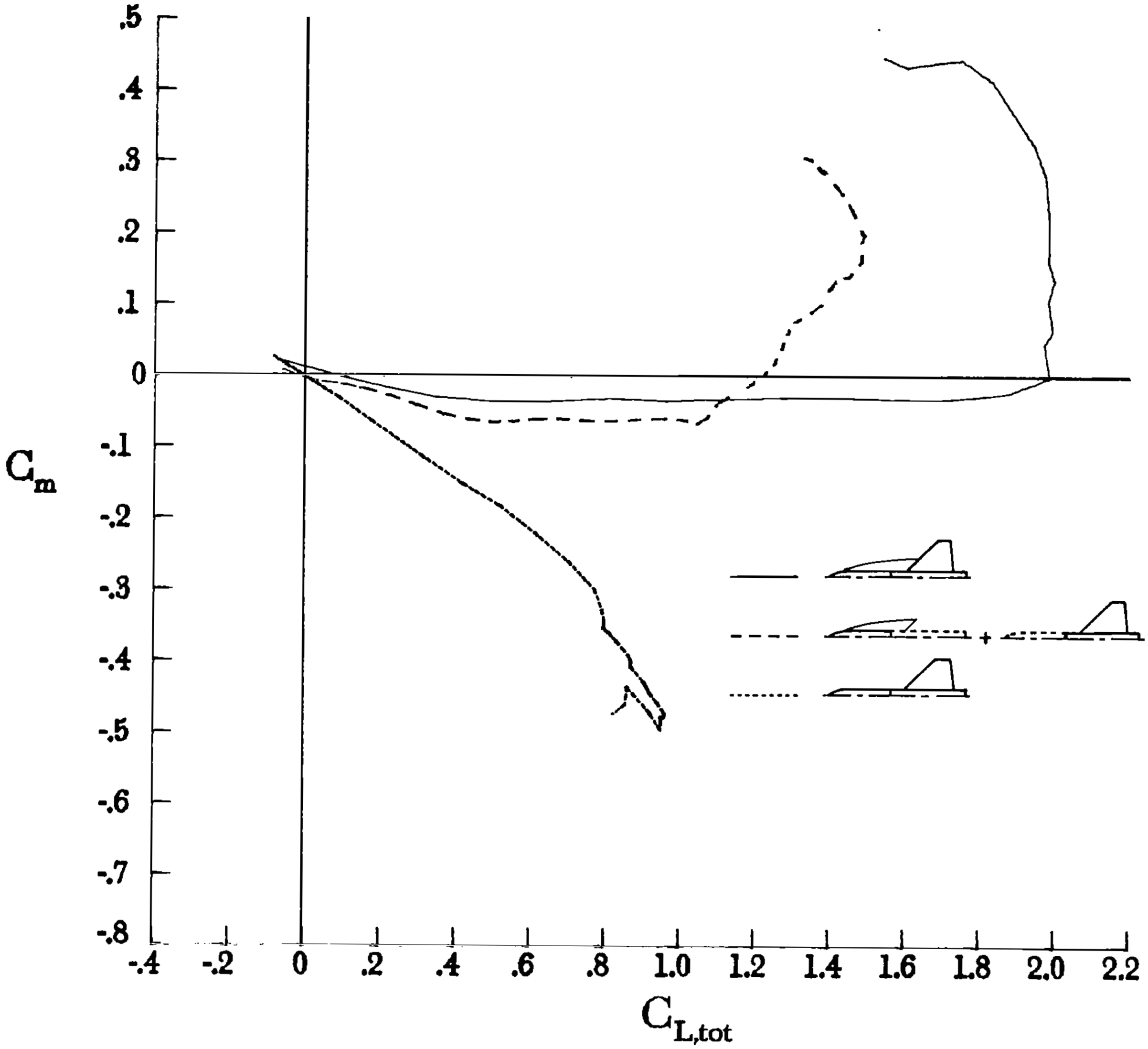

(g) AD 24.

Figure 14.- Continued.

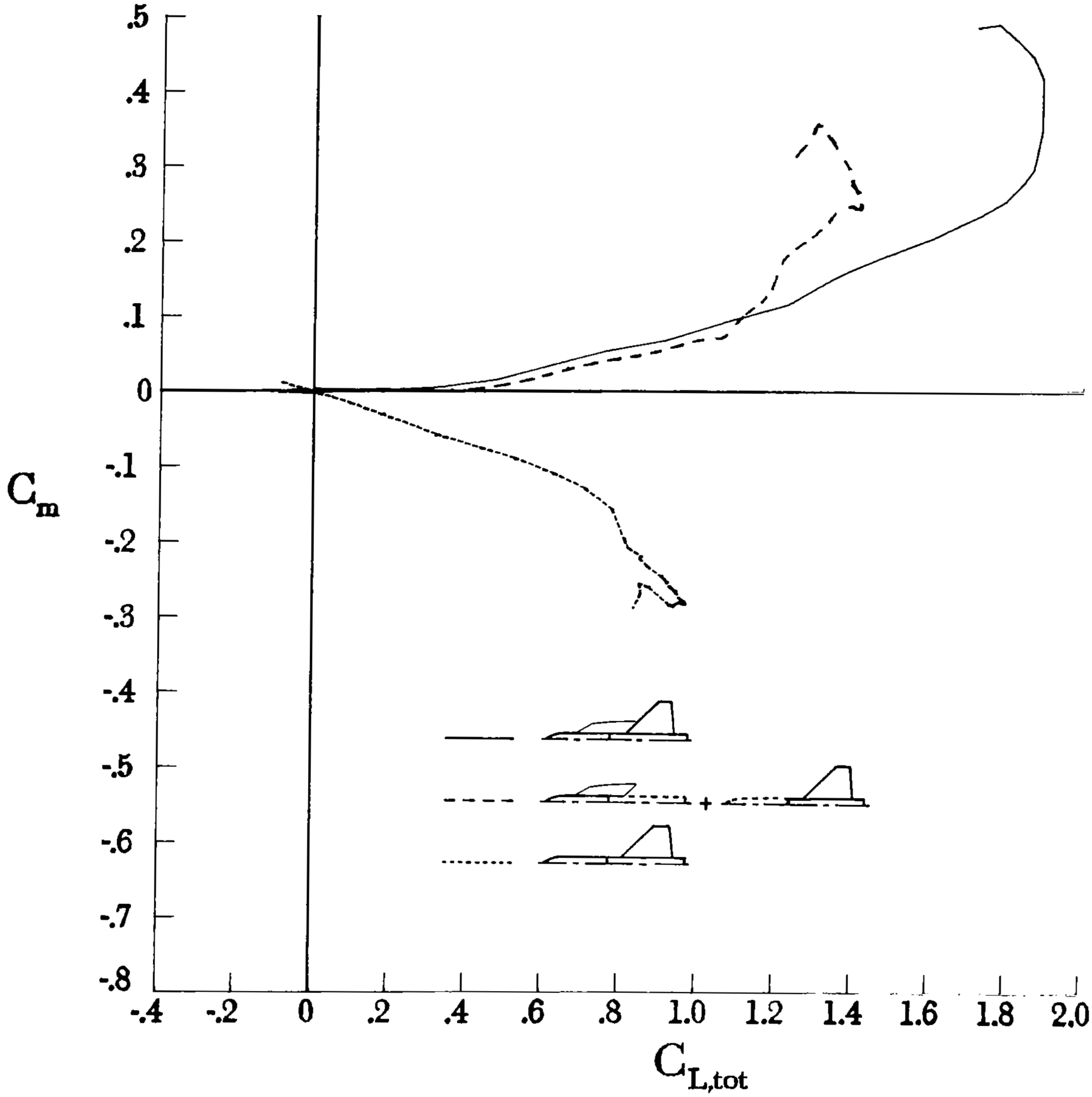

(h) ED 2.

Figure 14.- Continued.

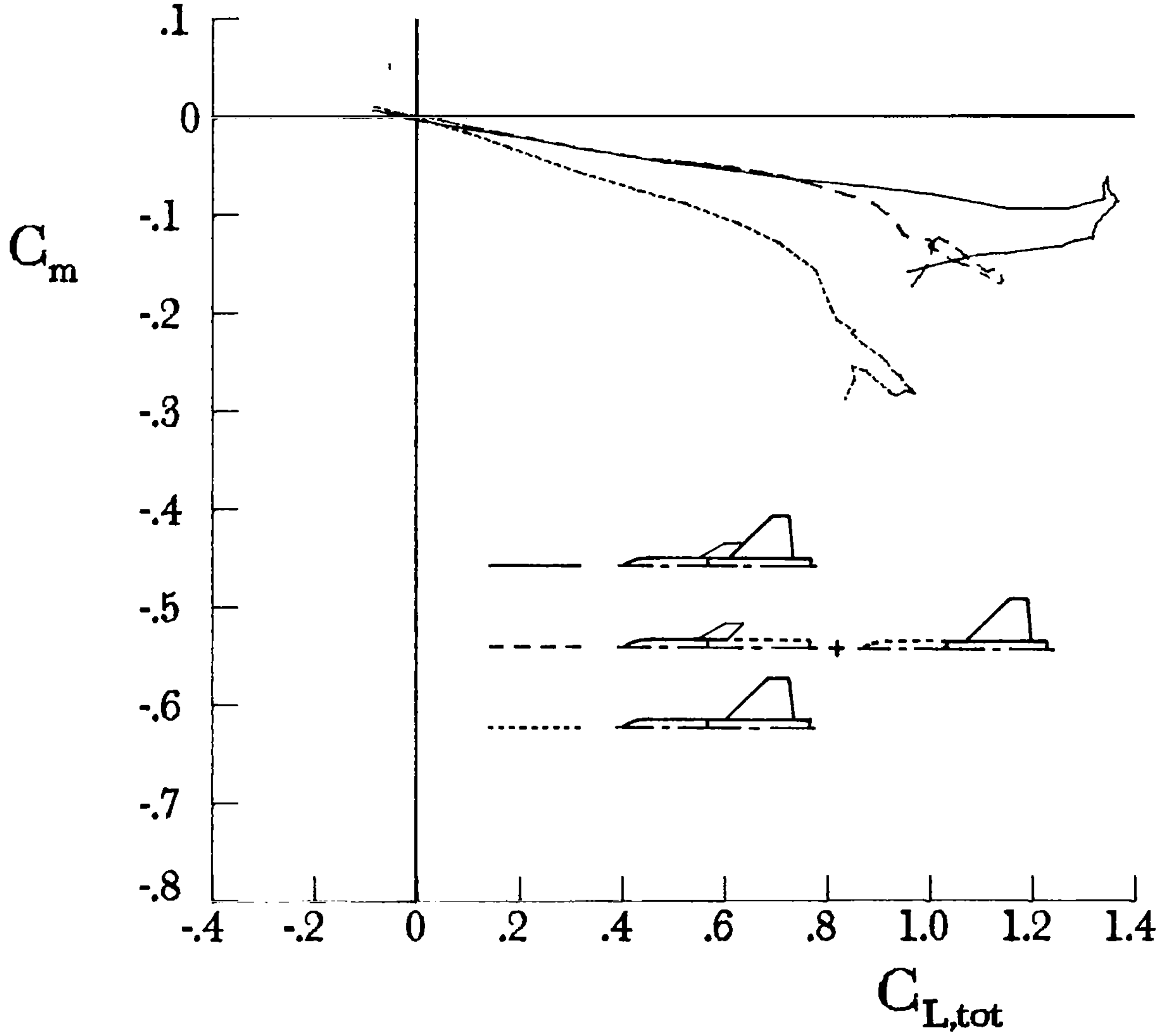

(i) ED 4.

Figure 14.- Continued.

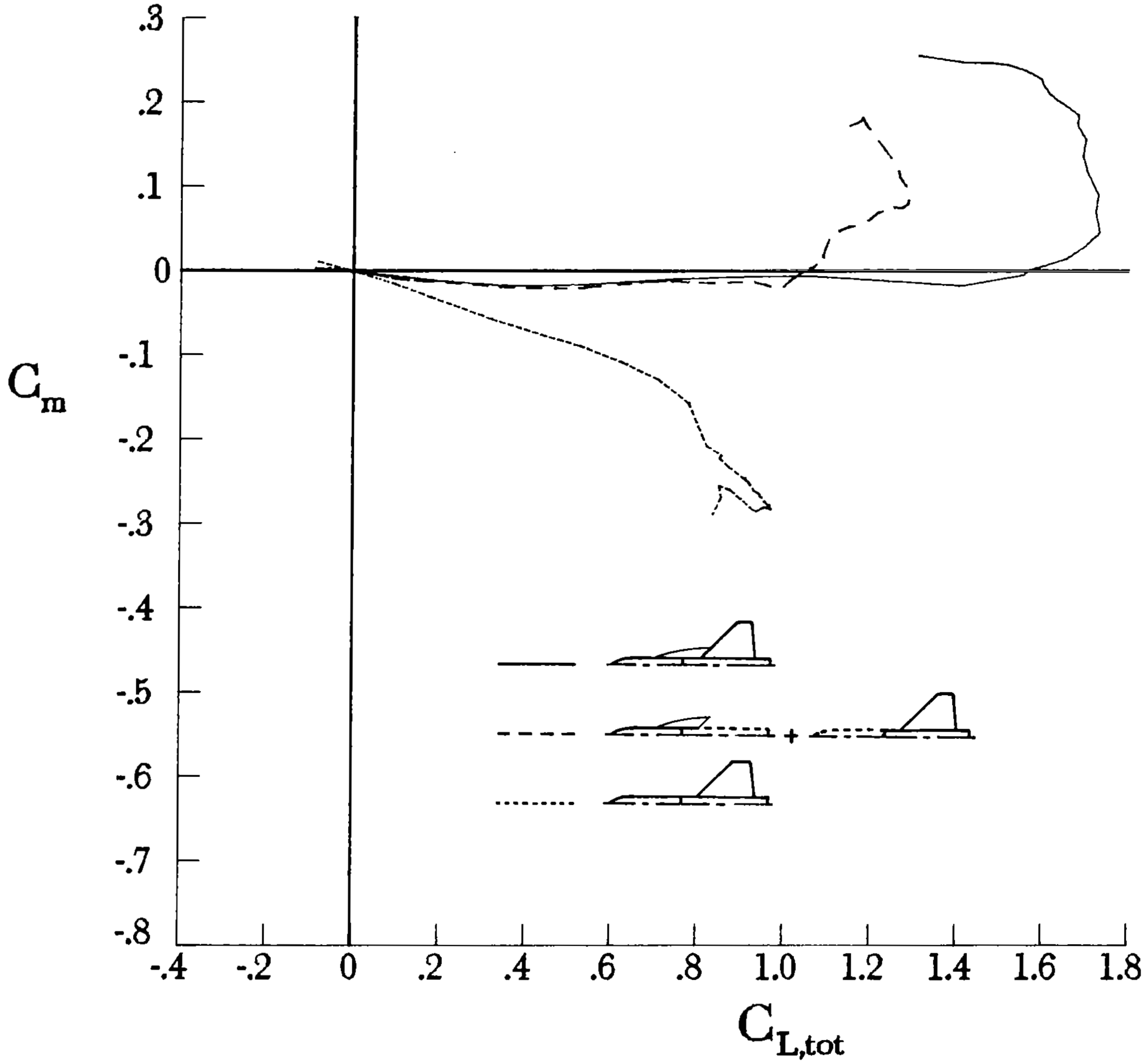

(j) ED 5.

Figure 14.- Continued.

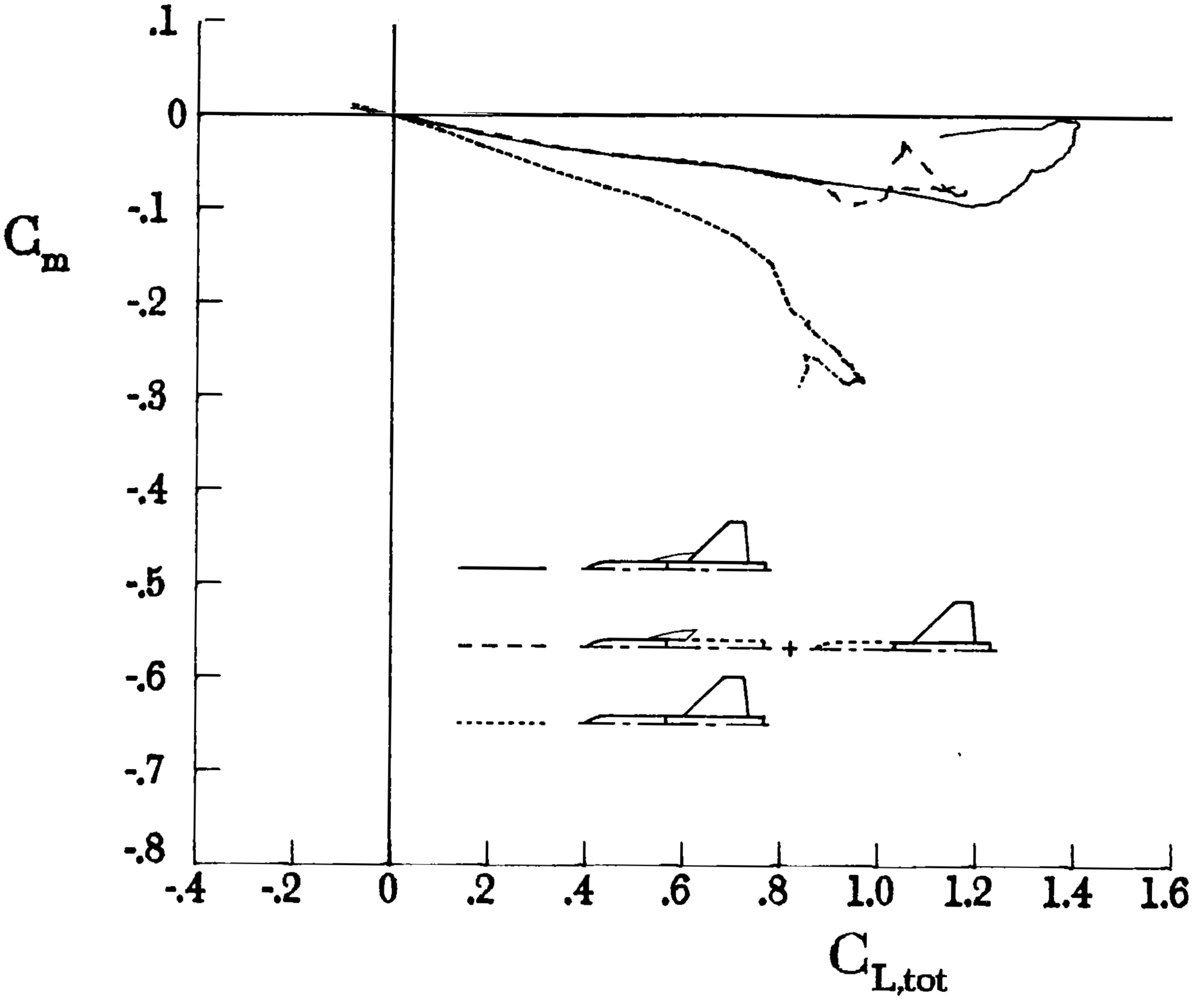

(k) ED 6.

Figure 14.- Continued.

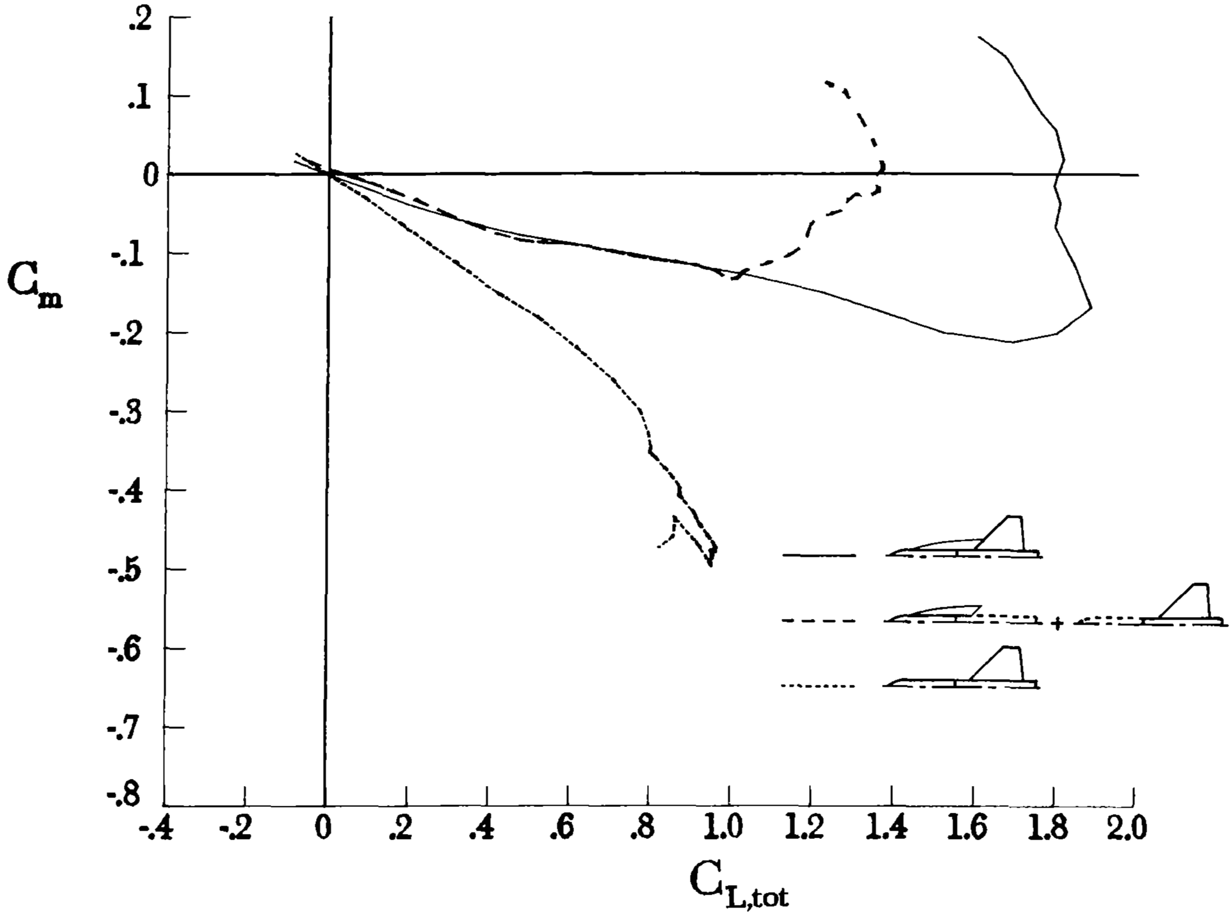

(l) ED 9.

Figure 14.- Continued.

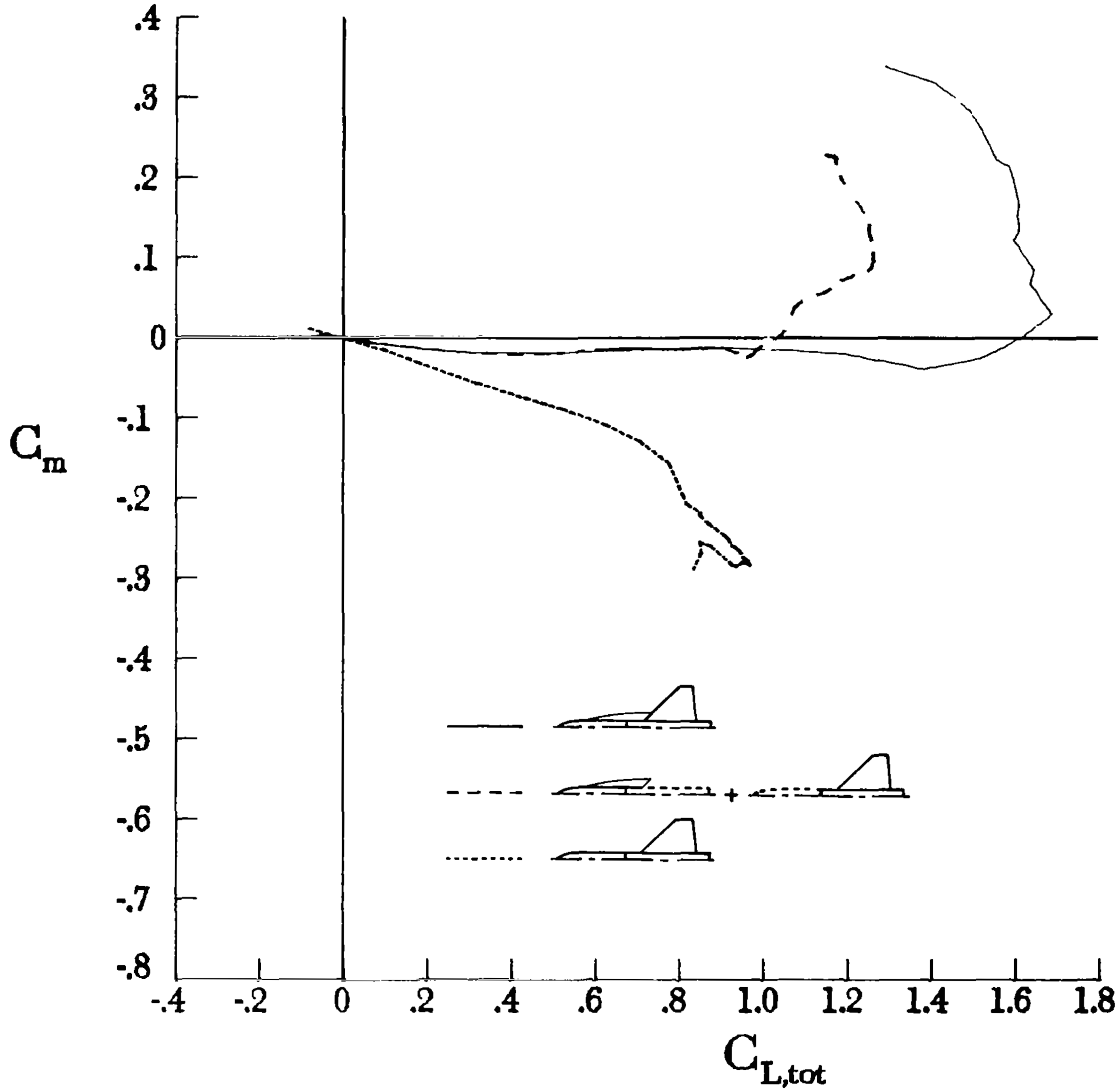

(m) ED 10.

Figure 14.- Continued.

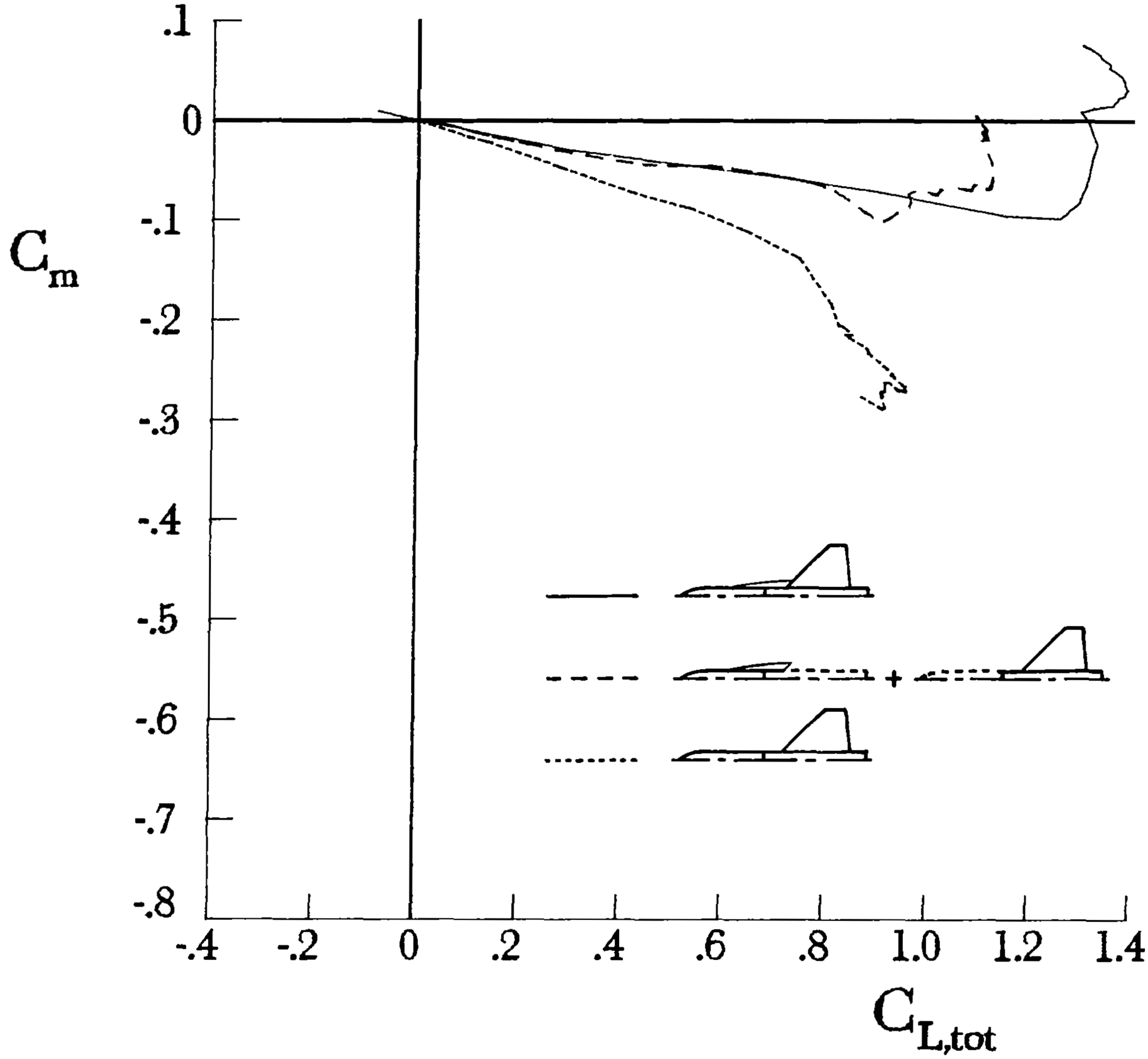

(n) ED 11.

Figure 14.- Continued.

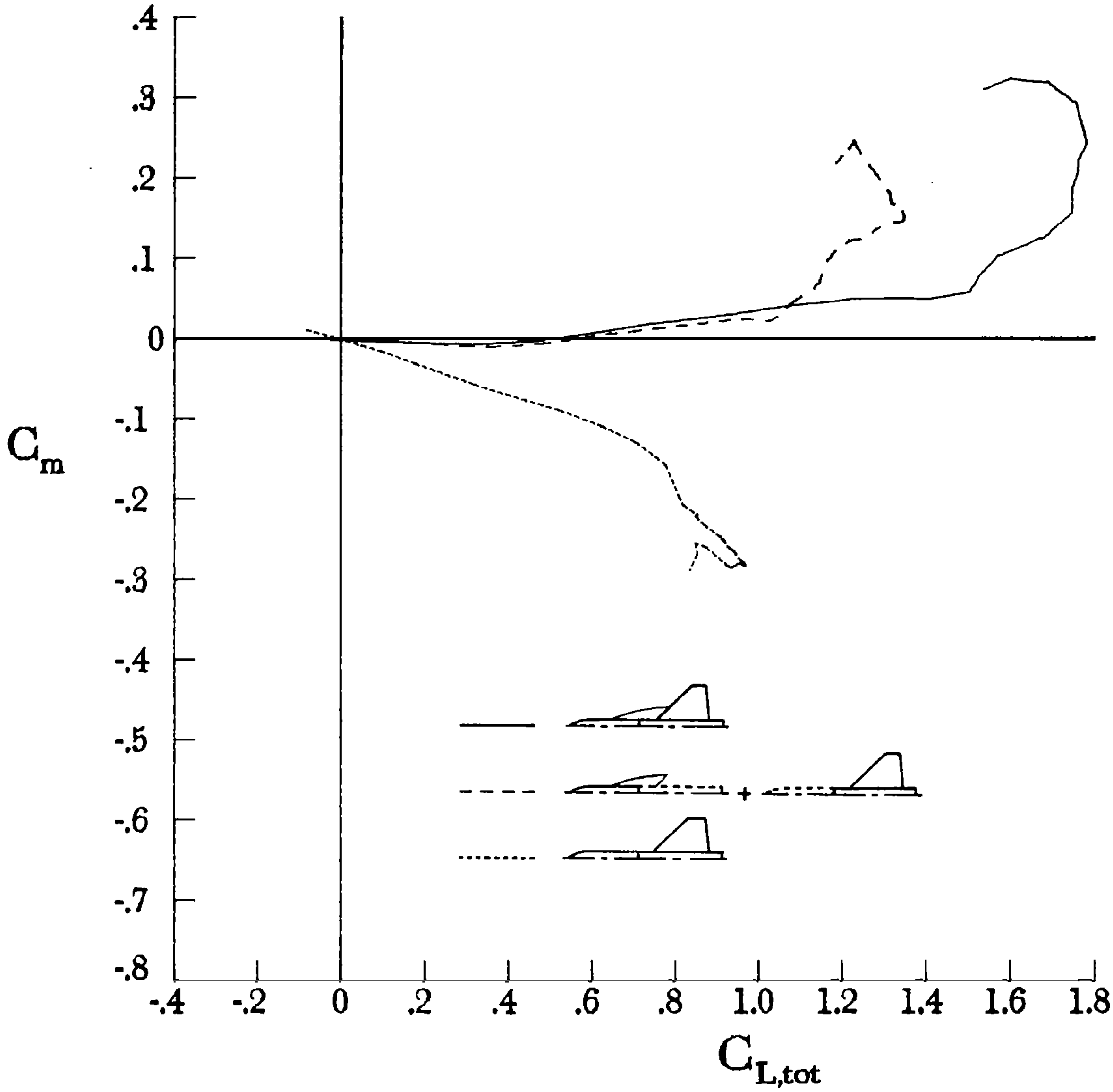

(o) ED 12.

Figure 14.- Continued.

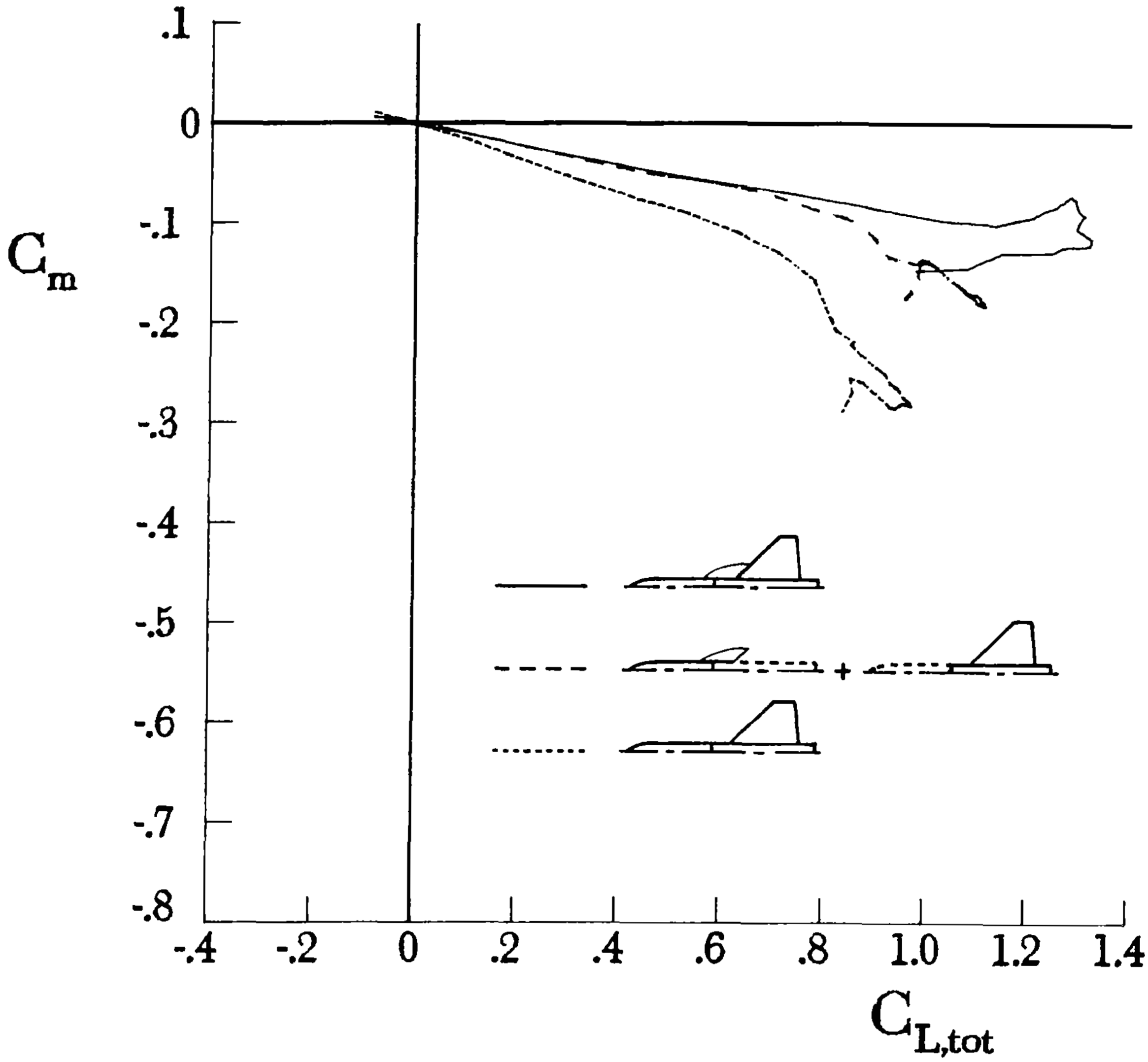

(p) ED 13.

Figure 14.- Concluded.

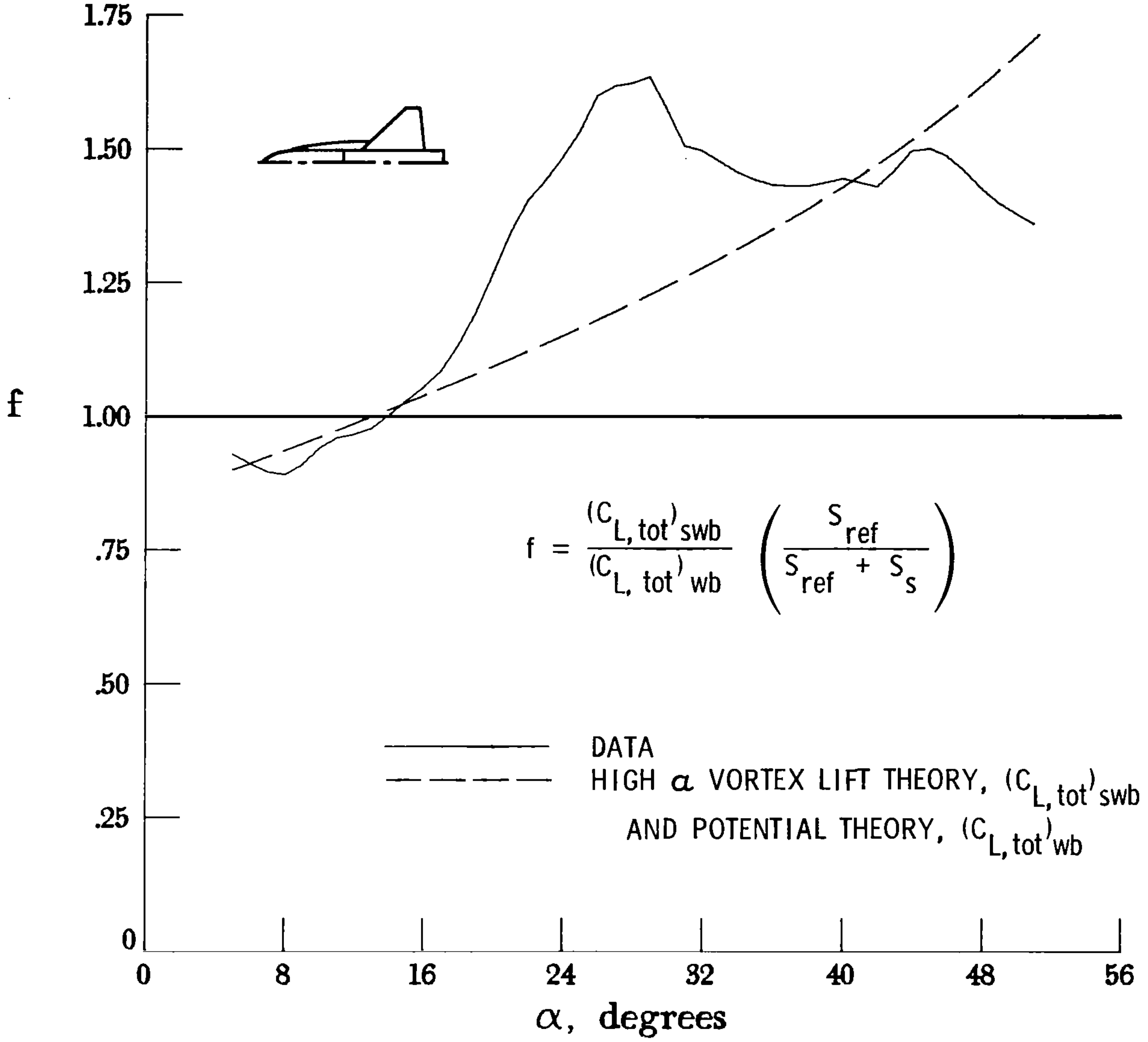

Figure 15.- Theoretical and experimental variation of f with α for AD 19 at M = 0.2.

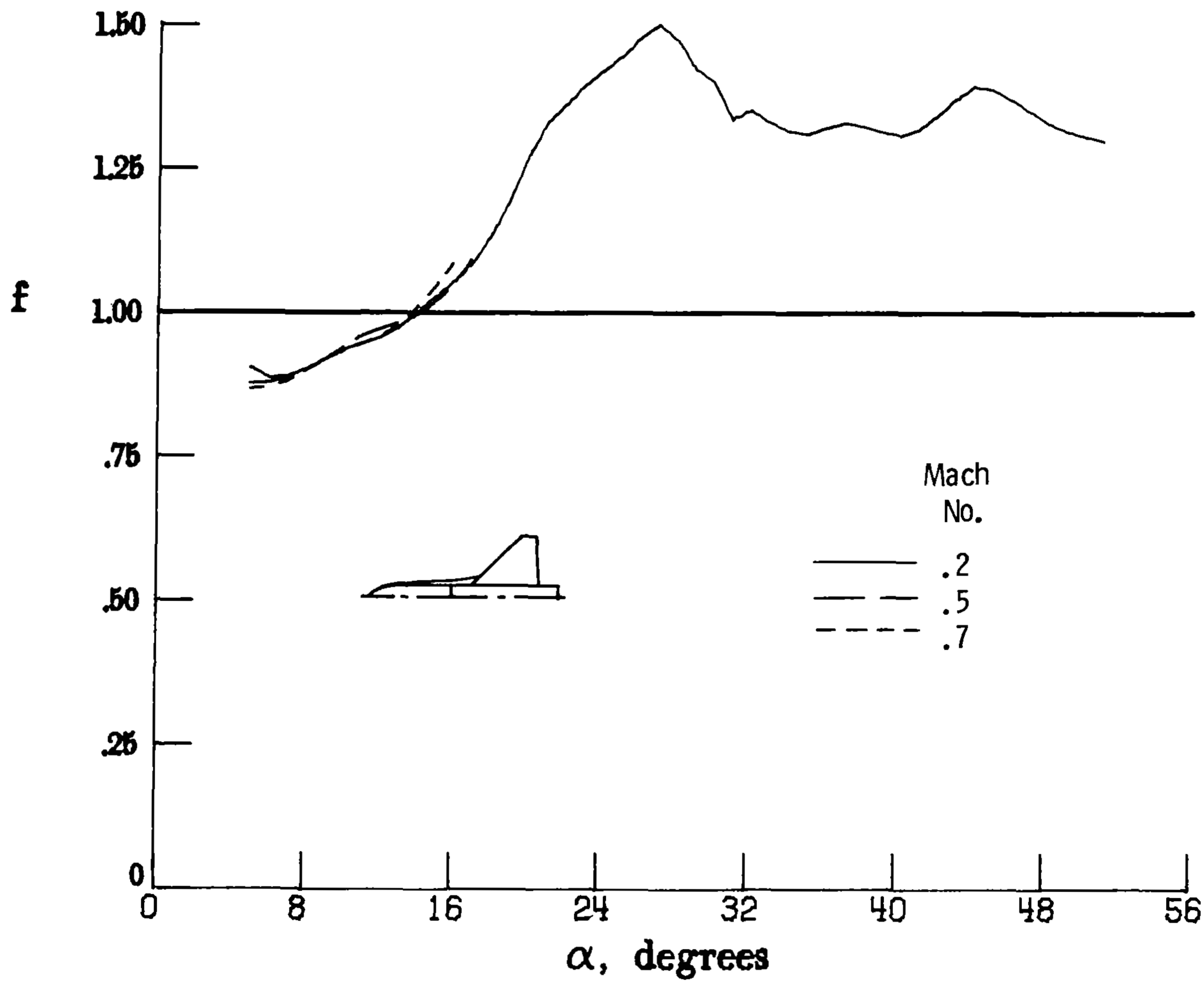

(a) AD 9.

Figure 16.- Effect of Mach number on additional lifting surface efficiency factor f.

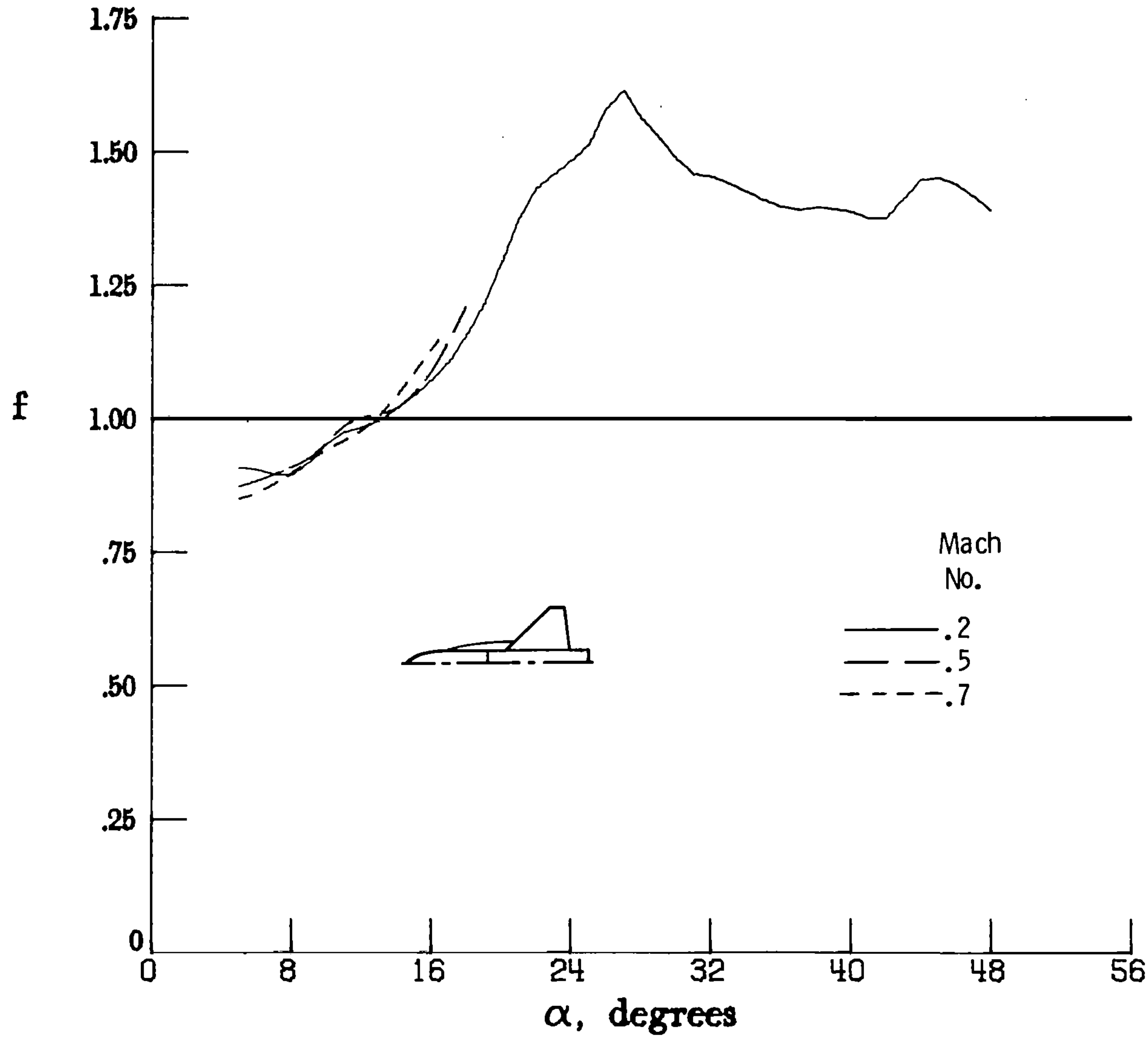

(b) AD 14.

Figure 16.- Continued.

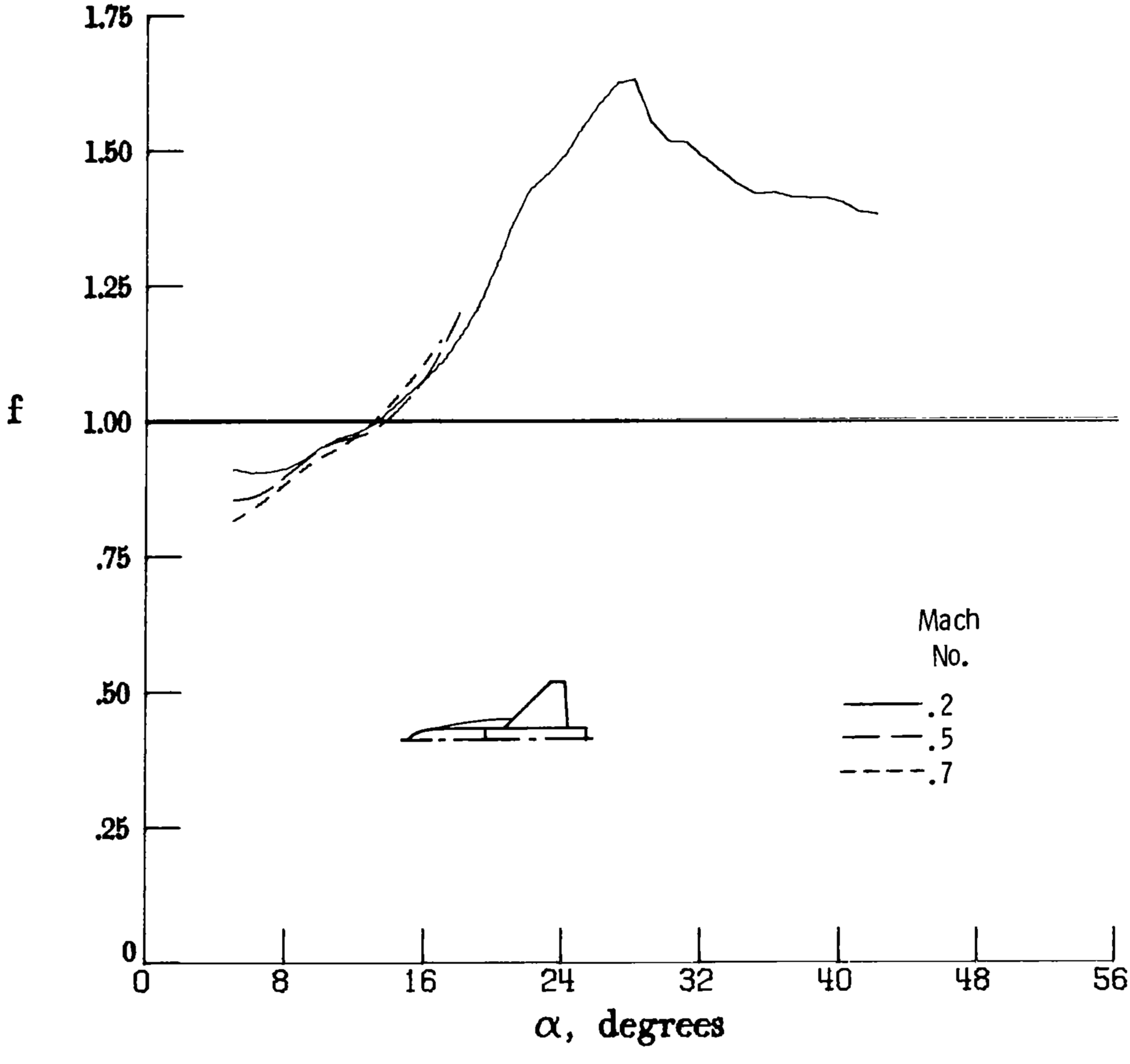

(c) AD 17.

Figure 16.- Continued.

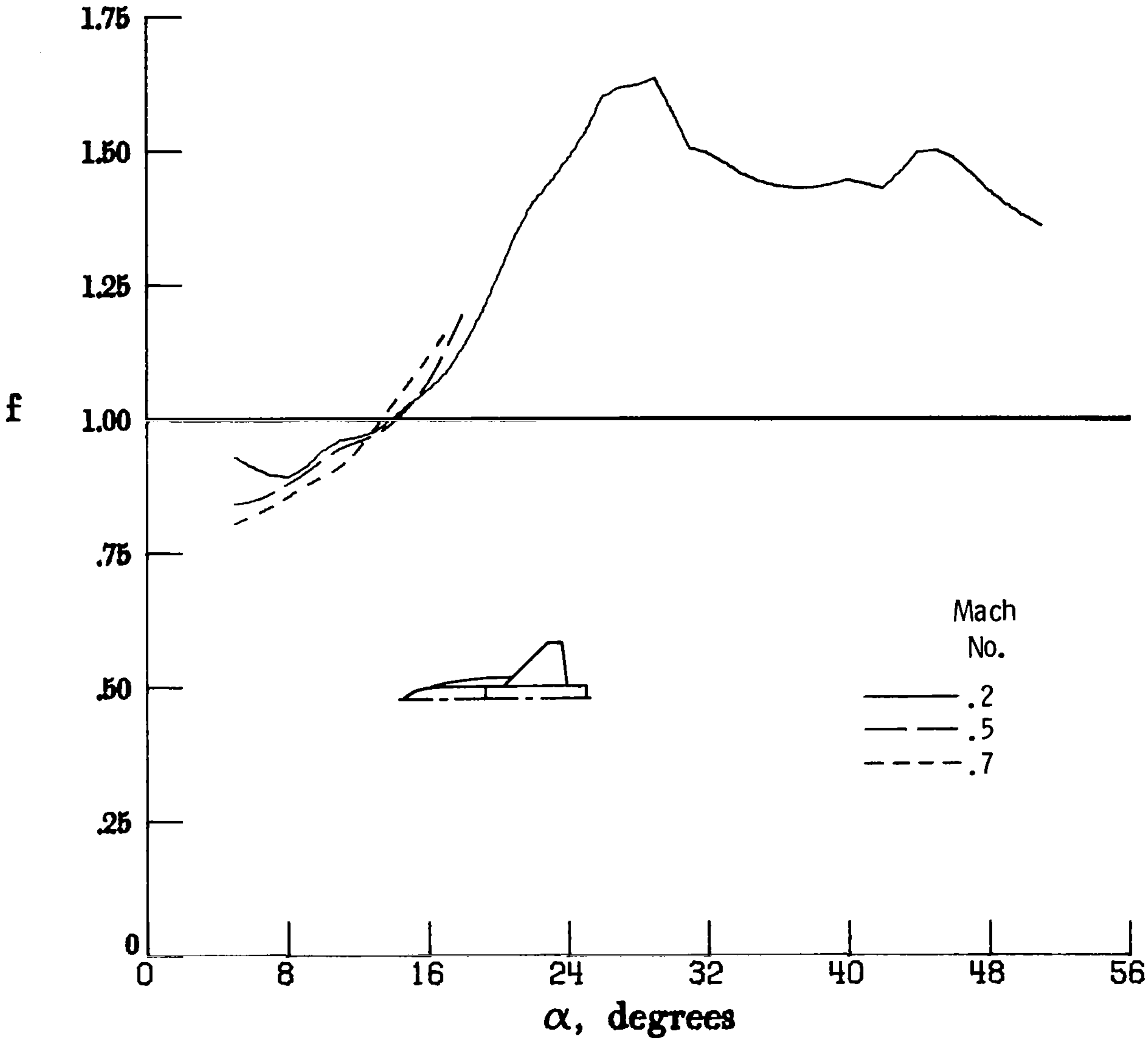

(d) AD 19.

Figure 16.- Continued.

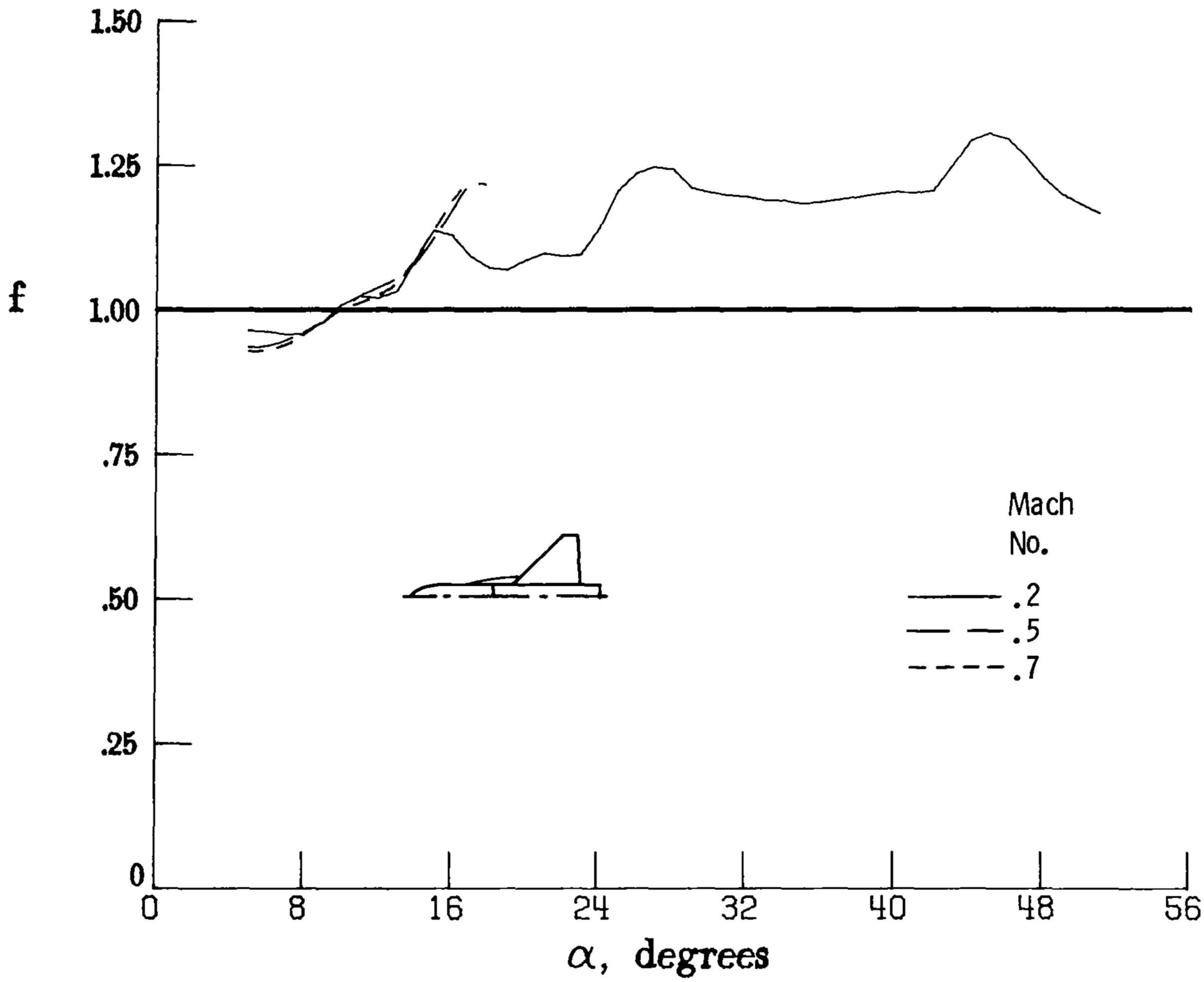

(e) AD 22.

Figure 16.- Continued.

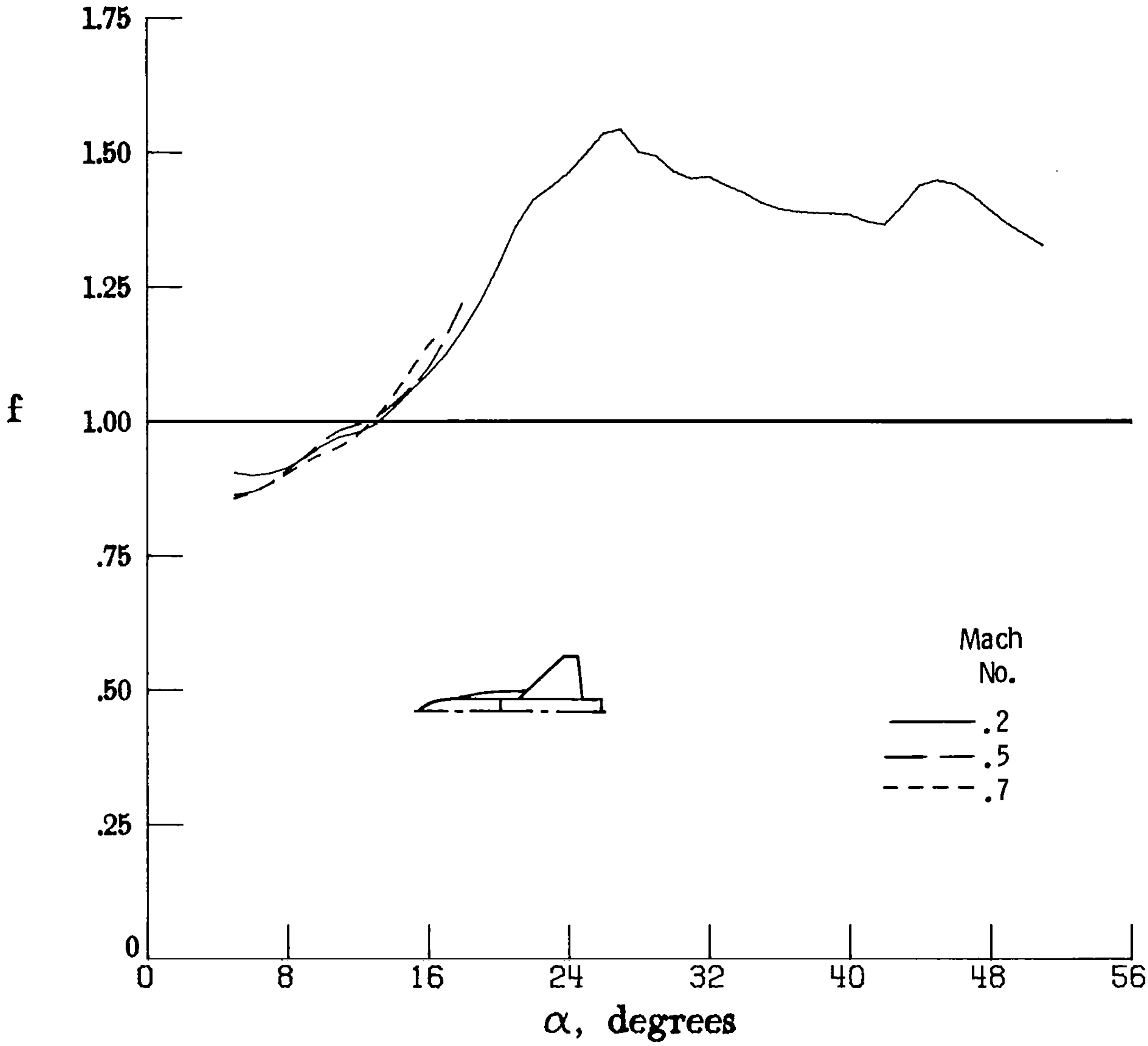

(f) AD 23.

Figure 16.- Continued.

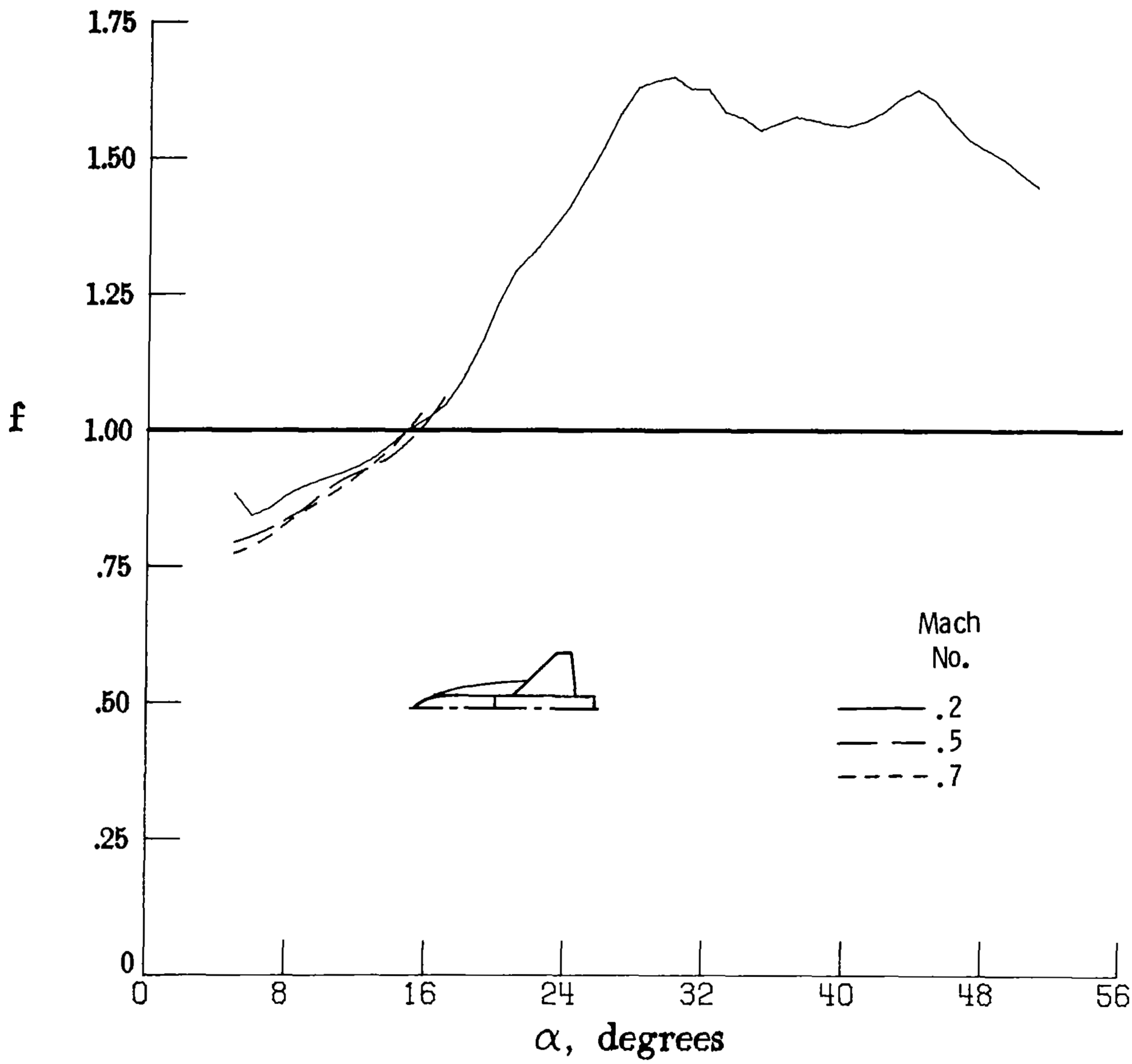

(g) AD 24.

Figure 16.- Continued.

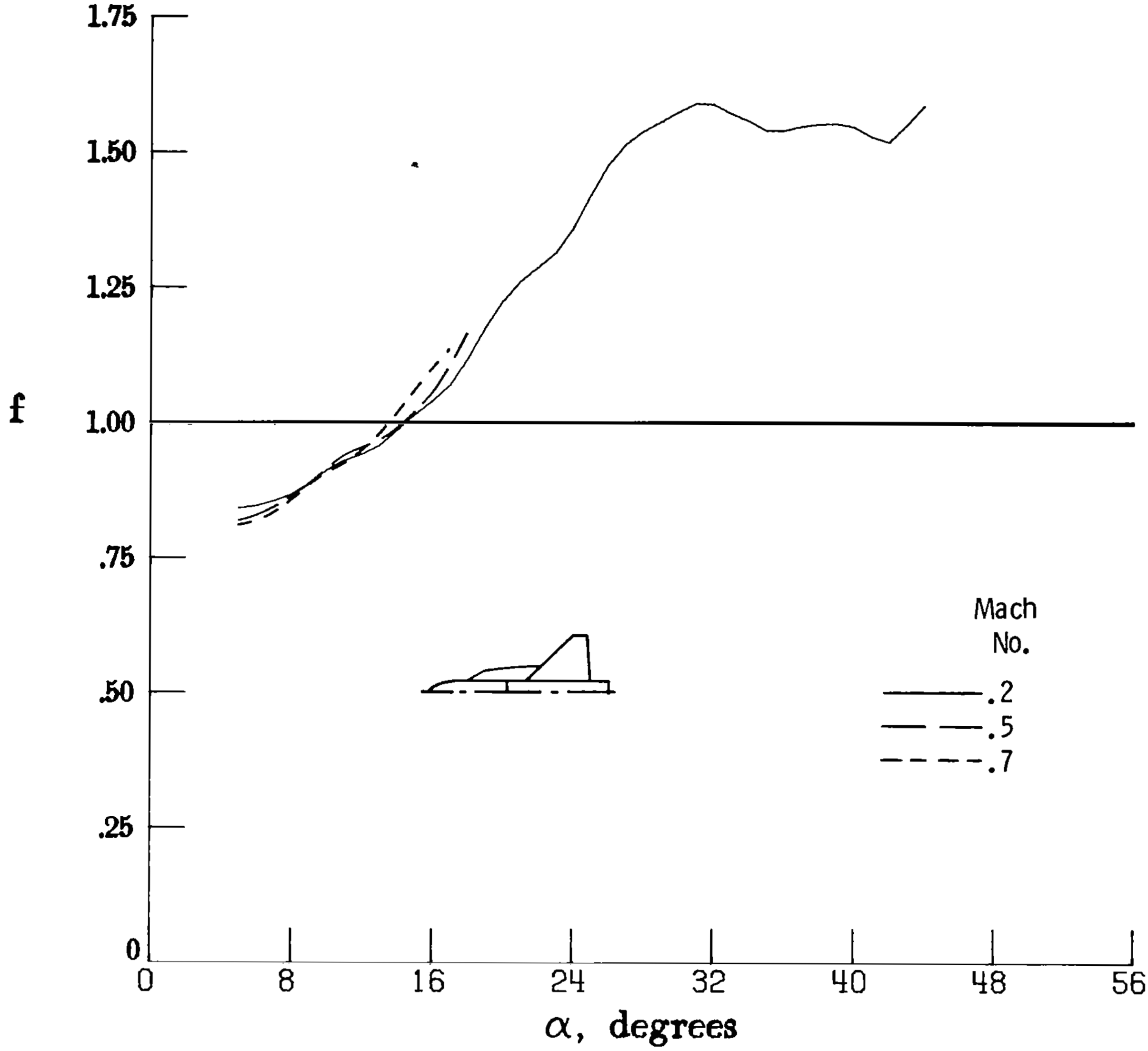

(h) ED 2.

Figure 16.- Continued.

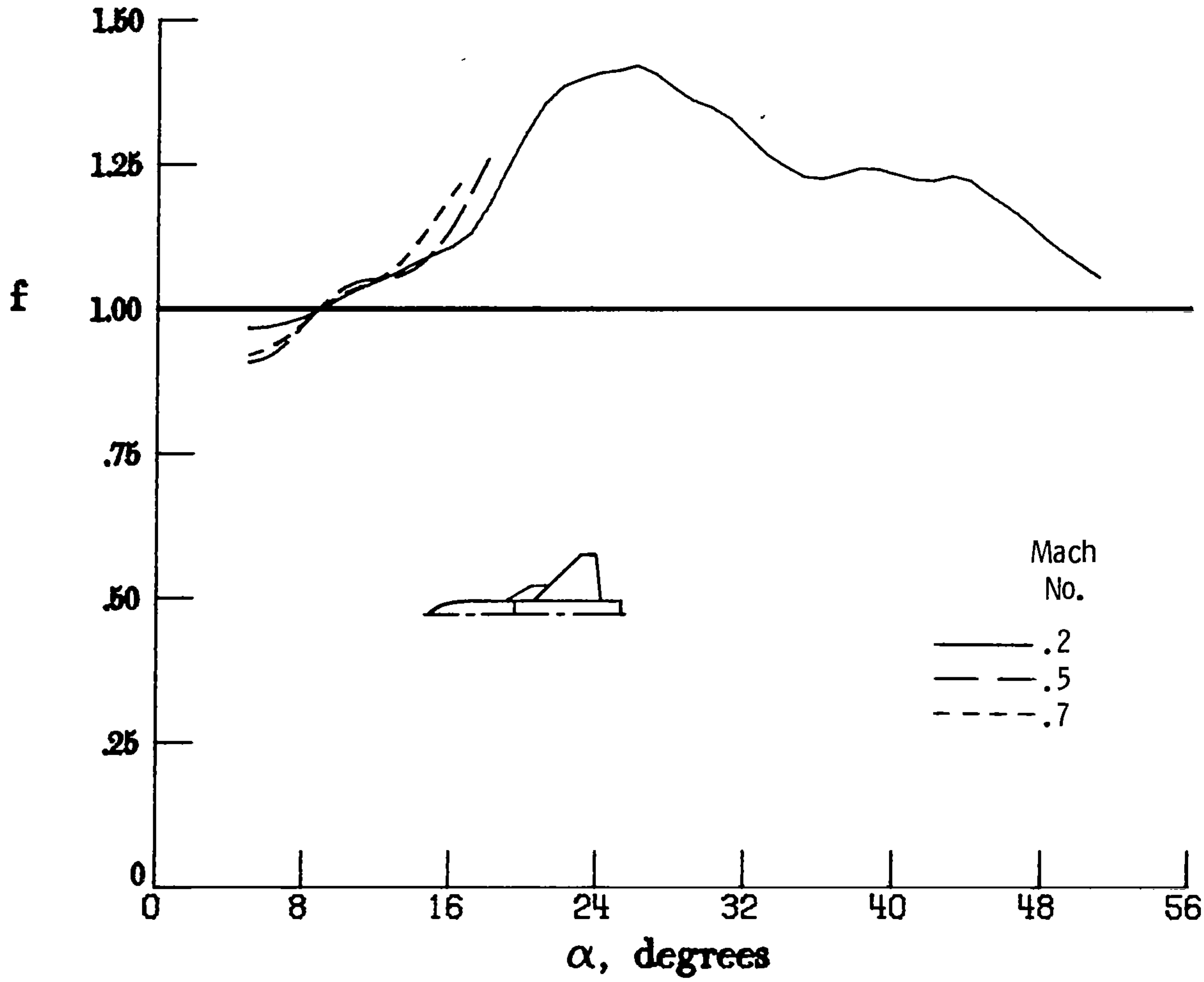

(i) ED 4.

Figure 16.- Continued.

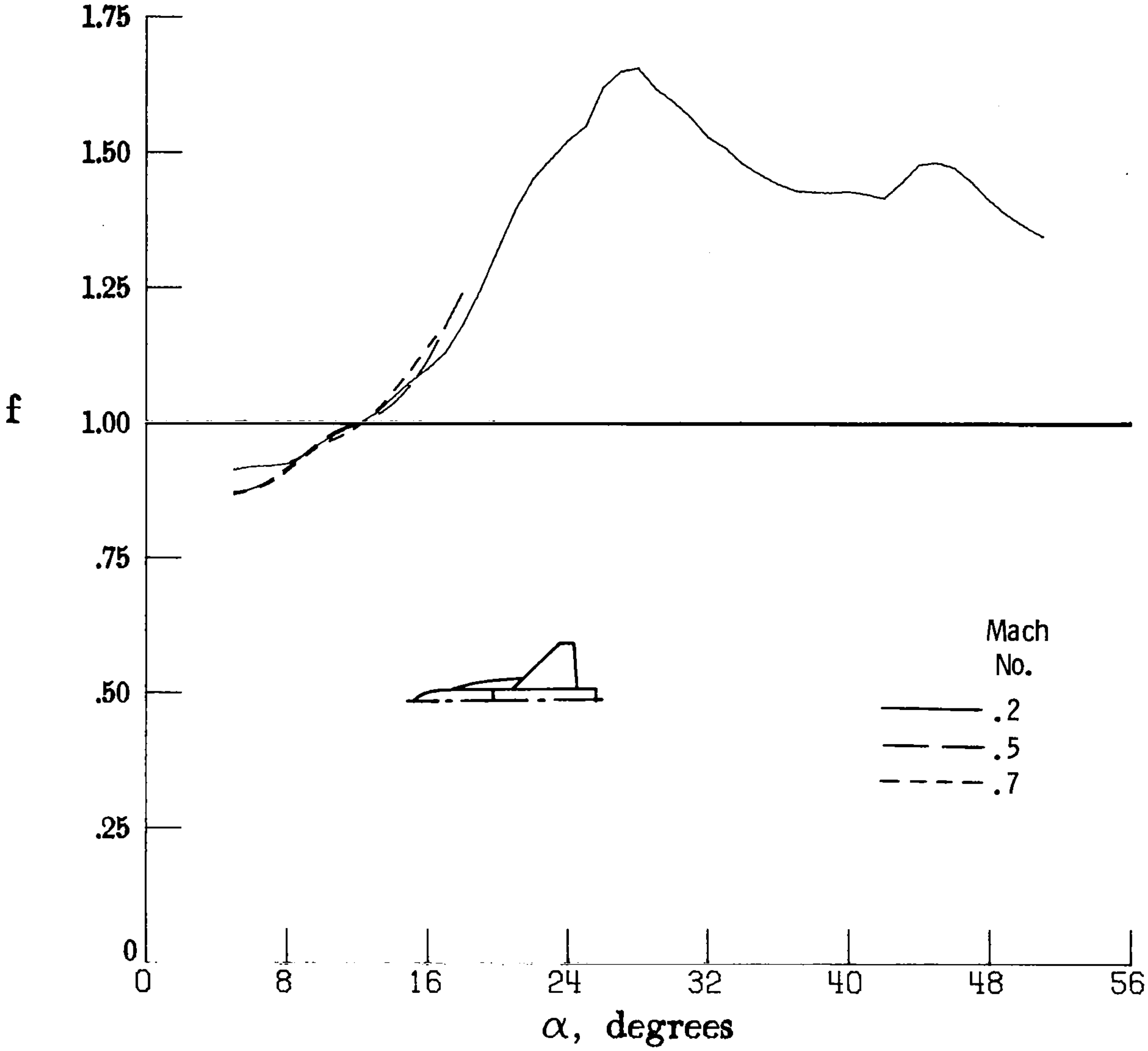

(j) ED 5.

Figure 16.- Continued.

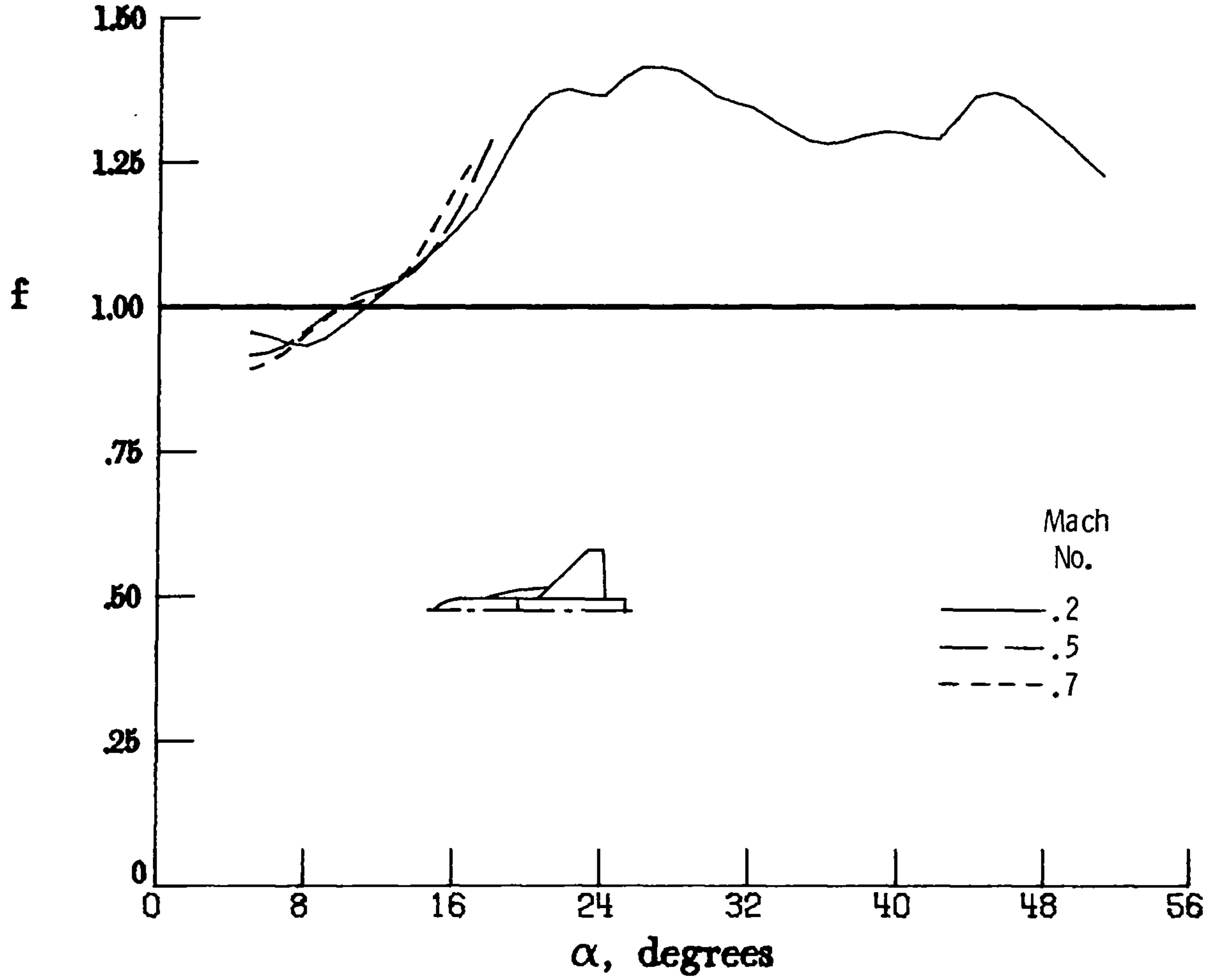

(k) ED 6.

Figure 16.- Continued.

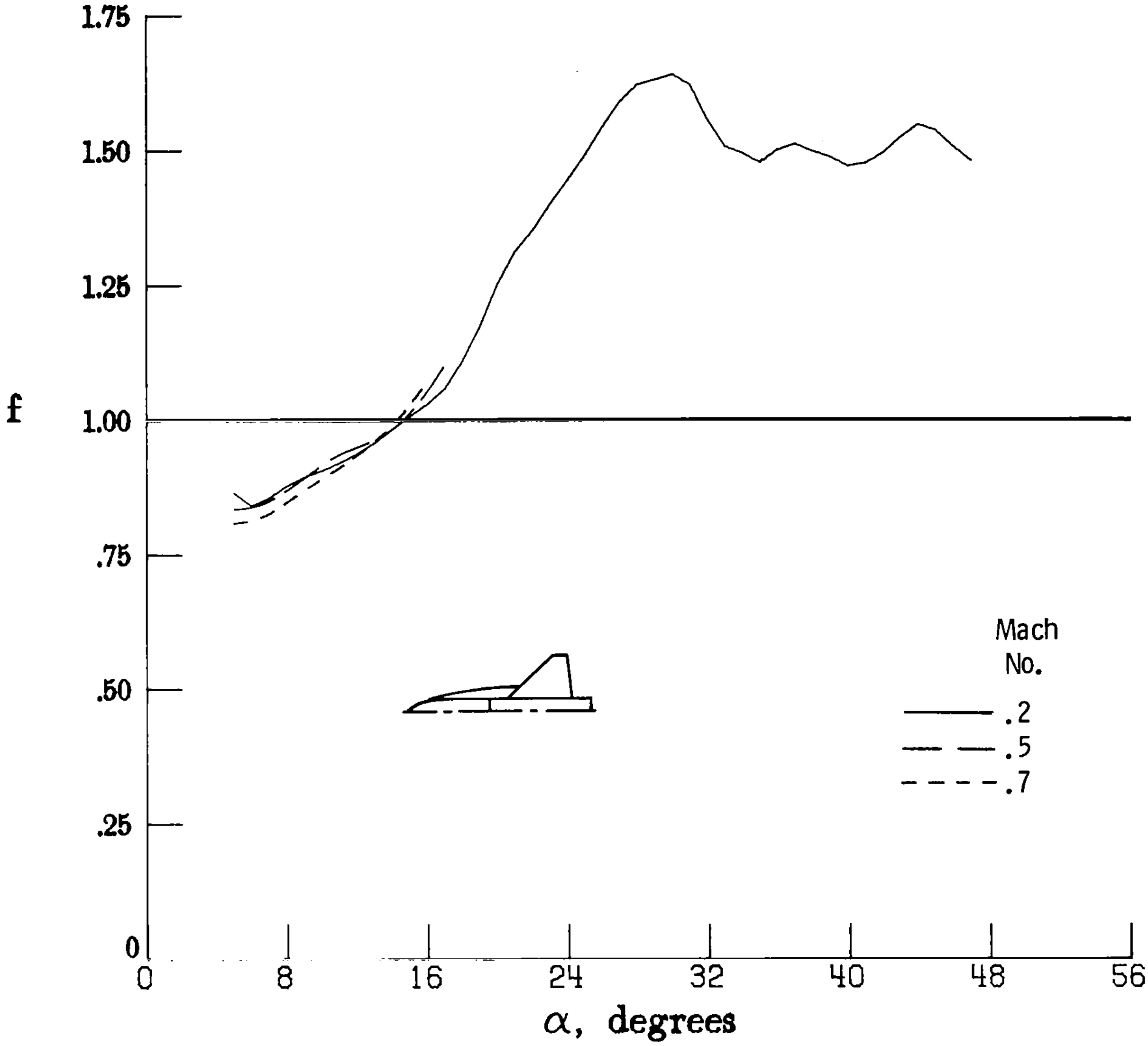

(1) ED 9.

Figure 16.- Continued.

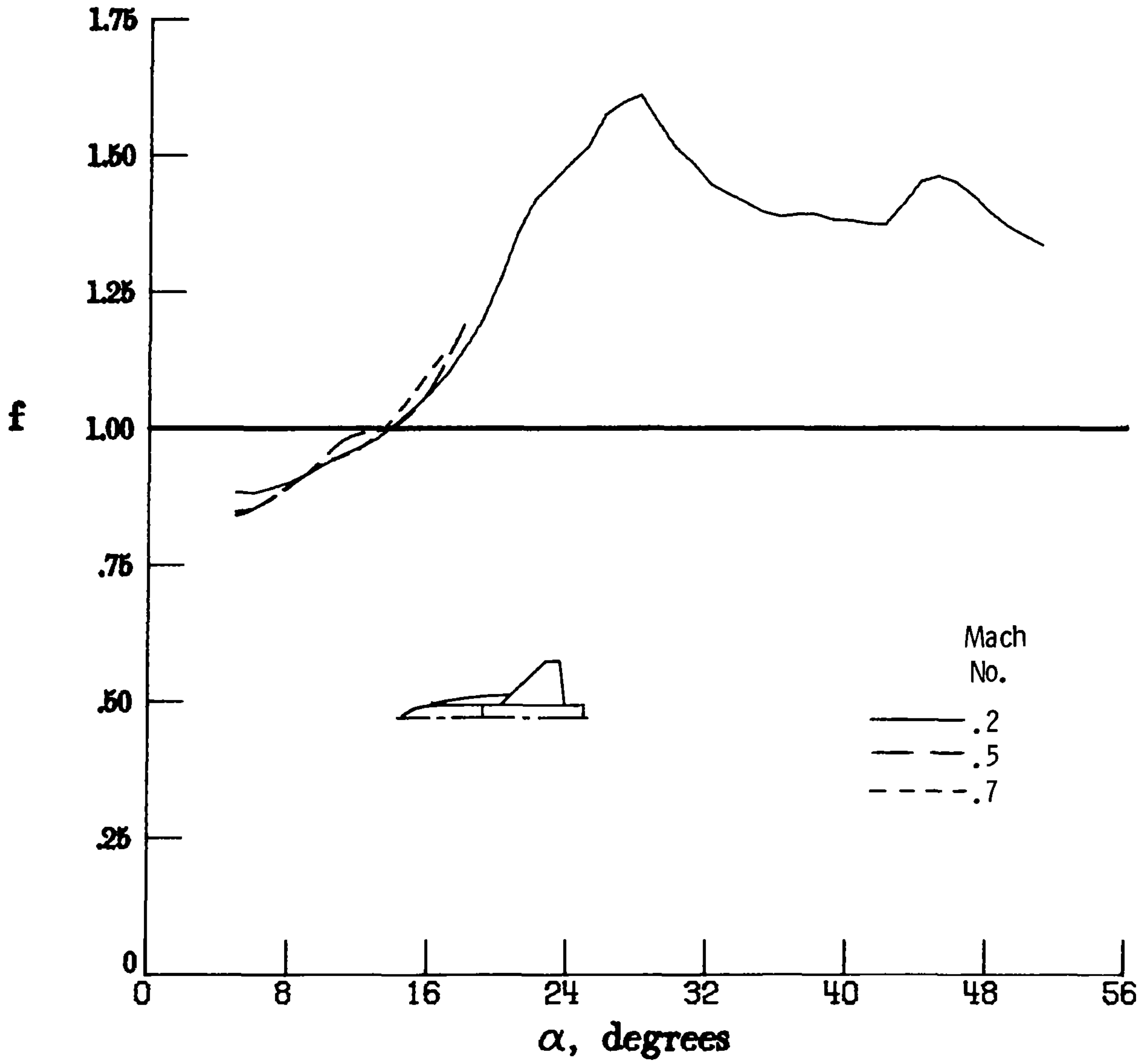

(m) ED 10.

Figure 16.- Continued.

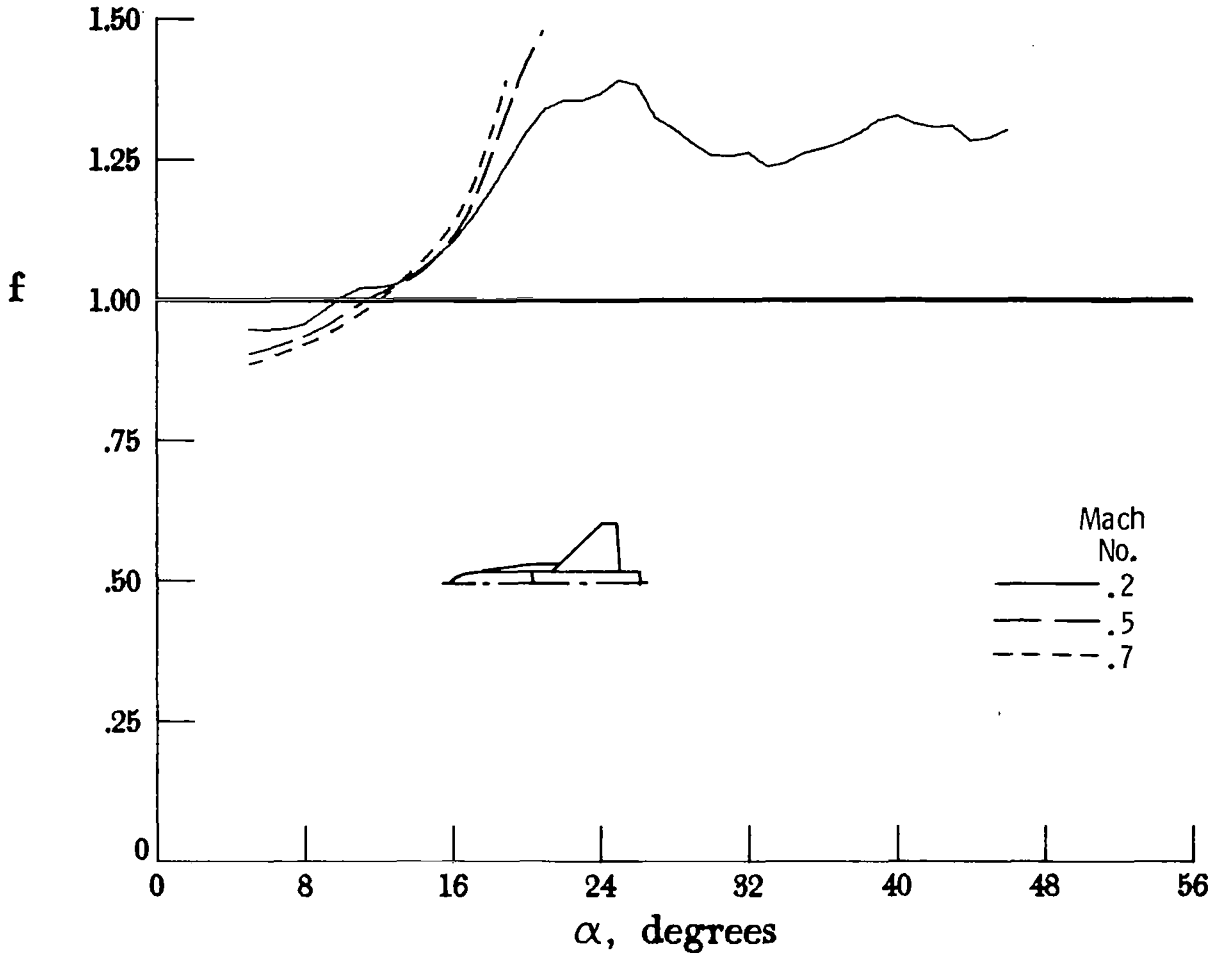

(n) ED 11.

Figure 16.- Continued.

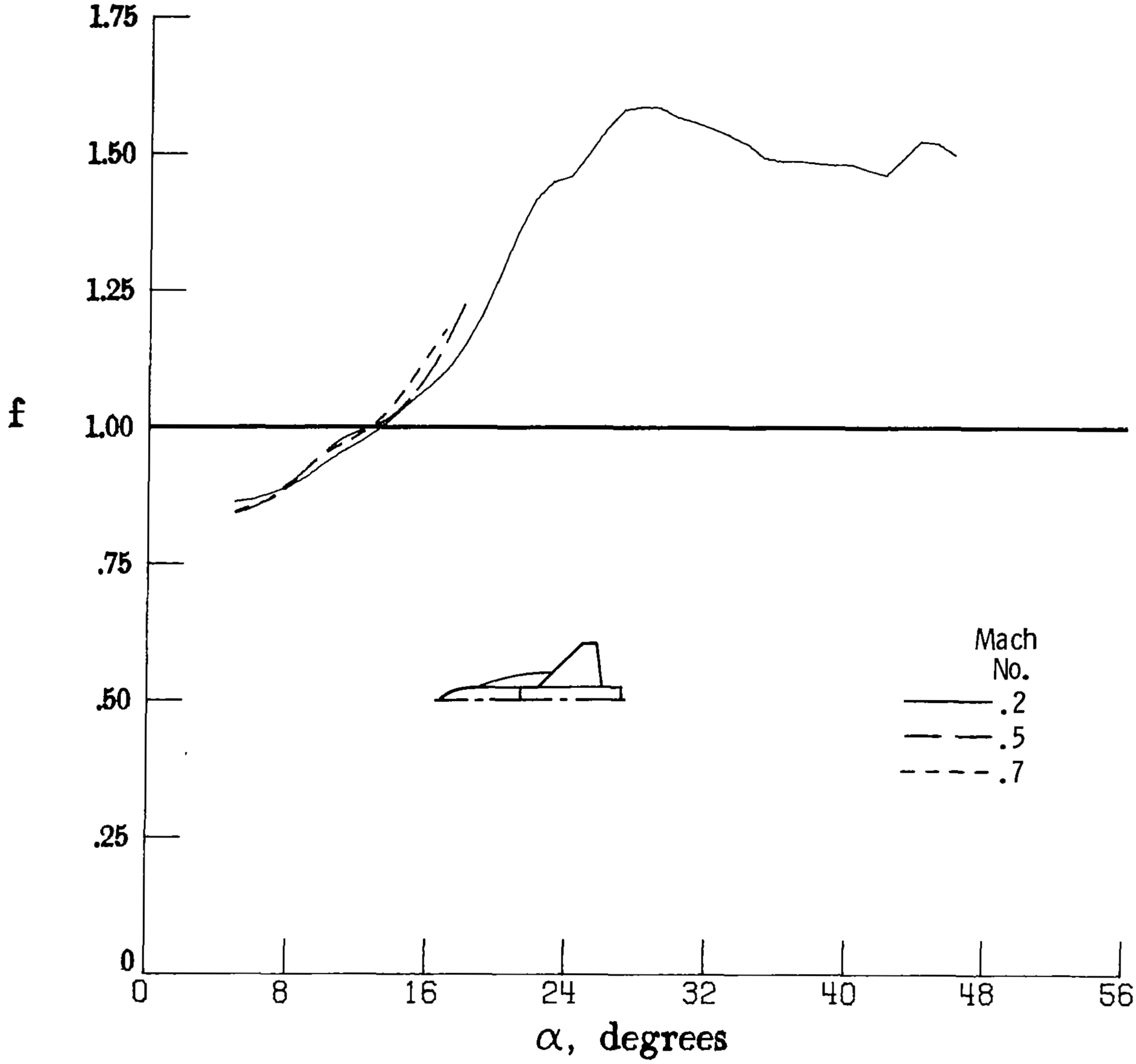

(o) ED 12.

Figure 16.- Continued.

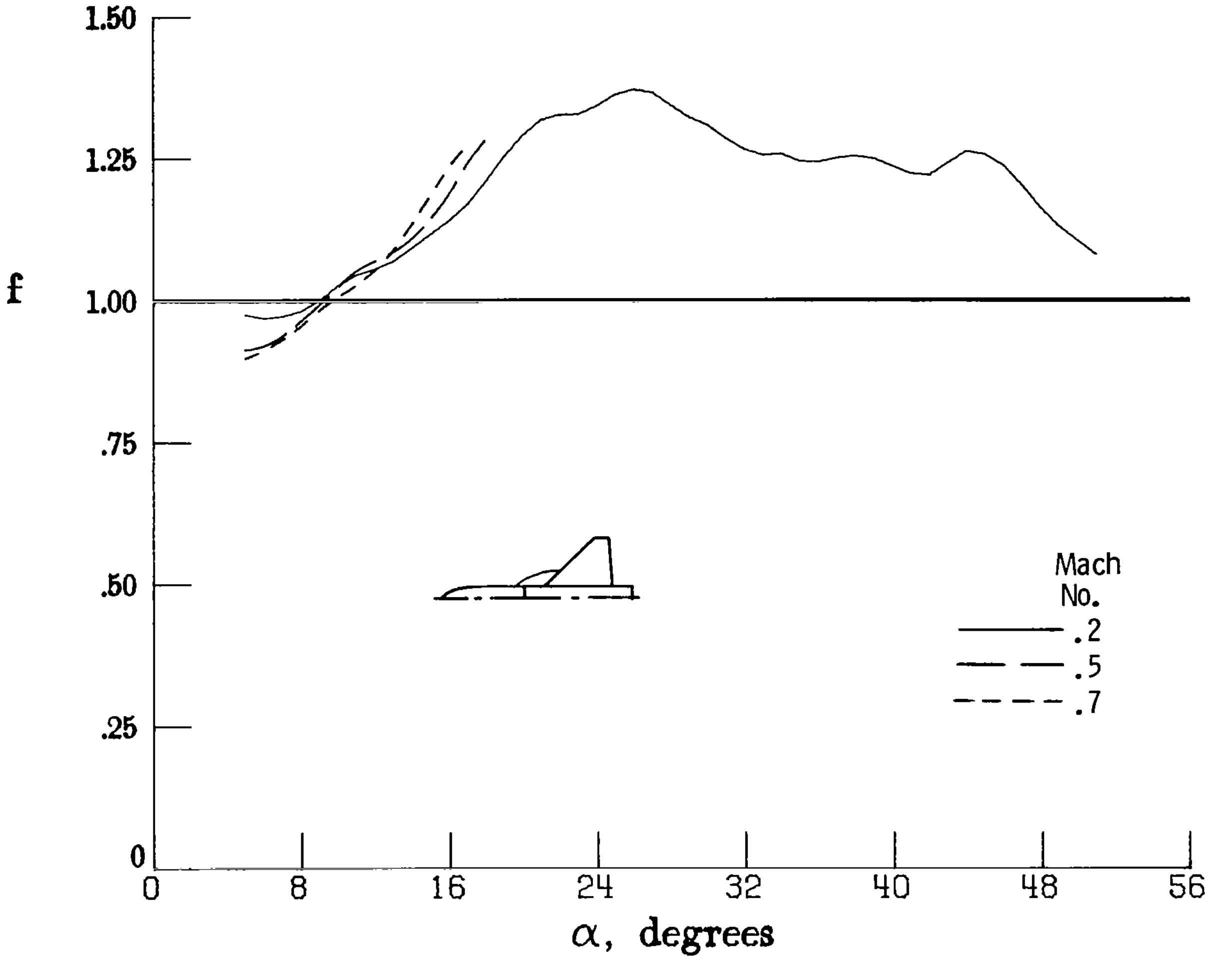

(p) ED 13.

Figure 16.- Concluded.

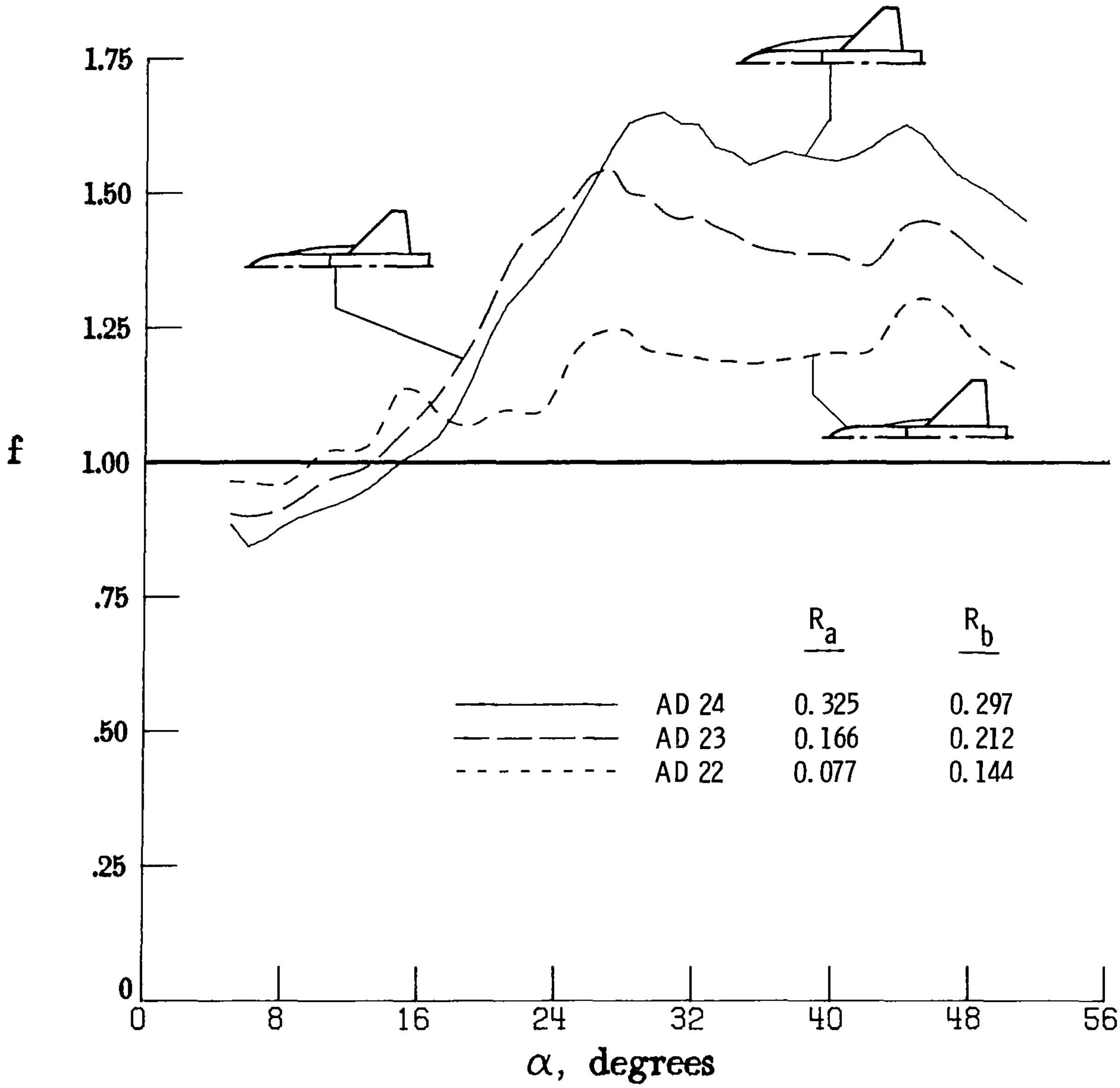

Figure 17.- Effect of R_a on f for a fixed gothic-strake shape at $M = 0.2$ and $R_s = 7.00$.

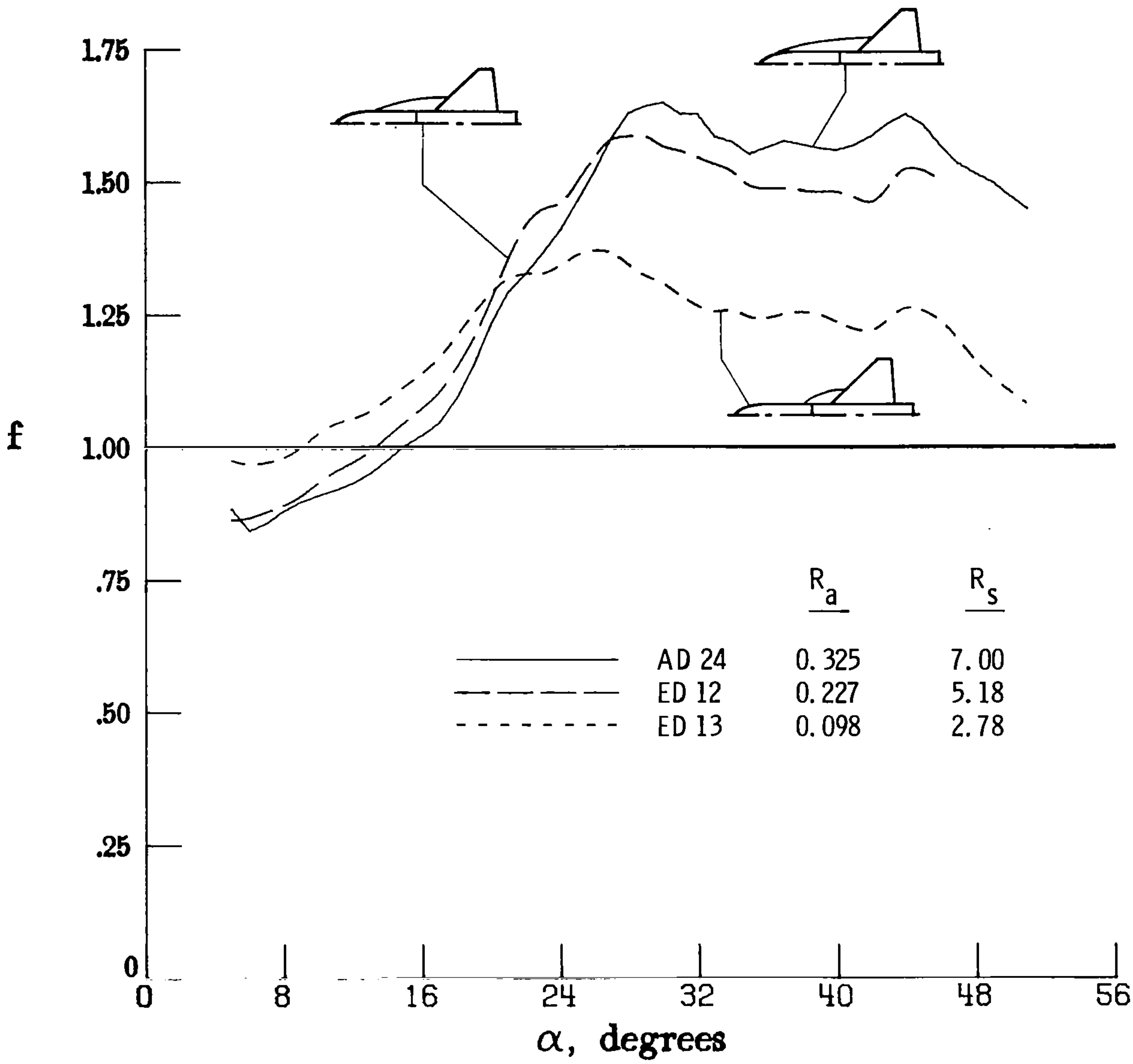

Figure 18.- Effect of chordwise scaling on f for AD 24 strake at $M = 0.2$ and $R_b = 0.297$.

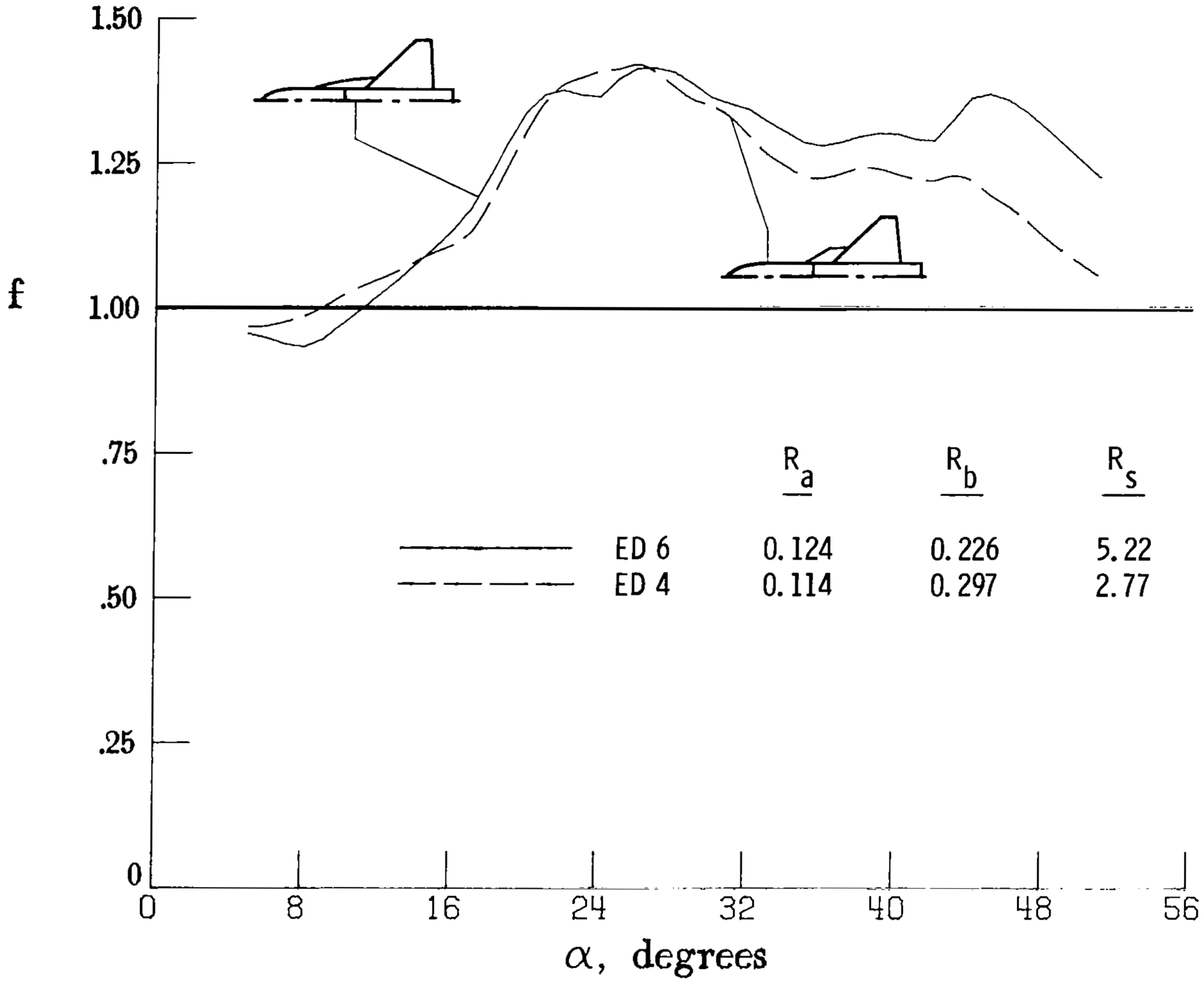

(a) $R_a \approx 0.119$.

Figure 19.- Effect of strake shape, R_s, and R_b on f at fixed R_a and $M = 0.2$.

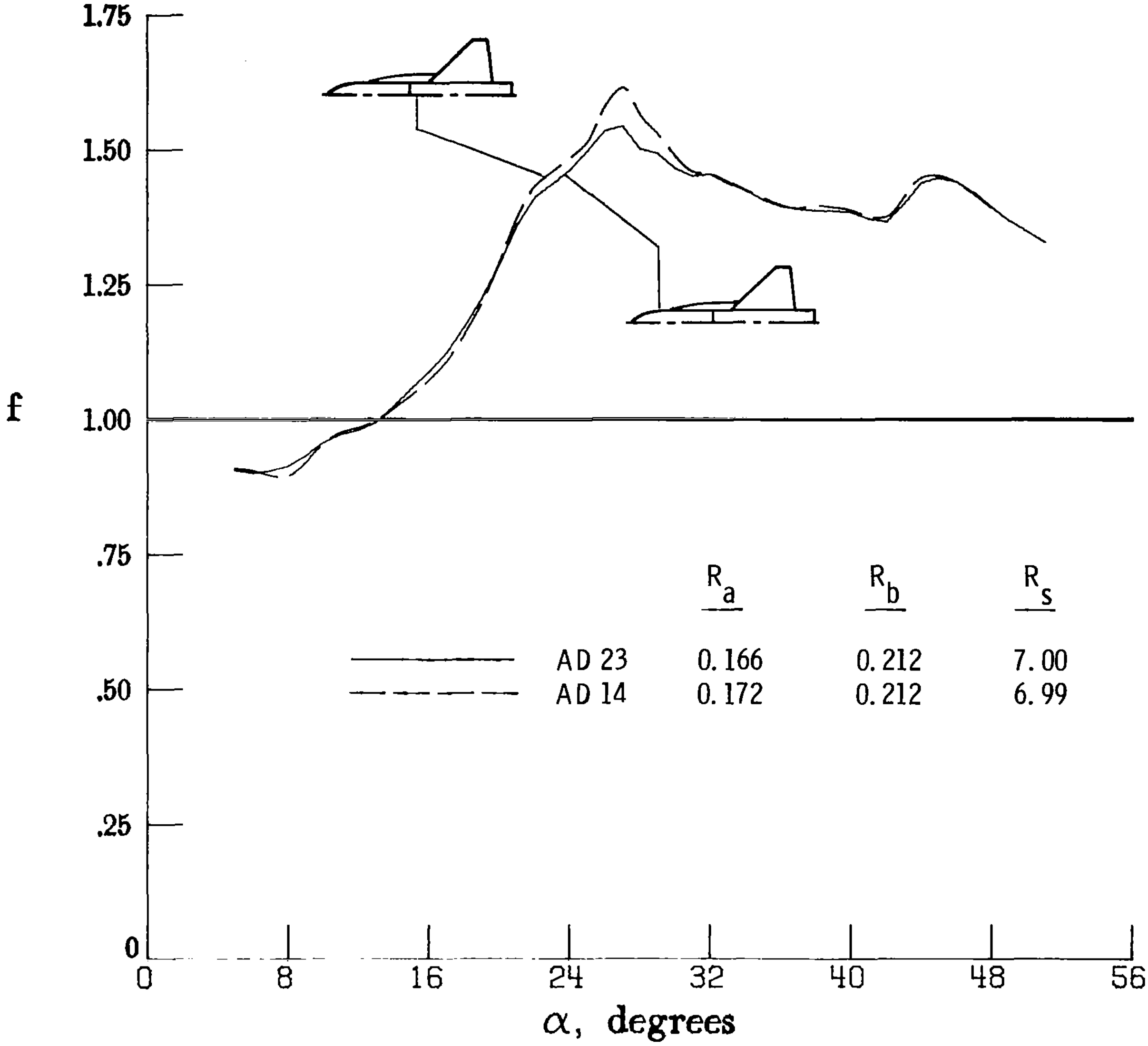

(b) $R_a \approx 0.169$.

Figure 19.- Continued.

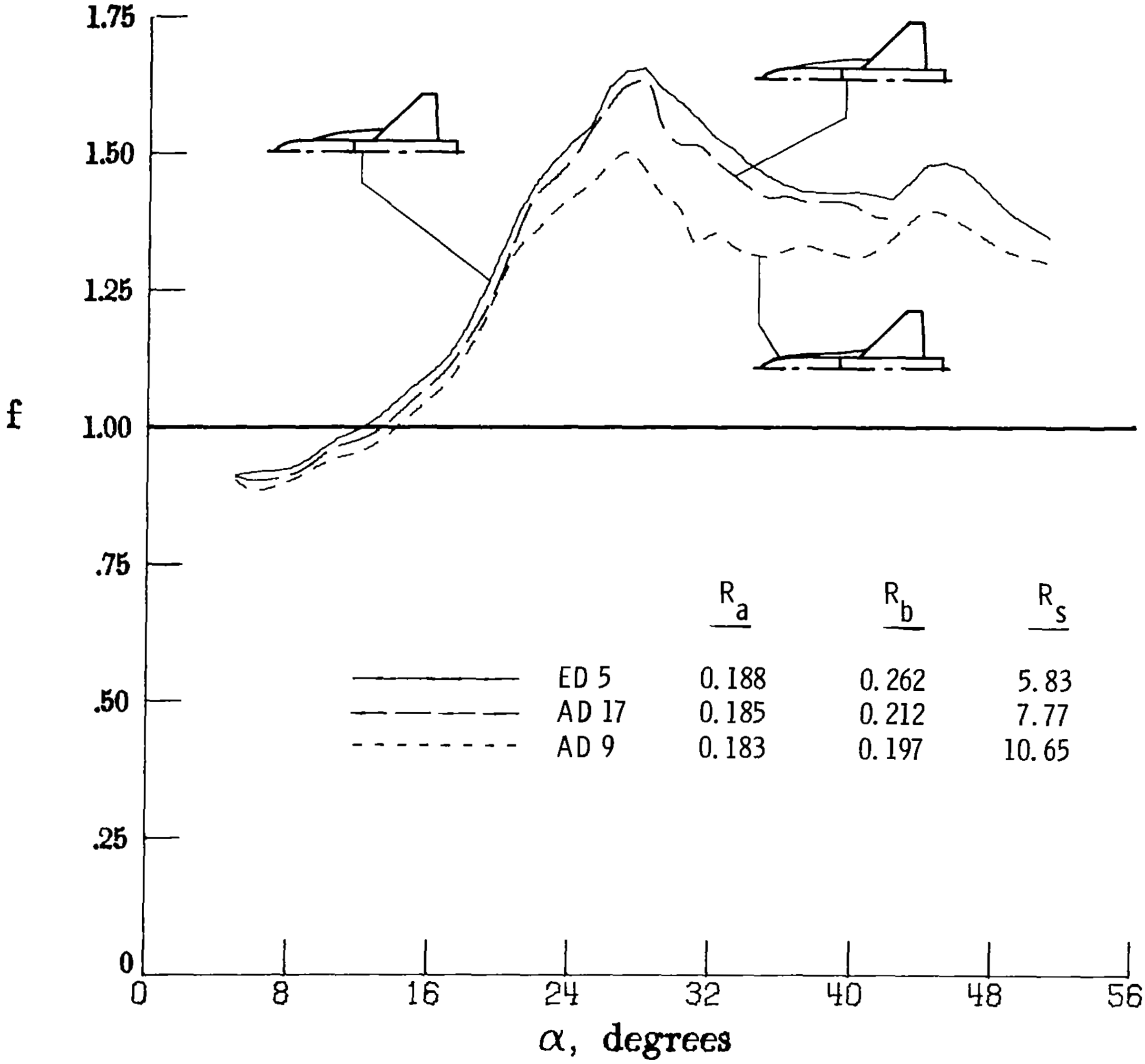

(c) $R_a \approx 0.185$.

Figure 19.- Continued.

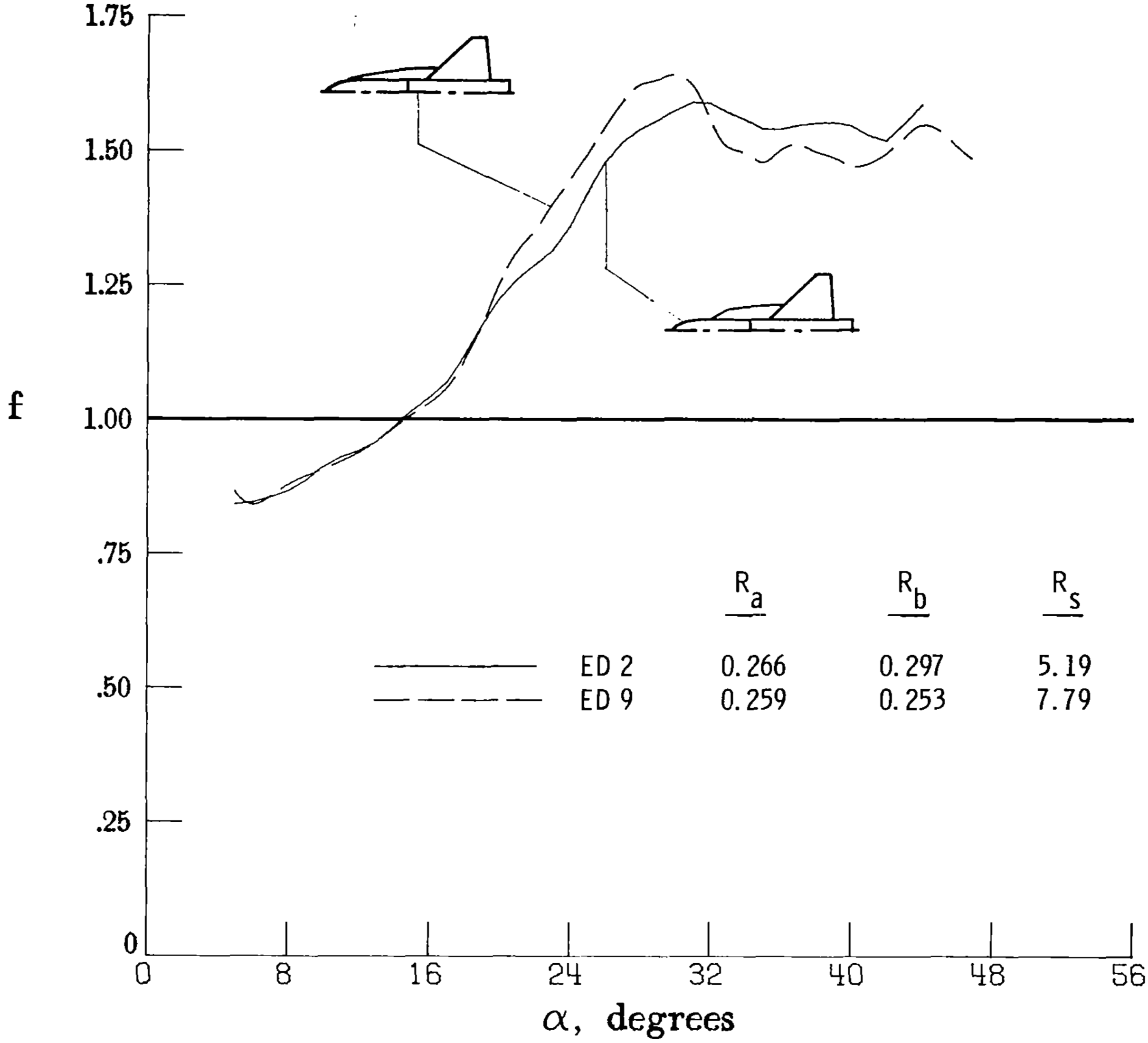

(d) $R_a \approx 0.263$.

Figure 19.- Concluded.

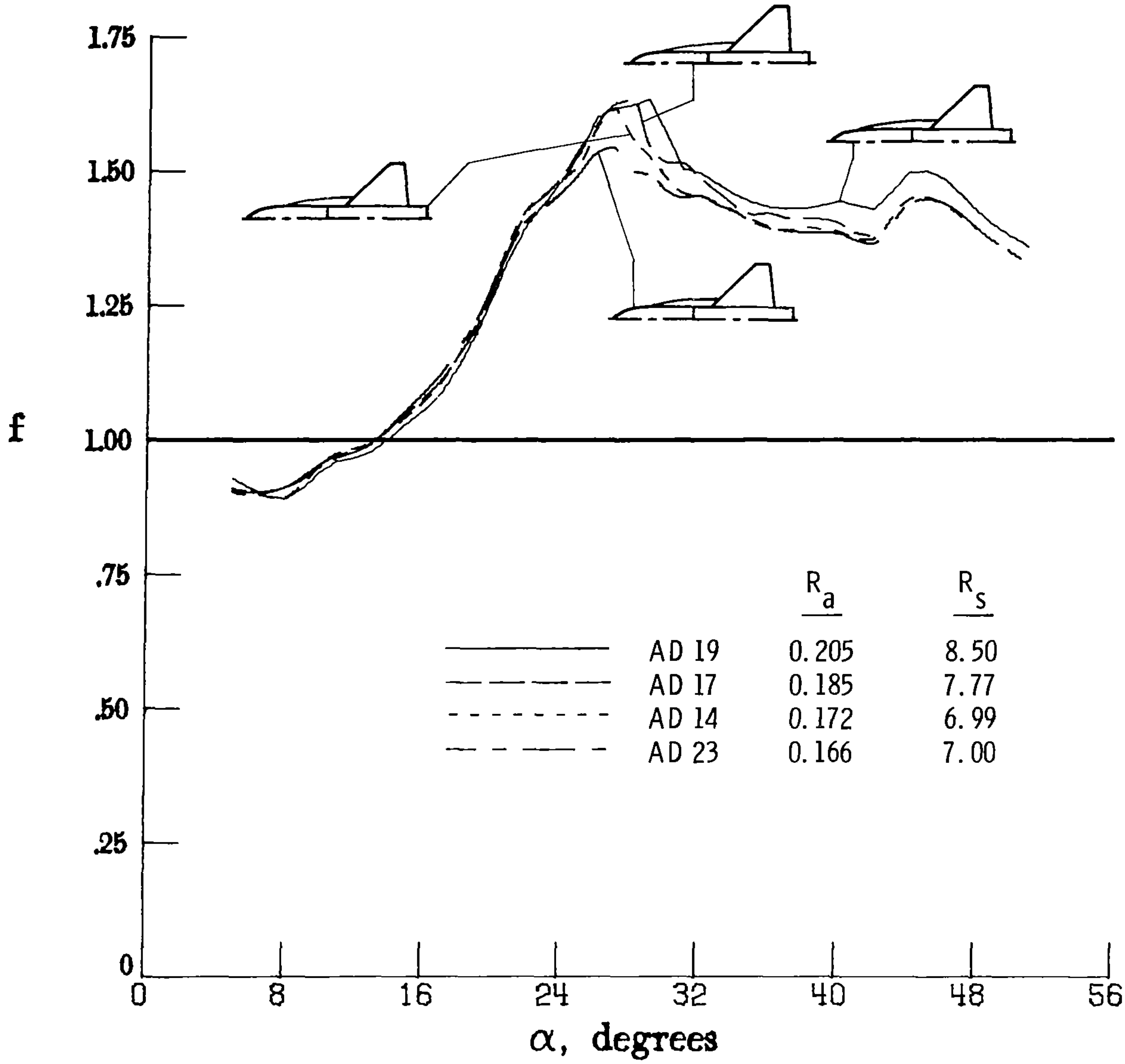

Figure 20.- Effect of strake shape on f at R_b = 0.212 and M = 0.2.

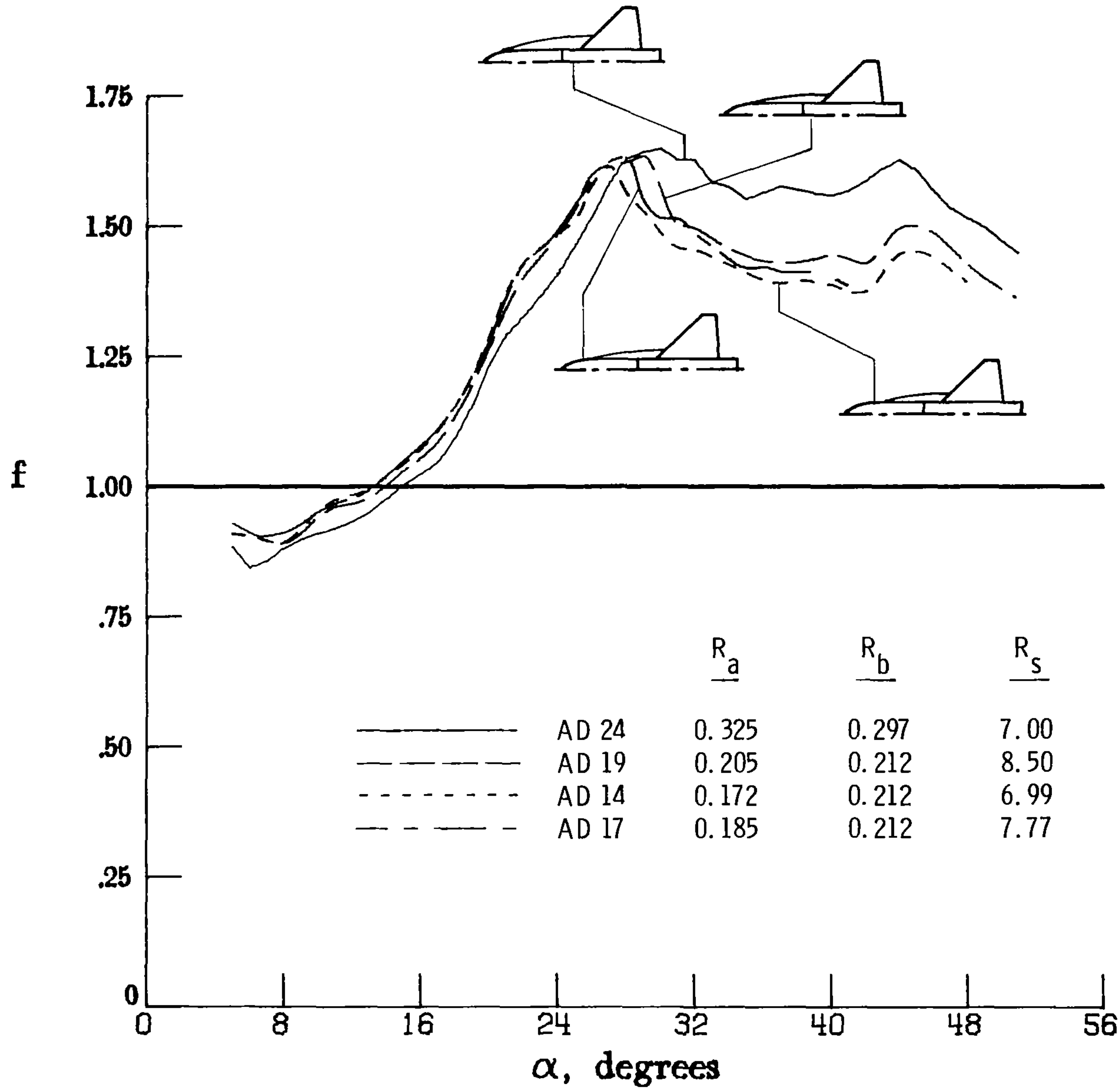

Figure 21.- Effect of R_a, R_b, and R_s on f for the "better" gothic strakes at M = 0.2.

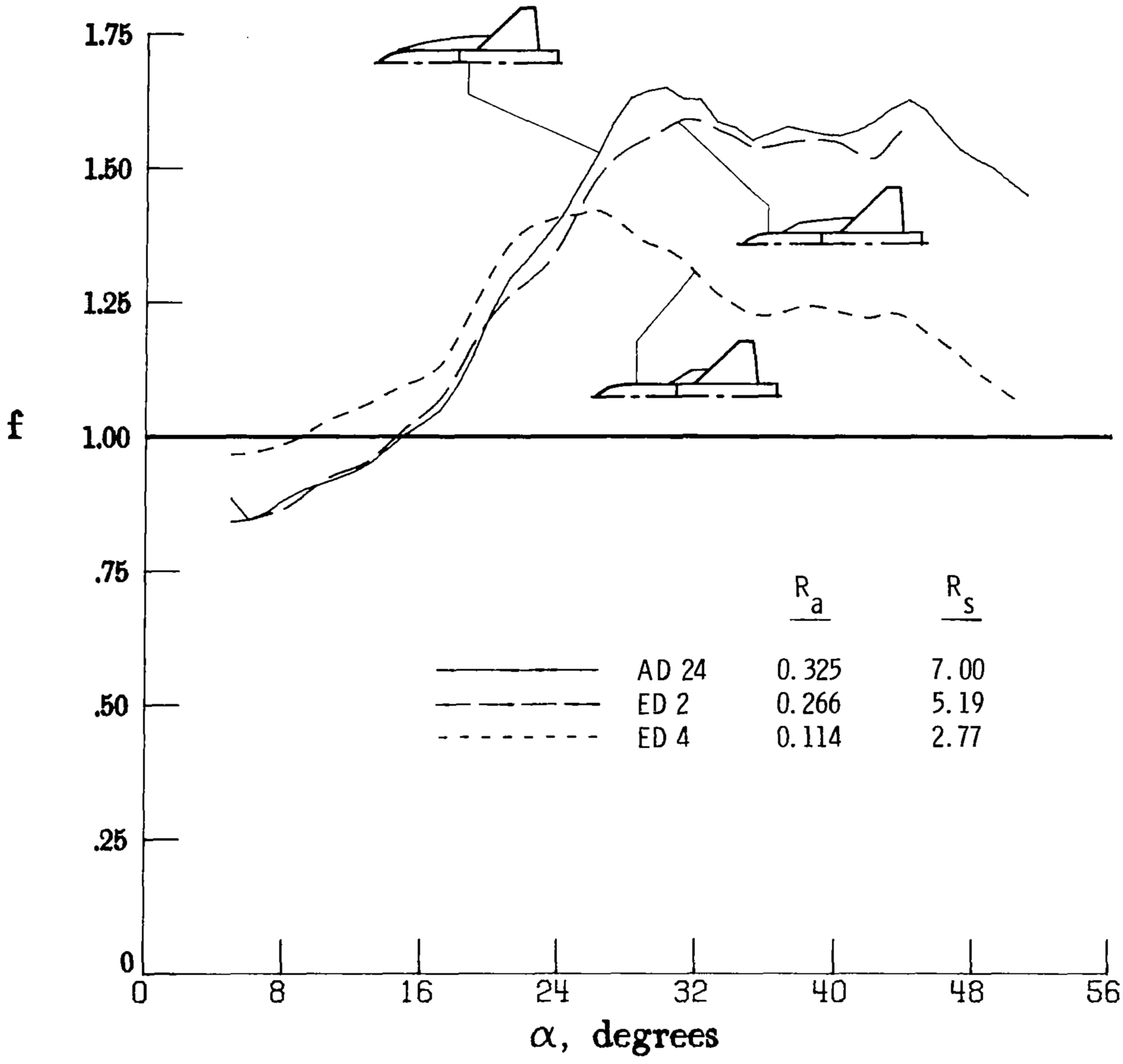

(a) Apex cut.

Figure 22.- Effect of removing area from AD 24 stake on f at M = 0.2.

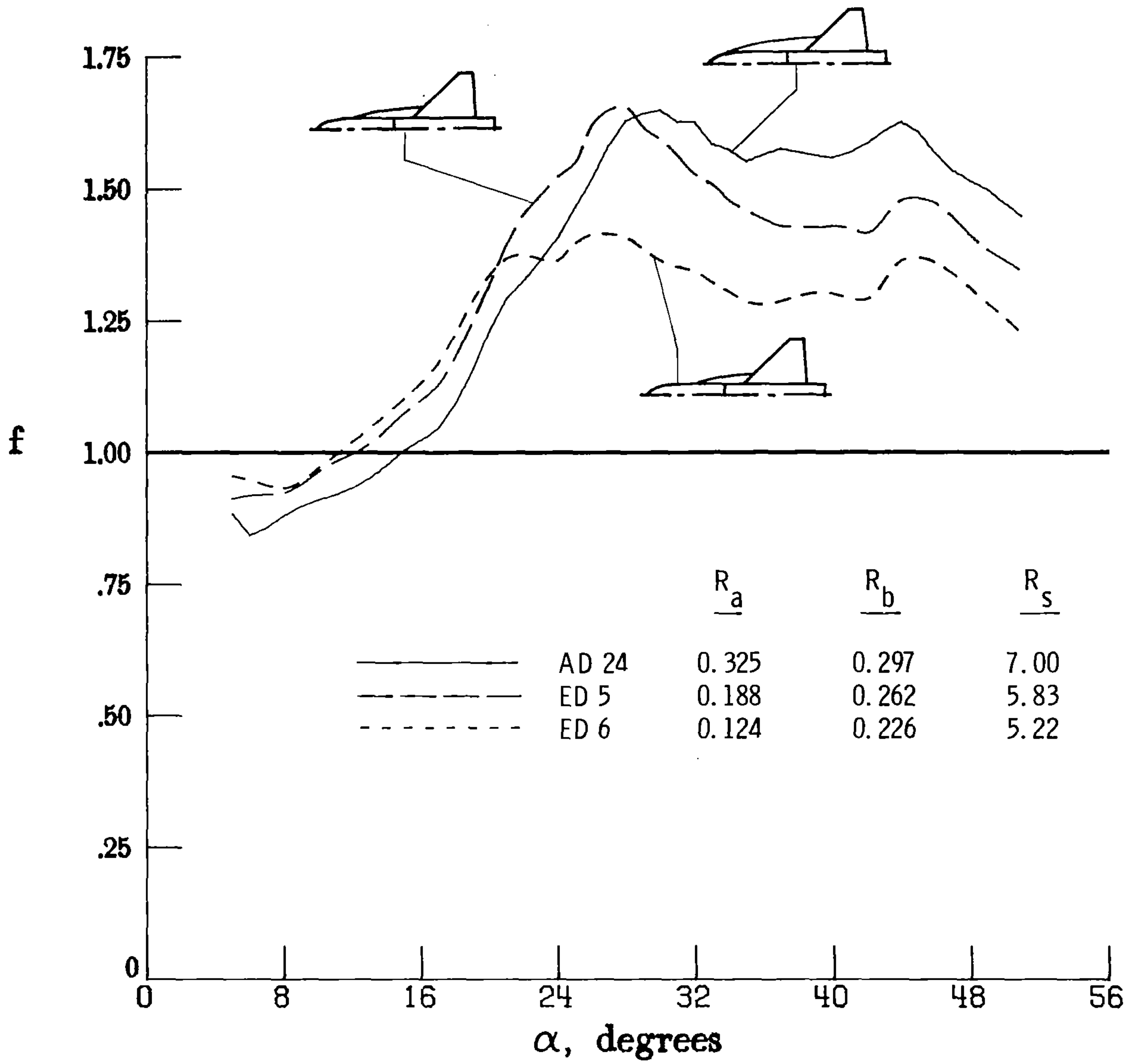

(b) Trailing-edge cut.

Figure 22.- Continued.

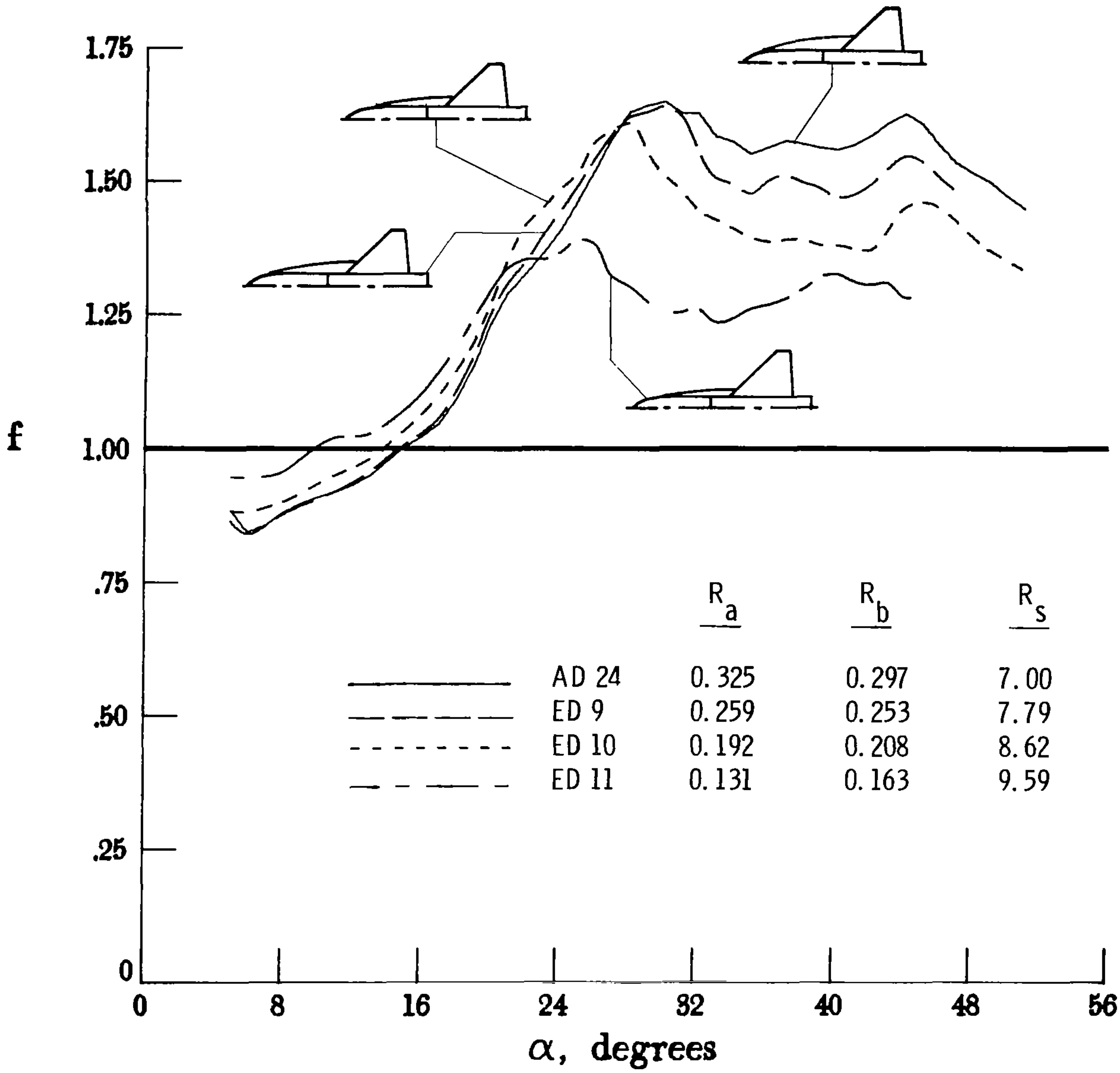

(c) Inboard-edge cut.

Figure 22.- Concluded.

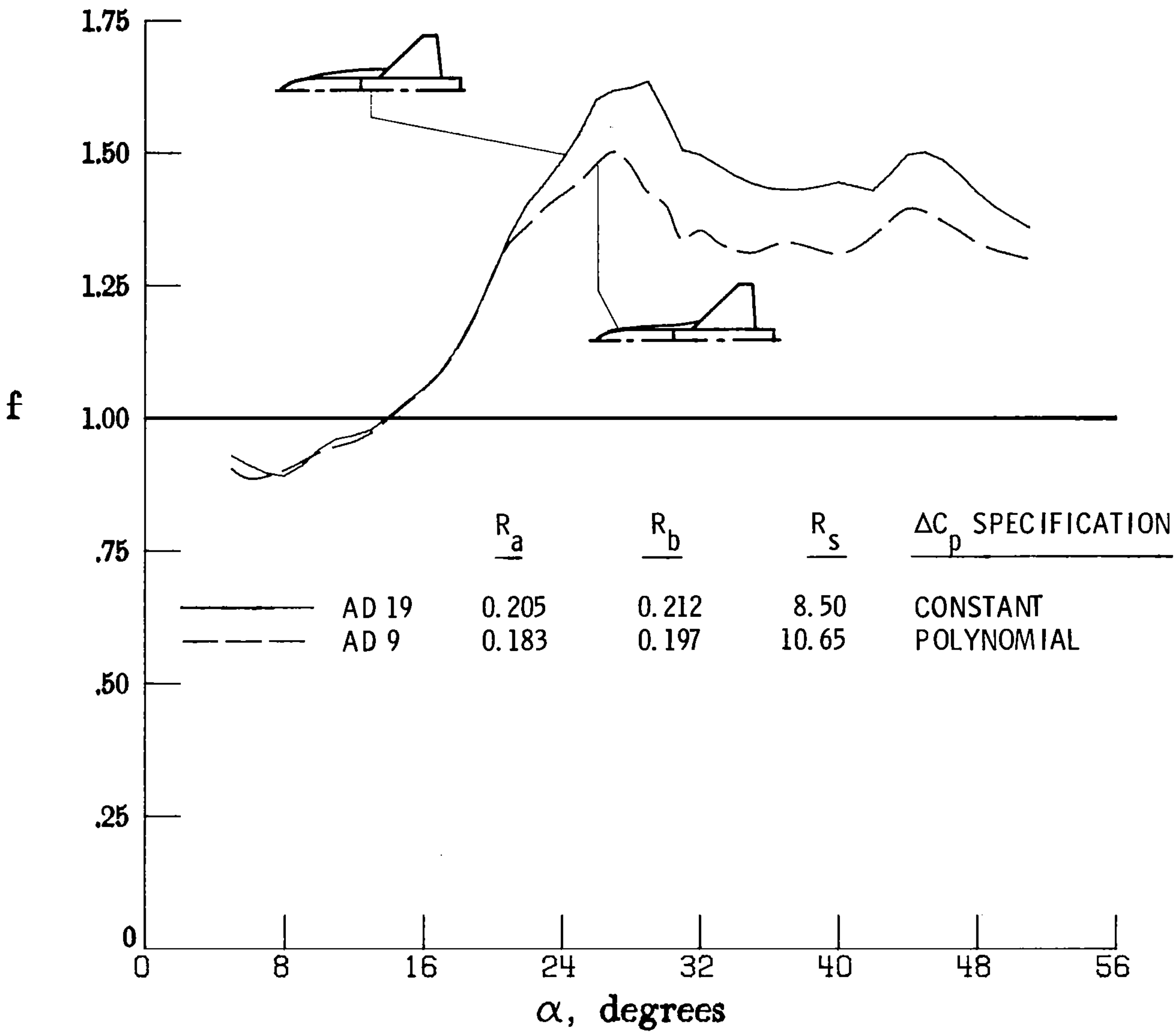

Figure 23.- Effect of strake-design pressure specification (for a fixed prescribed suction distribution) on f at M = 0.2.

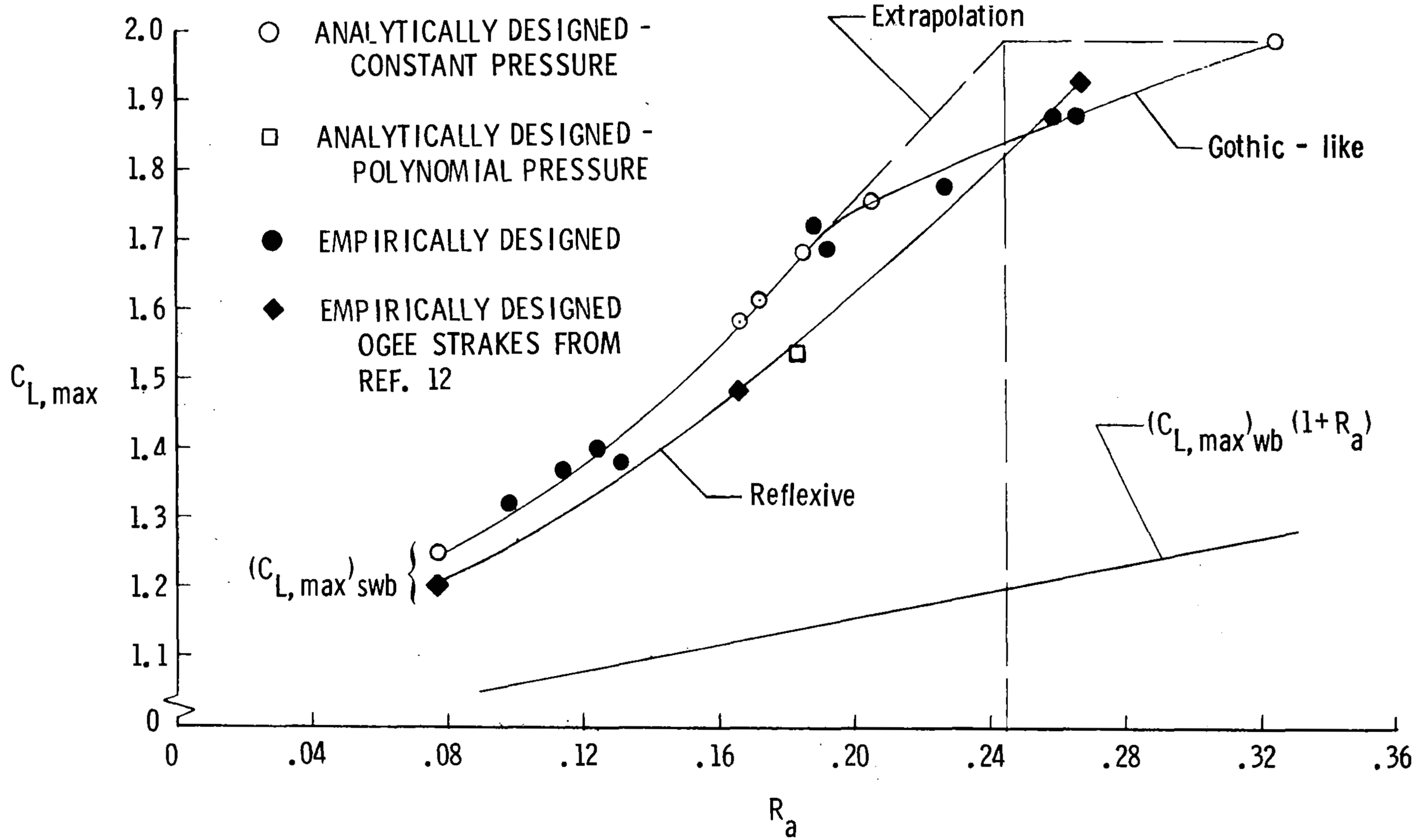

Figure 24.- Effect of strake shape on $(C_{L,max})_{swb}$ at $M \approx 0$.

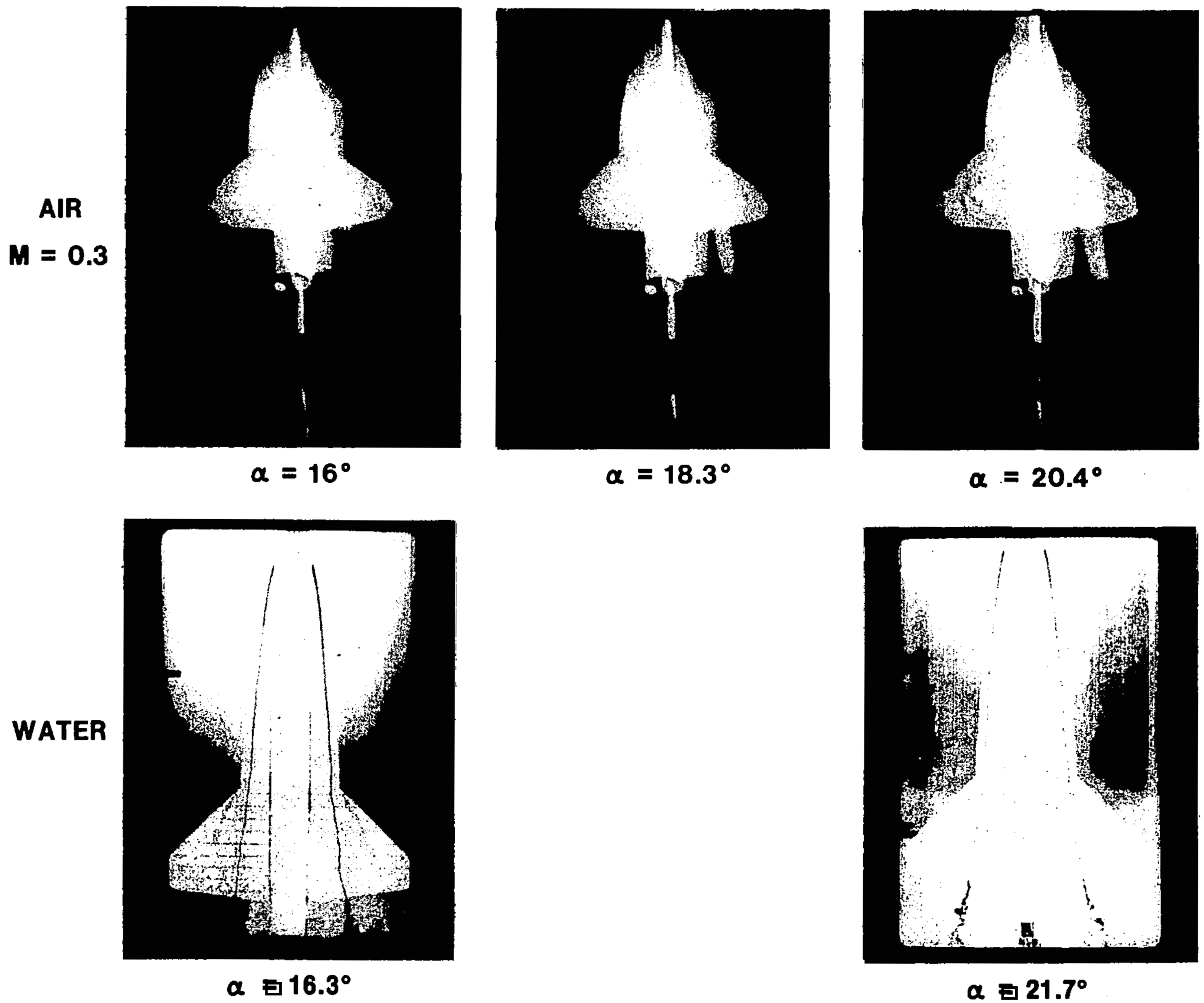

(a) $16^{\circ} \leqq \alpha \leqq 21.7^{\circ}$.

Figure 25.- Strake vortex as observed in air and water on AD 24 configuration.

AIR
M = 0.3

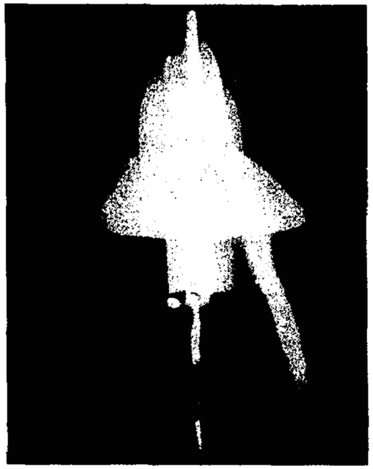

$\alpha = 23°$

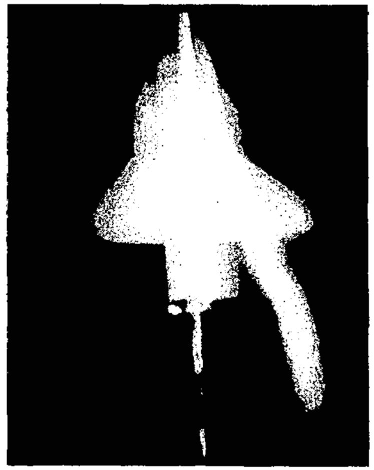

$\alpha = 25.4°$

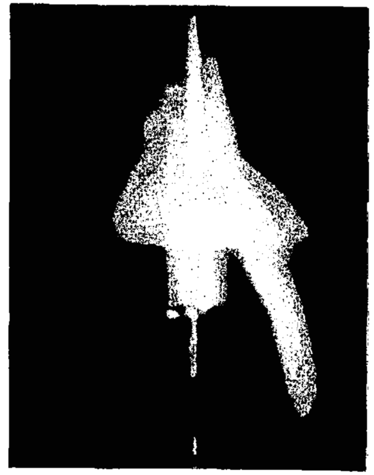

$\alpha = 27.8°$

WATER

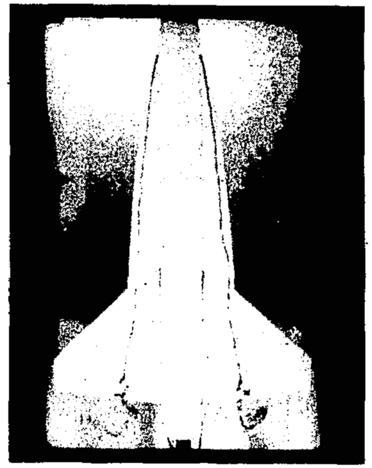

$\alpha = 27.2°$

(b) $23^{\circ} \leqq \alpha \leqq 27.8^{\circ}$.

Figure 25.- Continued.

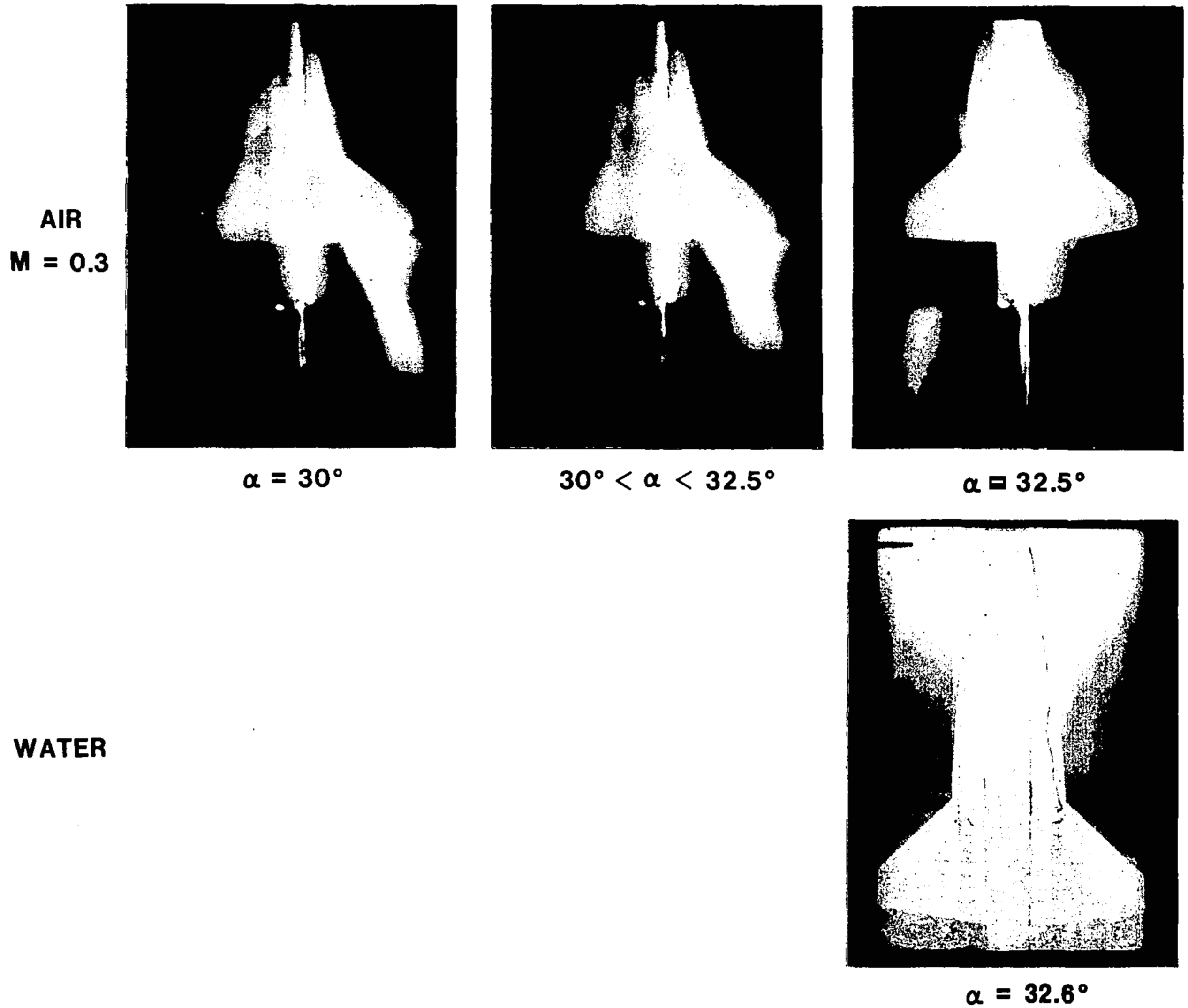

(c) $30^{o} \leqq \alpha \leqq 32.6^{o}$.

Figure 25.- Continued.

AIR
M = 0.3

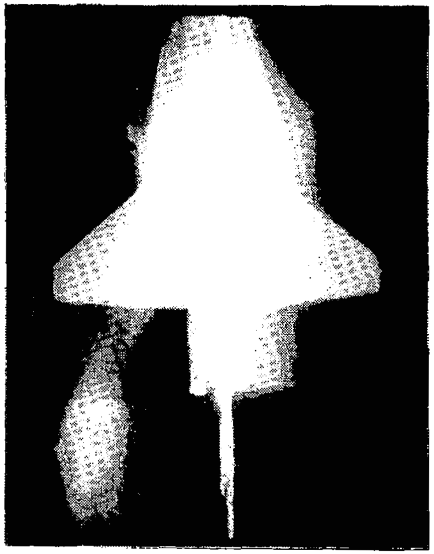

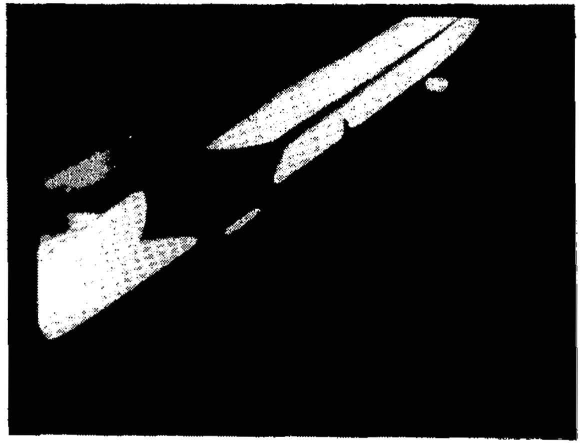

$\alpha \lessapprox 35.4°$

WATER

(d) $\alpha \lessapprox 35.4^{\circ}$.

Figure 25.- Continued.

AIR
M = 0.3

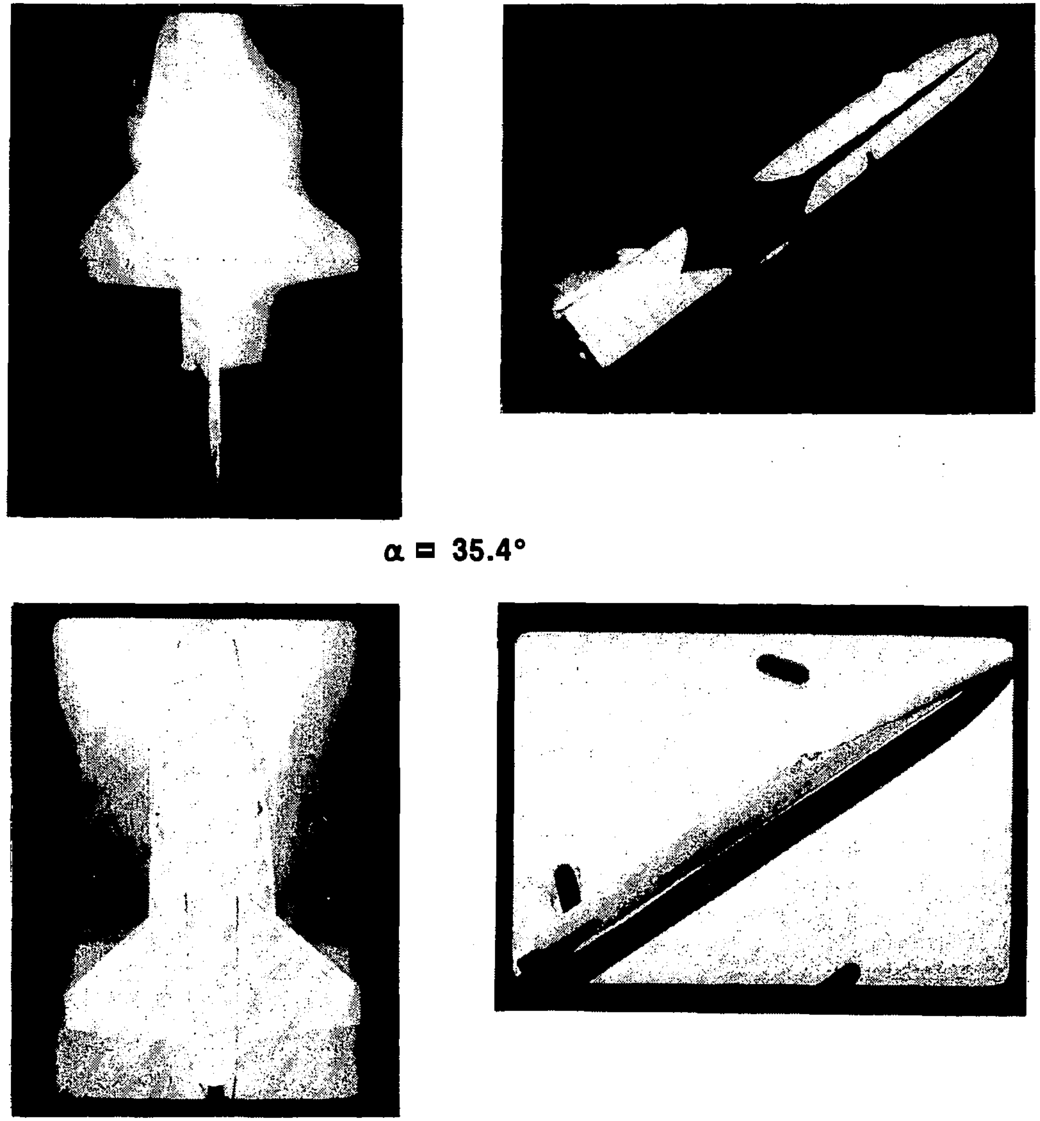

$\alpha = 35.4°$

WATER

$\alpha = 37.6°$

(e) $\alpha \geqq 35.4^{\circ}$.

Figure 25.- Concluded.

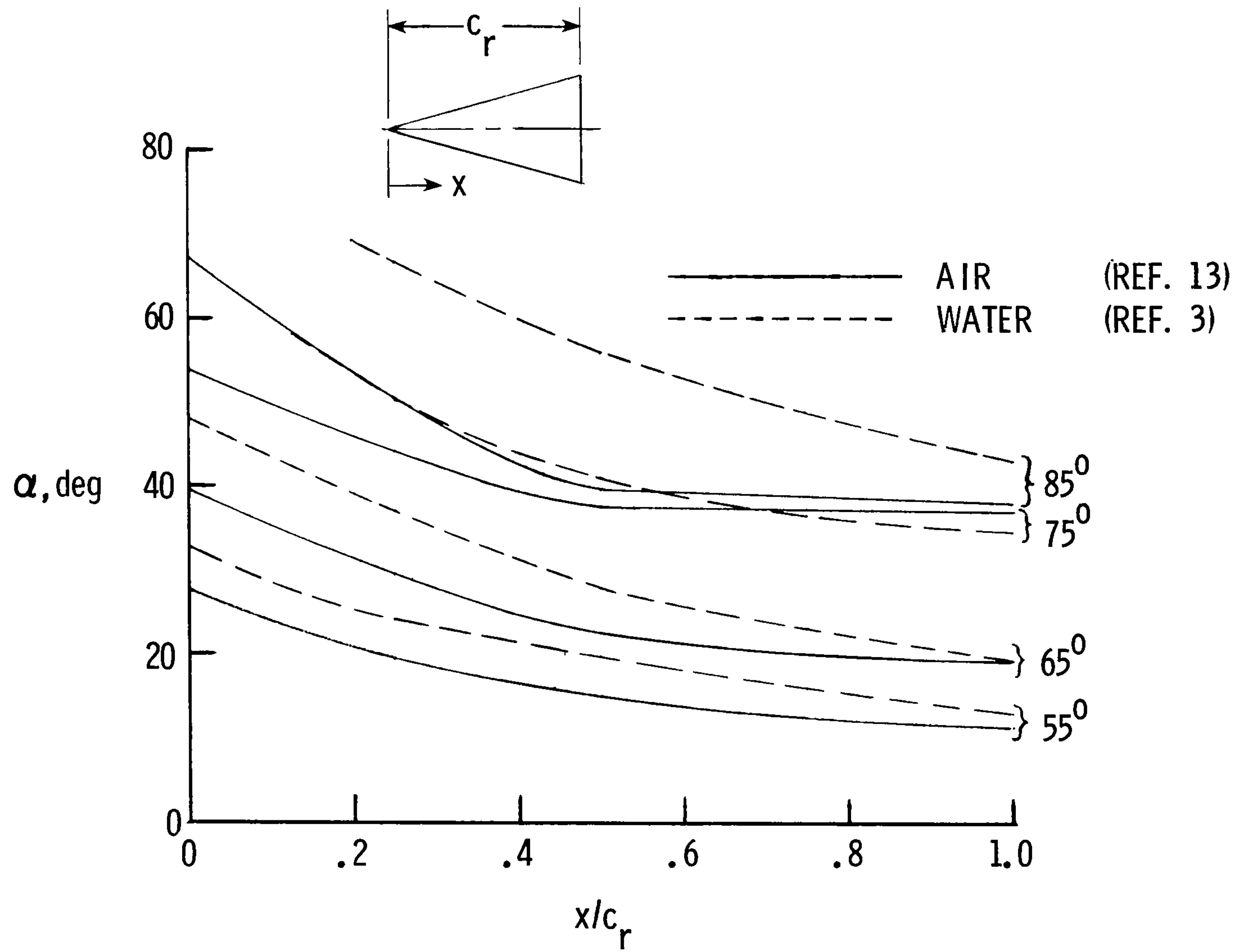

Figure 26.- Vortex breakdown progression on delta wings in air and water.

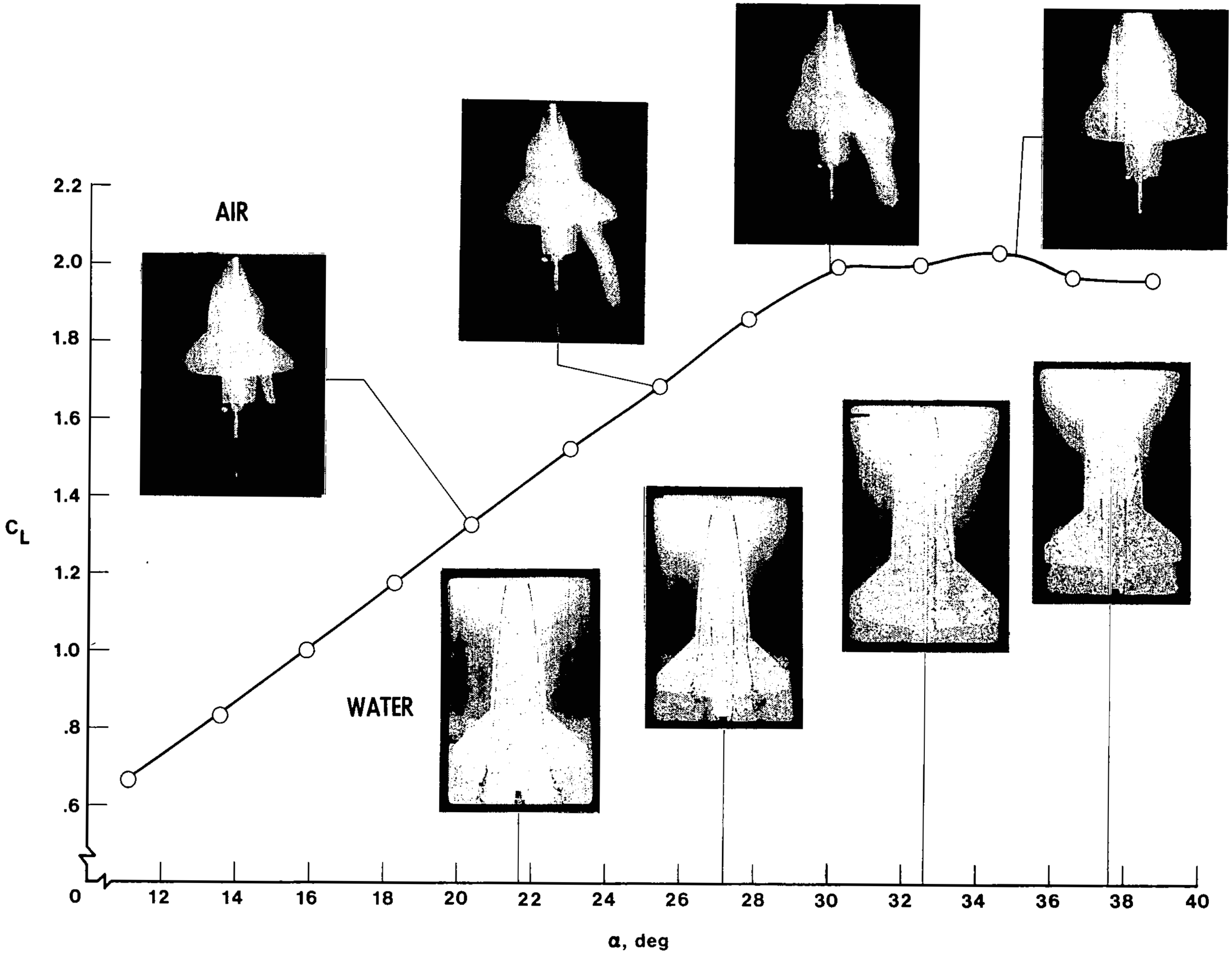

Figure 27.- Effect of strake vortex on lift data. AD 24; M = 0.3.

1. Report No.	2. Government Accession No.	3. Recipient's Catalog No.
NASA TP-1803		
4. Title and Subtitle EXPERIMENTAL AND ANALYTICAL STUDY OF THE LONGITUDINAL AERODYNAMIC CHARACTERISTICS OF ANALYTICALLY AND EMPIRICALLY DESIGNED STRAKE-WING CONFIGURATIONS AT SUBCRITICAL SPEEDS		5. Report Date June 1981 6. Performing Organization Code 505-31-43-03
7. Author(s) John E. Lamar and Neal T. Frink		8. Performing Organization Report No. L-14041
9. Performing Organization Name and Address NASA Langley Research Center Hampton, VA 23665		10. Work Unit No. 11. Contract or Grant No.
12. Sponsoring Agency Name and Address National Aeronautics and Space Administration Washington, DC 20546		13. Type of Report and Period Covered Technical Paper 14. Sponsoring Agency Code
15. Supplementary Notes		

16. Abstract

Sixteen analytically and empirically designed strakes have been tested experimentally on a wing-body at three subcritical speeds in such a way as to isolate the strake-forebody loads from the wing-afterbody loads. Analytical estimates for these longitudinal results have been made using the suction analogy and the augmented vortex lift concepts. The synergistic data are reasonably well estimated or bracketed by the high- and low-angle-of-attack vortex lift theories over the Mach number range and up to maximum lift or strake-vortex breakdown over the wing. Also, the strake geometry is very important in the maximum lift value generated and the lift efficiency of a given additional area. Increasing size and slenderness ratios are important in generating lift efficiently, but similar efficiency can also be achieved by designing a strake with approximately half the area of the largest gothic strake tested. These results correlate well with strake-vortex-breakdown observations in the water tunnel.

17. Key Words (Suggested by Author(s))	18. Distribution Statement
Strake efficiency; Theoretical estimates; Longitudinal aerodynamic characteristics; Subcritical speeds; Vortex-flow aerodynamics; Strake-wing; Analytical and empirical designs	Unclassified - Unlimited Subject Category 02

19. Security Classif. (of this report)	20. Security Classif. (of this page)	21. No. of Pages	22. Price
Unclassified	Unclassified	223	A10

For sale by the National Technical Information Service, Springfield, Virginia 22161

NASA-Langley, 1981